HARVARD UNIVERSITY
Graduate School of Arts and Sciences

DISSERTATION ACCEPTANCE CERTIFICATE

The undersigned, appointed by the

Department of Physics

have examined a dissertation entitled

Laser-Controlled Charge-Exchange Production of Antihydrogen

presented by

Robert Puryear McConnell

candidate for the degree of Doctor of Philosophy and hereby certify that it is worthy of acceptance.

Signature _____

Typed name: Professor Gerald Gabrielse, Chair

Signature _____

Typed name: Professor Eric Heller

Signature _____

Typed name: Professor Isaac Silvera

Date: August 24, 2011

Laser-Controlled Charge-Exchange Production of Antihydrogen

A thesis presented

by

Robert Puryear McConnell

to

The Department of Physics

in partial fulfillment of the requirements

for the degree of

Doctor of Philosophy

in the subject of

Physics

Harvard University

Cambridge, Massachusetts

September 2011

Thesis advisor

Gerald Gabrielse

Author

Robert Puryear McConnell

Laser-Controlled Charge-Exchange Production of Antihydrogen

Abstract

Antihydrogen, the bound state of an antiproton and positron, is a unique system that provides the opportunity for precise tests of matter-antimatter symmetry and CPT invariance. Confining antihydrogen atoms in a magnetic trap, first proposed over twenty years ago, is the most promising route to realizing precision comparisons of hydrogen and antihydrogen via laser spectroscopy. While a recent demonstration of small numbers of trapped atoms confirms the feasibility of this method, more trapped atoms will be required for precision spectroscopy of antihydrogen. This thesis reports three advances toward this goal. First, a field-boosting solenoid and rotating-wall technique allow the loading of up to 10 million antiprotons in a Penning-Ioffe trap for antihydrogen production experiments. Second, adiabatic cooling reduces the temperature of up to 3 million antiprotons to 3.5 K, the coldest antiproton temperature yet measured. Finally, a new apparatus produces antihydrogen by two-stage charge exchange. The production of 3600 ± 600 antihydrogen atoms per trial by this method is indicated, a factor of 200 increase over a previous proof-of-principle demonstration. Antihydrogen produced by charge-exchange should have the temperature of the antiprotons from which it forms, which could aid in the quest to trap sufficient numbers of atoms for precise comparisons of hydrogen and antihydrogen.

Contents

Papers and Publications

1. *Adiabatic cooling of antiprotons*
   G. Gabrielse, W.S. Kolthammer, R. McConnell, P. Richerme, R. Kalra, E. Novitski, D. Grzonka, W. Oelert, T. Sefzick, M. Zielinski, D. Fitzakerley, M.C. George, E.A. Hessels, C.H. Storry, M. Weel, A. Müllers, and J. Walz, Physical Review Letters **105**, 073002 (2011).

2. *Pumped helium system for producing 1.2 K positrons and electrons*
   J. Wrubel, G. Gabrielse, W.S. Kolthammer, P. Larochelle, R. McConnell, P. Richerme, D. Grzonka, W. Oelert, T. Sefzick, M. Zielinski, J.S. Borbely, M.C. George, E.A. Hessels, C.H. Storry, M. Weel, A. Müllers, J. Walz, and A. Speck, Nuclear Instruments and Methods in Physics Research **640**, 232 (2011).

3. *Centrifugal separation of antiprotons and electrons*
   G. Gabrielse, W.S. Kolthammer, R. McConnell, P. Richerme, J. Wrubel, R. Kalra, E. Novitski, D. Grzonka, W. Oelert, T. Sefzick, J.S. Borbely, D. Fitzakerley, M.C. George, E.A. Hessels, C.H. Storry, M. Weel, A. Müllers, J. Walz, and A. Speck, Physical Review Letters **105**, 213002 (2010).

4. *Antihydrogen production within a Penning-Ioffe trap*
   G. Gabrielse, P. Larochelle, D. Le Sage, B. Levitt, W.S. Kolthammer, R. McConnell, P. Richerme, J. Wrubel, A. Speck, M.C. George, D. Grzonka, W. Oelert, T. Sefzick, Z. Zhang, A. Carew, D. Comeau, E.A. Hessels, C.H. Storry, M. Weel, and J. Walz, Physical Review Letters **100**, 113001 (2008).

5. *Single-component plasma of photoelectrons*
   B. Levitt, G. Gabrielse, P. Larochelle, D. Le Sage, W.S. Kolthammer, R. McConnell, J. Wrubel, A. Speck, D. Grzonka, W. Oelert, T. Sefzick, Z. Zhang, D. Comeau, M.C. George, E.A. Hessels, C.H. Storry, M. Weel, and J. Walz, Physics Letters B **656**, 25 (2007).

6. *Density and geometry of single component plasmas*
   A. Speck, G. Gabrielse, P. Larochelle, D. Le Sage, B. Levitt, W.S. Kolthammer, R. McConnell, J. Wrubel, D. Grzonka, W. Oelert, T. Sefzick, Z. Zhang, D. Comeau, M.C. George, E.A. Hessels, C.H. Storry, M. Weel, and J. Walz, Physics Letters B **650**, 119 (2007).

7. *Antiproton confinement in a Penning-Ioffe trap for antihydrogen*
   G. Gabrielse, P. Larochelle, D. Le Sage, B. Levitt, W.S. Kolthammer, I. Kuljanishvili, R. McConnell, J. Wrubel, F.M. Esser, H. Glückler, D. Grzonka, G. Hansen, S. Martin, W. Oelert, J. Schillings, M. Schmitt, T. Sefzick, H. Soltner, Z. Zhang, D. Comeau, M.C. George, E.A. Hessels, C.H. Storry, M. Weel, A. Speck, F. Nillius, J. Walz, and T.W. Hänsch, Physical Review Letters **98**, 113002 (2007).

Acknowledgments

ATRAP is an intricate and complex experiment and gave me the opportunity to become familiar with many different technologies. I learned a great deal and had the chance to work with many exceptional people during my Ph. D. I would first like to thank my research advisor, Prof. Gerald Gabrielse, without whose encouragement and advice none of this work would have been possible. It is through Prof. Gabrielse's determination and vision that the project has reached the stage where it is now.

Many other members of ATRAP played an essential role in supporting and encouraging me through the years. ATRAP members from York University have worked tirelessly to keep the positron accumulator running at CERN. Matt Weel and Matt George have devoted time both to experiments and to design of new systems, while Cody Storry taught me that (nearly) anything can be built with just a hacksaw and a drill press. Eric Hessels was willing to discuss any and all aspects of the charge-exchange experiment, on occasion flying out to CERN to talk about the way forward. His encouragement when things weren't going as planned meant a great deal to me as well.

ATRAP members from Jülich kept the detector system working nearly flawlessly and were always willing to lend a hand in troubleshooting as well. Walter Oelert's words of encouragement kept us going in tough times. Dieter Grzonka frequently lent his impressive strength to apparatus repairs and upgrades. Thomas Sefzick would drop his other commitments to repair broken electronics for us. Marcin Zielinski spent many long nights at CERN making sure everything was running smoothly.

Several older members of ATRAP, including David Le Sage, Ben Levitt, and Irma Kuljanishvili, gave me valuable guidance on various pieces of the apparatus. I

appreciate the time I could spend with them and wish I coud have overlapped with them more. Andrew Speck allowed me to use a significant part of his lab space at the Rowland Institute while I was developing the cesium beam system and shared his invaluable experience with me. Many members of the Gabrielse lab at Harvard—Josh Goldman, Shannon Fogwell, Josh Dorr, Yulia Gurevich, Jack DiSciacca, Ben Spaun, Paul Hess and Elise Novitski—were willing to share their knowledge, celebrate successes, and commiserate when things didn't go as well. In addition, Josh and Elise were willing to perform the thankless job of shipping instruments and tools to CERN to help us out.

Throughout my graduate career, Jan Ragusa has kept on top of innumerable administrative details. She has always been willing to approve a last-minute purchase order, to get me a needed document, or to make sure that my stipend came through on time. Her efforts really keep the group running smoothly.

Stan Cotreau taught me how to machine, an invaluable skill which served me many times in my graduate career. Meanwhile, the workers at SEAS machine shop fabricated many challenging parts of our apparatus. Particular credit is due to Rich Anderson and Al Chandler, who took on the biggest jobs we could find for them, and to Louis Defeo, who allowed us to rush many parts through in order to get them to CERN in time for beam.

A special thanks is due to those students and postdocs who spent long hours running experiments at CERN with me. Matt George and I spent many late nights working on repairs and upgrades to the BTRAP apparatus, and his enthusiasm helped lighten a tough 2008 beam run. Adam Carew, Joe Borbely, and Dan Fitzakerley kept

positrons available for months on end and were willing to take beam, run plasma studies, or do whatever else was needed. Phil Larochelle and I lived and worked together during the 2008 beam run and shared many moments of excitement and despair together. Jonathan Wrubel introduced me to the BTRAP apparatus at CERN and taught me about all of the details involved in taking beam. Even after he left, he was always willing to answer emails about how some piece of equipment worked. Steve Kolthammer taught me the ins and outs of ATRAP when I first joined the group. We later spent two years working together at CERN, and I will always remember the times we spent together hashing out ideas for experiments and troubleshooting various aspects of the apparatus. Phil Richerme, always cheerful and upbeat, was willing to fly to CERN at a moment's notice and would selflessly direct his efforts to wherever they were needed. Rita Kalra has taken up the ATRAP mantle and has put in a lot of effort to get our next-generation apparatus going. Finally, Andi Muellers from the University of Mainz, who was responsible for the lasers used for the charge-exchange experiments, spent more time running experiments with me at CERN than anyone else. We spent many late hours taking data together and figuring out the intricacies of the charge-exchange process. I was fortunate to have such a patient and dedicated co-worker.

Finally, I would like to thank the friends and family who have supported me through my Ph. D. Their willingness to lend a sympathetic ear was especially important when the occasional setback occurred. Most important has been the constant support of my parents and brother. I have been lucky to have a family that have always stood behind me in my endeavors.

For my parents

Chapter 1

Introduction

Antihydrogen ($\overline{\mathrm{H}}$), the bound state of an antiproton ($\overline{\mathrm{p}}$) and positron (e^+), is the antimatter counterpart of hydrogen. As the simplest antimatter atom, antihydrogen is an obvious choice for the study of antimatter. Unanswered questions about the relationship between matter and antimatter still remain: are matter and antimatter truly opposites, possessing exactly equal mass but exactly inverse electrical charge? Why does our universe contain large amounts of matter but essentially no antimatter? While these questions have been approached from many angles—from cosmological observations, to experiments in high-energy accelerators, to studies in low-temperature antimatter traps—the ability to confine atoms of antimatter for long periods of time would present a unique opportunity for high-precision studies of the properties of these anti-atoms. This thesis presents recent progess towards the study of antihydrogen in a low-temperature trap.

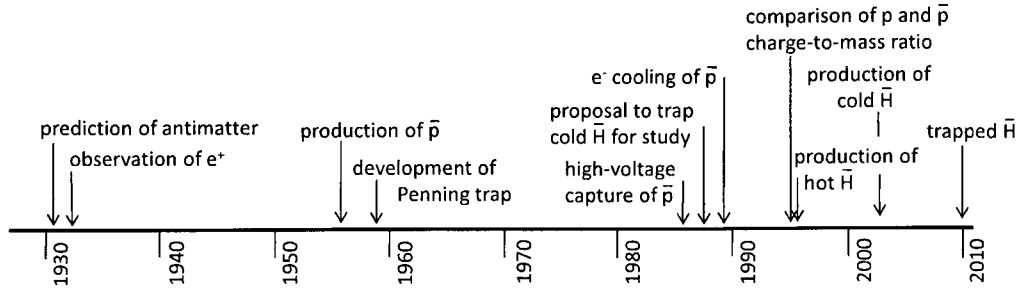

Figure 1.1: Timeline showing important milestones toward the production and study of $\overline{\mathrm{H}}$ since the discovery of antimatter.

1.1 A brief history of antimatter and antihydrogen

The existence of antimatter was first predicted in 1931 by Paul Dirac [1]. His new equation for the relativistic quantum mechanics of the electron predicted solutions for the electron of both positive and negative energy. He interpreted the negative energy states as a "sea" of electrons already in existence, and suggested that absences or "holes" in this sea would appear to observers as positively-charged particles. Initially interpreting these holes as protons [2], he soon realized that the negative-energy solutions also required the same mass as an electron. He therefore proposed the existence of "anti-electrons" with the same mass but opposite charge as the electron, and noted that electrons coming into contact with anti-electrons could annihilate and release their mass energy as radiation. Dirac also suggested that other fundamental particles, including the proton, should have their own antiparticles [1].

Dirac's theory found spectacular confirmation in the experimental observation of the positron just one year later [3]. In experiments in a cloud chamber in a strong magnetic field, scintillation tracks with the same radius of curvature but curving in

the opposite direction as an electron's track were observed. The conclusion was that a new type of particle with the same mass but opposite charge as the electron had been discovered, and these positive electrons or "positrons" were quickly identified with Dirac's anti-electron [4].

Positrons, e^+, are readily produced by the radioactive decay of certain elements, but the antiproton ($\overline{p}$) is much rarer in nature. The first observation of antiprotons required a particle accelerator to produce proton-antiproton pairs in the high-energy collision of a proton with a fixed target [5]. Antiprotons were later identified as a rare component of the cosmic ray spectrum [6].

The production of $\overline{p}$ in an accelerator led to innovative proposals for the precision study of the antiproton and its comparison to the proton [7, 8]. These proposals focused on the confinement of $\overline{p}$ within a device known as a Penning trap. The Penning trap confines charged particles with a combination of electric and magnetic fields [9]. Proposals to use the Penning trap for antiparticle confinement [7] reached fruition in the high-voltage trapping of $\overline{p}$ [10] and the subsequent electron-cooling of $\overline{p}$ to cryogenic temperatures [11]. These techniques, now used for all cold $\overline{p}$ and $\overline{H}$ research, allowed for a very precise comparison of the charge-to-mass ratio of the antiproton and proton [12, 13].

As research on trapped $\overline{p}$ was ongoing, proposals were made to produce slow antihydrogen in a nested Penning trap [14] and to trap the resulting $\overline{H}$ atoms in a magnetic trap to allow for precision spectroscopy [15]. A subsequent proposal to produce hot (i.e., relativistic) $\overline{H}$ from collisions between high-energy $\overline{p}$ and atomic nuclei [16] resulted in the observation of 11 antihydrogen atoms at CERN's Low-energy An-

tiproton Ring (LEAR) facility in 1996 [17] and the later observation of 57 high-energy $\overline{H}$ atoms at Fermilab [18]). This approach to $\overline{H}$ production was not pursued further owing to the difficulty of using relativistic $\overline{H}$ atoms in precision measurements.

The simultaneous confinement of e^+ and $\overline{p}$ in a Penning trap [19] and the observation of cooling of $\overline{p}$ by e^+ [20] were milestones that opened the way for the production of cold antihydrogen in a nested Penning trap [21, 22, 23]. Since then, efforts have focused on realizing the proposal [15] to confine the resulting $\overline{H}$ atoms in a magnetic trap for precision spectroscopy. Confinement of $\overline{p}$ and e^- within a combined Penning-Ioffe trap [24] demonstrated that the Penning trap for charged particles and magnetic trap for neutral atoms were sufficiently compatible with each other that charged particles could be held for long enough to produce $\overline{H}$. The first observed production of antihydrogen within a Penning-Ioffe trap, reported in 2008 by ATRAP [25], established that less than 20 $\overline{H}$ atoms were being trapped per trial. The first signal from trapped $\overline{H}$, the observation of approximately one trapped atom per 9 trials, was reported in 2010 [26]. This proof-of-principle demonstration was an important step, but more trapped atoms are needed to achieve the envisioned precision comparison of hydrogen and antihydrogen. Simultaneous efforts to develop the techniques required to trap a larger number of atoms have led to the observation of centrifugal separation of $\overline{p}$ and e^- [27] and the adiabatic cooling of $\overline{p}$ to 3.5 K [28]. The evaporative cooling of $\overline{p}$ to 9 K [29] has also been demonstrated.

During the past few years, the ATRAP Collaboration has chosen to develop methods that will allow us to scale up to larger numbers of trapped $\overline{H}$ atoms. These methods now allow us to load up to 10 million $\overline{p}$ and 4 billion e^+ for experiments

and to adiabatically cool the $\overline{\mathrm{p}}$ to 3.5 K or below. This thesis describes these recent advances. The method by which $\overline{\mathrm{H}}$ is formed may also be crucial for efforts to trap more atoms. This thesis focusses on one approach: laser-controlled charge-exchange production of antihydrogen.

1.2 Antihydrogen and fundamental symmetries

Although the production and trapping of antihydrogen is of some interest in itself, the larger motivation for its study is to perform high-precision tests of the fundamental symmetries of nature. The Standard Model of particle physics predicts exact symmetries between particle and antiparticle, so tests of this equivalence both test the validity of the Standard Model and search for possible physics beyond the Standard Model. In particular, experimental comparisons of matter and antimatter are a test of the symmetry in the Standard Model known as CPT invariance.

The combined operation CPT is a sequence of three discrete operations on a system. Charge-conjugation, C, inverts the charge of all particles. Parity inversion, P, inverts the coordinate system, taking all locations $\vec{r} \rightarrow -\vec{r}$ and effectively transforming the system into its mirror image. (Technically, P inversion also requires a rotation of the coordinate system by 180° about the mirror axis, which is expected to have no experimental consequences.) Time reversal, T, changes the time coordinate $t \rightarrow -t$; it can be thought of as inverting the velocities of all particles. CPT invariance requires equal masses and equal-but-opposite charges for particles and their corresponding antiparticles.

Although it initially seemed obvious that the physics of our universe would re-

main the same in a "mirror-image" universe, it was pointed out in [30] that a test for invariance under the P operator for weak-force interactions had not yet been performed. Such a test demonstrated, quite surprisingly, that the weak force (which governs radioactive decay) violates parity symmetry [31]. In this first demonstration of P violation, the emission of β particles by magnetically polarized, radioactive ^{60}Co nuclei was found to be preferentially anti-aligned with the polarization of the nuclei. In a mirror-image world, the β emission would be aligned with the nuclear polarization. Subsequent experiments and analysis confirmed that the weak interaction maximally violates parity symmetry [32, 33, 34].

This surprising result prompted further investigations. Proposals that the combined symmetry CP should be conserved in all physical processes [35] were contradicted by the 1964 observation of CP violation in the neutral kaon system [36]. Subsequent investigations, however, have confirmed invariance of the full symmetry CPT to a high degree of precision in a number of experiments. The CPT theorem in the Standard Model of physics requires CPT invariance in any quantum field theory obeying both locality and Lorentz invariance [37]. There is thus some reason to expect CPT symmetry to be preserved in nature. (This reason would be more compelling if quantum field theories which incorporate the gravitational force could be formulated.) Precise tests of CPT represent an important test of the Standard Model and any violations would point the way to physics beyond the Standard Model.

Figure 1.2 illustrates the relative precision of many tests of CPT invariance. The ratio of neutral kaon masses $m_K/m_{\overline{K}}$ has the lowest fractional precision of any test of CPT invariance due to the unique ability to use an interferometric measurement to

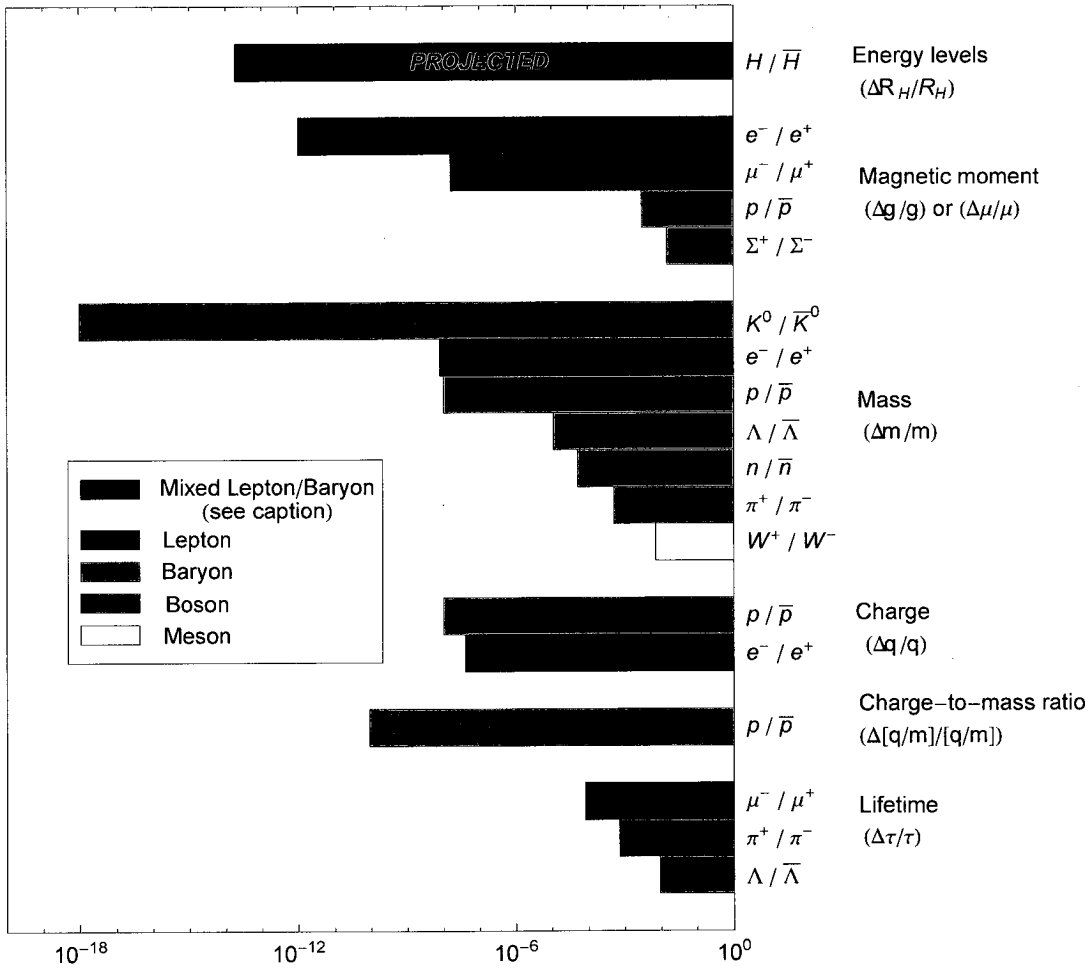

Figure 1.2: Comparison of fractional precision of tests of the combined symmetry CPT. The projected sensitivity for an H / $\overline{\text{H}}$ comparison is based on the currently achieved precision for the $1S$-$2S$ line in H. While an H / $\overline{\text{H}}$ comparison is an important potential CPT test for a combined lepton-baryon system, it only tests at the precision shown for CPT-violating terms coupling to leptons. CPT-violating terms coupling to baryons are tested at a factor of $\sim m_p/m_e = 1836$ times lower sensitivity.

determine the very small mass difference between the two observable kaon eigenstates K_{long} and K_{short}. This test is also important as it is a test of CPT invariance in a system which demonstrates CP violation. Nevertheless, this test confirms CPT invariance only for the masses of one meson system. Tests in other systems—particularly those involving leptons and baryons—thus seem warranted. It is difficult to know in advance in what way possible CPT violating terms might appear and in what sorts of measurements their effects might be seen.

A comparison of the $1S \rightarrow 2S$ transition in H and $\overline{\text{H}}$ would be a direct comparison of the Rydberg constant for hydrogen and antihydrogen,

$$\frac{R_{\overline{H}}}{R_H} = \frac{\left(1+\frac{m_{e^-}}{m_p}\right)}{\left(1+\frac{m_{e^+}}{m_{\overline{p}}}\right)} \left(\frac{m_{e^+}}{m_{e^-}}\right) \left(\frac{q_{\overline{p}}}{q_p}\right)^2 \left(\frac{q_{e^+}}{q_{e^-}}\right)^2 \tag{1.1}$$

and would therefore be a sensitive test of the equality of charges and masses for both leptons and baryons. The narrow 1.3 Hz linewidth of the $1S \rightarrow 2S$ transition allows for extraordinarily accurate measurements of this energy spacing. If spectroscopy on $\overline{\text{H}}$ can be performed to the same 1.8×10^{-14} fractional error of this measurement in H [38], the $\overline{\text{H}}$-H comparison promises the most accurate test of CPT violation in a lepton system. While the effect of the p and $\overline{\text{p}}$ masses on the Rydberg constants for H and $\overline{\text{H}}$ is smaller (as seen in Equation 1.1), the $\overline{\text{H}}$-H comparison is also a very sensitive test for CPT-violating terms coupling to baryons. Further theoretical work on possible CPT-violating terms in an extension of the Standard Model suggests that study of $\overline{\text{H}}$ $1S \rightarrow 2S$ and ground-state hyperfine transitions may provide a more precise constraint on CPT violation than other lepton and baryon measurements [39].

How many trapped antihydrogen atoms are required for precision spectroscopy? The two major requirements are a spectroscopy signal distinguishable from back-

ground fluctuations and a narrow measurement linewidth. One analysis of such a measurement at the 10^{-12} level suggests two-photon spectroscopy of the $1S \rightarrow 2S$ transition of 1,000 $\overline{\mathrm{H}}$ atoms [40]. Excitation is accompanied by microwave quenching of excited $\overline{\mathrm{H}}$ to the $2P$ level and subsequent detection of the 121.5 nm photons resulting from rapid decay of the $2P$ state. It may be possible to achieve even greater precision by an "annihilation spectroscopy" experiment where atoms are excited to the long-lived $2S$ state and then rapidly removed from that state in a way which ejects them from the magnetic trap; the resulting annihilation signal may provide better signal-to-noise than detection of Lyman-α photons.

Proposals have also been made to study the interaction of antimatter with gravity using larger numbers of trapped $\overline{H^-}$ ions laser-cooled to less than 1 mK [41, 42]. The weak nature of the gravitational interaction (10 cm height difference corresponds to approximately 100 μK of thermal energy) makes this measurement a challenge. Nevertheless, a new experimental group at CERN proposes to perform an interferometric measurement of antimatter gravity with an $\overline{\mathrm{H}}$ beam [43]. Both trapped $\overline{\mathrm{H}}$ and cold $\overline{\mathrm{H}}$ beams may ultimately be able to realize precision tests of antimatter's gravitational interaction with matter.

1.3 Overview of this thesis

The field of $\overline{\mathrm{H}}$ study has been especially active since the first observations of $\overline{\mathrm{H}}$ formation in a Penning trap in 2002 [21, 22]. Efforts have focused on studying the behavior of charged particles in combined Penning-Ioffe traps, on loading larger numbers of particles, on producing the coldest plasmas possible, and on experiments

to trap antihydrogen. This thesis discusses much of the work that has been done in these areas over the last few years.

Chapter 2 of this thesis discusses the ATRAP cryogenic Penning-Ioffe trap apparatus in detail. Chapter 3 reviews the methods developed by ATRAP to load the three species of particles we use: electrons, positrons, and antiprotons. It also discusses techniques for manipulating and detecting these particles. This chapter details the advances made in particle loading over the last two beam runs, now allowing us to efficiently load up to 10 million antiprotons and up to 4 billion positrons.

Chapter 4 discusses theory and experiments related to plasmas in a Penning trap. Chapter 4 also discusses the centrifugal separation of antiprotons and electrons, an important result from this collaboration in 2010 and the first observation of such separation with elementary particles. Another important ATRAP result from the 2010 beam run is the adiabatic cooling of up to 3×10^6 antiprotons to a temperature no more than 3.5 K. Chapter 5 discusses measurements of particle temperatures and describes the method used to obtain this result.

Chapter 6 discusses antihydrogen formation mechanisms with a focus on three-body recombination, the mechanism by which antihydrogen was first produced in a Penning trap. This chapter also discusses important studies by ATRAP and others into the stability of charged particles within a combined Penning-Ioffe trap, with important consequences for experiments to trap antihydrogen. Finally this chapter discusses the recent result of trapped antihydrogen and its implications for the future of antihydrogen spectroscopy.

Chapter 7 discusses the implementation of a cryogenic Rydberg Cs source to pro-

duce antihydrogen by two-stage charge exchange. This chapter discusses the benefits and drawbacks of this approach to forming antihydrogen. Results obtained from the past two years, including a factor of 500 increase in on-axis charge-exchange Ps production (the first stage of the reaction), and good evidence of the production of 3600 $\pm$ 600 $\overline{\mathrm{H}}$ atoms by this method, are also discussed. Finally, this chapter briefly describes the future outlook for antihydrogen production by two-stage charge exchange. A brief concluding chapter examines the state of antihydrogen research today and the outlook for high-precision $\overline{\mathrm{H}}$ spectroscopy in the near future.

ATRAP is a collaboration composed of many members, all of whom made significant contributions to the work discussed here. As one of two or three people primarily responsible for operation of the Penning-Ioffe trap apparatus at CERN over the past few years, I was heavily involved in construction and maintenance of apparatus and in the major results obtained by the collaboration. This thesis will focus on the work I have done and the results that I have obtained. Two particular projects for which I was primarily responsible include the design and implementation of the field-boosting solenoid for antiproton loading and the construction and operation of the cryogenic Rydberg Cs source for the production of antihydrogen by two-stage charge exchange.

Chapter 2

Apparatus

The production, detection, and trapping of cold $\overline{\mathrm{H}}$ necessitates a complex apparatus that must meet many requirements. The charged particles which are the constituents of $\overline{\mathrm{H}}$ must first be confined and made to interact to form $\overline{\mathrm{H}}$. A set of Penning trap electrodes, combined with a uniform axial magnetic field, are used for charged particle confinement. Neutral atoms (not confined by the Penning trap) require a different trapping mechanism. A Ioffe trap is added as a way to confine the neutral $\overline{\mathrm{H}}$. Additional requirements include ultra-high cryogenic vacuum to prevent annihilation of the antiparticles by matter vacuum contaminants, optical access for the excimer laser required for e^- loading (and other lasers for future laser cooling and spectroscopy of $\overline{\mathrm{H}}$), and a very large number of electrical connections.

The original Penning traps used by the ATRAP collaboration for the production of $\overline{\mathrm{H}}$, referred to as HBAR1 and HBAR2, are described more fully in [44, 45, 46]. In order to allow for the combination of a Penning trap and a Ioffe trap we built a new experimental platform, given the name ATRAP2. Two copies of this apparatus,

informally referred to as ATRAP and BTRAP, were constructed. The apparatus known as ATRAP is currently scheduled to be converted into an ultra-low-noise trap for precision measurements on single antiprotons. Experiments in the 2009 and 2010 beam runs were performed in the BTRAP apparatus, which has consequently diverged somewhat from ATRAP during this time. In addition, a third apparatus, referred to as CTRAP, is scheduled to come online in 2011. Further details about the CTRAP apparatus can be found in [47].

This chapter will discuss the essential pieces of the BTRAP apparatus, shown in Figure 2.1. The heart of the BTRAP apparatus consists of 39 hand-polished Penning trap electrodes. These electrodes are enclosed within a titanium vacuum enclosure that provides the required ultra-high vacuum. The Ioffe trap is a superconducting magnet surrounding the upper regions of the Penning trap electrode stack. Below the Ioffe trap, a field-boosting superconducting solenoid is mounted that is used to enhance antiproton loading. The Penning trap electrodes are cooled to 1.3 K by a pumped liquid helium system mounted above the Ioffe trap. Above this is a reservoir of liquid helium at 4.2 K. This helium dewar, with a capacity of 40 liters of liquid helium, cools the superconducting magnets and provides the helium input to the 1.1 K pumped helium system. A series of copper thermal isolation plates covered with sheets of aluminized mylar isolate the cryogenic parts of the apparatus from room-temperature radiation. Electrical connections and optical access to the trap are provided by the room-temperature top plate of the experimental platform. The entire Penning-Ioffe apparatus sits inside of a three-layer cryogenic insert dewar which is kept at high vacuum to prevent thermal coupling between the apparatus and room

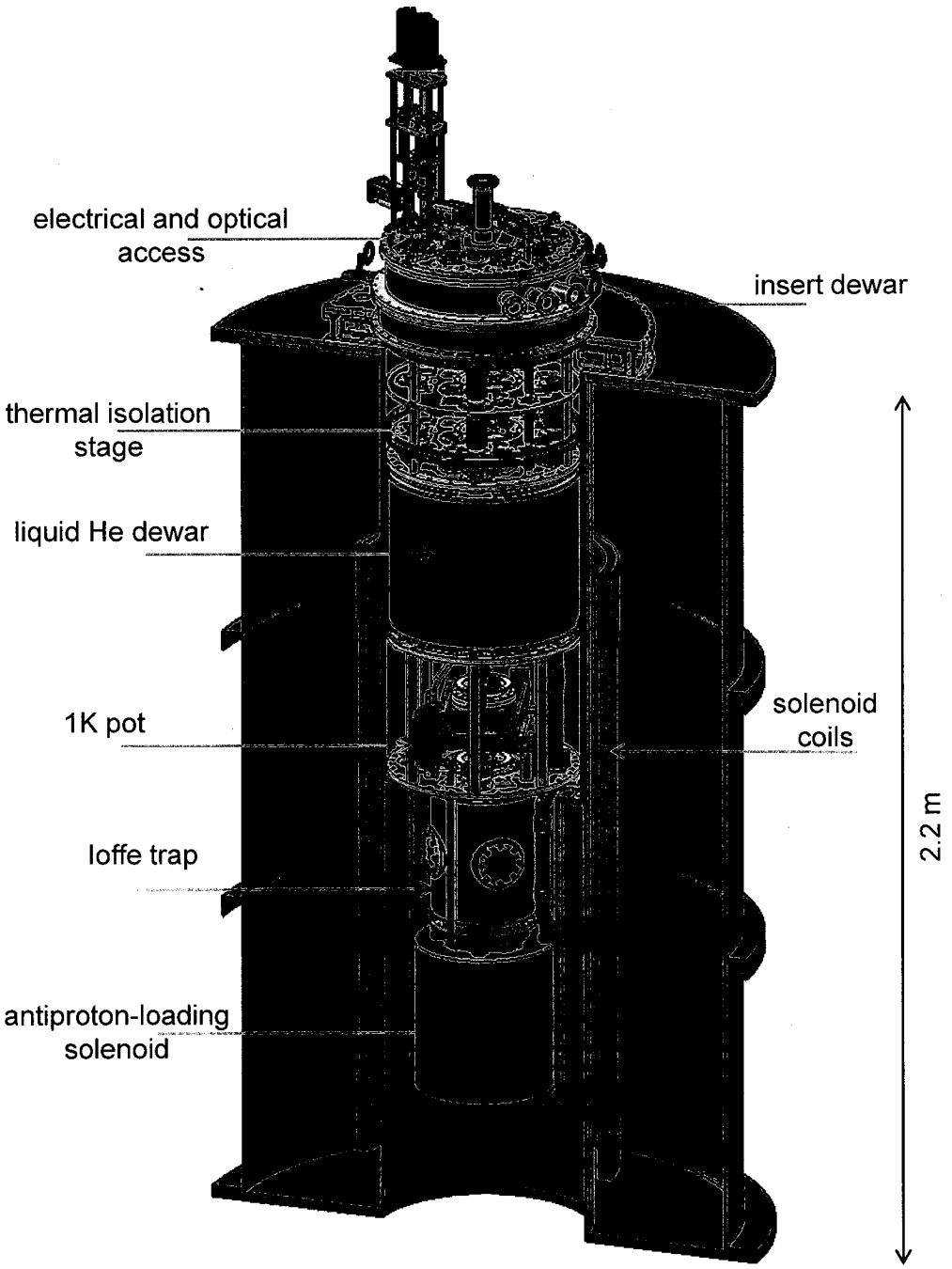

Figure 2.1: The BTRAP cryogenic Penning-Ioffe trap apparatus used for the production and trapping of $\overline{\mathrm{H}}$.

temperature. The two inner layers of this insert dewar are cooled by a pulse tube refrigerator (Cryomech PT405) to reduce the radiative heat load on the apparatus. Outside of the insert dewar are located four layers of scintillating fiber detectors used to monitor the annihilation signal from $\overline{\mathrm{p}}$. These detectors are in turn surrounded by the large superconducting solenoid which provides a constant and high uniformity background magnetic field of 1 T for the Penning trap. Finally, outside of this solenoid are located additional scintillating paddles for further detection of $\overline{\mathrm{p}}$ annihilations.

2.1 The Penning trap

2.1.1 Theory

The Penning trap uses a combination of electrostatic and magnetic fields to confine charged particles [9, 48]. Although an electrostatic field minimum seems like it would be the easiest way to confine charged particles, Gauss's law prevents such a minimum in a region free of external charges. Charged particles can, however, be confined in a trap consisting of a combination of a uniform axial magnetic field $B_0\hat{z}$ and an electrostatic quadrupole potential. The quadrupole potential provides a restoring force in the axial direction while the magnetic field causes particles to be confined to field lines, resulting in stable confinement.

The electrostatic quadrupole potential can be written as

$$\phi(\vec{r}) = \phi_0(z^2 - \frac{1}{2}\rho^2), \tag{2.1}$$

with z the axial coordinate and ρ the radial coordinate. This potential can be produced by applying a voltage V_0 to two hyperbolic electrodes located at $\pm z_0$ while

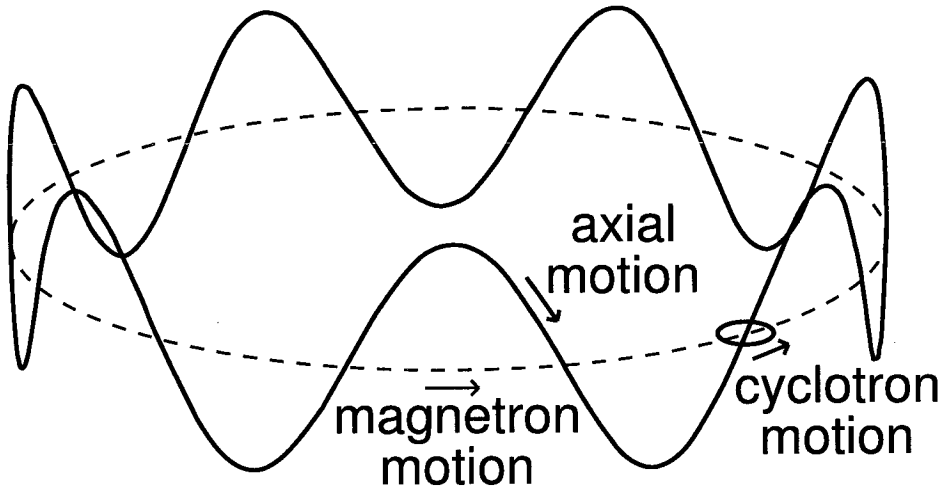

Figure 2.2: Three motions of a single particle in a Penning trap.

keeping two additional hyperbolic electrodes in the radial plane at $V = 0$. In practice, however, hyperbolic electrodes are difficult to machine and make the access required for loading particles very difficult. A good approximation to a quadrupole potential can be provided by a series of cylindrical electrodes [49].

The motion of a single particle in a Penning trap has been studied extensively [48] and will be reviewed only briefly here. The particle motion obeys the equation

$$m\ddot{\vec{r}} = q(-\nabla\phi - \dot{\vec{r}} \times \vec{B}), \tag{2.2}$$

which can be simplified to

$$\begin{aligned} m\ddot{z} &= -q\phi_0 z \qquad (2.3)\\ m\ddot{x} &= q\phi_0 x - q\dot{y}B_0 \\ m\ddot{y} &= q\phi_0 y + q\dot{x}B_0. \end{aligned}$$

Simple harmonic motion in the axial direction can easily be recognized with a fre-

Motion	Frequency (e^-)	Frequency ($\overline{p}$)
Cyclotron	28 GHz	15 MHz
Axial	35 MHz	820 kHz
Magnetron	22 kHz	22 kHz

Table 2.1: Typical frequencies of the three separable motions for particles confined within the BTRAP Penning trap.

quency

$$\omega_z = \sqrt{\frac{q\phi_0}{m}}. \tag{2.4}$$

The radial equations can be solved by making the substitution $u = x + iy$ and writing the cyclotron frequency $\omega_c = \frac{qB_0}{m}$ to give:

$$\ddot{u} + i\omega_c\dot{u} - \frac{1}{2}\omega_z^2 u = 0. \tag{2.5}$$

The solution to this equation (normally found by separation of variables [48]) is given by $u = e^{-i\omega_\pm t}$, with

$$\omega_\pm = \frac{1}{2}\left(\omega_c \pm \sqrt{\omega_c^2 - 2\omega_z^2}\right). \tag{2.6}$$

A requirement for the stability of the motion is that

$$\omega_c > \sqrt{2}\omega_z. \tag{2.7}$$

The motion of the charged particle is therefore the sum of three motions: simple harmonic motion at ω_z, high-frequency orbits around field lines at the modified cyclotron frequency ω_+, and a large-radius "magnetron" motion at frequency ω_-. The resultant motion is shown in Figure 2.2. In ATRAP's Penning traps the three frequencies obey the relation $\omega_+ \approx \omega_c \gg \omega_z \gg \omega_-$. Typical frequencies for these motions are shown in

Table 2.1. The magnetron motion can be understood by reference to the drift velocity $\vec{v_d} = \vec{E} \times \vec{B}/B^2$ of a charged particle in crossed electric and magnetic fields and is thus independent of the particle mass.

Cylindrical Penning trap electrodes do not produce perfect quadrupole potentials. In addition, we sometimes need to use complicated potential structures to simultaneously confine particle clouds of different species near one another, which will consequently depart further from the idealized quadrupole model. In order to understand how particles in the trap will behave, we need to know the potential produced at all points in the trap by the voltages applied to our electrodes. We can calculate this potential either by an analytic expansion [48] or by numerical relaxation methods [50].

The potential can be expanded about the center of the trap as the sum of a series of Legendre polynomials, $P_j(\cos(\theta))$; this expansion has been extensively described in other works and is crucial to the understanding of precision Penning trap experiments [48]. For a single electrode centered about $z = 0$, or a series of electrodes to which potentials symmetric about $z = 0$ are applied, the resulting trap potential can be written (in spherical coordinates) as

$$\phi(r,\theta) = \frac{1}{2}\sum_{\substack{j=0 \\ \text{even}}}^{\infty} C_j^{(0)} \left(\frac{r}{d}\right)^k P_j(\cos(\theta)). \tag{2.8}$$

Here the dimensional constant d satisfies $d^2 = 1/2(z_0^2 + \rho_0^2/2)$, with z_0 the half-length of the central electrode and ρ_0 the electrode radius. The advantage of this formulation is that the coefficient C_2 represents the quadratic or harmonic coefficient of the potential expansion, with all $C_{k>2}$ representing anharmonic coefficients (C_0 represents a constant and unobservable offset to the trap potential). An antisymmetric potential

applied to the electrodes can be written as a sum of only odd Legendre polynomials. The full trap potential can then be represented as a complete sum of all even and odd terms.

It can be convenient to first represent the trap potential as a sum of modified Bessel functions, $I_0(z)$:

$$\phi(\rho, z) = \sum_{n=0}^{\infty} S_n I_0(k_n \rho) \cos(k_n z), \tag{2.9}$$

with

$$k_n = \frac{(n + \frac{1}{2})\pi}{L}. \tag{2.10}$$

The coefficients S_n can be calculated in a straightforward way from the boundary conditions:

$$S_n = \frac{2}{I_0(k_n \rho_0) L} \int_0^L V(\rho_0, z) \cos(k_n z) dz, \tag{2.11}$$

where the length of the electrode stack is $2L$, the electrode radius is ρ_0 and $V(\rho_0, z)$ represents the potential applied to the electrodes as a function of axial position. Typically, grid files for the electrode stack are generated by determining the expansion coefficients S_n for each electrode held at potential of 1 V while all others are held at 0 V. The total trap potential is then calculated by voltage superposition,

$$\phi_{trap}(\vec{r}) = \sum_i V_i \phi_i(\vec{r} - z_i), \tag{2.12}$$

to find the potential due to all electrodes i at positions z_i in the stack. The coefficients S_n of the Bessel function expansion and C_j of the Legendre polynomial expansion are related by

$$C_j = 2\frac{(-1)^{j/2}}{j!} \sum_{n=0}^{\infty} (k_n d)^j \frac{S_n}{V_0}. \tag{2.13}$$

Calculation of the coefficients C_j allows traps to be built with minimum anharmonicity, which has been especially important for precision measurements of single particles in a Penning trap.

While good convergence from the analytic expansion is obtained for radii $\rho \ll \rho_0$, an increasing number of terms is required to obtain convergence of the series at large radii. Numerical relaxation calculations can instead be used to calculate the potential $\phi(\vec{r})$ in our trap [50]. These relaxation calculations find the unique potential satisfying Laplace's equation $\nabla^2\phi = 0$ through an iterative method. The procedure can be thought of as solving a "diffusion" equation, $\partial\phi/\partial t = D\,\nabla^2\phi$. As $t \to \infty$ the rate of change $\partial\phi/\partial t \to 0$ and the resulting potential expression becomes an arbitrarily good solution to Laplace's equation. To use the relaxation method in our trap, the potential is discretized on a grid of points subject to boundary conditions given by the electrode voltages. In rectangular coordinates a solution can be found by repeatedly setting the potential at each point equal to the average of its neighbors' potentials. The cylindrical geometry renders the solution somewhat more complicated due to the divergence at $\rho = 0$, but the equations can be recast in cylindrical form as

$$\begin{aligned}
\phi_{i,j}(n+1) &= \frac{1}{4}\left(\phi_{i+1,j}(n) + \phi_{i-1,j}(n) + \left(1+\frac{1}{\rho}\right)\phi_{i,j+1}(n) + \left(1-\frac{1}{\rho}\right)\phi_{i,j-1}(n)\right), \\
\phi_{i,0}(n+1) &= \frac{1}{6}\left(\phi_{i-1,0}(n) + \phi_{i+1,0}(n) + 4\phi_{i,1}(n)\right).
\end{aligned} \tag{2.14}$$

Here $\phi_{i,j}(n)$ represents the nth iteration of the potential at axial coordinate i and radial coordinate j. The second equation is used to avoid the singularity at $\rho = 0$.

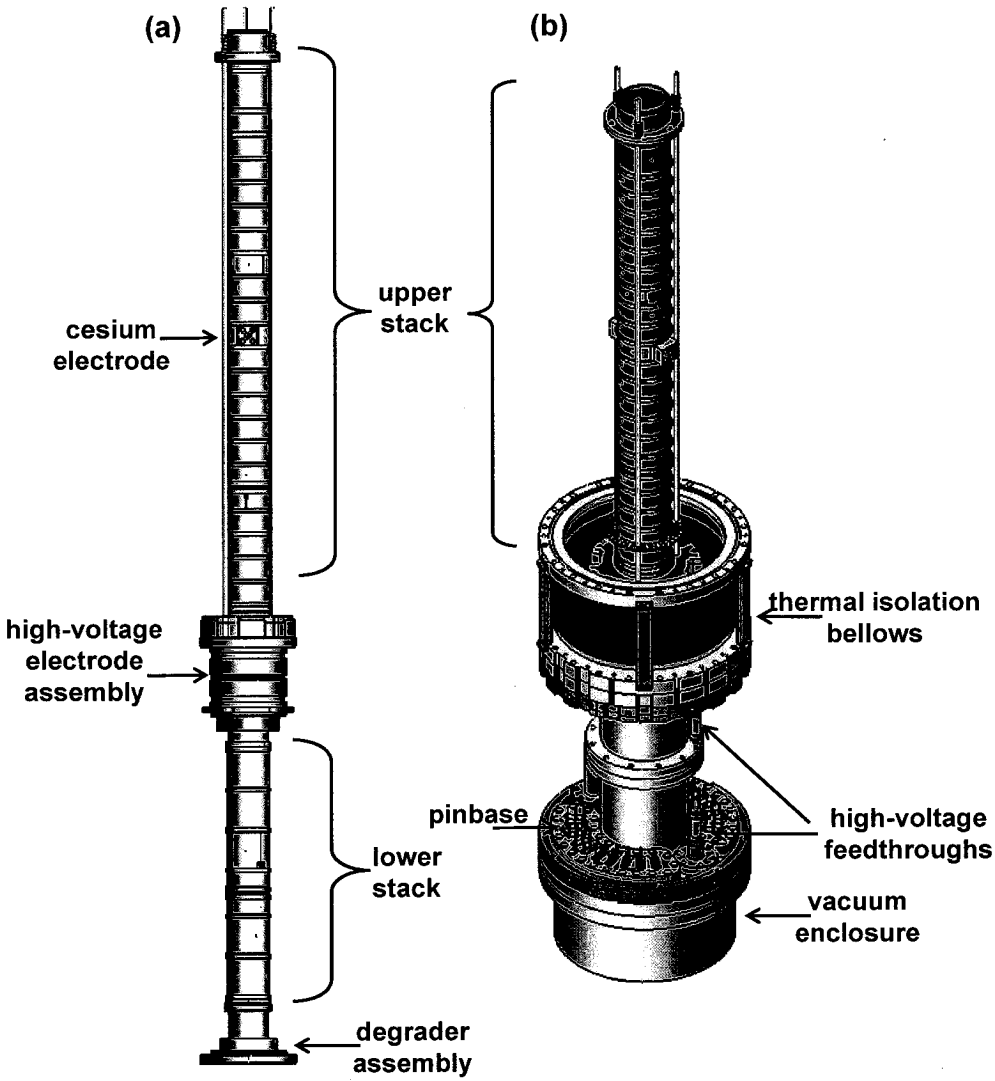

Figure 2.3: (a) Side view of the Penning trap electrode stack used for confinement of charged particles. (b) Electrode stack with some of the surrounding titanium vacuum enclosure.

2.1.2 The ATRAP2 Penning trap

Figure 2.3 shows the electrode stack used in the BTRAP apparatus. The need to load many species of particles, perform various manipulations on them, bring multiple species into close proximity and to vary potentials to produce the interactions allowing $\overline{H}$ formation led to the construction of a stack of 39 hand-polished, gold-plated electrodes. The potential applied to each of these electrodes can be independently set.

The electrode stack consists of two main sections, the lower and upper regions. The lower stack is the region in which antiprotons are loaded. Two electrodes, the Be degrader and the high-voltage electrode, are capable of being biased to 5 kV in order to trap high-energy $\overline{p}$ entering the apparatus. The other electrodes typically operate at voltages less than 1 kV. Macor spacers electrically isolate the electrodes and are precision-machined to guarantee proper alignment of the electrode stack. One special electrode in the upper stack, the cesium electrode, is designed with a small hole in two ends in order to allow a beam of laser-excited Cs atoms to enter the Penning trap region. This Cs beam is used to induce $\overline{H}$ formation by two-stage charge-exchange, which will be described in greater detail in Chapter 7.

The electrode stack is contained within a titanium vacuum enclosure; the absence of any ferrous materials (including stainless steel) from the Penning trap regions of our apparatus minimizes distortion of the uniform 1 T bias field. Copper pinbases containing brazed electrical feedthroughs permit DC and high-frequency electrical signals to be applied to the electrodes. Two high-voltage feedthroughs allow voltages up to 5 kV to be applied to the Be degrader and the high-voltage electrode. The

titanium vacuum enclosure makes a vacuum connection to the Ioffe trap (described below) through a custom titanium thermal isolation bellows section. This thermal-isolation bellows assembly allows the stack vacuum enclosure and trap stack to be cooled to 1.2 K by a pumped helium system [51] while the Ioffe trap remains at 4.2 K with its superconducting coils bathed in atmospheric pressure liquid helium.

A series of custom-built, low-noise, high-voltage "UberElvis" amplifiers allow us to independently set potentials up to 1 kV on any of the trap electrodes. These amplifiers are connected to a "high-voltage matrix" system which allows us to switch a number of special supplies or monitors, including a Keithley digital multimeter and a custom ramp generator, to any electrode. Custom-built filter boards mounted above the pinbases provide *RC* filtering with a 1 ms time constant for each electrode. The electrodes are also capacitively coupled to micro-coax lines which allow fast pulses to be applied to any of the electrodes. These RF lines are 50 Ω terminated to prevent reflections of applied pulses. Exceptions are lines applied to the segmented rotating-wall (RW) electrodes, to which twisted foursomes of wire allow the application of a phased sinusoidal drive for control of plasma radius; this technique will be described further in Chapter 4.

2.2 Ioffe trap for neutral atoms

The Penning trap provides excellent and stable confinement of charged particles for very long times. However, it cannot be used to trap neutral atoms. Trapping of neutral atoms, including $\overline{\mathrm{H}}$, requires a different technology. The BTRAP apparatus incorporates a Ioffe trap which traps neutral atoms via a gradient magnetic field, as

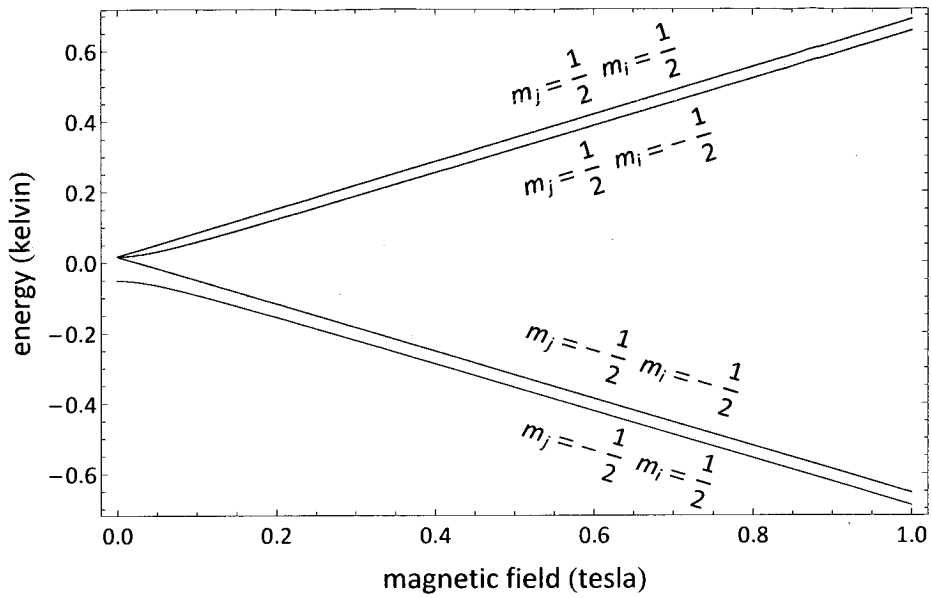

Figure 2.4: Zeeman shift of the ground state levels of H in a magnetic field. Those states whose energy increases with increasing field ("high-field-seeking") can be trapped by a magnetic field minimum.

suggested long ago [15].

In its ground state the energy levels of H undergo a Zeeman shift in a magnetic field B. For sufficiently large field (on the order of 0.1 T) the energy shift is given by

$$\Delta E = \mu_B g_j m_j B + \mu_B g_I m_I B, \tag{2.15}$$

with μ_B the Bohr magneton, g_j and g_I the spin-orbit and nuclear g-factors, respectively, and $m_j = \pm 1/2$ and $m_I = \pm 1/2$ the electron and nuclear magnetic quantum numbers. This energy splitting is shown in Figure 2.4. The energy splitting is of order 1 K for magnetic fields of order 1 T.

A Ioffe trap uses a strong magnetic gradient to produce a magnetic field minimum that can confine atoms in the weak-field-seeking states (those whose energy increases with increasing field) [52]. The use of such a trap for cold $\overline{\mathrm{H}}$ studies was proposed

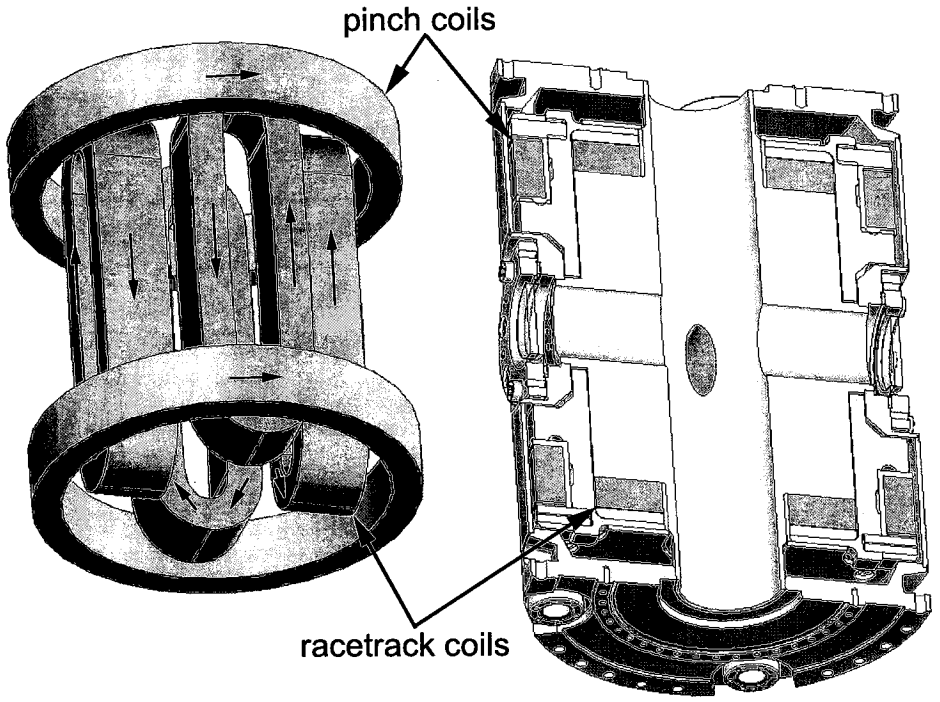

Figure 2.5: The superconducting Ioffe trap. Racetrack coils produce a quadrupole magnetic field for radial confinement of atoms, while solenoidal pinch coils produce axial confinement. The Ioffe trap is housed in a titanium enclosure with four elliptical side ports for optical or other access.

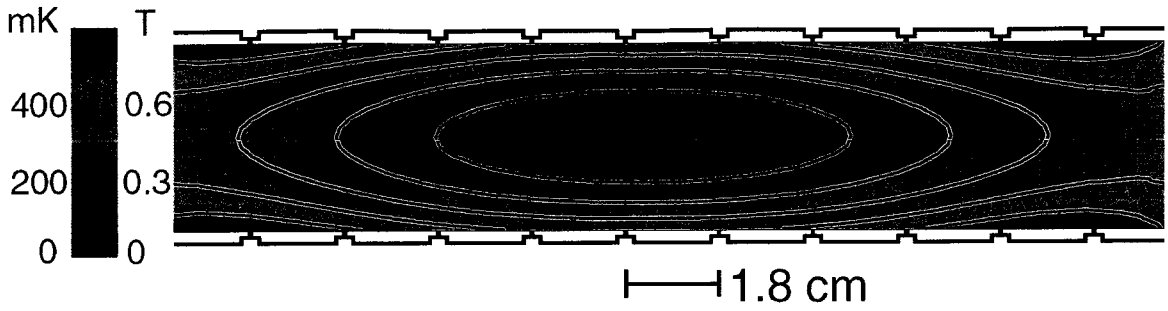

Figure 2.6: Trapping depth for ground-state H (or $\overline{\mathrm{H}}$) atoms of the nonunifom magnetic field produced by the Ioffe trap.

long ago [15]. Magnetic confinement of neutral atoms was subsequently used for the realization of Bose-Einstein condensation in atomic vapors [53, 54] and for high-precision two-photon spectroscopy of the H 1S-2S transition [55]. The particular configuration used in the BTRAP Ioffe trap is shown in Figure 2.5. It consists of four "racetrack" coils producing a quadrupole magnetic field given to lowest order near the center of the trap by

$$B_{quad} = \beta(x\hat{x} - y\hat{y}). \tag{2.16}$$

The magnitude of the quadrupole field increases with distance ρ from the central axis of the trap. The Ioffe trap also includes two circular "pinch" coils (shown in Figure 2.5) which provide an additional gradient in the axial direction. The field from the Ioffe trap is superimposed on the 1 T background field generated by our large superconducting solenoid. The 1 T background field degrades the trapping depth of the Ioffe trap to approximately 375 mK from its zero-field value of 650 mK. At the same time, the Ioffe trap destroys the cylindrical symmetry of the Penning trap, leading to questions about the stability of charged particles in the combined fields. These issues will be addressed further in Chapter 6.

Figure 2.6 shows the Ioffe trap depth within the upper electrode stack region of our trap at full field, corresponding to 69 A of current within the quadrupole racetrack coils and 80 A within each solenoidal pinch coil. The Ioffe trap center is located close to the cesium electrode shown earlier, so that $\overline{\mathrm{H}}$ produced by two-stage charge exchange will form close to the center of the Ioffe trap. The BTRAP Ioffe trap has four elliptical 51 mm $\times$ 19 mm side ports. These side ports provide space for mounting the assembly used to introduce Rydberg Cs atoms into the trap and allow us to couple laser light into the trap (for future laser cooling or spectroscopy on trapped $\overline{\mathrm{H}}$). The Ioffe trap body is constructed of titanium while the windings are superconducting NbTi wire. Laser windows on the side ports are made from MgF, a material transparent to 121.5 nm Lyman-α light for laser cooling of $\overline{\mathrm{H}}$.

Figure 2.7 shows the position of the Ioffe trap within the BTRAP apparatus. The Ioffe trap is mounted below the "octopod" area of our apparatus. This area also includes a movable two-dimensional stage, which will be described later in this chapter and allows us to place different experimental elements (a laser access window, e^+ admittance, or plasma-imaging system) on axis. Three custom titanium bellows sections connect the Ioffe trap to the 4.2 K liquid helium reservoir and contain the three sets of current leads and superconducting bus bars coupling current to the racetrack coil and the two pinch coils. The bellows sections allow for differential thermal contraction between the aluminum octopod stage supports and the titanium construction of the Ioffe trap. Within the 4.2 K liquid helium reservoir connections are made between the superconducting bus bars for the Ioffe trap and the retractable vapor-cooled current leads (AMI L-100) that minimize the heat load on the experiment when the Ioffe trap

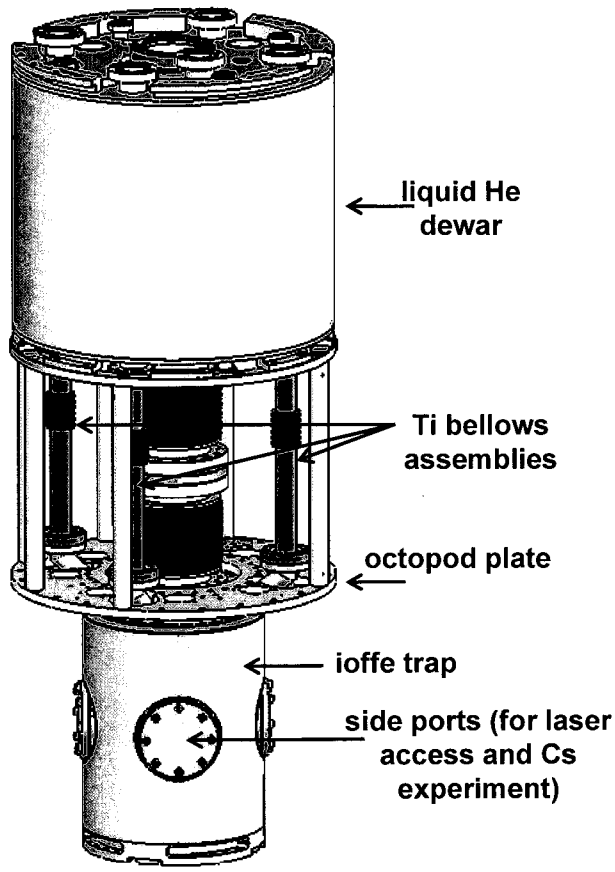

Figure 2.7: Location of the Ioffe trap within the entire cryogenic Penning-Ioffe trap apparatus and connections to the liquid helium dewar.

is not in use.

The Ioffe trap is equipped with protection diodes that allow current to bypass the superconducting coils in the event of a quench (in which the superconducting wires cease superconducting and become resistive, rapidly heating and boiling off significant amount of liquid helium). The diodes protect the superconducting coils from damage during the quench. Each diode activates at a potential difference of approximately 5 V. In doing so, the diodes limit the time in which the fields from Ioffe trap can be turned off to approximately 1 s. Since a rapid turn-off of the Ioffe trap is the main mechanism by which we look for trapped $\overline{\mathrm{H}}$, this time and the consequent background signal limits the number of trapped $\overline{\mathrm{H}}$ atoms we can reliably detect. Experiments in 2007 set a limit of less than 20 trapped $\overline{\mathrm{H}}$ atoms per trial [25], while improvements in our ability to discriminate $\overline{\mathrm{p}}$ annihilation events from background counts (described in Chapter 3) have since reduced this limit to approximately 12. A next-generation Ioffe trap which can be turned off in 10 ms is currently under construction and should provide us with background-free detection of any trapped $\overline{\mathrm{H}}$.

The current BTRAP Ioffe trap was designed at Harvard and fabricated by the ACCEL company in collaboration with ATRAP team members from Juelich.

2.3 Field-boosting solenoid for improved $\overline{\mathrm{p}}$ capture

Previous generations of TRAP and ATRAP apparatus have used magnetic fields higher than 1 T for the capture of $\overline{\mathrm{p}}$ in Penning traps. However, these high background fields are not compatible with reasonable trapping depths in a Ioffe trap for neutral atoms. As a result, in the BTRAP apparatus the large solenoid background field is

held only at 1 T. We have observed that the efficiency of our $\overline{p}$ capture is significantly reduced in lower magnetic fields [56]. As a result, we implemented a field-boosting solenoid in the lower stack region of the trap (where $\overline{p}$ are high-voltage captured and cooled by e^-).

Figure 2.8 shows a cross-section of the antiproton-loading solenoid. When operating at its typical current of 55 A, the solenoid boosts the field in the lower-stack region of the trap to 3.7 T. The solenoid is compatible with a 40-s ramp up and ramp down time, allowing us to rapidly increase the field in this region of the trap for $\overline{p}$ catching and then reduce the field in order to transfer $\overline{p}$ into the lower-field regions of the trap for $\overline{H}$ production experiments. For the 2009 and 2010 beam runs, our electronics limited us to ramping times of approximately six minutes. New power supplies available for the 2011 beam run allow us to ramp the solenoid in under one minute. The 7.4-inch bore of the solenoid allows room for the electrode stack, vacuum enclosure, and trap wiring within the solenoid's inner diameter. The solenoid inductance is 28 H. At its typical operational current of 55 A, the energy stored in the solenoid is enough to boil off 40 % of the liquid helium stored in our helium reservoir. Such a quench has occurred once, due to a faulty room-temperature high-current connection, but aside from boiling off large amounts of liquid helium the quench did not damage the solenoid or any parts of the cryogenic apparatus.

Figure 2.9 shows the field produced by the antiproton-loading solenoid. Shim coils within the magnet produce a high field uniformity within most of the lower stack where $\overline{p}$ are loaded. The field is at least 3.0 T at all points between the high-voltage electrode and the degrader.

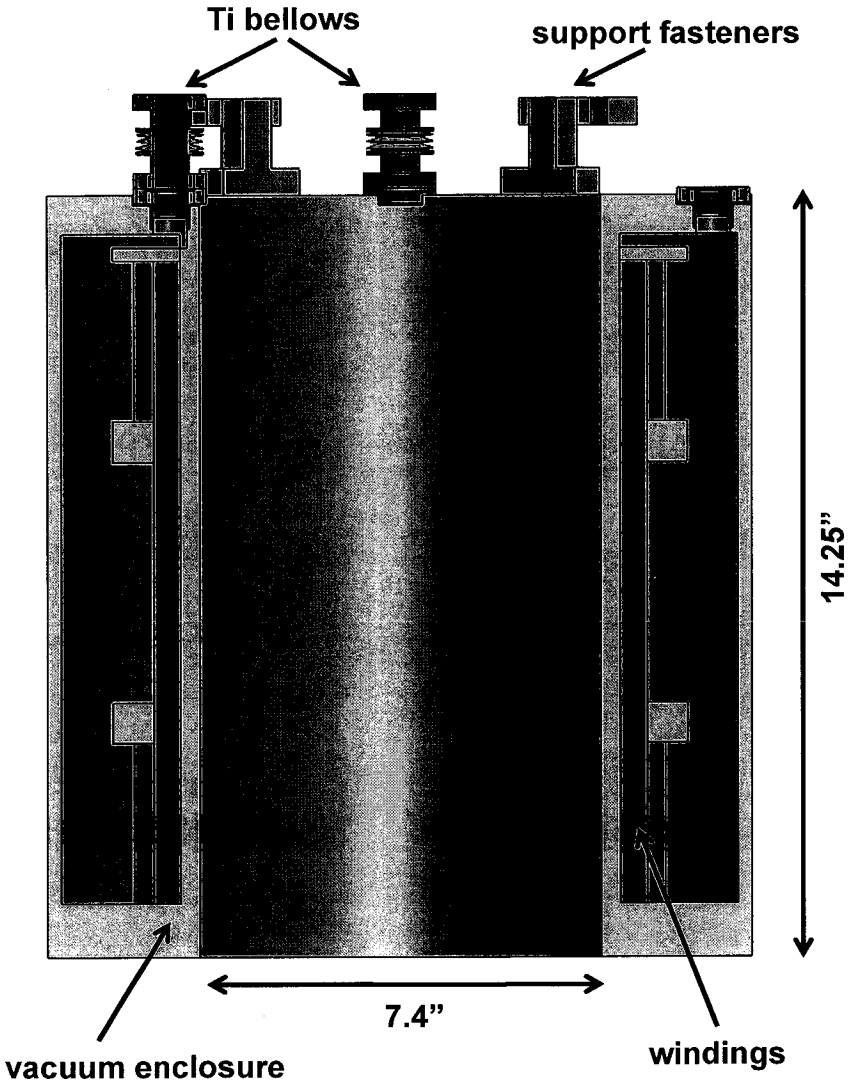

Figure 2.8: Side view of antiproton-loading solenoid.

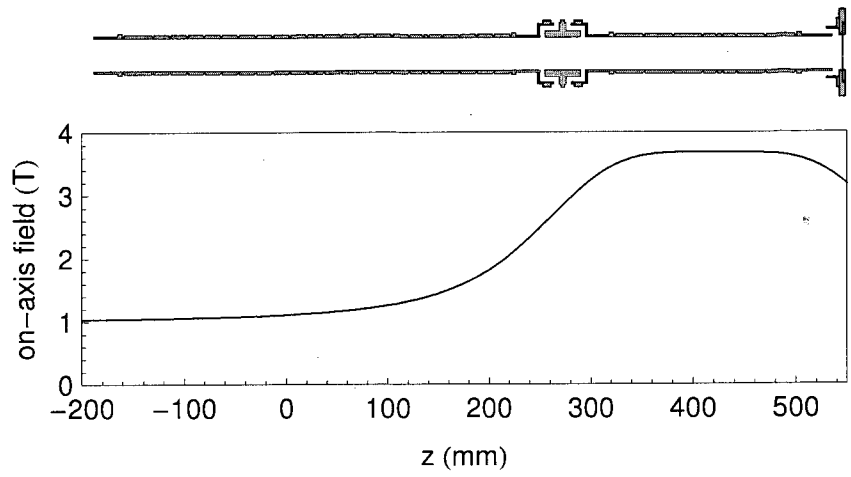

Figure 2.9: On-axis magnetic field produced by the antiproton solenoid at typical operating current of 55A (includes the 1 T background field produced by the large solenoid).

The antiproton-loading solenoid was fabricated by Cryomagnetics, Inc. to design specifications provided by ATRAP. Implementation of the solenoid including the system which connects the superconducting solenoid leads to a pair of retractable current leads and then to room-temperature cables was performed by ATRAP members.

Figure 2.10 shows the position of the antiproton-loading solenoid relative to other components of the BTRAP apparatus. Titanium bellows sections make leak-tight connections to ports on the bottom of the Ioffe trap, allowing liquid helium to flow into the antiproton-loading solenoid. Mechanical connection to the Ioffe trap is made by four aluminum fasteners which bolt to the top of the antiproton-loading solenoid. A hand-bent copper tube with brass bellows sections to account for differential thermal contraction contains the superconducting current leads for the solenoid. Two aluminum pieces fasten the top flange of this tube assembly to the octopod plate of

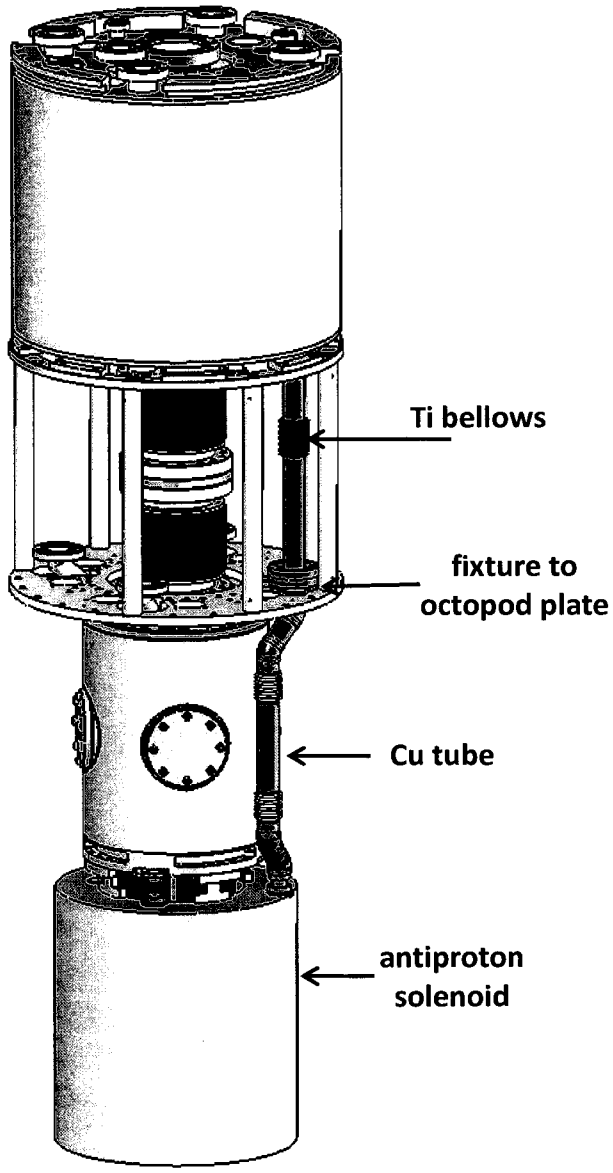

Figure 2.10: Location of the antiproton-loading solenoid within the entire cryogenic Penning-Ioffe trap apparatus and connections to the Ioffe trap and liquid helium dewar.

the apparatus to provide mechanical stability for the leads. Here a connection is made to a titanium bellows assembly similar to those used for the Ioffe trap. Inside this bellows assembly the flexible superconducting leads are coiled and then compressed inside of a smaller G-10 tube mechanically fastened to the bellows assembly. This arrangement allows enough flexibility to account for differential thermal contraction during cooldown, but provides enough stability that quenches do not occur from motion of the leads as the magnet is charged. Above this section of the solenoid leads a 4-inch-long solder joint is made to a pair of semi-rigid Nb_3Sn superconducting bus bars (American Magnetics, Inc.). These bus bars pass upwards through the liquid helium dewar. They are mechanically fastened to aluminum tabs glued into the inside of one vacuum port at the top of the helium dewar, where they make a retractable connection to a pair of vapor-cooled current leads (AMI L-100).

The antiproton-loading solenoid has enabled us to boost our $\overline{p}$ loading by a factor of 5. We are now able to trap up to 10 million antiprotons in two hours of loading and retain 90 % of these $\overline{p}$ in the 1-T field for $\overline{H}$ experiments [27]. Results obtained from the $\overline{p}$ solenoid will be discussed further in Chapter 3.

2.4 Octopod plate section

Figure 2.11 shows the octopod plate region of the apparatus. The octopod plate is supported below the liquid helium dewar by eight aluminum posts. This region contains a two-dimensional translation stage that allows motion of a 6" diameter flange. This window flange, described in more detail below, separates the room-temperature e^+ transfer vacuum from the cryogenic Penning trap vacuum. The two-

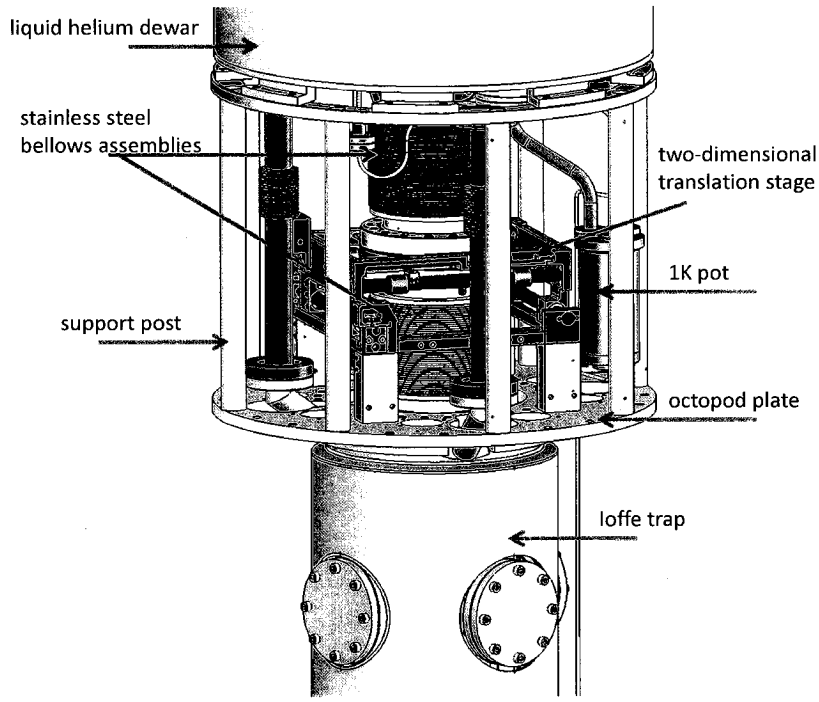

Figure 2.11: Octopod plate region of the Penning-Ioffe trap apparatus, showing the two-dimensional translation stage and connections to the liquid helium dewar and Ioffe trap.

dimensional translation stage allows us to move this window flange in order to put different elements on axis. The two-dimensional translation stage is described in greater detail in [56].

The octopod plate region also contains the pumped helium system for 1.2 K trap operation (described below). The Ioffe trap mounts to the bottom of the octopod plate. The window flange makes vacuum connections to the Ioffe trap and liquid helium dewar via two 6" stainless-steel bellows assemblies. These assemblies preserve the ultra-high vacuum of the experiment space while allowing motion of the two-dimensional translation stage.

Initially, commercially-available all-titanium bellows assemblies were installed in this region to prevent any possible magnetic inhomogeneities due to residual or induced magnetism of stainless steel. These bellows assemblies proved to be very failure-prone in this application. During the 2008 beam run, multiple failures of the commercial titanium bellows assemblies in this region prevented us from operating the BTRAP apparatus until the last few months of beam and greatly hindered progress. To prevent a repeat of this experience, we installed stainless steel bellows assemblies as replacements. We also redesigned and replaced the vacuum connections in this region to allow modular replacement of failed bellows assemblies. This major apparatus upgrade, completed in the spring of 2009, allowed reliable operation of BTRAP throughout the 2009 and 2010 beam runs.

2.5 Pumped He system for 1.3-K trap operation

In order to produce the highest fraction of $\overline{\mathrm{H}}$ atoms that can be confined in the sub-Kelvin depth of our Ioffe trap, we desire the coldest possible clouds of particles. The lowest temperature we expect clouds of e^- or e^+ to reach via synchrotron is the temperature of the electrode stack itself. To this end, we installed a pumped He system to reduce the temperature of our stack from 4.2 K to 1.2 K [51].

The boiling point of liquid helium depends on the partial pressure of the surrounding He gas. For ^{4}He, the boiling point at 1 atm pressure is the well-known number 4.2 K; however, as the pressure is reduced, the boiling point of ^{4}He drops. This can be used to reduce a bath of ^{4}He to below 4.2 K. Below 2.2 K the He becomes superfluid, flowing without viscosity, and its thermal conductivity becomes remarkably high. The limit to this cooling technique is that the cooling power $\dot{Q} \propto e^{-1/T}$ decreases sharply at low temperatures due to the rapidly decreasing vapor pressure of ^{4}He. The practical limit for pumped ^{4}He systems is slightly above 1 K. Similar systems with liquid ^{3}He can be operated at temperatures down to 300 mK, but require additional effort to implement as the extreme cost of ^{3}He necessitates a closed cycling system.

Figure 2.12 shows the pumped He system incorporated into the BTRAP platform. This system and its specifications are described in much greater detail in [51]. A titanium body holds the low-temperature liquid helium. This "1K pot" contains a solid copper sleeve to prevent thermal gradients in the system. The 1K pot receives liquid helium through a very high impedance flow line that allows a significant pressure difference between the 1 atm helium dewar and the low-pressure 1K pot. A rotatable G-10 shaft which passes up to room temperature can be turned in order to loosen or

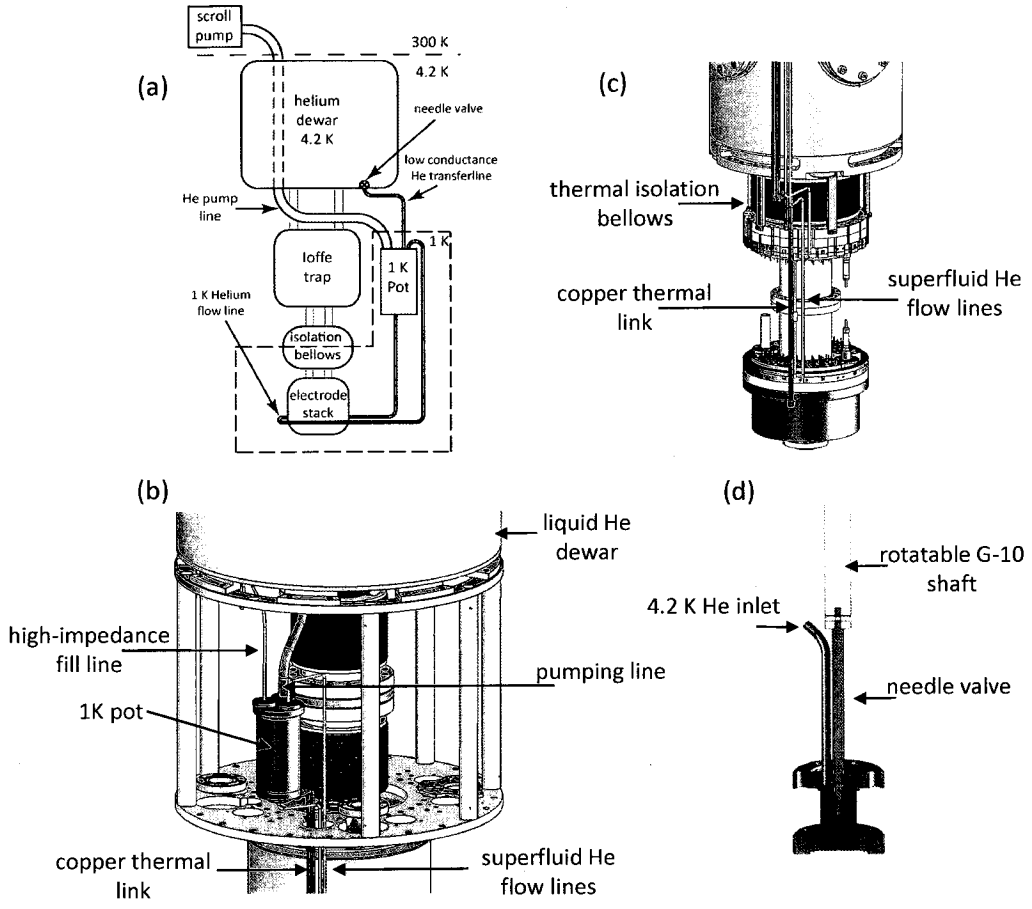

Figure 2.12: Pumped helium system for sub-4 K operation. (a) Schematic of the pumped helium system. (b) The 1K pot and its connections to the helium reservoir and pumping line. (c) Connections of the superfluid flow lines and copper thermal links to the titanium vacuum enclosure for the stack. (d) The needle valve used to manually restrict liquid helium flow into the 1K pot.

tighten a needle valve which allows some control over the flow rate of liquid helium into the pot.

The 1K pot is pumped by a scroll pump at room temperature through a pumping line designed to be large enough not to be a limitation to to achievable pressure. Superfluid He from the pot flows through a gold-plated copper flow line which passes down to the vacuum enclosure for the electrode stack and is thermally anchored to the outside of this enclosure. The return line then allows superfluid He to re-enter through the top of the 1K pot. The electrode stack and its vacuum enclosure must be thermally isolated from the 4.2 K Ioffe trap and antiproton-loading solenoid. Isolation from the Ioffe trap is provided by a titanium edge-welded bellows connecting the vacuum enclosure to the Ioffe trap; G-10 supports hold this bellows assembly in place.

The thermal isolation of the electrode stack from the parts of the apparatus containing liquid helium is not a problem when the 1K pot contains superfluid helium; the thermal conductivity is good enough that the electrode stack operates at only 0.1 - 0.2 K higher than the 1K pot temperature of 1.1 K. However, the coupling between the 1K pot and electrode stack is much worse when the pot is over 4.2 K and does not contain any liquid helium. This increases the time necessary to cool down the entire experiment from room temperature. In order to ameliorate this problem, two solid 5mm diameter OFE copper thermal links were installed to improve the high-temperature thermal conductivity between 1K pot and electrode stack. Figure 2.13 shows the time required for apparatus cool-down with and without these additional links. The copper thermal links reduce the cool-down time of the apparatus from over

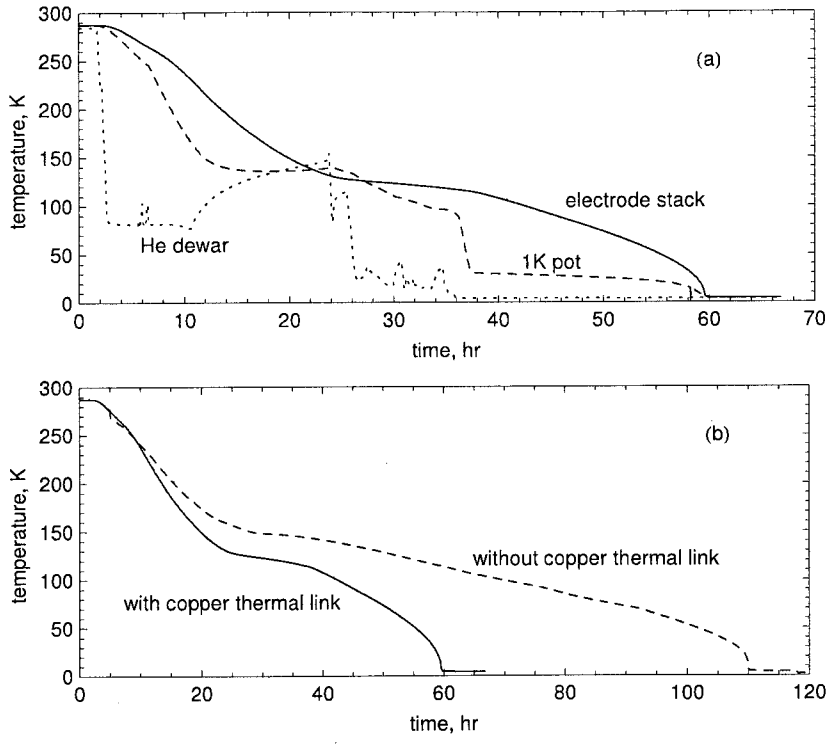

Figure 2.13: (a) Typical cooldown of the ATRAP2 apparatus showing the helium dewar, 1K pot and electrode stack. The thermal isolation measures to allow 1.3 K stack operation also limit the cooldown time. (b) Cooldown of the electrode stack with and without the copper thermal links between 1K pot and electrode stack.

100 hours to a more manageable 60 hours. This improvement agrees with a model of the stack cool-down we developed which assumes that the stack cool-down proceeds by thermal conduction through the copper LHe flow lines, the Ti thermal isolation bellows, and the extra copper lines (once added).

2.6 Window flange for e^+ admittance and plasma imaging

Figure 2.14 (a) shows the window flange used during the 2009 and 2010 beam runs for e^+ admittance. This window flange is mounted on the two-dimensional cryogenic translation stage described previously. The two-dimensional stage allows us to move the window flange to put one of five separate ports on axis. The window flange also serves to decouple the room-temperature vacuum space through which e^+ enter the apparatus and the cryogenic vacuum in which we trap $\overline{p}$. For the 2011 beam run, a new window flange (Figure 2.14 (b)) was installed. This window flange requires less horizontal motion to place its ports on axis, and was installed because we sometimes have difficulty achieving the full motion of the translation stage when it is at cryogenic temperatures.

During typical operation so far, the positron admittance (center) is placed on axis. This 1.5 mm diameter aperture allows e^+ from the accumulator to enter the electrode stack. It also permits the focused beam from the excimer laser to enter the electrode stack and hit the degrader, where it liberates photoelectrons used for collisional cooling of $\overline{p}$. The positron admittance is surrounded by a four-quadrant gold-plated

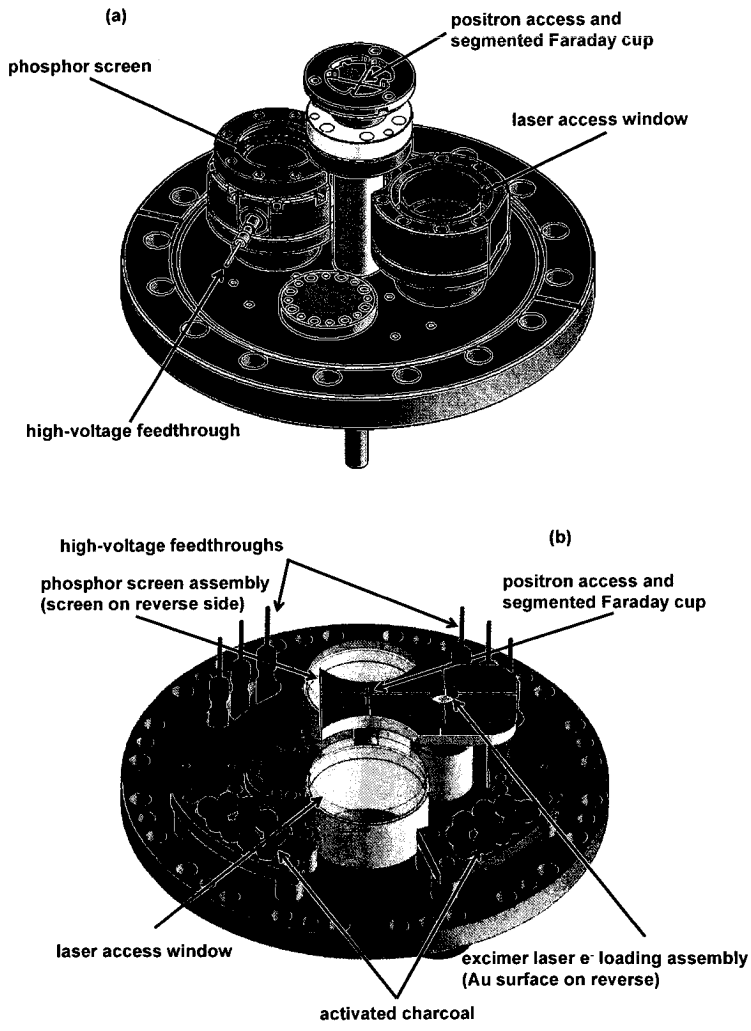

Figure 2.14: (a) Window flange assembly used for the 2009 and 2010 beam runs, showing (center) 1.5 mm aperture for e^+ admittance and excimer laser access with its surrounding segmented Faraday cup for steering, (left) phosphor screen assembly for plasma imaging, (right) MgF window for Lyman-α laser access. (b) New window flange assembly installed for the 2011 beam run. This window flange requires less motion to place the MgF window or phosphor screen assembly on axis, making better use of the travel allowed by the translation stage.

copper Faraday cup that is an important diagnostic for aligning the excimer laser and the e^+ beam. The charge deposited by the e^+, or the e^- liberated by the intense laser pulses, can be counted with a charge-sensitive amplifier. Information from the four quadrants then allows us to align these beams so that they enter the apparatus.

The window flange also has a 1" diameter MgF laser access window. The laser access window will allow us to couple 121.5 nm Lyman-α light into the trap; its larger size will make it easier to couple the far-UV light into the trap as the intensity of a Lyman-α source may be too weak for us to use our charge-counting methods to steer the beam into the smaller e^+ admittance.

The final important component of the window flange is the phosphor screen for plasma imaging. This screen consists of a fluorescent phosphor (Torr Scientific P-20) deposited onto a fused silica window. The P-20 phosphor emits an average of 240 photons per incident e^- with incoming energy of 6 keV. P-20 emits light over a broad spectrum of about 150 nm with an average wavelength of 550 nm; the typical decay time for the fluorescence is 4 ms. This phosphor was chosen for its high quantum efficiency and short decay time.

The plasma imaging system is designed to work by accelerating a cloud of particles into the screen at high energy. The screen itself is backed by a conducting layer that allows it to be biased to a high voltage to give additional energy to the particles, since the number of photons produced per incident particle scales with the particle energy. (Unfortunately, the annihilations of antiparticles on the phosphor are likely to produce decay products and γ-rays which will not interact strongly with the phosphor, so little gain in signal is likely to be realized when imaging clouds of antiparticles). All

elements of the phosphor screen system are designed to withstand 5 kV except for the feedthrough pin for the phosphor bias; this feedthrough (Insulator Seal 9411004) is rated only to 1,000 V. It was hoped that under cryogenic conditions the feedthrough would operate at 5 kV. In practice, breakdown tests showed that the plasma imaging system could reliably operate at 2.5 kV but would break down at or slightly below 3 kV. The system nevertheless allows for e^- to impinge on the phosphor screen with a total of 3.5 keV of energy, since the stack electrodes themselves can be biased to 1 kV. The light produced by the phosphor screen then travels up through the apparatus and exits via a 4.5" diameter vacuum window on the top of the e^+ transfer guide. Here, a CCD camera (Sensicam QE) is used to collect the light and produce an image of the plasma.

Difficulties with the two-dimensional translation stage prevented a full exploration of the capabilities of the plasma imaging system. In one test with a cloud of 10^8 e^-, no image could be seen of the plasma. Without fully automated and robust control of the translation stage, moving the window flange off-access to take a plasma image required a full realignment of the excimer once the positron admittance was moved back on axis. Plans to fully automate the translation stage movement are underway. If the current signal level is not sufficient to observe a plasma, further signal may be obtained by means of a micro-channel plate (MCP). Making the electrical connections required to operate the MCP in the cramped region of the window flange is a non-trivial task.

Chapter 3

Particle loading, detection, and manipulation

A first requirement for antihydrogen production and trapping is confinement of its constituents, e^+ and $\overline{p}$. Also important are the e^- used for collisional cooling of $\overline{p}$. This chapter will describe the methods we use to load these three species of particles. Greatly improved loading methods developed in the 2009 and 2010 beam run allow us to load up to 10 million $\overline{p}$ and up to 4 billion e^+. This chapter will also describe techniques used to count the number of particles loaded and to manipulate the particles.

3.1 Electron loading

Although electrons are not a constituent of antihydrogen, they are essential to the ATRAP experimental platform. Most importantly, e^- are used to collisionally cool

antiprotons from the keV-energies at which the $\bar{p}$ are loaded and are the only way that large numbers of $\bar{p}$ can be reduced to the very low energies ($\ll 1$ eV) necessary for the production of cold antihydrogen [57, 11]. Since we are easily and quickly able to load large numbers of e^-, we also use e^- for trap diagnostics and debugging and in the development of new experimental tools.

As part of the ATRAP2 experimental platform, we introduced a new and improved way of loading e^- via photoemission of e^- from a metal surface by excimer laser pulses [58]. This technique, which was introduced to increase the rate at which we load e^-, replaced the previous method of loading via field-emission point [11]. With this earlier technique a high voltage applied to a very thin metal tip causes emission of electrons due to the high electric field. The emitted e^- have enough energy to liberate background gas cryopumped to the cold electrode walls, and collisions with this background gas allow the e^- to cool into a static potential well. The advantage of the field-emission technique is that it is relatively easy to implement and robust. One disadvantage is that, because e^- must undergo collisions with the low-pressure background gas in order to cool into the potential well, loading many millions of e^- requires a very long time: approximately 10 minutes per 5×10^6 e^- were required in the previous-generation apparatus [46]. In addition, difficulties were encountered in working stably with more than 10 million e^- loaded by this method [11]. As ATRAP sought to greatly increase the number of particles used in experiments, a new method of electron loading was developed.

The new ATRAP technique to rapidly load much larger numbers of e^- takes advantage of the photoelectric effect [59], where single photons of energy exceeding the

work function of a metal liberate electrons from the metal surface. Such electrons have been used to produce e^- beams for photolithography by pulses of 248-nm excimer laser light incident on a gold surface [60]. An observed quantum efficiency of 10^{-4} allowed a 200 mW laser to produce a 1 μA photocurrent, a yield of more than 10^{12} e^-/s.

The work function of vacuum-deposited Be has been measured to be 5.08 eV, but typically decreases to a stable value of 3.6 eV after exposure to oxygen [61]. Since this energy is less than the single-photon energy of a 248-nm laser ($E = h\nu = 5.0$ eV) it is possible to use the Be degrader in ATRAP's apparatus as a substrate from which photoelectrons can be liberated. In order to load electrons, we thus couple pulses from an excimer laser (GAM Laser EX5/250) into our apparatus from optics mounted off of the room-temperature apparatus top plate (see Chapter 2). These 18-mJ, 10-ns laser pulses are deflected downwards by a single mirror mounted inside the room-temperature vacuum space and enter the Penning trap region of our apparatus through the 1.5 mm diameter aperture for e^+ admittance. By moving this single mirror out of the way with an electronically-controlled translation stage, we allow for e^+ access to the trap; we can switch between loading the two species of particles within 30 s.

Figure 3.1 shows the potential structure we use for loading e^- by photoemission. A positive voltage applied to the electrode nearest the Be degrader forms a potential which serves to accelerate emitted e^- away from the degrader and ensures that they are not recaptured. A voltage "door" is opened by a 2-μs voltage pulse applied to electrode LBE2, allowing the e^- to enter into a potential well, and is then "closed" behind so that e^- cannot escape the potential well. The cyclotron motion of the

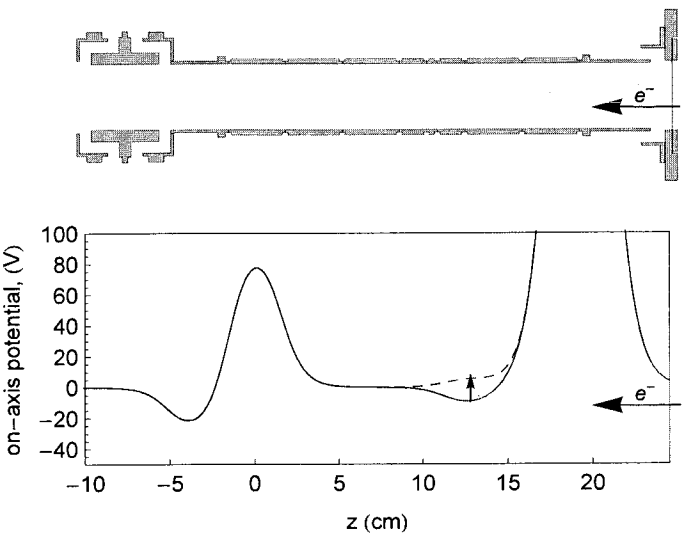

Figure 3.1: Potential scheme used for electron loading. The dashed curve represents the modified potential as a rapid voltage pulse allows electrons to enter the potential well, where they are subsequently trapped and cooled.

e^- cools by synchrotron radiation and collisions rapidly couple the axial motion and cyclotron motion so that the e^- kinetic energy reduces to $\ll 1$ eV. We have found the highest rate of loading when the potential well begins at a very shallow voltage and the depth is increased by 1 V for each additional laser pulse. This scheme minimizes the potential energy acquired by e^- as they enter the well: the well depth is initially very shallow, and as the applied voltage increases the space charge potential due to the larger number of e^- already trapped limits the effective well depth seen by incoming e^-.

Figure 3.2 shows the number of e^- loaded as a function of number of laser pulses using our optimized loading parameters. We observe linear loading up to 250×10^6 e^- and have loaded as many as 10^9. With a pulse repetition rate of 0.5 Hz and a load rate of 2.5×10^6 e^- per pulse, we can now load 75 million e^- per minute and can

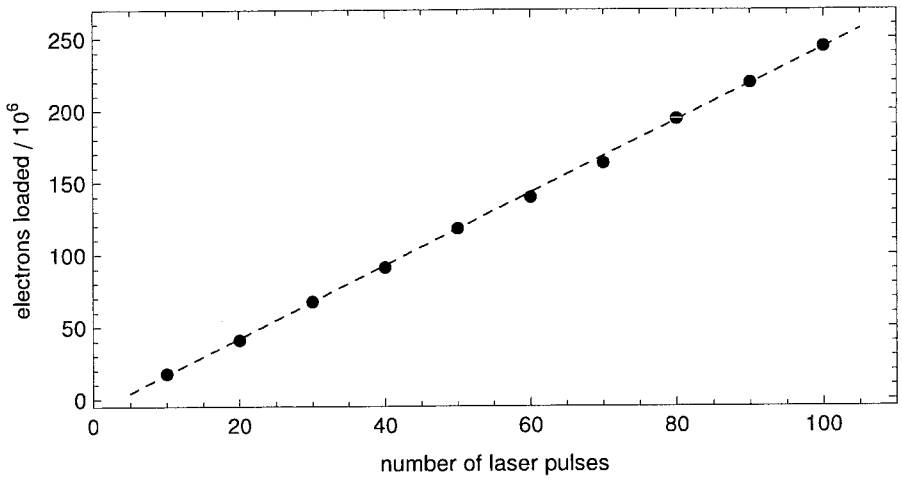

Figure 3.2: Number of e^- loaded as a function of number of laser pulses used for loading. The linear fit shows a slope of 2.5×10^6 e^- loaded per laser pulse.

obtain e^- plasmas of esentially arbitrary size in a timely fashion.

3.2 Positron loading

Positrons, one of the constituent particles of antihydrogen, are obtained from the radioactive β-decay of a ^{22}Na source. The e^+ are emitted at very high energies so some mechanism is required to reduce their energy to a level which we can trap with voltage pulses in the 100-V range. Previous ATRAP experiments used a 2-mm thick W (tungsten) moderator in which metastable Rydberg Ps can form and subsequently be ionized by a small electric field, allowing e^+ to be captured in the resulting potential well [46]. Limitations in the accumulation rate imposed by this technique led ATRAP to the construction of a separate buffer-gas e^+ accumulator.

Figure 3.3 shows the buffer-gas accumulation apparatus for e^+. The design is based on [62], and was first used for $\overline{H}$ production by the ATHENA Collaboration

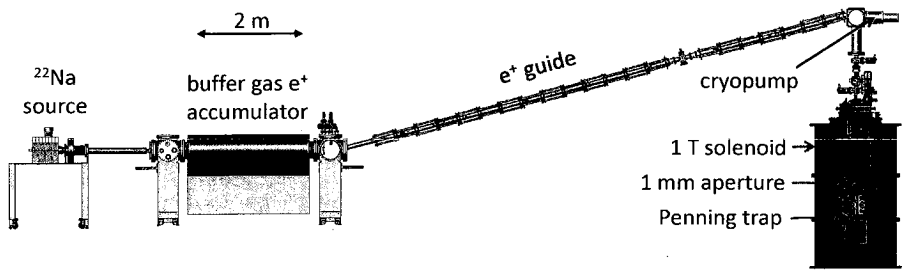

Figure 3.3: The ATRAP positron accumulator, showing the long magnetic guide used to transfer positrons into the cryogenic Penning trap apparatus.

[21]. ATRAP's present implementation, spearheaded by collaborators from York University, is described in greater detail in [63, 56].

Positrons resulting from radioactive decay of a ^{22}Na source (half life of 2.6 yr and current strength of roughly 20 mCi) encounter a frozen neon moderator [64] and emerge with approximately 15 eV of energy. Positrons then enter the main region of the accumulator, which consists of a multiple-electrode room-temperature Penning trap with a 0.14 T bias field provided by a water-cooled room-temperature solenoid. The accumulation region contains a small amount of N_2 buffer gas and differential pumping is used to produce a pressure gradient ranging from 10^{-3} torr to 10^{-6} torr. Collisions with N_2 molecules in the higher-pressure region allow the e^+ to cool into the lowest-potential region of the accumulator where the pressure is kept very low to reduce background annihilations. In a typical 50-second accumulation cycle we can accumulate approximately 25 million positrons within the accumulator.

The buffer-gas accumulator cannot fit inside the cryogenic Penning trap apparatus used for $\overline{\mathrm{H}}$ production (and the buffer gas used would also freeze to the cryogenic trap walls), so we must transfer the accumulated e^+ into the cryogenic apparatus. Space constraints prohibit us from locating the e^+ accumulator closer than 8 m from the

cryogenic Penning trap apparatus. A long high-vacuum guide region surrounded by 95 independently-tunable magnets is used to transfer e^+ over this distance, through the 1.5-mm diameter aperture on the window flange and into the electrode stack where $\overline{H}$ formation experiments are performed.

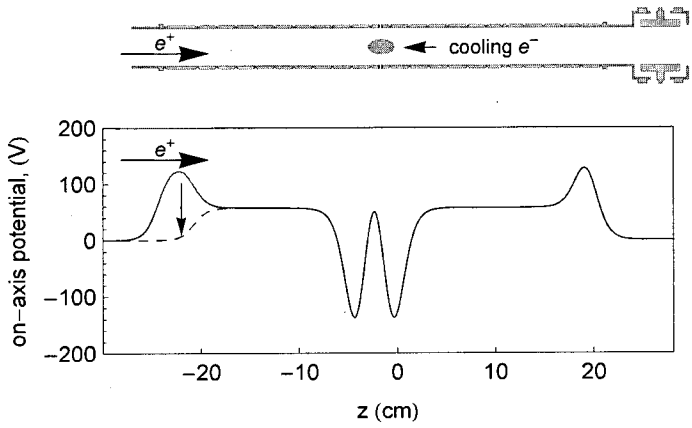

Figure 3.4: Potential structure used for loading e^+ into the Penning trap electrode stack.

Figure 3.4 shows the potential structure used when loading e^+ into the cryogenic Penning trap apparatus. A long trapping well is formed through the entire upper stack. A voltage "door" is opened by a fast voltage pulse with each transfer and then closed again to prevent e^+ from exiting the electrode region. In order to more rapidly cool the incoming e^+, a cloud of 150×10^6 e^- is located in the middle of the e^+ trapping region. Collisions with these e^- cause the e^+ to lose energy and cool into the deep trapping wells located to either side of the e^- plasma. Although the electron-cooling of positrons would seem to invite annihilation of the e^+, the long-range Coulomb collision makes annihilations less likely. The primary mechanism for e^+ loss is formation of Rydberg Ps through three-body recombination and subsequent

decay to the short-lived ground state of this metastable atom. However, three-body formation of Ps is strongly suppressed at the high initial e^+ energies and as the e^+ cool into the deep side wells they are no longer in contact with the e^-. As a result, annihilations due to the cooling e^- are reduced and we see a significant enhancement of e^+ trapping by use of the cooling e^-.

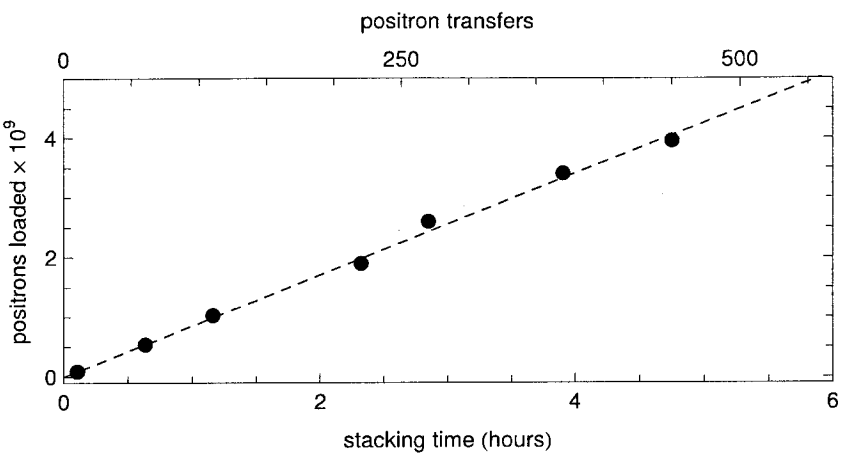

Figure 3.5: Number of e^+ accumulated in the cryogenic Penning trap as a function of number of shots transferred from the buffer-gas accumulator.

Figure 3.5 shows the e^+ stacking as a function of number of shots. Significant efforts at optimization of the accumulator and transfer process by collaborators from York University allow the trapping of 10 million e^+ per transfer, a transfer efficiency of nearly 40 %. Positron stacking remains linear up to 400 transfers and the accumulation of 4×10^9 e^+ in the cryogenic Penning trap apparatus, a number simply unattainable with previous methods of e^+ loading. This linear stacking to very high numbers requires occasional use of the rotating-wall technique to prevent radial losses due to long-time-scale radial expansion of the e^+ plasma; this technique will be de-

scribed in greater detail in Chapter 4.

3.3 Antiproton loading

Antiprotons are the second constituent of $\overline{\mathrm{H}}$ and are the more difficult species to load and trap. Trapping and cooling of $\overline{\mathrm{p}}$ uses many of the techniques developed by the TRAP and ATRAP collaborations over a period of many years. These techniques include the use of matter to slow $\overline{\mathrm{p}}$ down to keV-level energies [65], the use of high-voltage pulses to trap $\overline{\mathrm{p}}$ in a Penning trap [65], and the collisional cooling of $\overline{\mathrm{p}}$ below 100 meV of energy with electrons [11]. These methods are now used for all antihydrogen experiments.

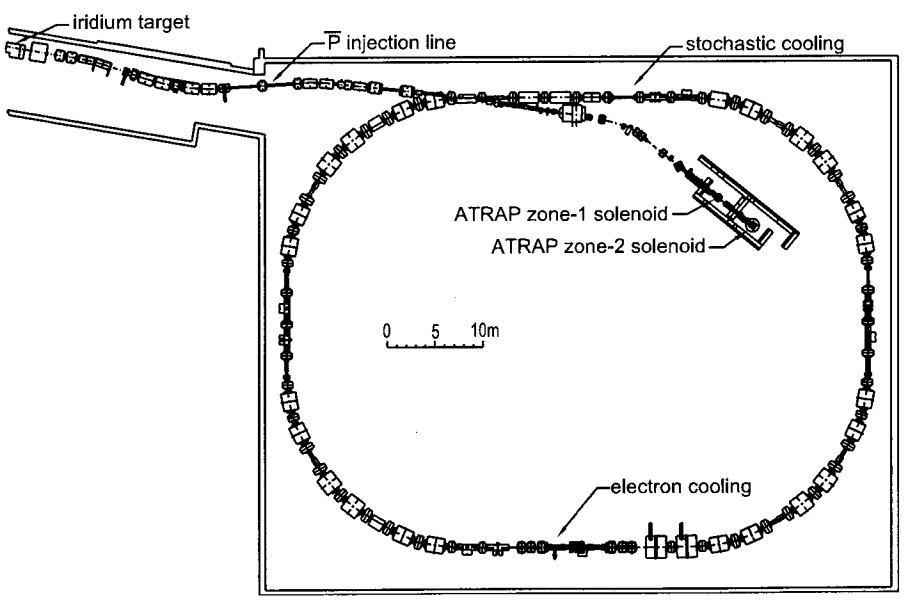

Figure 3.6: Schematic of the Antiproton Decelerator.

Low-energy antiprotons are uniquely available at CERN's Antiproton Decelerator (AD) facility. The AD, shown in Figure 3.6, decelerates high-energy antiprotons

to energies of 5.3 MeV, enabling ATRAP and other antiproton users to slow and capture the $\overline{p}$. The AD has been extensively described elsewhere [66, 67]. An initial beam of 10^{13} high-energy protons is incident on an iridium target at sufficient energy to produce antiprotons with an efficiency of approximately 10^{-6}. These $\overline{p}$ are then magnetically guided into the AD, where a series of RF pulses is used to decelerate them to an energy of 5.3 MeV (longitudinal momentum 100 MeV/c). Stochastic cooling and collisional electron cooling of the transverse motion of the $\overline{p}$ beam prevent losses due to transverse broadening of the $\overline{p}$ beam. A 200-ns "bunch" of approximately 30 million $\overline{p}$ at 5.3 MeV is delivered to one of four experimental zones every 100 s.

Antiprotons at 5.3 MeV are still too energetic to be trapped by kV electrical pulses, so the $\overline{p}$ energy must first be reduced by other means. Figure 3.7 shows the region of the ATRAP apparatus where the $\overline{p}$ are slowed in matter. This region also contains the Parallel-Plate Avalanche Counter (PPAC) which is used as an aid for steering the $\overline{p}$ beam into the cryogenic Penning trap apparatus.

The PPAC consists of several thin aluminum strips coated on thin Mylar windows. The PPAC has two anode layers of five strips each; each strip is 2mm wide and is separated from the neighboring strips by 0.5 mm. The PPAC cathode layers consist simply of a Mylar sheet with one side coated entirely with aluminum. The two PPAC layers have strips oriented in two orthogonal directions which form an x-y plane perpendicular to the direction of travel of the incoming $\overline{p}$. The PPAC is filled with 1 atm of argon gas and a potential difference of 75 V is applied between each anode-cathode pair. As $\overline{p}$ pass through the PPAC region, they can ionize Ar atoms and the resulting e^- are accelerated by the potential difference, collected by the anode strips,

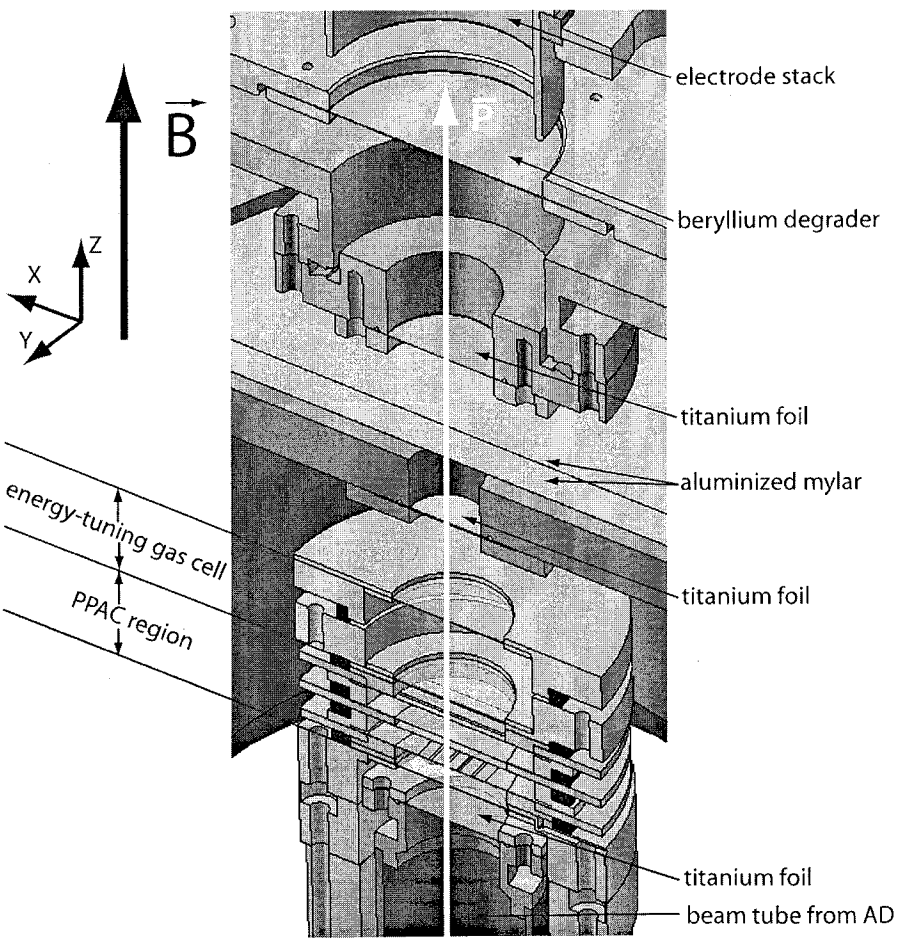

Figure 3.7: Diagram of the PPAC and energy tuning cell region of the trap.

and counted. Despite its name, the PPAC is typically operated in a linear (rather than avalanche) mode so that the collected signal is proportional to the intensity of the $\overline{\mathrm{p}}$ beam. The thin aluminum-coated Mylar sheets cause minimal energy loss of the $\overline{\mathrm{p}}$; the signal from the PPAC is not due to collecting $\overline{\mathrm{p}}$. The PPAC signal allows us to steer the $\overline{\mathrm{p}}$ beam into our apparatus by controlling the current in the final few AD bending magnets immediately beneath our apparatus. We are typically able to focus the beam onto a single 2-mm PPAC strip in both the x and y directions.

The energy-tuning region of the apparatus contains several 10-μm thick Ti foils which reduce the energy of the $\overline{\mathrm{p}}$ beam and also separate regions of 1 atm pressure from high-vacuum regions. Further energy loss occurs in the energy-tuning gas cell, which contains a tunable mixture of He and SF_6 gas. The energy reduction in the cell is much greater when the cell contains a high proportion of the more dense SF_6 gas; overall the energy tuning cell allows us to tune the final energy of the $\overline{\mathrm{p}}$ beam by 0.6 MeV, allowing us to compensate for slight differences in the incoming energy of the $\overline{\mathrm{p}}$ beam. The majority of the energy loss of the $\overline{\mathrm{p}}$ (approximately 3.5 MeV) occurs in a 125-μm thick Be degrader at the very base of the Penning trap electrode stack.

Figure 3.8 shows the antiproton trapping efficiency as a function of SF_6 percentage (by molecule number) in ATRAP's apparatus. The broad distribution indicates a spread in $\overline{\mathrm{p}}$ kinetic energies of 150 keV. As the $\overline{\mathrm{p}}$ pass through the Be degrader, they are expected to emerge in an isotropic angular distribution, so that their energy is distributed between the axial and radial (cyclotron) degrees of freedom. The cyclotron radius of a particle with cyclotron energy E_c is given by

$$r_c = \frac{\sqrt{2E_c m}}{qB}, \tag{3.1}$$

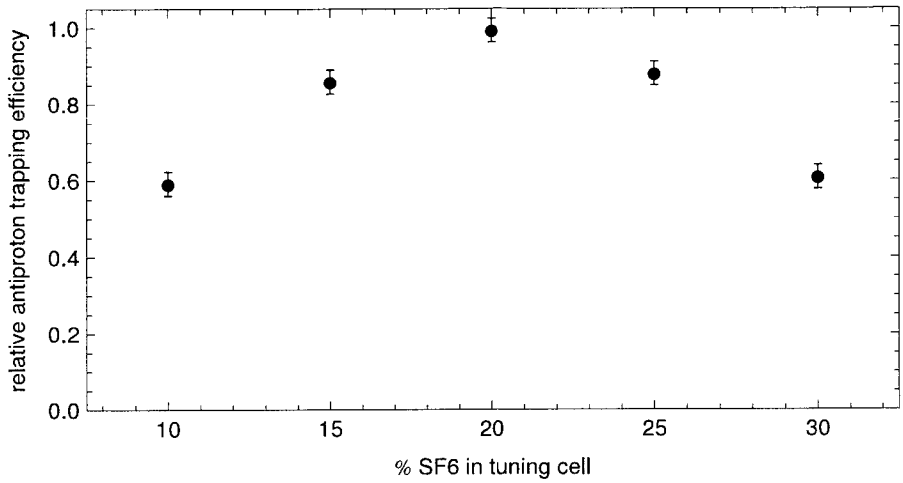

Figure 3.8: High-voltage trapped $\overline{p}$ as a function of percentage of SF_6 gas (by molecule number) in the energy tuning cell; the remainder of the gas mixture is He.

with B the magnetic field in T. We expect that those particles with cyclotron radius greater than the electrode radius cannot be trapped. In a 1 T field, the cyclotron energy corresponding to the 18-mm radius of our electrodes is 15.5 keV. Thus, at 1 T, we expect to trap those $\overline{p}$ entering the trap on-axis with axial energies less than 5 keV and cyclotron energies less than 15.5 keV. Equation 3.1 shows that the maximum cyclotron energy of trappable $\overline{p}$ should increase as the square of the electrode radius and with the square of the trapping magnetic field. The dependence on electrode radius was one motivation for ATRAP's development of larger "x3" electrodes with 18 mm radius, while the dependence on magnetic field motivated the implementation of a field-boosting solenoid for $\overline{p}$ catching (described below).

Figure 3.9 shows the potential structure used for high-voltage trapping of $\overline{p}$. A bias voltage of -5 kV is initially applied to the high-voltage (HV) electrode as shown. The Be degrader is initially biased to +1200 V to prevent any emission of secondary

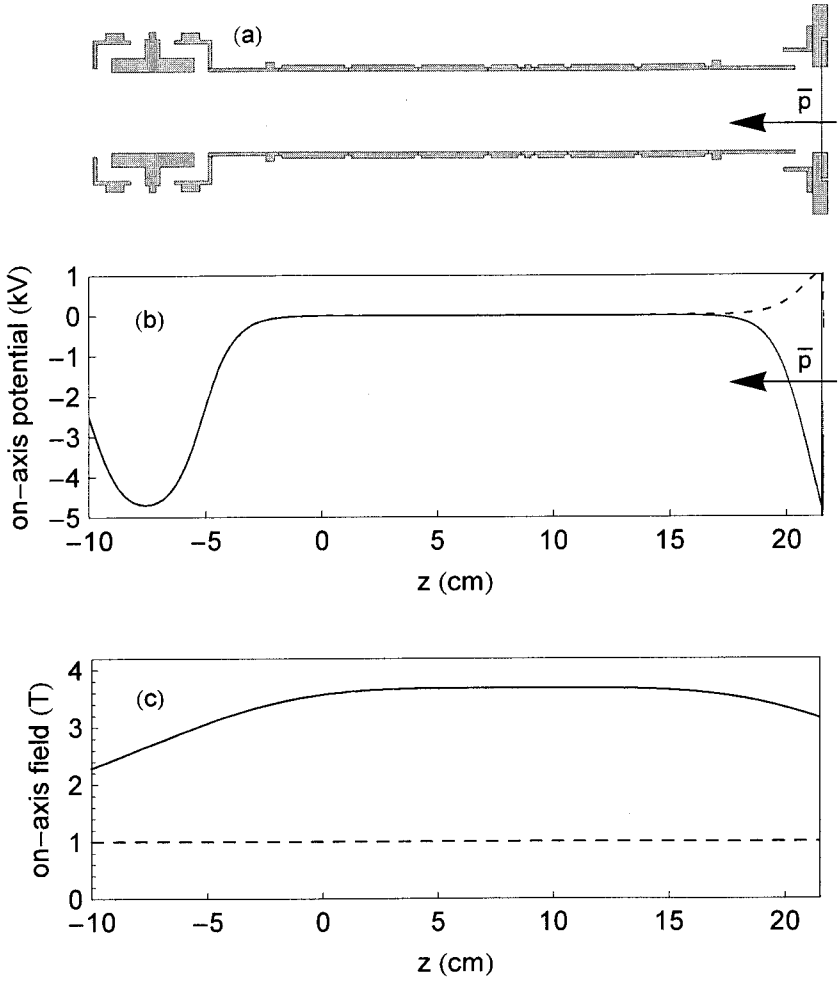

Figure 3.9: (a) Schematic view of the lower stack where we high-voltage capture $\bar{p}$. (b) Potential structure used for high-voltage trapping of $\bar{p}$. (c) Magnetic field for $\bar{p}$ trapping with (solid curve) and without (dashed curve) the additional field from the antiproton-loading solenoid.

electrons as $\overline{p}$ pass through it. As the $\overline{p}$ enter the apparatus, a custom-built high-voltage switch applies a -5 kV bias to the degrader, closing the voltage "door" behind the $\overline{p}$ and preventing any $\overline{p}$ with axial energies less than 5 keV from escaping axially. When no cooling e^- are present, we cannot cool the $\overline{p}$ below their initial keV-scale energy.

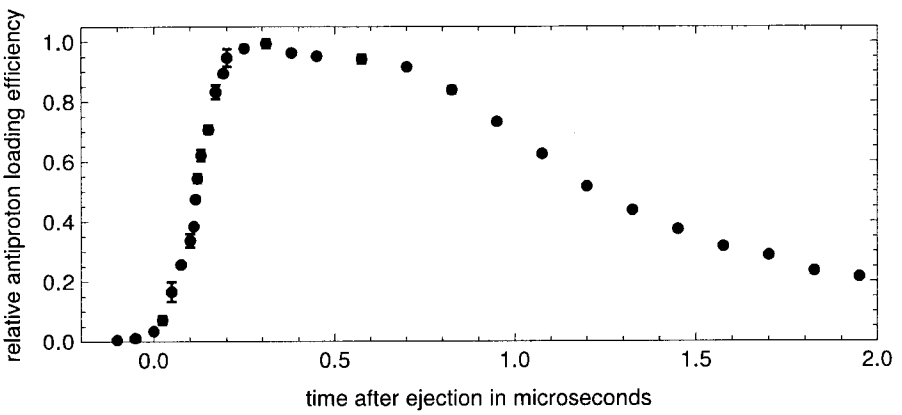

Figure 3.10: High-voltage captured $\overline{p}$ as a function of delay of the high-voltage switch.

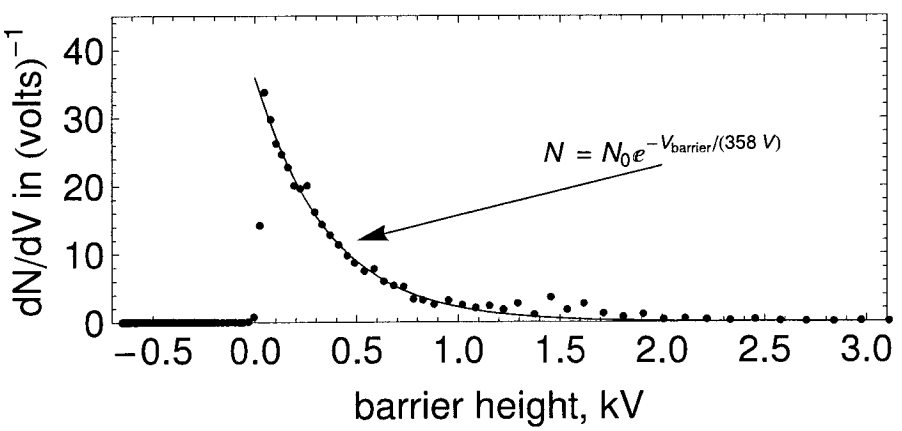

Figure 3.11: $\overline{p}$ loss spectra as a function of axial voltage in the 1-T solenoid field. The fit shows that captured $\overline{p}$ have an axial energy distribution corresponding to approximately 400 eV of energy.

Figure 3.10 shows the $\overline{p}$ trapping efficiency as a function of the timing of the

high-voltage switch pulse relative to the incoming $\overline{p}$ beam. For very short delays, no $\overline{p}$ are caught. The trapping efficiency then rises quickly to a maximum and slowly decays for much longer times. Figure 3.11 shows the energy distribution of trapped $\overline{p}$ as the high voltage applied to the degrader is reduced over 100 ms. At the 1-T bias field shown in this figure, the distribution indicates that only $\overline{p}$ with axial energies less than 1 keV are being trapped. The reason for this is not entirely clear. Over the 60-s time in which the $\overline{p}$ are held before release, collisions between $\overline{p}$ should result in evaporative cooling which ejects some higher-energy $\overline{p}$ and reduces the energy of those which remain behind, but we have not studied this in detail.

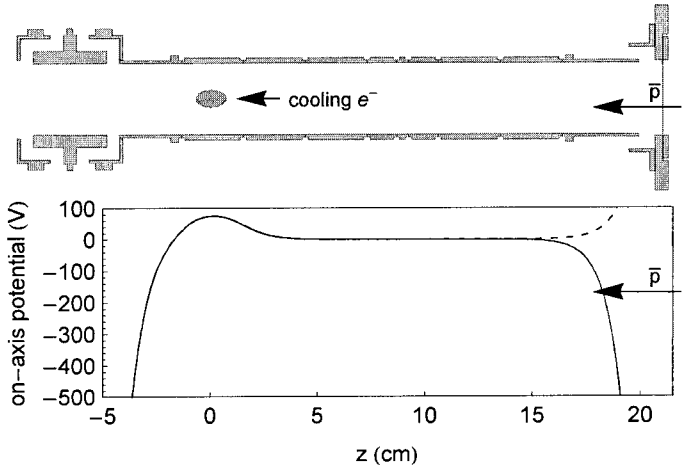

Figure 3.12: Potential structure used for e^- cooling and trapping of $\overline{p}$.

Figure 3.12 shows the potential structure used for trapping and collisionally cooling $\overline{p}$ to energies much less than 1 eV. In this case, a cloud of $N = 100$ million e^- is held on one electrode while the same pulsed-door procedure for high-voltage $\overline{p}$ trapping is employed. The high-voltage trapped $\overline{p}$ collide with low-energy e^- and lose energy over a time period of 60 s. After this 60-s period, the high voltages on the

degrader and HV electrode can be removed and the $\overline{p}$ are now confined at low energies in the same potential well as the e^-. At this point we typically no longer need the e^- and eject them from the trap with a series of four high-voltage pulses. These 75-ns, 120-V pulses produced by a saturated switch (DEI HV1000) are applied to a coaxial cable which is 50-Ω terminated at the electrode to prevent reflections, with the result that the actual pulse voltage delivered at the electrode is approximately 45 V. These pulses are long compared to an e^- axial bounce time in the well but short relative to the bounce time for a more massive $\overline{p}$ and therefore leave the $\overline{p}$ in the voltage well.

3.4 Improved antiproton loading with the field-boosting solenoid

Trapping $\overline{H}$ is a difficult and low-efficiency process, and we desire the largest number of trapped antiparticles possible from which to produce $\overline{H}$ so as to maximize our number of trapped atoms. To this end, the 0.6-cm radius electrodes from previous-generation ATRAP apparatus were scaled by a factor of three to the current ATRAP2 1.8-cm radius electrodes. The larger area within the electrode stack should allow us to trap a larger fraction of the entering $\overline{p}$, which are expected to diverge over a large solid angle after passing through the degrader. However, a competing requirement limits the trappable fraction of incoming $\overline{p}$: trapping $\overline{H}$ requires the gradient magnetic field of a Ioffe trap, whose trapping depth is severely reduced at bias fields over 1 T. As a result the large superconducting solenoid surrounding the BTRAP apparatus is operated at a field of only 1 T. This field is significantly less than the bias field of 5.2

T used in earlier generations of ATRAP apparatus, including the HBAR1 apparatus in which ATRAP first produced antihydrogen. The lower bias field limits the gains we obtain from larger-radius electrodes. The efficiency of $\overline{p}$ loading in BTRAP at 1 T is in fact similar to that seen in previous apparatus.

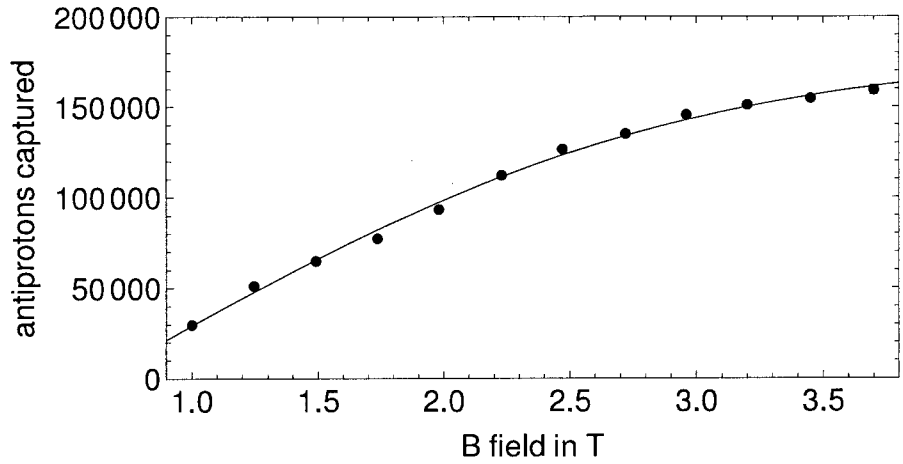

Figure 3.13: HV counts as a function of magnetic field B.

In order to improve our $\overline{p}$ loading, a field-boosting solenoid for $\overline{p}$ loading was installed in the high-voltage trapping region of the cryogenic Penning trap. This solenoid is described further in Chapter 2. The solenoid boosts the field to 3.7 T in this region of the trap and is compatible with rapid charging and discharging. Figure 3.13 shows the high-voltage trapped $\overline{p}$ as a function of magnetic field B. Antiproton trapping is boosted by a factor of 5 in the higher field produced by the solenoid, allowing us to trap up to 160,000 $\overline{p}$ per ejected bunch of $\overline{p}$. The counts appear to be close to saturation at the field of 3.7 T; although the antiproton solenoid is designed to operate at even higher currents, it is not clear that our $\overline{p}$ trapping can be improved without also increasing the high voltage used for trapping.

Figure 3.14 shows examples of $\overline{p}$ high-voltage trapped as a function of trapping

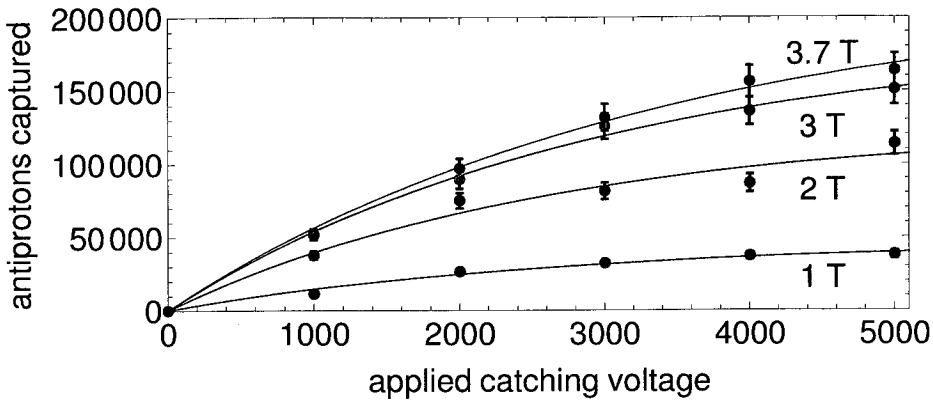

Figure 3.14: Number of $\overline{p}$ high-voltage captured as a function of high-voltage trapping potential for different magnetic fields B.

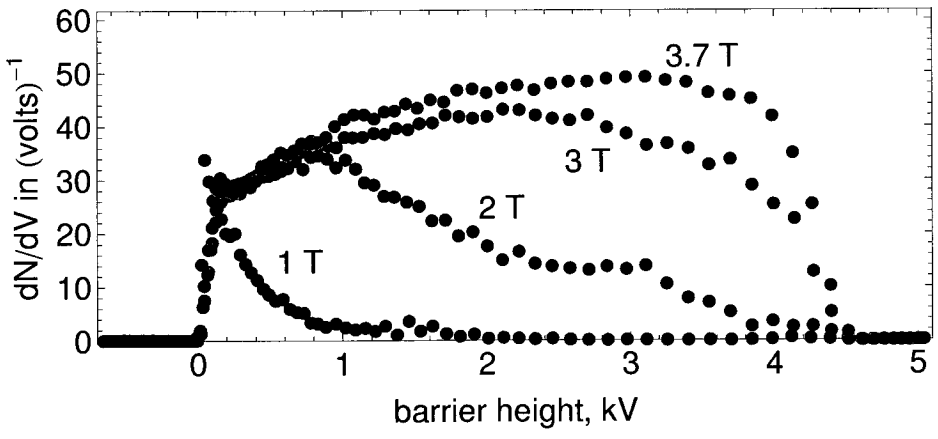

Figure 3.15: $\overline{p}$ loss spectra as a function of axial voltage for different magnetic fields B.

voltage for different magnetic fields. Figure 3.15 shows the observed $\overline{p}$ loss spectra as the trapping voltage is reduced to zero over 100 ms. The figure indicates that at higher solenoid fields a significant number of $\overline{p}$ are trapped at axial energies up to 5 keV. This contrasts with Figure 3.14, which suggests that saturation as a function of trapping voltage may be appearing even at our highest bias fields. The combination of these effects suggests that trapping larger numbers of $\overline{p}$ will likely require further increasing both the bias magnetic field in the high-voltage trapping region and the high voltage used for trapping. Other possibilities for increasing the number of trapped $\overline{p}$ include radio-frequency quadrupole deceleration [68] or a lower-energy $\overline{p}$ source with an electrostatic beam line that would eliminate the need for energy reduction in matter [69].

The observed saturation of our $\overline{p}$ trapping as a function of magnetic field is understandable. Antiprotons appear to enter our trap with a 150-keV thermal distribution of energies (as suggested by data from the energy-tuning cell). Given the expression for cyclotron radius (Equation 3.1), a 3.7-T field should result in a cyclotron radius less than 18 mm for $\overline{p}$ with cyclotron energies less than 212 keV. Thus we would expect that, for $\overline{p}$ entering close to the center of our trap, only $\overline{p}$ with energies significantly higher than the average thermal energy would escape radially. Our ability to steer the beam onto a single 2-mm PPAC strip in both directions provides some indication that $\overline{p}$ enter the trap within a few mm of the center of our electrodes. The observed saturation of high-voltage $\overline{p}$ trapping as a function of applied voltage is less easy to understand. Since our maximum axial trapping depth is 5 kV, it would appear that we should axially trap only a small fraction of entering $\overline{p}$, and that there should be a

strong dependence of trapping efficiency on applied electric potential. This remains to be studied in greater detail.

3.4.1 Stacking of antiprotons

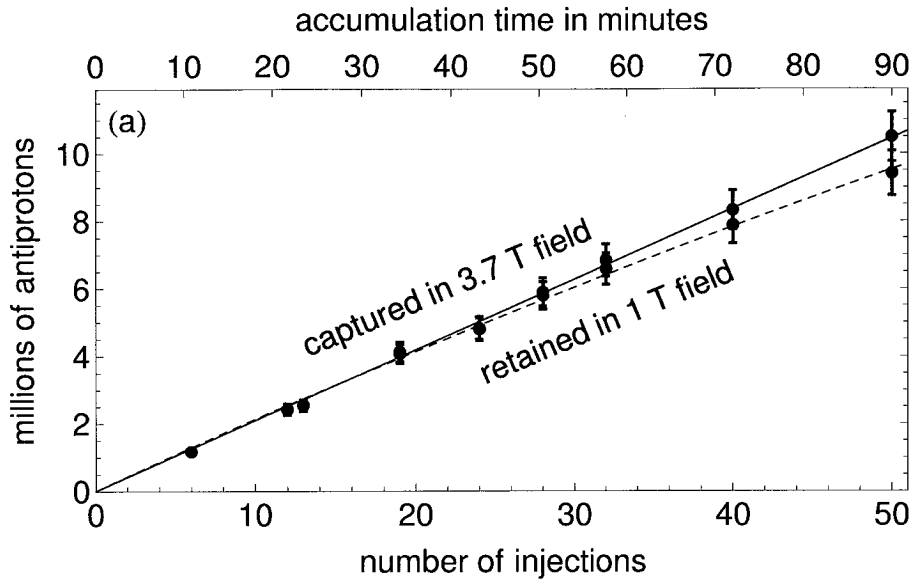

Figure 3.16: Stacking of $\overline{p}$. Number of $\overline{p}$ stacked (red) in the 3.7-T field produced by the antiproton solenoid. (Blue) $\overline{p}$ retained in the 1-T trap background field after the antiproton solenoid has been ramped down.

We desire to perform $\overline{H}$ production and trapping experiments with substantially more than 150,000 $\overline{p}$, the largest number we can currently load per shot in ATRAP's apparatus. In order to load more $\overline{p}$, we "stack" successive shots [70]. In this accumulation procedure, a single cloud of e^- can be used to cool the $\overline{p}$ from several sequential shots and the $\overline{p}$ can be confined in a single potential well for the duration of the particle loading. After the stacking procedure is finished the e^- are pulsed from the trap as described above. Figure 3.16 shows the linear stacking of up to 10 million antiprotons in the 3.7 T bias field. The figure also demonstrates that at the end of stacking,

and after pulsing out the e^-, we can retain over 90 % of the trapped $\overline{p}$ in the 1-T background field to use in $\overline{H}$ trapping experiments. In order to achieve these gains, it is necessary to compress the radius of the loaded particles with a rotating-wall (RW) drive, which will be described in greater detail in Chapter 4. The antiproton-loading solenoid, with the larger electrodes of the ATRAP2 apparatus, allows us to routinely load many millions of $\overline{p}$ and retain them in a 1-T bias field. This is a a factor of 11 more $\overline{p}$ than were stacked in previous ATRAP apparatus and a factor of 12 times more $\overline{p}$ available in the 1T field of the ATRAP2 apparatus than were ever achieved without this technique.

3.5 Particle counting

Detection of the number of trapped electrons, positrons, and antiprotons is essential to understanding our apparatus, performing repeatable experiments and searching for a signal from trapped $\overline{H}$. To this end, a number of particle-detection techniques are used by the collaboration. In previous TRAP and ATRAP experiments a variety of resonance measurements [71, 72] for non-destructive particle detection have been used. In general these measurements have not been very useful for clouds with many millions of trapped particles, so ATRAP2's experiments have mostly used destructive detection techniques. One notable exception is the recent resonance signal from a single $\overline{p}$ seen in the ATRAP2 apparatus [73], a result which could open the way to a search for trapped $\overline{H^-}$ (the single bound state of a $\overline{p}$ and two e^+).

3.5.1 Counting by charge integration

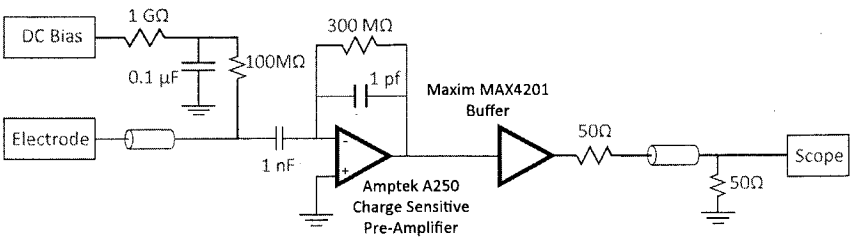

Figure 3.17: Schematic of the circuit used for charge-counting of particles.

The first important destructive particle counting technique is that of charge counting via a charge-sensitive amplifier. A schematic of the circuit used for this process is shown in 3.17. The heart of the circuit is an operational amplifier (Amptek A-250) with negative feedback produced by a 1-pF capacitor C connected between input and output. The voltage V produced by charge on the capacitor is proportional to the number of particles:

$$V = NC/q_e, \tag{3.2}$$

with N the number of particles. In order to initiate a charge-counting measurement, high-voltage pulses rapidly eject particles from the trap and into the Be degrader, where they induce the measured voltage. The Be degrader is biased to +100 V in order to prevent any emission of secondary e^- from the impact, which could affect our count. A 300 MΩ resistor in parallel with the charge-counting capacitor causes the induced signal to decay with a characteristic time constant of $RC = 0.3$ ms, allowing us to rapidly perform multiple charge-counting measurements to count all of the particles within a confined plasma.

Figure 3.18 shows the potential structure we use for charge-counting of a confined

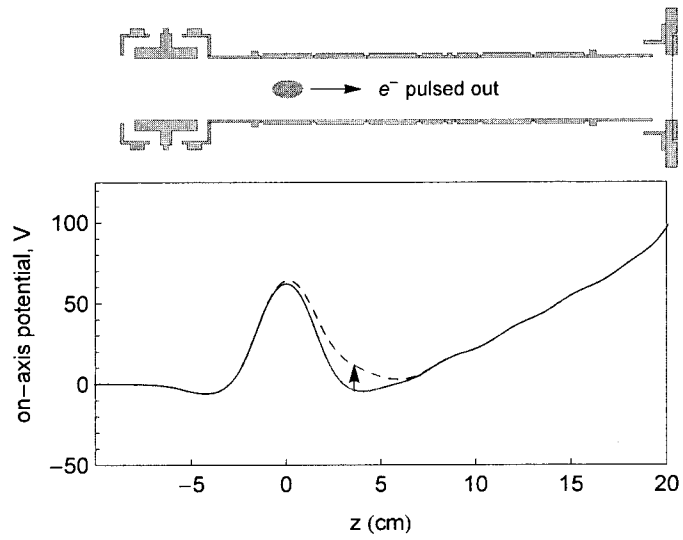

Figure 3.18: Potential structure used for charge-counting of e^-.

e^- plasma. The potential confining the e^- is reduced by a series of 3-V steps. At each potential depth, a fast voltage pulse is used to release those e^- confined by less than approximately 5 V. The number of e^- charge-counted at each voltage step is then summed to obtain the total number of confined e^-. Use of this incremental-pulsing method allows us to avoid saturation of the charge-sensitive amplifier by very large amounts of charge, which occurs around 50 million charges counted at once.

Figure 3.19 shows a typical oscilloscope trace from the charge-sensitive amplifier due to charge-counting of e^- by pulse-out. The recorded voltage V is used to determine the number of particles incident on the degrader from that pulse. The signal decays over 300 μs, allowing us to rapidly count larger numbers of particles with many pulses.

Figure 3.20 shows the charge-counting of 100 million e^- as the confining voltage is reduced in a series of 3-V increments. The distribution in the figure provides an image

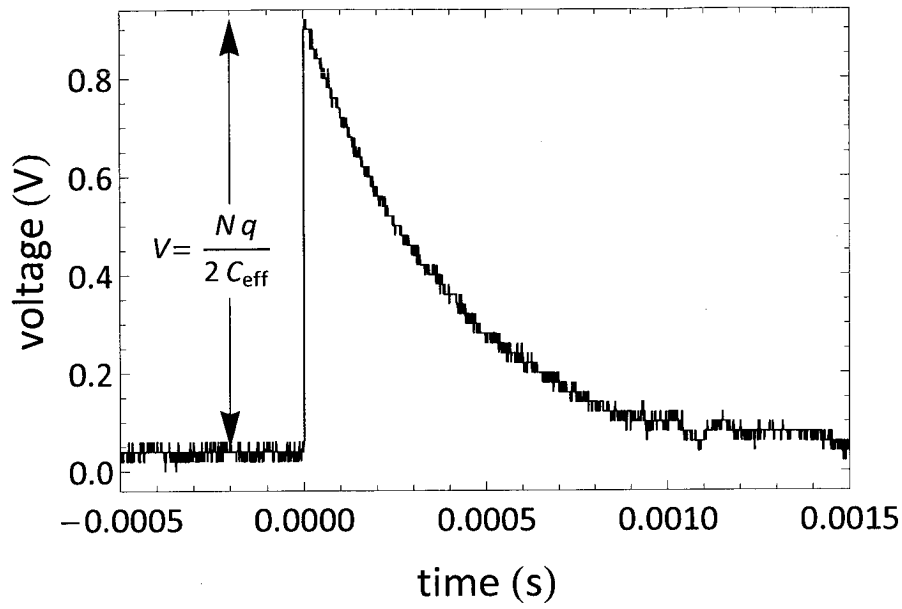

Figure 3.19: Typical scope trace from charge-counting of e^-.

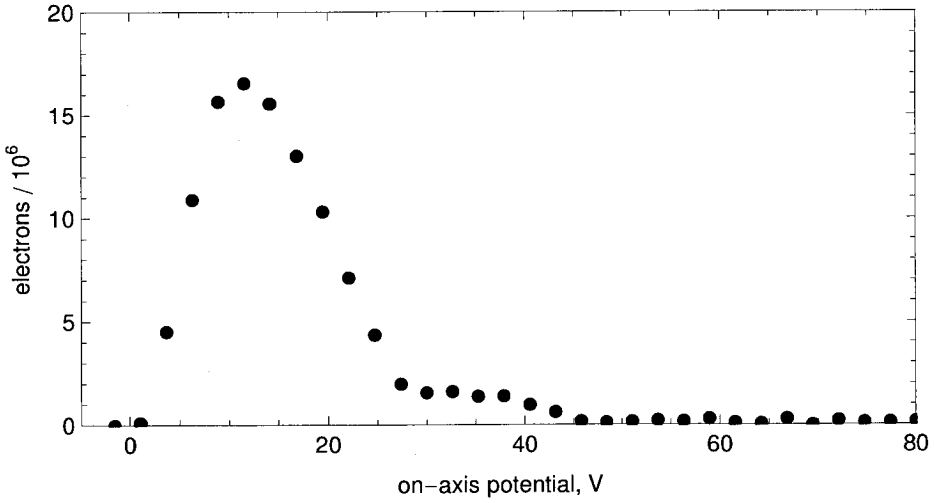

Figure 3.20: Charge-counting signal from 100 million e^- counted through incrementally lowering the confining potential in small steps and counting those e^- that escape as a fast pulse briefly lowers the confining barrier.

of the confining potential at which most e^- rest; however, the deeper trap potential off-axis is convolved with the space charge potential of the e^- themselves, so that this method does not provide a complete diagnostic of the plasma geometry.

The charge-sensitive preamplifier is also used in a similar fashion to count the number of e^+ loaded. For e^+ counting, a voltage ramp accelerates e^+ toward the Be degrader but the degrader itself is biased to a small positive voltage. This creates a voltage barrier to the emission of secondary electrons. However, e^+ annihilations with core e^- in a nucleus can result in the emission of Auger electrons, some of which may have energies high enough to escape and affect the count [74]. An earlier study by ATRAP [56] did not observe a change in the signal from e^+ pulse counting as this voltage barrier height was changed, leading us to believe that this method of e^+ counting is accurate.

Although e^+ loading is fast and robust, it is still somewhat slower than e^- loading. When we calibrate e^+ loading, we typically use less particles than we do when we calibrate e^- loading. We therefore suffer from somewhat higher noise on the measurement. One way around this has been to use the scintillating fiber detectors (described below) to detect the γ photons emitted when e^+ annihilate on the degrader. This measurement usually produces a more precise count of the number of e^+ loaded. However, in order to get an absolute calibration of the annihilation detection of e^+, we compare the charge-counting signals and annihilation signals produced by identically-loaded clouds of e^+.

3.5.2 Counting by annihilation detection

Counting by charge-sensitive amplifier is a reliable and fast method for counting large numbers of particles. Each charge-counting signal from a pulse of particles onto the degrader introduces noise on the order of 100,000 particles to the measurement, so the technique is best suited to clouds of many millions of particles. For antiprotons, where our largest clouds are on the order of a few million particles, a more sensitive and lower-noise detection method is desired. The annihilation of $\overline{\mathrm{p}}$ as they encounter produces a number of high-energy charged particles, typically pions, whose interactions with matter can be used as a very sensitive detection mechanism. The average annihilation event in vacuum can be written [75]:

$$\overline{\mathrm{p}} + \mathrm{p} \rightarrow 3.0\pi^{\pm} + 2.0\pi^{0} \ \text{(average)} \tag{3.3}$$

The high-energy charged pions can excite photons as they pass through and deposit energy in scintillating crystals. Photomultipliers can be used to amplify this signal, resulting in a very high efficiency for detecting the passage of a single charged particle through the detectors. Figure 3.21 shows the multiple annihilation detectors used in the ATRAP2 apparatus. Two sets of 3.8-mm diameter plastic scintillating fibers (Bicron BCF-12) are located inside the 1-T superconducting solenoid. The first set consists of a total of 448 "straight" fibers in two vertically-oriented layers. The second set consists of 336 "helical" fibers, again in two layers. Each helical fiber is oriented in a spiral which subtends approximately 155° of arc. Outside of the 1-T solenoid are two sets of plastic scintillating paddles (Bicron BC404). The outer paddle layer includes 8 large paddles in an octagonal configuration around the experiment. In front of each large paddle are two smaller inner paddles which combine to subtend

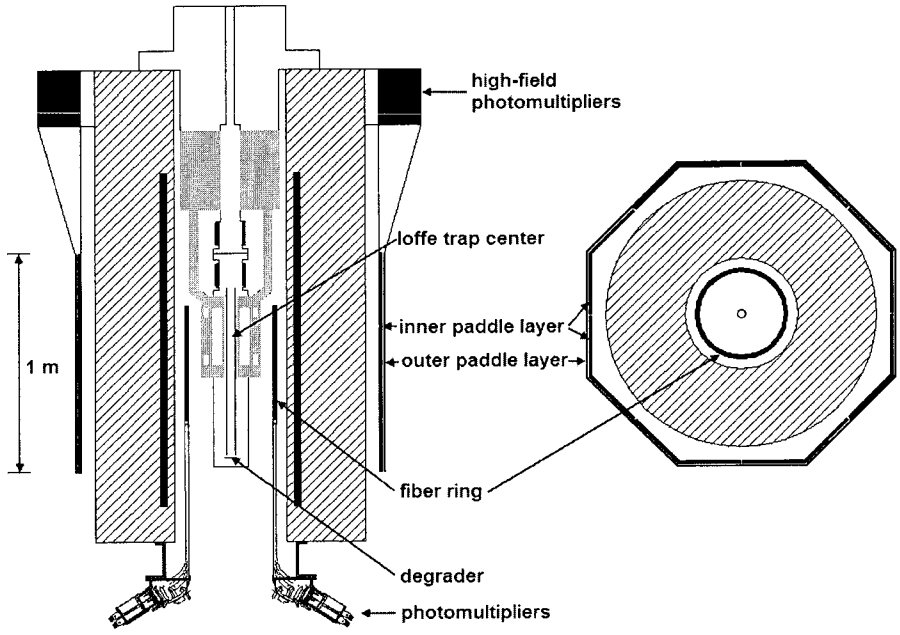

Figure 3.21: Schematic of the scintillating detectors used for counting annihilations of $\overline{p}$ and e^+.

the same total arc as the large paddle; thus, there is nearly a 100 % chance that a particle which passes through one of the two inner paddles also goes through the corresponding outer paddle. All of these detectors have a very high efficiency for detecting the passage of a single high-energy charged particle. The major limit in our detection sensitivity is therefore set by the solid angle for the charged particles resulting from $\overline{p}$ annihilations to pass through the detectors.

The scintillation light from the detectors is then read out by a photomultiplier. A discriminator changes the analog voltage seen by the photomultiplier into a digital signal which is passed into the fast data-acquisition system. The detector and data-acquisition system is described in much greater detail in [76].

Although the detectors have inherently low noise, cosmic rays consisting of high-energy charged particles constantly bombard the experiment, resulting in a finite

background count rate. In order to reduce this background rate we can select only those events which cause multiple detectors to fire simultaneously. Signals from our detectors are recorded in 50-ns bins, with a required 50-ns "wait" after each count, so that we can record a maximum of 10 million events in one second. Our apparatus is currently configured to rapidly discriminate and record the counts produced by four types of events, as depicted in Table 3.1. A "fiber" count is recorded when at least one scintillating fiber in any of the layers fires during a time bin and is therefore our most sensitive detector measurement (at the cost of a very high background rate). A "paddle coincidence" count is registered whenever at least one large outer paddle and at least one of its two corresponding smaller inner paddles fire in the same window. "Trigger-1" type events require at least two fibers and one paddle coincidence during the same 50-ns time window, while "Trigger-2" events require at least two fibers and two paddle coincidences during the time window. This table indicates the expected detection efficiency for $\overline{p}$ annihilating at the degrader; the expected efficiency is somewhat higher for those $\overline{p}$ annihilating at the center of the Ioffe trap.

Detection type	Efficiency	Background rate, Hz
Fiber	2.1	2,500
Paddle coincidence	0.75	450
Trigger-1	0.48	30
Trigger-2	0.16	4

Table 3.1: Calculated efficiencies and measured backgrounds for the different coincidence detection methods used in the ATRAP detectors.

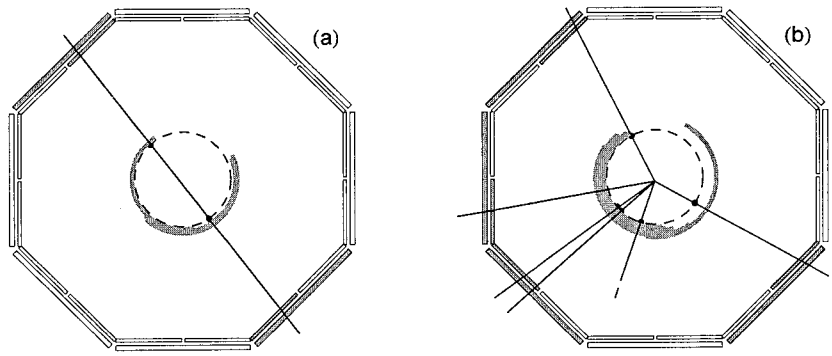

Figure 3.22: Events recorded by the full detector data recording system corresponding to (a) a cosmic ray traveling in a straight-line trajectory, (b) a $\overline{p}$ annihilation which cannot be reconciled with a single straight-line trajectory.

The ability to observe annihilation events meeting these four criteria in real-time allows us to react to changing conditions within the experiment. When very sensitive detection is required, though, we have the capability to record full data from each detector event for later analysis, showing exactly which fibers and paddles fired. Examples of the data produced by this "full acquisition" are shown in Figure 3.22. By analyzing exactly which detectors fired in an event, we can discriminate the spurious signals produced by cosmic rays (which typically activate detectors only in a straight line) from those produced by $\overline{p}$ annihilations (which are typically not consistent with a single straight-line trajectory). The full acquisition can record a maximum of 500 events per second; to minimize the inclusion of events of limited interest we typically run this system so as to record only events already meeting the Trigger-1 criteria. Due to the large data files generated by the process (and the time-consuming post-processing required to analyze these events), we typically only use this mode to record the results of antihydrogen production or trapping trials or other trials requiring the highest sensitivity.

In order to take full advantage of the information provided by the full acquisition system, we first determine a number of characteristics of each event. We look at the straight fibers which fired and divide them into "clusters" of neighboring fibers, since a single cosmic passing through along a tangent of the fiber circle could easily activate multiple adjacent fibers. We require a gap of at least 2 fibers between different clusters in case there is a single fiber in between which did not happen to fire (the induced voltage did not reach the threshold for firing, for example). We also record whether each cluster consists of a single straight fiber firing (which could possibly be due to electrical noise) or if the cluster has at least two fibers firing. We refer to clusters with at least two fibers firing as multiplicity-2 clusters. Finally, we look at how many straight fiber clusters are separated by at least $\pi/8$ radians (this angle, although arbitrary, also corresponds to the arc subtended by each of the 16 inner paddles). We do the same for the helical fiber clusters. We record the number of paddle coincidences (an inner paddle firing in coincidence with its corresponding outer paddle), and also the number of non-neighboring paddle coincidences. Finally, we do a number of checks to see if the detectors which did fire are consistent with a straight-line trajectory. This analysis enables us to determine which of twelve separate criteria each event satisfies. The criteria used are as follows:

1. At least 1 paddle coincidence

2. At least 3 helical fiber clusters of any kind

3. At least 3 straight fiber clusters of any kind

4. At least 3 non-neighboring paddle coincidences

5. The sum of the number of helical fiber clusters of any kind plus the number of straight fiber clusters of any kind is at least 5

6. At least 3 multiplicity-2 helical fiber clusters separated by more than $\pi/8$, at least 4 multiplicity-2 helical fiber clusters, at least 4 helical fiber clusters separated by more than $\pi/8$, OR at least 5 helical fiber clusters of any kind

7. At least 3 multiplicity-2 straight fiber clusters separated by more than $\pi/8$, at least 4 multiplicity-2 straight fiber clusters, at least 4 straight fiber clusters separated by more than $\pi/8$, OR at least 5 straight fiber clusters of any kind

8. At least two helical fiber clusters of any kind and at least one paddle coincidence or straight fiber; a straight line through these helical fiber clusters cannot pass through the paddle coincidence or straight fiber

9. At least two straight fiber clusters of any kind and at least one paddle coincidence or helical fiber; a straight line through these straight fiber clusters cannot pass through the paddle coincidence or helical fiber

10. At least two paddle coincidences and at least one straight fiber or helical fiber; no straight line which passes through the paddles can pass through this fiber as well

11. At least 2 multiplicity-2 helical fiber clusters separated by more than $\pi/8$ where a straight line through the helical fiber clusters is more than $\pi/8$ away from 1 paddle coincidence or more than $\pi/8$ away from 2 straight fiber clusters

12. At least 2 multiplicity-2 straight fiber clusters separated by more than $\pi/8$

where a straight line through the straight fiber clusters is more than $\pi/8$ away from 1 paddle coincidence or more than $\pi/8$ away from 2 helical fiber clusters

We next divide events into one of $2^{12} = 4096$ possible mutually exclusive classes based on which of the twelve criteria are satisified by each event. The software is then "trained" on approximately 20,000 events due to cosmic background and a separate set of 20,000 events produced by a radial dump of $\overline{p}$ in the trap. Each of the 4096 event classes is given a merit rating based on the ratio of $\overline{p}$ events falling into the class to cosmic events falling into the class (i.e., a class with a merit rating of 100 means that 100 times as many $\overline{p}$ annihilation events as cosmic events fall into this class). This procedure then allows us to make a "cut" by selecting all events from a data set with a merit rating greater than a certain value. Those cuts which use high merit ratings accept less $\overline{p}$ events (giving less signal) in return for a reduced background count rate (i.e., less noise).

Figure 3.23 shows the overall detection efficiency and cosmic background rate for cuts that select events according to different merit factors. (The data used for this plot is a different set of events than those events used for "training.") Although those cuts with strictest sensitivity might initially appear most useful, their low efficiency of detection can be a liability. The strictest cuts also show a precipitous decline in detection efficiency for only a modest reduction in background rate. A cut with a detection efficiency of 25 % and background rate of 0.5 Hz is typically what we use when looking for very low numbers of events in a limited time window (for example, when looking for a signal from trapped $\overline{H}$). When we look for larger signals we can decide which cut to use in an objective way by minimizing the uncertainty in the

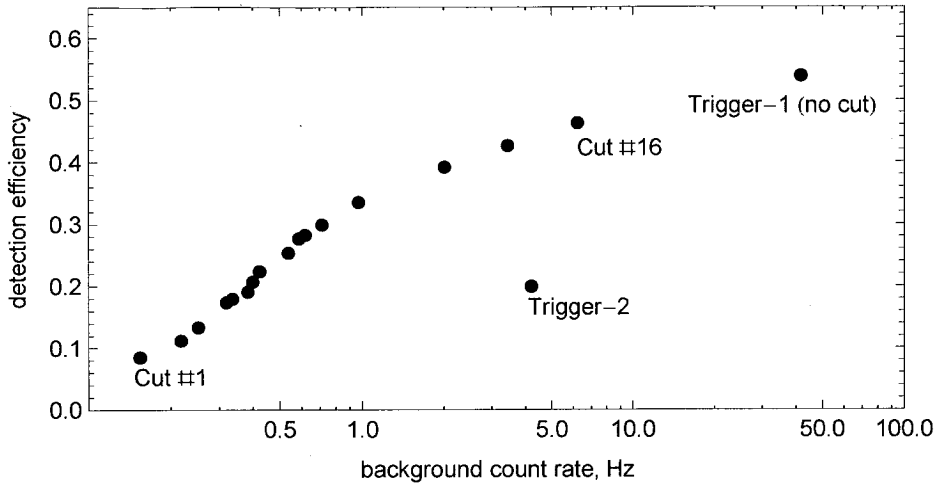

Figure 3.23: Detection efficiency and background rate of event cuts of different merit factors. Cut 1 is the strictest cut while Cut 16 is least strict. Efficiency and background for Trigger-1 and Trigger-2 type events are also shown for reference.

number of $\overline{p}$ based on the best prior estimate of the number of $\overline{p}$ and the known efficiency and background rate of the cut.

We are also able to use annihilation detection to count e^+. The energetic γ photons from e^+ annihilation trigger the scintillating fibers with an observed efficiency of 1 fiber count per 200 e^+. (This efficiency is obtained by comparing charge-count signals from equal-number clouds of e^- and e^+). We do not reliably observe paddle counts from e^+ annihilation. Due to the high background counts of the fiber detectors, our sensitivity for e^+ detection is not as good as that for $\overline{p}$.

3.6 Particle movement and manipulation

In order to produce $\overline{H}$, we need to not only load its constituent e^+ and $\overline{p}$, but must also manipulate these particles in order to get them to interact. An important

process is the movement of clouds of particles within the Penning trap. This allows us to transfer $\overline{p}$ from the lower stack region, where they are trapped, into the upper stack region where we perform $\overline{H}$ production experiments. We must also move e^+ plasmas in order to get them into the center of the Ioffe trap field and as close to the $\overline{p}$ as possible.

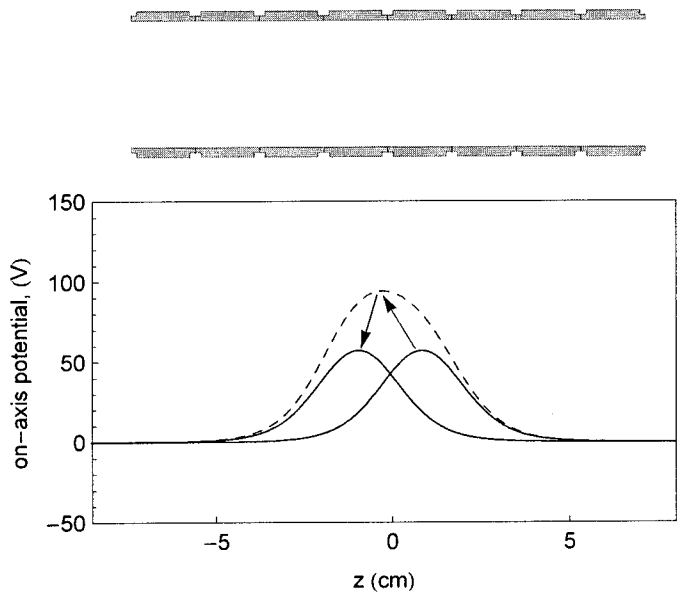

Figure 3.24: Previous procedure used for adiabatic transfer of particles from one electrode to an adjacent electrode.

Figure 3.24 shows the method first developed by ATRAP for the adiabatic transfer of particles from one electrode to another. The particles begin in a potential well located on one electrode. The potential is then increased on the neighboring electrode over a period of 1 ms, much longer than an axial bounce time for the particles. This satisifies the adiabatic condition $(d\omega/dt)/\omega \ll \omega$ and prevents heating of the particles during the transfer. The potential on the original electrode is then ramped down to zero over 1 ms, leaving the particle cloud on the new electrode. This technique can

be repeated to transfer particles through many electrodes in an "inchworm" style.

This "adiabatic transfer" technique has been a robust method for moving particles from one location to another within the electrode stack. One limitation is that it cannot be used to move one species of particles (e.g., positrons) past another species (e.g., electrons or antiprotons). In previous incarnations of ATRAP the technique of pulse-catching, where one high-voltage pulse ejects a cloud of particles from one well and a second pulse is used to catch and trap them in a distant voltage well, has been used to get around this limitation [46]. This technique has not yet been demonstrated reliably for the very large numbers of particles typically used in the BTRAP apparatus.

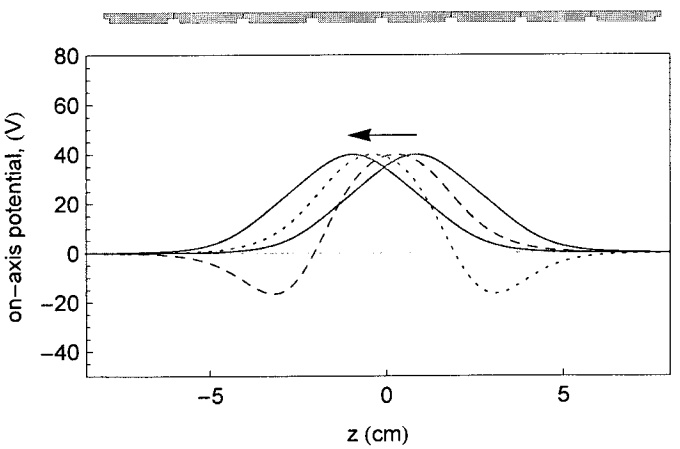

Figure 3.25: More sophisticated transfer procedure used to keep constant and quadratic terms in the potential fixed and linear and cubic terms equal to zero as the particles are transferred from one electrode to the next.

When moving many millions of $\overline{p}$, particularly from the lower stack to the upper

stack, we observed disproportionate losses when transferring by the standard "inch-worm" technique described above. In order to reduce these losses we developed a more sophisticated technique of particle transfer. This technique is shown in Figure 3.25. The confining voltages are slowly changed in a series of 50 steps in such a way that the linear and cubic terms of the on-axis potential are kept at zero and the constant and quadratic terms are held fixed. Thus the well in which the particles are confined remains unchanged throughout the transfer except for the slow translation in the axial direction. This technique is slower than the simpler transfer technique, requiring up to 30 seconds per electrode, set by the time constants of the existing electrical filters multipled by the large number of steps necessary to execute this motion. We have observed less losses of valuable $\overline{\mathrm{p}}$ with this technique, though. We also hope that this new movement technique further restricts the possibility of heating the $\overline{\mathrm{p}}$ as no potential energy is added to the particles at any time. We typically do not use this technique for the transfer of lepton species, since their synchrotron cooling allows them to radiate away any energy introduced in the transfer process and any losses in transfer can be easily compensated by loading a slightly larger number of particles initially.

Chapter 4

Theory and measurements on plasmas in a Penning trap

A plasma is an ionized gas or a collection of charged particles. Plasmas in nature typically occur at a temperature so high that thermal fluctuations exceed the binding energy of the atoms or molecules of the material, so that electrons from the atoms or molecules are collisionally ionized and become unbound. Most plasmas in nature are also electrically neutral, since otherwise Coulomb repulsion between charged particles would cause the plasma to expand and blow apart. Examples of such plasmas include flames, lightning bolts, and the Sun.

Laboratory techniques have made it possible to produce non-neutral plasmas by confining a cloud of charged particles or ions with electric and magnetic fields. The fields allow confinement of like charges by overcoming the Coulomb repulsion between the particles. Since the plasma in this case has a net charge (and may in fact consist of a single species of particle or ion), recombination into neutral atoms will not readily

occur, and cooling techniques can be used to produce a plasma with a temperature far below the limits observed in plasmas in nature. The dense clouds of charged particles used in ATRAP's experiments are plasmas of this type, with temperatures as low as $T \approx 3.5$ K, which is much smaller than the typical scale of atomic or molecular binding energies.

In the low-density limit, our clouds of particles will generally obey the single-particle dynamics described in Chapter 2, subject to perturbations due to the Coulomb interaction between the particles and to collisions which can couple different motions together. Two requirements are necessary for a particle cloud to be considered a plasma. Both relate to the Debye length of the plasma [77], given by

$$\lambda_D \equiv \sqrt{\frac{\epsilon_0 k_B T}{nq^2}} \tag{4.1}$$

with n the density, q the charge (of magnitude e for all particles used in ATRAP's experiments), and T the temperature of the plasma. The Debye length is the distance at which electrostatic forces on a test charge within the plasma are screened out by the motion of charged particles close to that test charge. One requirement for a plasma is thus that this screening length is significantly smaller than the overall dimensions of the plasma. The second requirement is that the interparticle spacing a, defined implicitly by $4\pi na^3/3 \equiv 1$ and sometimes referred to as the Wigner-Seitz radius, be significantly less than the Debye length. In other words, many particles are located within a Debye length of a test charge to provide the electrostatic screening that is needed.

For an antiproton cloud of 5×10^6 $\bar{\text{p}}$ with a typical radius of 6 mm, the axial extent in a 100-V well will be roughly 1.5 mm. The Debye length of this particle cloud is

82 μm, and the interparticle spacing is 22 μm. This particle cloud thus satisfies the inequality $a < \lambda_D < \ell_{plasma}$ (22 μm < 82 μm < 1500 μm) and can be considered a plasma, albeit barely. Roughly 50 $\overline{p}$ are contained within the volume $4\pi\lambda_D^3/3$ of one "Debye sphere," enough so that we can consider these $\overline{p}$ to screen out the electrostatic effects of particles located further away.

In the plasma regime, the electrostatic potential due to the particles themselves (the "space charge" potential) can become comparable to the potential depth by which the particles are confined and must be taken into account in analyzing the system. A rough estimate of the space charge potential can be obtained by assuming a spherical plasma of uniform density n and radius R. Charges with this geometry generate a potential (at the plasma center, and assuming $V = 0$ at infinity) of

$$V = \frac{enR^2}{2\epsilon_0}. \tag{4.2}$$

For the case of $N = 10^8$ particles and a density of 5×10^7 cm^{-3} (parameters typical for ATRAP's e^- and e^+ plasmas), the space charge potential is approximately 28 V. This is the minimum potential well depth required to confine this number of particles at this density.

4.1 Length and time scales in trapped plasmas

Several length scales besides the Debye length are also relevant in trapped plasmas. The first of these, known as the distance of closest approach, characterizes collisions within the plasma. Collisions between particles in the plasma are an important mechanism for redistributing energy and achieving the plasma's equilibrium

shape (described below). Particles within a plasma interact primarily through the long-range Coulomb potential

$$V(r) = \frac{\pm e}{4\pi\epsilon_0 r}. \tag{4.3}$$

The total Coulomb cross-section is infinite due to the long-range interaction. The plasma screens out those interactions with range longer than the Debye length, though, so we expect that the effective collisional cross-section in the plasma will be finite. An approximate expression for the collisional cross-section is given by [77, 78]

$$\sigma_c = 4\pi b_c^2 \ln\Lambda, \tag{4.4}$$

with

$$b_c = \frac{e^2}{4\pi\epsilon_0 k_B T}, \tag{4.5}$$

and

$$\ln\Lambda = \ln\frac{\lambda_D}{b_c}. \tag{4.6}$$

The quantity b_c is known as the classical distance of closest approach; it represents the smallest distance two particles within the plasma can get before the electrostatic potential energy due to their interaction equals the particles' average thermal energy. The Coulomb logarithm, $\ln\Lambda$, results from the upper and lower cutoffs for the integral of the Coulomb potential. Since $\ln\Lambda$ does not vary strongly with the parameters λ_D and b_c and is typically in the range 5 - 20, $\ln\Lambda \approx 10$ is often a reasonable approximation.

The collision rate within a plasma is then given by

$$\nu_c = n\sigma_c v, \tag{4.7}$$

with v the average particle velocity. Taking into account the temperature dependence of b_c and v, the collision rate scales as $T^{-3/2}$. This counterintuitive result suggests that the collision rate increases sharply with decreasing temperature. For a typical e^- plasma of density $n = 5 \times 10^7$ cm^{-3}, the collision time $\tau_c = \nu_c^{-1} = 14$ ns and is faster than any other process within the plasma. However the collision rate is much lower when the particles involved have energies on the order of eV.

The correlation parameter $\Gamma \equiv q^2/4\pi\epsilon_0 a k_B T = b_c/a$ represents the ratio of nearest-neighbor Coulomb potential energy to thermal energy $k_B T$ in the plasma [79]. When $\Gamma \ll 1$ the plasma is uncorrelated and random motion analogous to an ideal gas is expected; for $\Gamma > 1$ correlations between neighboring particles become important. Fluidlike behavior is expected for $\Gamma \geq 2$ and crystalline behavior is expected for $\Gamma \geq 174$ [79]. For a typical e^- plasma of density 5×10^7 cm^{-3}, the correlation parameter is less than 0.1, so our plasmas exhibit uncorrelated behavior.

Two other important length scales come into play in a confined plasma. One is the thermal cyclotron radius, given by

$$r_c = \frac{\sqrt{m k_b T}}{qB}, \tag{4.8}$$

where m is the mass and q the charge of the confined species. The plasma can be considered to be strongly magnetized when the magnetization parameter $b_c/r_c > 1$ [80]; note that $r_c \to \infty$ in the limit that $B \to 0$. Magnetic field effects become important in the strongly-magnetized regime. In particular, it becomes increasingly difficult for collisions to couple axial energy to radial energy as the particles become pinned to field lines, leading to the possibility of different axial ($T_\parallel$) and radial ($T_\perp$) temperatures. The isotropization rate of $T_\parallel$ and $T_\perp$ in the weakly-magnetized case

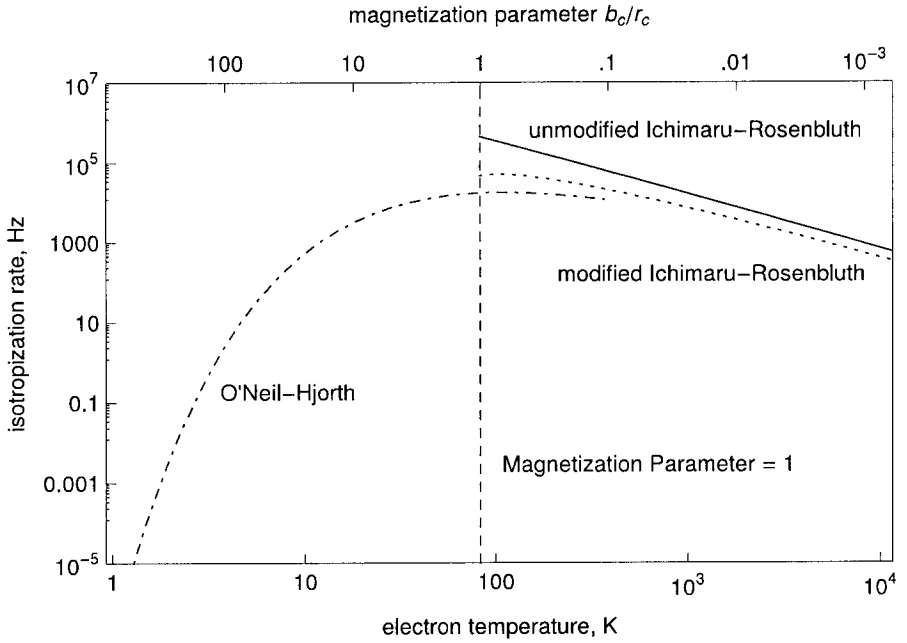

Figure 4.1: Predictions of isotropization rate of parallel and perpendicular temperatures in an electron plasma as a function of magnetization parameter.

was found to be similar to the zero-field collision rate [81], with a later analysis finding that the isotropization rate in the regime $b_c < r_c < \lambda_D$ requires replacing the Debye length λ_D with the cyclotron radius r_c in the Coulomb logarithm [82]. This analysis breaks down in the strongly magnetized regime, where $b_c/r_c > 1$ and the Coulomb logarithm becomes undefined. In this regime the isotropization rate has been calculated to be suppressed by a factor $I(\bar{\kappa})$ [83], with $\bar{\kappa} = \sqrt{m_e/\mu}\, b_c/r_c$ the magnetization parameter with reduced electron mass μ, and

$$I(\bar{\kappa}) \approx 0.67 \int_0^\infty \frac{e^{-\sigma^2/2}}{\sigma} e^{-3.14\bar{\kappa}/\sigma^2}, \tag{4.9}$$

which in the limit $\kappa \gg 1$ reduces to

$$I(\bar{\kappa}) \approx 0.47 \bar{\kappa}^{-1/5} e^{-2.04\bar{\kappa}^{2/5}}. \tag{4.10}$$

Fig. 4.1 shows the changing isotropization rate for a typical ATRAP e^- plasma as

a function of temperature. Experiments on trapped electron plasmas confirmed this suppression of temperature isotropization for magnetic fields B such that $r_c < b_c$ [84].

As we will see in Chapter 5, the typical equilibrium temperature for our plasmas is in the range 10 - 30 K, where the isotropization rate still exceeds 1 kHz so we expect $T_{\parallel} \approx T_{\perp}$. However, collisional coupling of $T_{\parallel}$ and $T_{\perp}$ becomes exponentially suppressed below 10 K, which may have consequences for the effectiveness of antihydrogen production from particle clouds whose axial motion has been cooled below 10 K by one of a few realized schemes.

One additional feature of strong magnetization in a plasma is a long time scale for radial redistribution of the particles in their approach to the equilibrium geometry. This time constant for radial transport has been found to be approximately [85]

$$\tau_{r.t.} \approx \frac{8}{3}\left(\frac{\omega_c}{\omega_p}\right)^4 \tau_{coll}, \tag{4.11}$$

with τ_{coll} the collision time and $\omega_p = \sqrt{q^2 n/\epsilon_0 m}$ the plasma frequency (discussed below). In an ATRAP e^- plasma of 10^8 e^- at $B = 1$ T, this time constant is evaluated to be 200 s to within an order of magnitude. Such a time constant is in general agreement with measurements on the expansion of plasmas within our trap (discussed below).

The final important length scale in the plasma is the de Broglie wavelength of the electron, given by

$$\lambda_{dB} = \frac{2\pi\hbar}{mv}, \tag{4.12}$$

which is the length scale at which quantum mechanical effects become important.

For a typical e^- plasma of density $n = 5 \times 10^7$ cm^{-3}, Fig. 4.2 shows many of the relevant length scales as a function of temperature. Our plasmas typically fall

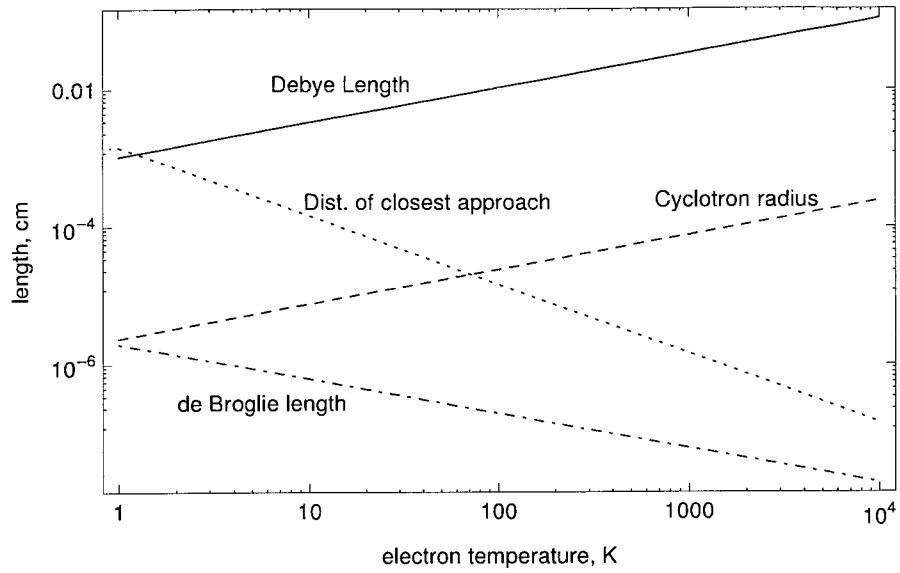

Figure 4.2: Various length scales of interest within an e^- plasma of density $n = 5 \times 10^7$ cm^{-3} as a function of plasma temperature T.

into the temperature range 3 - 30 K, with the result that $\lambda_{dB} < r_c < b_c < a < \lambda_D$. We thus typically work within the regime of a strongly magnetized but uncorrelated plasma where quantum mechanical effects can largely be neglected.

4.2 Equilibrium geometry of a plasma in a Penning trap

The cylindrical symmetry of a plasma confined within a Penning trap allows greater information to be obtained about the plasma, and in fact allows an exact solution of the equilibrium plasma shape if an ideal quadrupole potential is assumed. One feature of the cylindrical symmetry is a conserved angular momentum given by

[86]

$$P_\theta = \sum_j m\omega_{r_j}\rho_j^2 + \frac{1}{2}eB\rho_j^2. \tag{4.13}$$

In a typical ATRAP e^- plasma of 10^8 particles with radius of 5 mm, the mechanical term in the angular momentum sums to 7.6×10^{-22} kg m^2 /s, while the field term is 8.0×10^{-17} kg m^2 /s, five orders of magnitude larger. The field angular momentum then dominates, and implies that the product of magnetic field B and mean square radius of the plasma is conserved.

The thermal equilibrium condition for a confined plasma at zero temperature is that the density within the plasma is constant and that the plasma exhibits a uniform rotational frequency ω_r [79]. The rotational frequency is analogous to the large-radius magnetron motion of a single particle and can also be thought of as an $\vec{E} \times \vec{B}$ drift, with the self-field of the plasma now playing an important role in producing the $\vec{E}$ field. In a plasma of finite temperature and $\omega_r \ll \omega_c$, the density will remain constant through the bulk of the plasma but will drop exponentially to zero at the edges of the plasma with a length scale given by the Debye length [87].

Solving Poisson's equation, $\nabla^2\phi = \rho/\epsilon_0$ within the constant-density plasma leads to the result that the density n obeys [88]

$$n = \frac{2\epsilon_0 m\omega_r(\omega_c - \omega_r)}{q^2}. \tag{4.14}$$

This result is often expressed in terms of the plasma frequency ω_p, the frequency at which collective excitations ("plasmons") travel within the plasma. The plasma frequency is written as

$$\omega_p^2 = \frac{q^2 n}{\epsilon_0 m} = 2\omega_r(\omega_c - \omega_r). \tag{4.15}$$

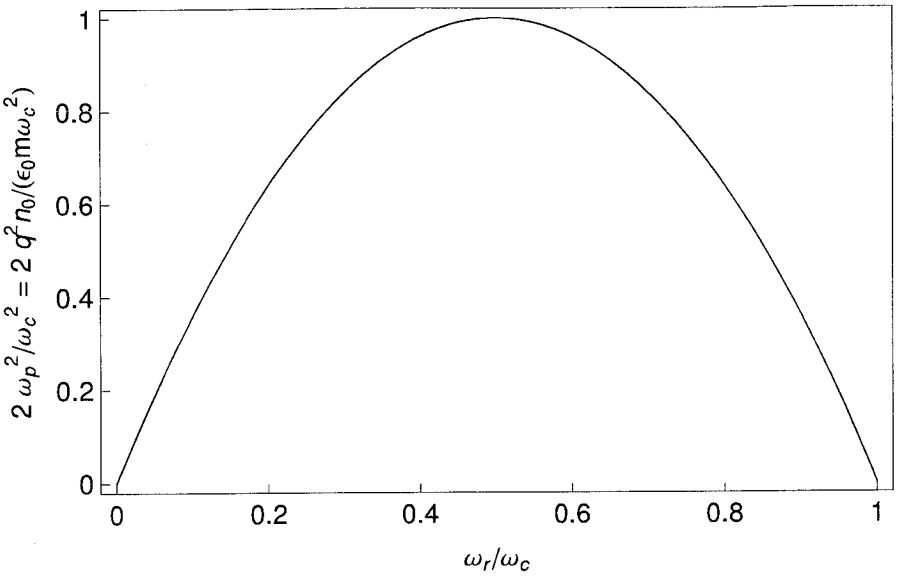

Figure 4.3: Behavior of plasma frequency ω_p or plasma density n as a function of ω_r/ω_c.

The possible plasma frequencies (and therefore densities) as a function of rotation frequency ω_r are shown in Fig. 4.3. One consequence of the behavior of the plasma frequency is that the plasma has a maximum density at $\omega_r = \omega_c/2$ of

$$n_{max} = \frac{B^2 \epsilon_0}{2m}. \tag{4.16}$$

By recognizing that $\epsilon_0 \mu_0 = 1/c^2$ we can rewrite this as

$$mc^2 n_{max} = \frac{B^2}{2\mu_0}, \tag{4.17}$$

or that the maximum mass energy density which can be confined in the Penning trap is equal to the energy density stored in the magnetic field. This fact has important (and unfortunate) consequences for efforts to use trapped antimatter plasmas as fuel for interstellar travel. For plasmas used in ATRAP, typical rotation frequencies are less than 200 kHz while the cyclotron frequency for leptons is 28 GHz, so $\omega_r/\omega_c \approx$

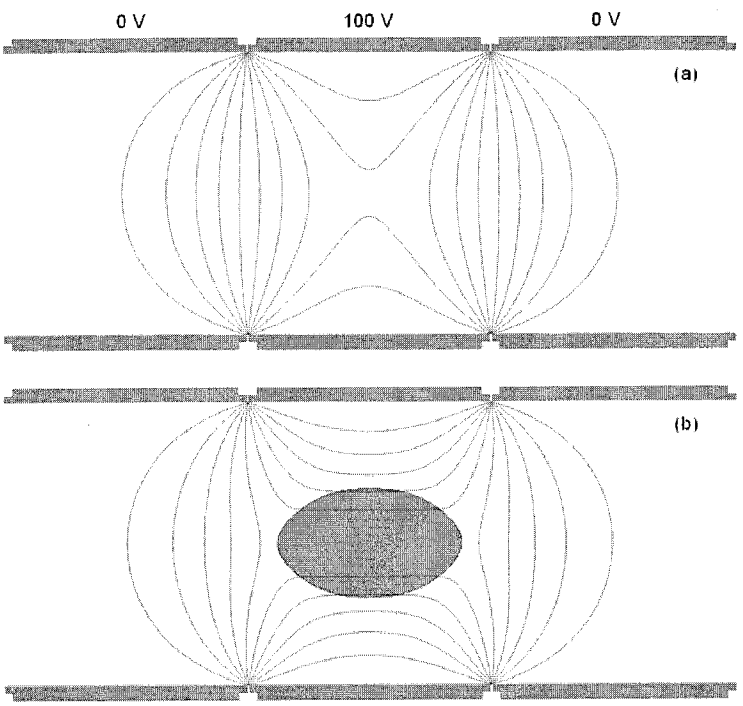

Figure 4.4: (a) Equipotential lines due only to the trapping electrodes. (b) Equilbrium plasma geometry (dark gray shape) and modified equipotential curves in the presence of an $N = 10^8$ e^- plasma with radius of 5 mm.

10^{-5}. ATRAP's plasmas therefore possess a density much smaller than the maximum possible density of a confined plasma.

For an ideal quadrupole potential, the equilibrium zero-temperature plasma shape has been calculated to be a spheroid [89]. In an actual Penning trap the effects of image charges and deviations from an ideal quadrupole potential modify this shape in a manner that does not admit of analytic solution. Instead we use finite-difference calculations to self-consistently solve Poisson's equation in the presence of a uniform-

density plasma. The computer program *equilsor* [90] calculates the thermal equilibrium plasma geometry in the presence of realistic trap potentials which we calculate through methods of numerical relaxation. Fig. 4.4 shows the equilibrium shape for a plasma of 10^8 e^- of radius 5 mm confined in a 100V well on electrode LTE3. The figure indicates that the deviation from a spheroid is not severe for plasmas of relatively small radius. However, larger-radius plasmas show greater deviations from the spheroidal approximation [46].

For a given trap (empty-well) potential ϕ_{trap}, particle number N, and plasma radius r, there is a unique zero-temperature equilibrium geometry for the plasma [91]. We can thus specify other parameters for the plasma including axial extent z, aspect ratio α, and density n in terms of these parameters. More generally, for a fixed ϕ_{trap} only two parameters are needed to completely specify the zero-temperature equilibrium. In addition the finite-temperature equilibrium in general involves only the exponential decrease of plasma density to zero over a Debye length at the edge of the plasma [87].

4.3 Collective excitations within a trapped plasma

If a perturbation is applied to a plasma in thermal equilibrium, normal modes within the plasma can be excited [92, 93]. An analytic theory for the frequencies of these modes in a spheroidal plasma has been developed [94]. The modes can be characterized by two integers (ℓ, m) with $\ell > 0$ and $|m| < \ell$. Modes with $|m| = 0$ are cylindrically symmetric. The lowest-order mode, $(1, 0)$, is simply a center-of-mass oscillation of the plasma in the axial direction, analogous to the harmonic axial motion

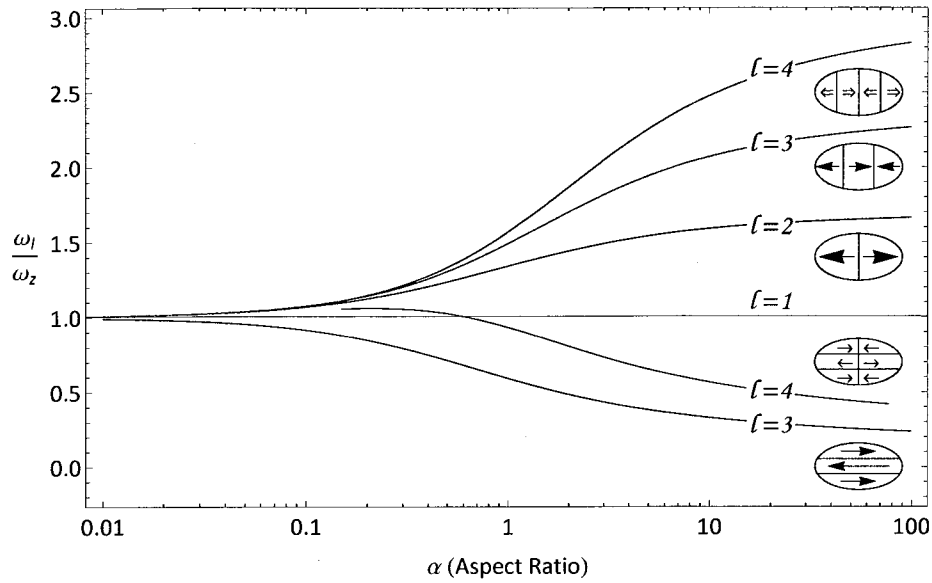

Figure 4.5: Axial oscillation modes of a plasma as a function of plasma aspect ratio.

of a single particle, with frequency $\omega_{10} = \omega_z$. The $(2,0)$ mode, known as the "axial quadrupole" mode, represents an oscillation of the plasma's aspect ratio in time. Fig. 4.5 shows the frequencies and a representation of the motion for several higher-order modes with $|m| = 0$ as a function of plasma aspect ratio (in the approximation of a spheroidal plasma).

Figure 4.5 shows that the frequencies of plasma modes can be used to determine the aspect ratio of the plasma and, in conjunction with knowledge of the particle number N and trap potential, thus completely characterize the plasma. The equations governing this relation are

$$1 - \frac{\omega_p^2}{\omega_\ell^2} = \frac{k_2}{k_1} \frac{P_\ell(k_1) Q'_\ell(k_2)}{P'_\ell(k_1) Q_\ell(k_2)} \tag{4.18}$$

with

$$k_1 = \frac{\alpha}{\sqrt{\alpha^2 - 1 + \frac{\omega_p^2}{\omega_\ell^2}}}, \tag{4.19}$$

$$k_2 = \frac{\alpha}{\sqrt{\alpha^2 - 1}}. \tag{4.20}$$

P_ℓ and Q_ℓ are Legendre functions of the first and second kind, respectively, and the prime symbol denotes their derivates. The final equation needed to specify plasma geometry as a function of modes is [95]

$$\frac{\omega_z^2}{\omega_p^2} = \frac{Q_1^0(k_2)}{\alpha^2 - 1}, \tag{4.21}$$

with Q_1^0 an associated Legendre function of the second kind. Using these equations, the knowledge of two modes of plasma motion (typically axial center-of-mass and axial quadrupole) allows us to determine the geometry of the plasma under the assumption that the plasma is a spheroid.

4.3.1 Measurements of collective plasma modes

Normal modes of a nonneutral plasma were first observed by detecting the transmission of an applied drive through a cylindrical pure-electron plasma [92]. Normal modes were first observed in a spheroidal plasma by detecting the Doppler shift in an optical transition due to excitation of the plasma modes in a cold $^9Be^+$ plasma [93]. Further work observed normal modes in a spheroidal pure electron plasma through peaks in the noise resonance of a cryogenic tuned circuit [96]. Normal modes have become an important diagnostic tool for studying the e^- and e^+ plasmas used for $\overline{p}$ cooling and $\overline{H}$ formation [97, 91, 98, 46]. Previous ATRAP measurements used an RF drive applied to one electrode adjacent to the plasma and measured transmission of

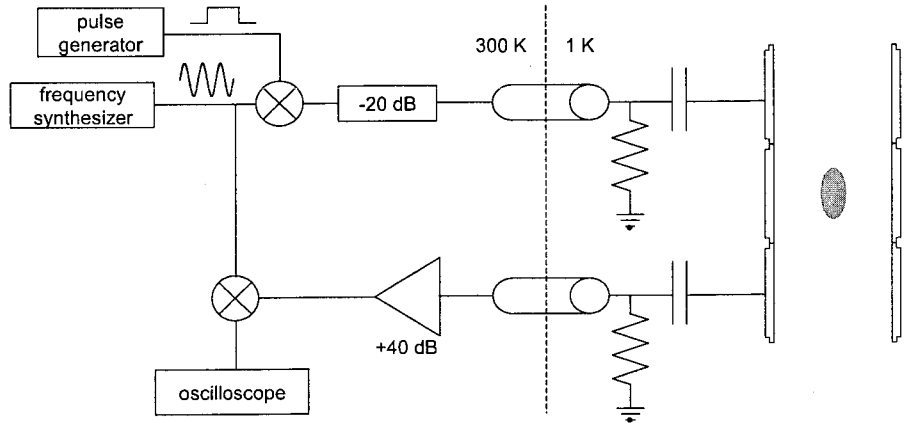

Figure 4.6: Schematic of setup used for measurements of plasma modes.

the drive through to a receiver located on the other electrode adjacent to the plasma [98].

Fig. 4.6 shows a newer method ATRAP recently implemented to measure collective excitations within a plasma. A drive to excite the plasma (Programmed Test Source PTS250) is applied to an electrode adjacent to the plasma while the resulting signal is read from the other electrode adjacent to the plasma. The drive is applied at the estimated oscillation frequency of the plasma and is gated by a 1 μs voltage pulse (Stanford Research Systems DG535, Mini-circuits ZYSWA-2-50DR). The resulting excitation therefore has a bandwidth of $\Delta f \approx 1/(2\pi\Delta t) \approx 170$ kHz and allows us to excite the plasma within a range of frequencies. We then wait typically 5 μs before measuring the induced signal on the readout electrode. This measured signal will be at the plasma oscillation frequency. The resulting signal is amplified and recorded and a Fourier transform is taken to determine the oscillation frequency. This technique allows us to make a measurement in approximately 5 s, with the time required dominated by the time needed to calculate the best fit to the observed signal. Even

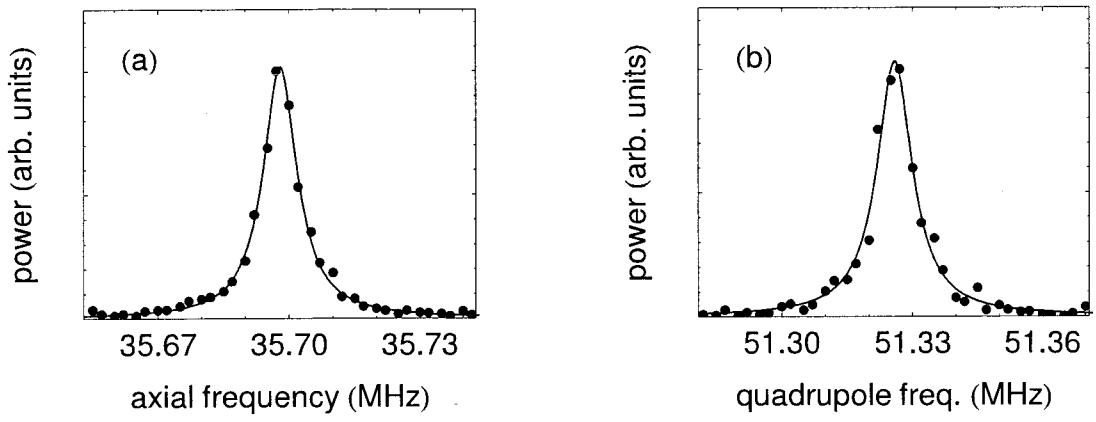

Figure 4.7: (a) Axial center-of-mass and (b) axial quadrupole modes of an $N = 10^8$ e^- plasma.

when we do not have a good estimate of the plasma oscillation frequency in question we can scan over a range of many MHz in 500 kHz steps, which we have found are steps sufficiently small to ensure we do not step over the oscillation frequency. We can thus find the desired oscillation frequency in at most a few minutes. The efficiency of this technique allows us to characterize the geometry of the plasmas used in each experiment we run, and also avoids any particles losses we have sometimes observed with other mode measurement techniques [98].

Fig. 4.7 shows the axial center-of-mass and axial quadrupole frequency spectra for an $N = 10^8$ e^- plasma. The fit allows us to determine the oscillation frequency to within 1 kHz; the linewidth of the spectrum is determined mainly by collisional broadening. The modes have a quality factor $Q \approx 5 \times 10^3$.

Fig. 4.8 shows variations of the modes as the confining trap potential V and magnetic field B are varied. As the trap potential is lowered, the axial confining force on the plasma is reduced and the plasma expands. The approximately harmonic axial

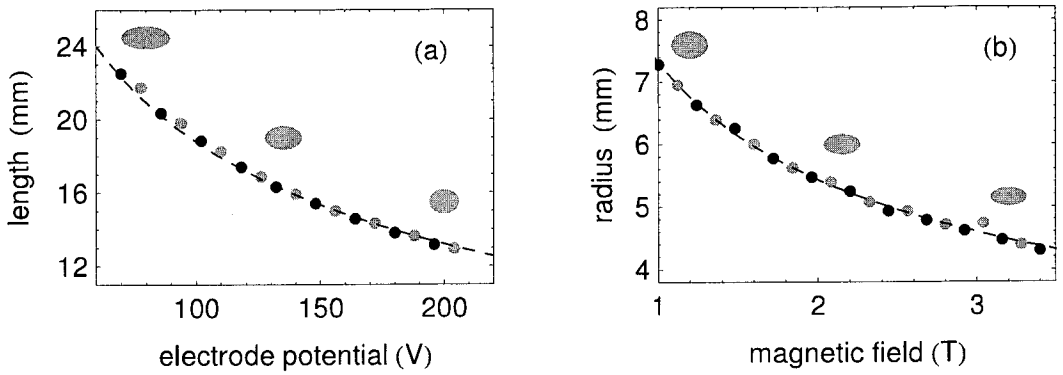

Figure 4.8: Variation of the modes as (a) confining potential and (b) magnetic field are varied. Black points indicate measured dimension as the potential or field is increased, while gray points indicate measured dimension as potential or field is subsequently returned to its orginal value. Gray ellipses represent the dimensions of the plasma assuming it is spheroidal.

confining potential $\phi \approx kz^2/2 \propto V$, so that a reduction in applied voltage V leads to an equivalent increase in z^2_{max}. The length of the plasma therefore scales as $1/\sqrt{V}$. As the magnetic field is lowered, the conservation of angular momentum $B\rho^2/2$ implies that plasma radius scales as $1/\sqrt{B}$.

The conserved angular momentum expressed above suggests that the radius of a trapped particle cloud should remain stable. Fig. 4.9 shows a study of this stability in the upper stack. An $N = 6 \times 10^7$ e^- plasma is initially prepared with a radius of 2.35 ± 0.1 mm via the rotating wall technique (described below). We follow the modes of the plasma as it remains in the confinement well over time. In a well formed by applying a symmetric set of voltages to 5 electrodes which are calculated to minimize anharmonicities in the trapping potential, no expansion is observed for many minutes of confinement. Even in a very shallow "harmonic well" of this nature, no expansion is observed to within the uncertainty. However, in a less-harmonic well formed from

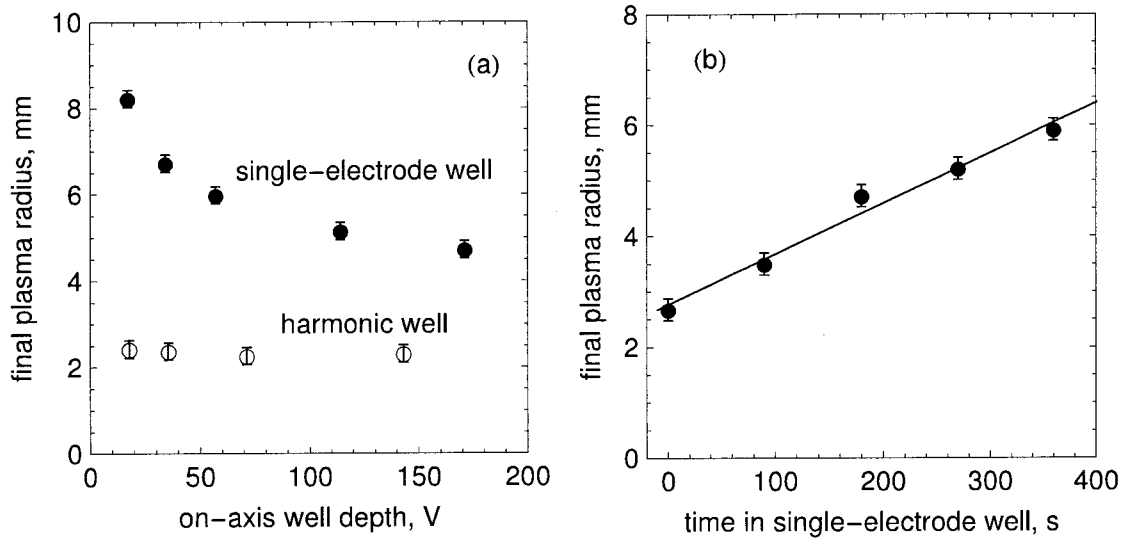

Figure 4.9: (a) Final radius of an $N = 6 \times 10^7$ e^- plasma, initially of radius 2.35 ± 0.1 mm, held for 360 s in either five-electrode harmonic wells or single radius-length electrode wells of varying on-axis depths. No expansion is observed in the harmonic wells to within the measurement uncertainty, but the single-electrode wells exhibit significant expansion. (b) Expansion in a single radius-length electrode well as a function of time. The fit is to linear increase of the plasma radius with rate 1 mm / 110 s.

a single radius-length electrode with 57 V on-axis depth, the plasma expands linearly in time at a rate of 1 mm / 110 s. The expansion is seen to be even more extreme for shallower single-electrode wells. We have found that this rapid expansion occurs only in potential wells of limited axial extent: a longer well formed from two radius-length electrodes set to the same voltage V prevents expansion. Furthermore, we do not see expansion of e^- plasmas confined in the lower stack for long periods of time, where the typical electrode length of 3.06 cm approximates the length of a two-radius-electrode-long well.

4.4 Manipulation of plasma radius with a rotating wall technique

The mode-measurement technique discussed above allows the determination of normal modes of the plasma and therefore a good estimate of the plasma geometry, but an additional technique is required to control plasma geometry. Such control has numerous applications. In room-temperature trapped plasmas, limited confinement times on the order of $1 - 10^4$ s are observed due to plasma expansion, with a general scaling of B^{-2} [99]. This expansion results from breaking of the cylindrical trap symmetry due to background gas collisions and small asymmetries in the trapping potential. In ATRAP's cryogenic plasmas confinement times do not suffer from such a limitation, but control over plasma geometry can increase the overlap between $\bar{p}$ and e^+ plasmas, allow for greater repeatability of experiments, and prevent particle loss when the higher field for $\bar{p}$ catching produced by the antiproton-loading solenoid

is reduced to the 1-T field compatible with $\overline{\mathrm{H}}$ trapping experiments. In addition, radial compression can counteract observed effects of plasma expansion within single-electrode wells or from the movement of particles throughout the apparatus.

Radial compression of a confined plasma has recently been produced by the application of a phased "rotating wall" drive [100]. In this technique, the plasma has typically been confined in a long Malmberg-style trap with aspect ratio $\alpha \gg 1$ with an electrode cut into 4, 6, or 8 segments located near one end of the plasma [100, 101, 102]. To each segment of the electrode a sinusoidal drive is applied with phase $\phi = 2\pi j/j_{max}$, with j the number of the segment and j_{max} the total number of segments. The drive thus breaks the cylindrical symmetry and applies a torque to the plasma; when the drive is applied such that increasing phase ϕ corresponds with the direction of plasma rotation, the plasma rotation speed will increase and the plasma will compress.

The rotating-wall technique has been applied to trapped Mg^+ [100] and Be^+ ions [103] and to plasmas of pure electrons [101]. The rotating-wall drive has been found to be most effective when coupling to collective plasma modes of nonzero angular momentum [104] and has been observed to have a relatively broad frequency dependence [103]. In the case of uncorrelated plasmas the frequency of drive f_{RW} applied has been much larger than the plasma rotation frequency $\omega_r/2\pi$ [101, 104]. In contrast, in a laser-cooled $^9Be^+$ plasma exhibiting crystalline behavior the plasma rotation frequency was observed to "phase-lock" to the drive frequency [103, 105]. Rotating wall drives have even been used to compress a trapped e^+ cloud of density so low that single-particle Penning trap dynamics applied [105]; in this case the compression was

observed in a narrow frequency band centered on the axial frequency ω_z of the e^+ which exceeded the rotation frequency by a factor of 10 - 100.

More recent experiments have found a "strong-drive" regime where the plasma can be compressed to a point where the final rotational frequency is equal to the drive frequency [106, 107]. In these experiments there is little dependence of compression on drive frequency and therefore the final rotational frequency of the plasma can be quickly changed by changing the drive frequency f_{RW}.

A rotating wall drive has been used to enhance the brightness of e^+ beams [105], to prepare e^+ plasmas for antihydrogen production experiments [108, 109], and to extend the lifetime of room-temperature trapped plasmas from the minutes scale to greater than 24 hours [106]. (The plasma expansion and limited lifetime in this case were due to collisions with residual gas in the room-temperature vacuum environment. In the ATRAP experiment, the extremely good cryogenic vacuum allows long plasma lifetimes even without an applied rotating wall, but the rotating wall technique is still useful as it allows us greater control over the plasma radius).

Figure 4.10 shows the segmented electrode to which phased rotating wall drives are applied and the potential structure in which particles are held for rotating wall compression. Following the method outlined in [106], we hold plasmas either in an axially long "flat well" produced by applying identical potential V_0 to 3-5 electrodes or by a multiple-electrode "harmonic well" where a least-squares routine is used to minimize anharmonicities of the trap potential. The "flat well" structure is more closely analogous to the Malmberg-style traps used in previous rotating wall experiments. We have successfully compressed plasmas in long harmonic wells, though, and

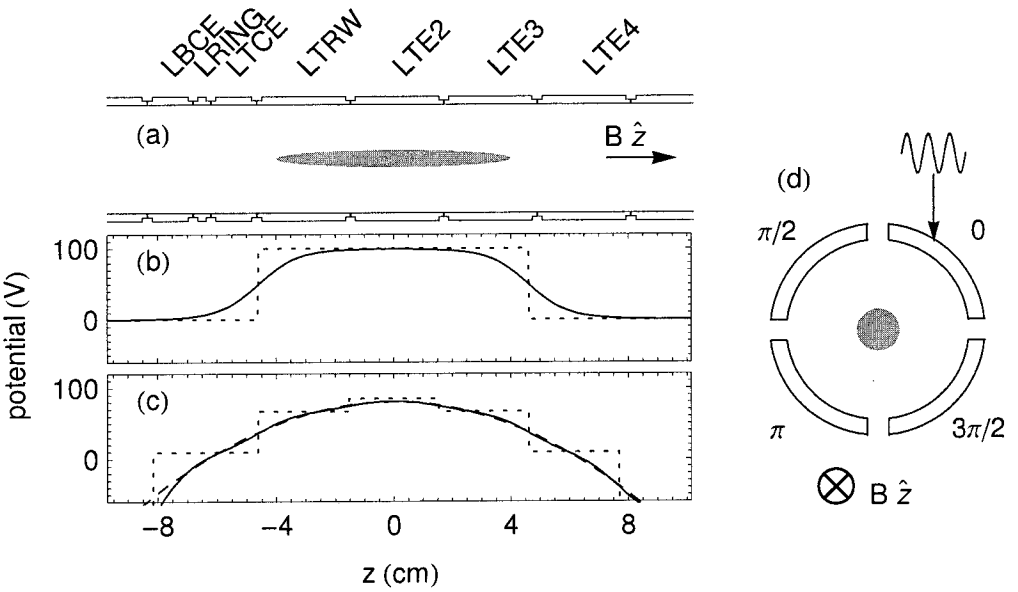

Figure 4.10: Potential structure used for rotating-wall compression of plasmas in the lower stack. (a) Location and approximate shape of the plasma during rotating-wall compression. (b) Flat and (c) harmonic potential wells used to confine particles while the rotating wall drive is applied. (d) Rotating wall electrode split into four segments to which sinusoidal drives differing by phases of $\pi/2$ are applied to radially compress the plasma.

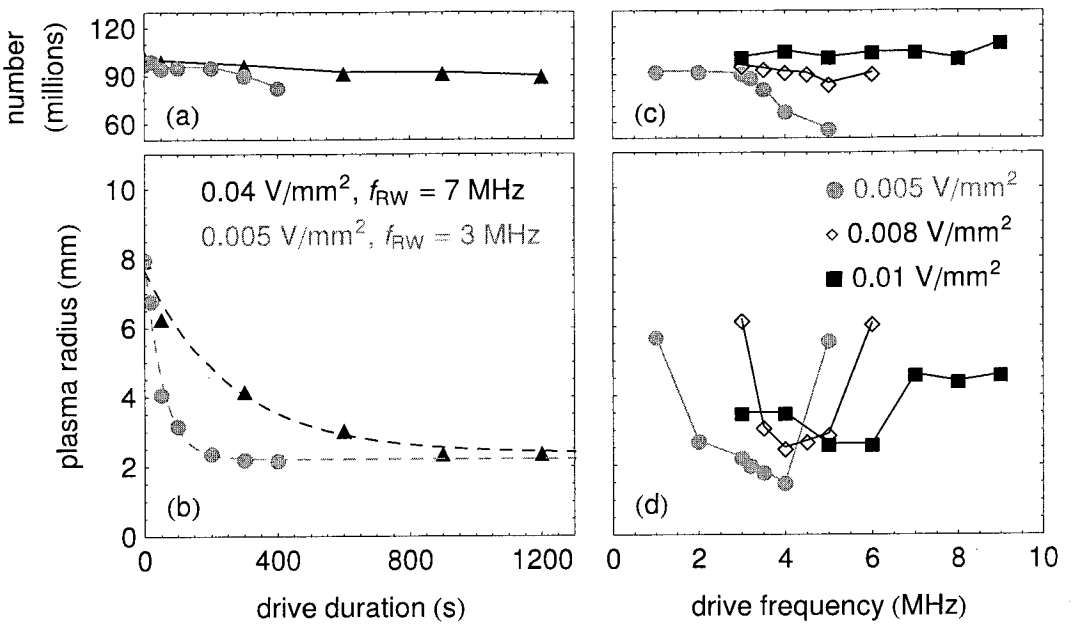

Figure 4.11: Rotating wall compression of an $N = 10^8$ e^- plasma. (a) particle losses and (b) final plasma radius as a function of drive duration for drive frequencies of 3 MHz and 7 MHz. (c) particle losses and (d) final plasma radius as a function of drive frequency for drive duration of 400 s.

have found these well structures to reduce the losses observed during rotating wall compression.

The rotating wall drive itself is a custom multichannel synthesizer built around four phase-locked single-chip direct digital synthesizers (Analog AD9954). A signal of 9 V peak-to-peak is typically applied to the segmented rotating wall electrode. Fig. 4.11 shows the compression and particle loss observed as a function of drive duration and frequency, for a plasma of $N = 10^8$ e^- confined in a seven-electrode harmonic well of varying depth. The initial radius of these clouds was 8 mm in all cases. Maximal compression is observed for drive frequencies in the range of a few MHz, which obey $\omega_r/2\pi \ll f_{RW} \ll \omega_z/2\pi$. We observe the strongest compression, but

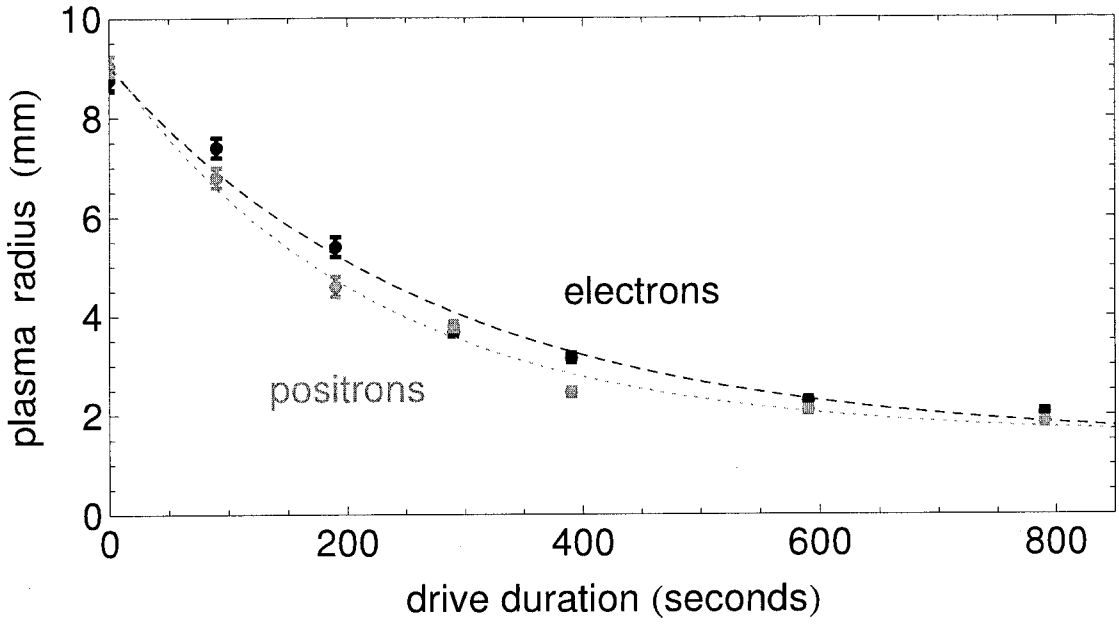

Figure 4.12: Radial compression of e^- and e^+ by the rotating wall drive as a function of drive duration.

also the largest particle losses, in the shallowest wells. In all cases the compression appears to approach a minimum radius of 2 mm. This corresponds to a plasma rotation frequency of 100 - 200 kHz, much less than f_{RW}, so that we do not appear to be in the strong-drive regime.

Fig. 4.12 shows the results of rotating wall drives applied to e^+ and e^- clouds of 10^8 particles each. The direction of the applied drive must be reversed to account for the inverse sign of charge. Aside from this one change, we are equally able to compress clouds of e^- and e^+, as expected.

4.5 Centrifugal separation of $\overline{\mathrm{p}}$ and e^-

The Penning trap geometry allows for the confinement of multiple species of charged particle in the same potential well, presuming that they have the same sign of charge. ATRAP, for example, confines both e^- and $\overline{\mathrm{p}}$ in a single potential well during the time that e^- are used to sympathetically cool $\overline{\mathrm{p}}$ [11]. When multiple species of different mass are confined in a single well, the centrifugal force experienced by a particle in the frame rotating with the plasma leads to an effective energy difference between the two species, $\Delta E = (m_1 - m_2)\omega_r^2\rho^2$. When this energy difference becomes on the order of the thermal energy $k_B T$, centrifugal separation in the plasma has been predicted [110], with the more massive species moving to larger radius. In 2010, centrifugal separation of $\overline{\mathrm{p}}$ and e^- was reported by the ATRAP Collaboration [27]. This demonstration of centrifugal separation in a two-component plasma was the first done with elementary particles and the first where neither species can be laser-cooled. Similar separation was subsequently reported by the ALPHA Collaboration [111]

By use of Equation 4.15 and the fact that $m_p \gg m_e$, we can write the temperature at which centrifugal separation is expected as

$$T_{sep} = \frac{m_p e^2}{8\epsilon_0^2 k_B}\left(\frac{n\rho}{B}\right)^2. \tag{4.22}$$

For early experiments with e^- cooling of trapped $\overline{\mathrm{p}}$, the combination of high magnetic field and low density produced $T_{sep} \approx 1$ K, less than the 4.2 K temperature of the trap electrodes at that time [57]. Therefore, no centrifugal separation of the particles was expected or observed. Experiments with laser-cooled plasmas of two ion species [112] did observe centrifugal separation, as did later experiments with simultaneously

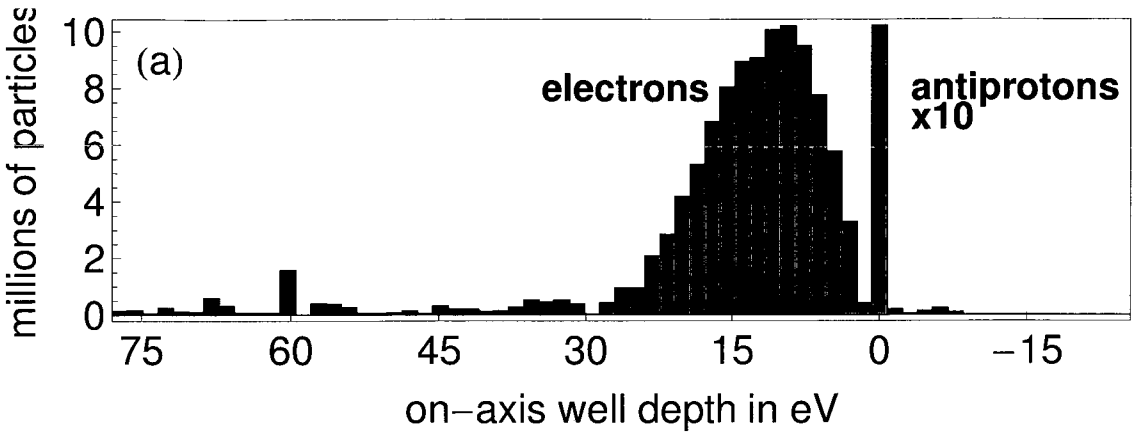

Figure 4.13: e^- and $\overline{p}$ lost as the confining potential is reduced to 0 V in a series of rapid steps. The different potentials at which e^- and $\overline{p}$ are observed to emerge indicates that the $\overline{p}$ are more deeply confined, and therefore at a larger radius, than the e^-.

confined laser-cooled ions and symathetically cooled positrons [113]. For ATRAP's current experimental parameters, the plasma density $n \approx 10^8$ cm^{-3}, $\rho \approx 5$ mm and $B = 3.7T$ combine to produce a separation temperature $T_{sep} \approx 90$ K, well above the temperature of the trapped particles.

In order to investigate centrifugal separation of trapped $\overline{p}$ and e^-, we performed two types of experiments. In the first, the confining potential for the particles was lowered while $\overline{p}$ and e^- were simultaneously confined in the potential well. The regime is such that the space charge effects of the trapped particles greatly exceed the thermal energies. Because the potential well is least deep on-axis, those particles closest to the center leave the well first.

Fig. 4.13 shows the number of e^- and $\overline{p}$ lost as the confining potential is reduced by a series of rapid 2-V steps. The e^- can be counted with a charge-sensitive amplifier, while the $\overline{p}$ annihilations are counted via our detector system. The resulting plot shows that the $\overline{p}$ are located at lower confining potential and thus at a larger radius

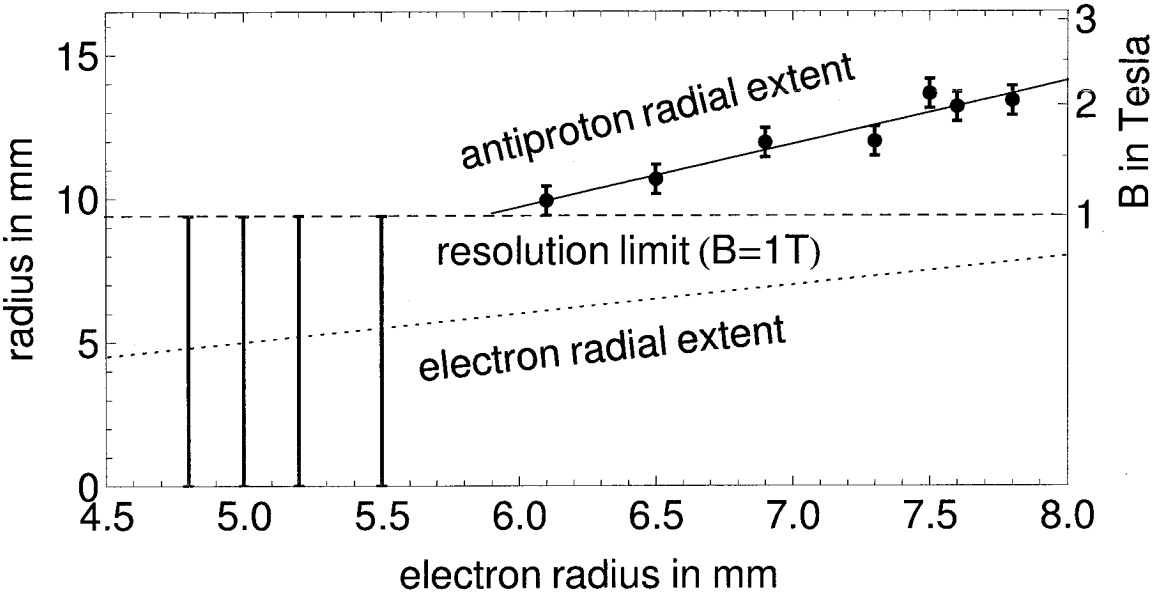

Figure 4.14: Onset of $\overline{\mathrm{p}}$ loss as the confining magnetic field is reduced from 3.7 T to 1 T. From the field at which $\overline{\mathrm{p}}$ loss begins, we can extrapolate the initial radius of the $\overline{\mathrm{p}}$. No detectable number of e^- is lost during the field ramp-down; for a starting e^- radius of less than 5.5 mm we do not observe any $\overline{\mathrm{p}}$ loss during the ramp-down.

than the e^-.

In the second type of experiment done to investigate centrifugal separation, we first load $\overline{\mathrm{p}}$ and e^- in the $B = 3.7$ T field of the antiproton-loading solenoid, then ramp down the solenoid to reduce the magnetic field to 1 T. Because of the conservation of angular momentum $p_\theta \propto B\rho^2$, as the field is ramped down we expect the radius of the plasma to expand and scale as $B^{-1/2}$. During this process we find that significant $\overline{\mathrm{p}}$ loss occurs as the $\overline{\mathrm{p}}$ expand into the trap walls and annihilate, but no e^- are lost. Fig 4.14 shows the field (and $\overline{\mathrm{p}}$ radius) at which $\overline{\mathrm{p}}$ losses begin as a function of the initial radius of the cooling e^-. The initial e^- radius is produced by compression with the rotating wall drive and is determined by measurement of collective plasma modes, as

described earlier in this chapter. The magnetic field measurements confirm that the $\overline{p}$ are located at a radius greater than that of the e^-.

This demonstration of centrifugal separation is the first with elementary particles and the first where neither confined species can be laser-cooled. The observed separation has some important consequences for $\overline{H}$ production, not all of which are positive. Centrifugal separation may increase the effectiveness of the pulse-out technique used to remove e^- once collisional cooling has reduced the $\overline{p}$ temperature to $\ll 1$ eV, and may also limit the amount of kinetic energy that the $\overline{p}$ acquire as the space charge potential of the confined e^- is rapidly reduced during these pulses. However, centrifugal separation makes it more difficult to produce a $\overline{p}$ cloud with a very small radius. With $\overline{p}$ and e^- initially confined in the same voltage well used to initially cool the $\overline{p}$, the $\overline{p}$ will be located at a larger radius than the e^-. When the e^- are ejected from this well by voltage pulses (described in Chapter 3), some of the $\overline{p}$ will fill in the central region vacated by the e^-, but the conserved angular momentum $\sum B\rho^2$ requires that other $\overline{p}$ must then move outward as well. As the magnetic field from the antiproton loading solenoid is ramped down, some further expansion of the $\overline{p}$ cloud will also take place. As will be discussed in Chapter 6, it can be desirable to introduce $\overline{p}$ into a e^+ cloud at the smallest radius possible when forming antihydrogen by three-body recombination methods. One way we may be able to get around this constraint is to directly apply a rotating wall drive to a cloud of trapped $\overline{p}$. We have not yet demonstrated this technique, and some experiments have found it difficult to achieve rotating wall compression of a particle species where no cooling mechanism is present [114].

Chapter 5

Particle temperature: Measurement and cooling methods

State-of-the-art superconducting Ioffe traps confine only those atoms with velocities corresponding to thermal energies of a fraction of 1 K. For this reason, the temperature of $\overline{\mathrm{H}}$ produced is a crucial parameter to optimize as we pursue increased trapping of $\overline{\mathrm{H}}$. $\overline{\mathrm{H}}$ production by two-stage charge-exchange is expected to produce $\overline{\mathrm{H}}$ at the temperature of the $\overline{\mathrm{p}}$ from which they form [115]. $\overline{\mathrm{H}}$ production by three-body recombination [20, 22, 116] is expected to take advantage of e^+ cooling of $\overline{\mathrm{p}}$ as the $\overline{\mathrm{p}}$ enter and interact with an e^+ plasma, as well as possible collisional cooling of $\overline{\mathrm{H}}$ as it exits the e^+ plasma. There is thus a strong incentive to produce the coldest possible $\overline{\mathrm{p}}$ and e^+ clouds.

This chapter discusses methods by which we measure and reduce the temperature of particle clouds. It begins with a discussion of cooling by radiative damping. Collisions allow this single-particle effect to cool both axial and cyclotron motions of

particles in a plasma, and allow e^- cooling of $\overline{p}$ to cryogenic temperatures [11]. The chapter continues with a discussion of two methods studied by ATRAP to measure the temperature of confined particle clouds. Finally, this chapter discusses ATRAP's recent result of adiabatic cooling of $\overline{p}$ [28], in which clouds of up to 3 million antiprotons were cooled to temperatures of 3.5 K or below. This result, the coldest temperature yet observed for $\overline{p}$, is a crucial step on the way to producing $\overline{H}$ with a few-K (or less) distribution of thermal energies.

5.1 Cooling by radiative damping

A single particle in a Penning trap exhibits harmonic and circular motions which involve continuous acceleration and therefore constantly emit radiation [117]. The Larmor formula gives the radiated power,

$$P = \frac{e^2}{6\pi\epsilon_0 c^3}|\ddot{\vec{r}}|^2. \tag{5.1}$$

For the cyclotron motion, $\ddot{\vec{r}} = q\vec{v}\times\vec{B}/m = \omega_c \times \vec{B}$ and $E_c = \frac{1}{2}m(\dot{\vec{r}})^2$. Thus the energy damping can be written as

$$\frac{dE}{dt} = -P = -\gamma_c E \tag{5.2}$$

with γ_c the time constant equal to

$$\gamma_c = \frac{e^2\omega_c^2}{3\pi\epsilon_0 mc^3}. \tag{5.3}$$

Similar calculations for the magnetron motion give

$$\gamma_m = \frac{e^2\omega_m^2}{3\pi\epsilon_0 mc^3}, \tag{5.4}$$

	e^- or e^+		$\overline{p}$	
Motion	Frequency	Damping time	Frequency	Damping time
Cyclotron	28 GHz	2.6 s	15 MHz	1.7×10^{10} s
Axial	35 MHz	3.3×10^{6} s	820 kHz	1.1×10^{13} s
Magnetron	22 kHz	4.2×10^{12} s	22 kHz	7.7×10^{15} s

Table 5.1: Typical radiative damping times for different motions of a particle in the BTRAP Penning trap at a magnetic field of 1 T.

and for the axial motion

$$\gamma_z = \frac{e^2\omega_z^2}{6\pi\epsilon_0 mc^3}. \tag{5.5}$$

Table 5.1 shows typical damping times for a particle in our trap at a field of 1 T. Only the cyclotron motion for leptons has a damping time that allows reasonable cooling rates on experimental time scales. In the higher, 3.7-T field produced by the antiproton-loading solenoid, this damping time for leptons is reduced further to 0.2 s.

Cooling by radiative damping is a single-particle effect and on its own cools only the cyclotron motion of a particle. In a cloud of particles, though, elastic collisions couple the axial and cyclotron motion together and allow significant cooling of the particles' axial motion as well. (The magnetron motion, which is an $\vec{E} \times \vec{B}$ drift, will be determined by trap and plasma fields, so it will not cool by collisions.) This allows us to use clouds of e^- as a cooling mechanism for $\overline{p}$ in our trap. (The fact that e^- will not annihilate with $\overline{p}$ is also essential here. Annihilations of p and $\overline{p}$ limit the use of some other cooling methods, such as sympathetic cooling with laser-cooled

trapped ions). Electron cooling of $\overline{p}$ [11] is the technique used by all groups studying antiprotons to cool high-voltage-trapped $\overline{p}$ to energies much less than 1 eV.

The synchrotron radiation can theoretically cool the leptons until they reach thermal equilibrium with the electrode walls. However, such equilibration will not be attained if external noise sources can enter the trap and induce heating of the particles. Since there is such a premium on using the coldest possible particles for $\overline{H}$ production, we have investigated methods of measuring the temperature of cold plasmas.

5.2 Measurements of plasma temperature

Several techniques have previously been used to measure the temperature of $\overline{p}$. When the kinetic energies of high-voltage-captured $\overline{p}$ greatly exceed the potential energy due to space charge, the $\overline{p}$ loss rate as the confining potential is reduced can be fit to an exponential to estimate temperature [70]. When electrons were first used to cool $\overline{p}$, an upper bound for the thermal energy of the $\overline{p}$ at 9 meV = 100 K could be established by the width in voltage over which $\overline{p}$ left a harmonic well as the confining potential was inverted [11]. In cold particle clouds, the potential energy due to repulsive electric interactions among the particles themselves causes a finite width in voltage over which particles leave the harmonic well. This space charge effect initially prevented a more precise measurement of the temperature of cold confined plasmas.

Since that time, ATRAP has investigated two techniques for more accurately measuring the temperature of trapped plasmas when the thermal energy of the particles is less than the potential energy due to space charge. One technique exploits the shift

in electrostatic plasma modes due to a change in plasma temperature [118], while the second samples only the high-energy tail of a Maxwell-Boltzmann distribution of particle velocities as the confining potential for the plasma is rapidly reduced to zero [119].

5.2.1 Temperature measurement by shift of plasma modes

In the first temperature measurement method we investigated, the axial center-of-mass frequency ω_0 and axial quadrupole frequency ω_2 of a trapped plasma are monitored as the temperature of the plasma is changed by some external source (for example, an applied noise drive, or by changing the temperature of the surrounding electrodes). A change in plasma temperature will lead to a shift in frequency of the axial quadrupole mode. For a finite-temperature plasma, the thermal particle motion leads to an effective pressure [120]. By changing the equilibrium geometry and the restoring force experienced by the plasma, the temperature-dependent pressure leads to changes in the frequency of the plasma's response to an external perturbation. These frequency shifts relate to changes in the plasma temperature and on their own do not determine the base temperature of the plasma. For a plasma confined in an ideal quadrupole electric potential, and in the limit that the Debye length is much less than the plasma size, the temperature-dependent shift of the axial quadrupole frequency has been calculated to be [118]

$$(\omega_2)^2 = (\omega_2^c)^2 + 20[\gamma - g(\alpha)]\frac{k_B T}{mL^2}, \tag{5.6}$$

with

$$g(\alpha) = \frac{\alpha^2}{2}\frac{\omega_p^2}{(\omega_2^c)^2}\frac{\partial^2 A_3}{\partial \alpha^2}, \tag{5.7}$$

where ω_2^c is the zero-temperature quadrupole frequency, α the plasma aspect ratio, ω_p the plasma frequency, L the length of the plasma, γ (the number of degrees of freedom of the particles) is 3, and

$$A_3 = 2\frac{Q_1\left(\frac{\alpha}{\sqrt{\alpha^2-1}}\right)}{\alpha^2-1}, \tag{5.8}$$

where Q_1 is a Legendre function of the second kind. Although the derivation is complicated, the formula predicts a small quadrupole mode shift for our experimental conditions of order of magnitude 1 kHz / K (the exact value of the shift will depend on the plasma geometry). This method was used to investigate temperature changes in e^- plasmas [121] and to measure a temperature shift in an e^+ plasma of 150 meV = 1700 K [97]. ATRAP now uses this method to study temperature shifts in trapped e^- and e^+ plasmas with temperatures much less than this limit. One complication is that the the shift in quadrupole frequency determines only a change in temperature and not the base temperature of the plasma. More details on our studies of plasma temperatures via this effect can be found in [47].

5.2.2 Temperature measurement by rapid plasma ramp-out

A second method to measure the temperature of a trapped plasma involves rapidly reducing the confining potential for the plasma and measuring the increase of particle loss rate with decreasing confining potential [119]. This method has been used for some time to measure the energy distribution of $\bar{p}$ prior to electron cooling [70]. The finite space charge potential of the particles initially made it more difficult to use this method to study very cold particle clouds. In the 2009 and 2010 beam runs, ATRAP began to look carefully at the first few particles to escape the well as the confining

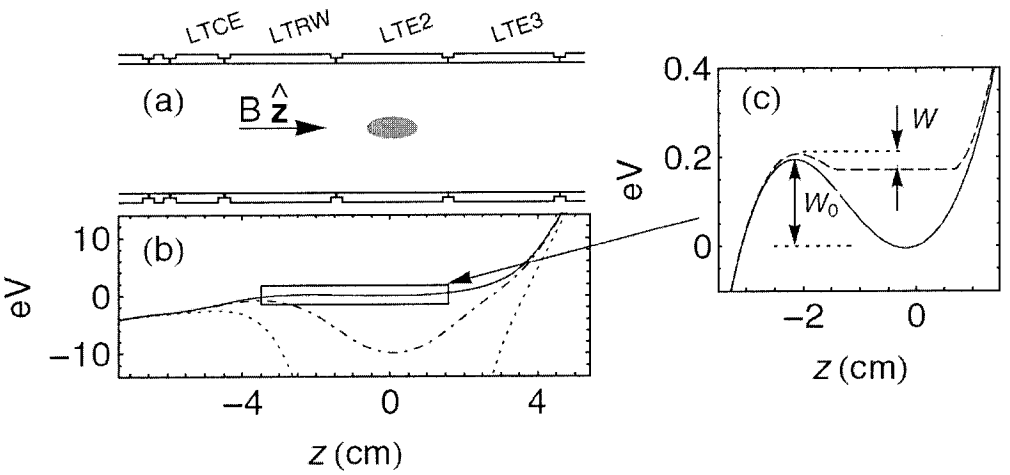

Figure 5.1: Potentials applied in order to measure the temperature of a $\overline{\mathrm{p}}$ cloud. (a) Location of the $\overline{\mathrm{p}}$ plasma within the lower stack. (b) The well depth W is decreased until $\overline{\mathrm{p}}$ begin to leave the well. (c) Close-up of the well structure showing the single-particle well depth W_0 and modified well depth $W < W_0$.

potential is reduced (amounting to no more than a few percent of the particles), to avoid the problems introduced by the finite space charge of the particles. This method was also independently used by the ALPHA Collaboration [29] to measure the temperatures of antimatter plasmas at about the same time.

Figure 5.1 shows the potential structure used to implement this temperature measurement. A $\overline{\mathrm{p}}$ cloud is initially confined in a potential well. This well can be characterized by the potential energy depth W_0 that would be experienced by a single particle in the well, which is a well-understood property of the electrode geometry and the potentials applied. The $\overline{\mathrm{p}}$ cloud modifies the single-particle well depth W_0 to a depth W.

In addition to the potential energy, $\overline{\mathrm{p}}$ at a finite temperature have a distribution of kinetic energies. Elastic collisions within the plasma serve to distribute the kinetic energy among the particles and to couple the cyclotron and axial temperatures together. The axial component of kinetic energy, $E_{||}$, thus acquires a Maxwell-Boltzmann distribution

$$f(E_{||}) = \sqrt{\frac{E_{||}}{\pi k_B T}}\, e^{-E_{||}/k_B T}. \tag{5.9}$$

As we reduce the confining potential W_0, those particles with the highest energy leave first. The loss rate increases exponentially with the change in confining potential, obeying the relation [119]

$$\frac{d \ln N}{dW} = -\frac{1.05}{k_B T}. \tag{5.10}$$

We derive the temperature by fitting a line to the slope of the logarithm of the loss rate versus W_0. In order not to perturb the bulk of the plasma, the measurement is made only on the first few percent of the particles to escape the trap, and is ideally

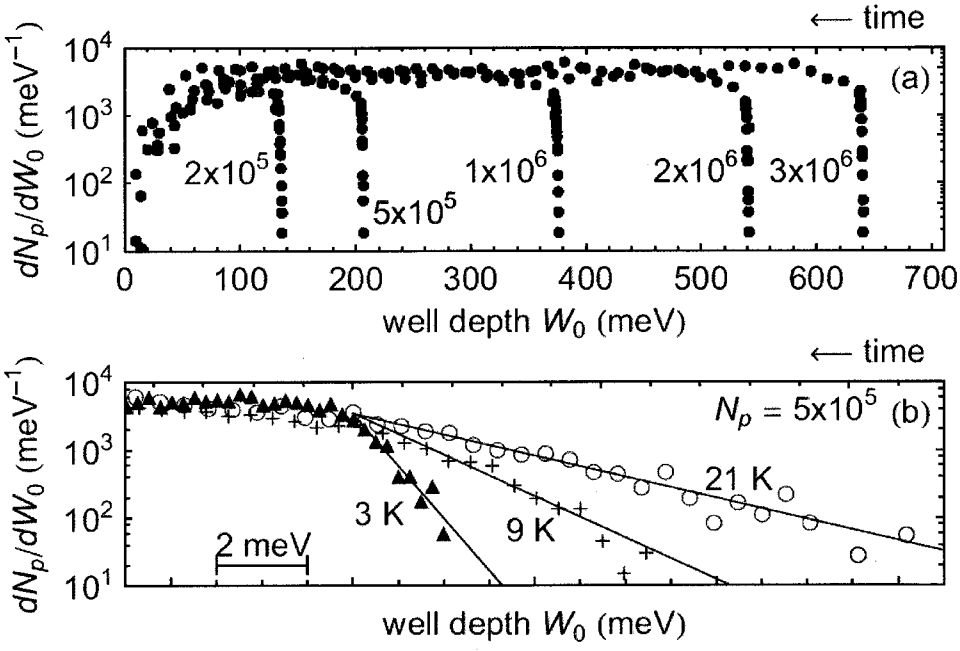

Figure 5.2: (a) Loss spectra as well depth W_0 is reduced for $N = 2 \times 10^5$ up to $N = 3 \times 10^6$ $\overline{\text{p}}$. (b) The logarithm of $\overline{\text{p}}$ loss rate vs. W_0 can be fit to extrapolate the $\overline{\text{p}}$ axial temperature.

performed fast enough that collisions cannot cause a re-equilibration of the plasma temperature.

We must make a significant correction to this raw fit to account for the modified well depth W that results from the self-field of the $\overline{p}$. Initially, the repulsive plasma interactions reduce the "zero-particle" well depth, W_0, to a smaller value W. As we reduce W_0 by reducing the voltage applied to the confining electrode, the equilibrium plasma shape will also change, changing W as well. We account for this shift by using finite-difference calculations (described further in Chapter 4) to find the equilibrium plasma shape in different zero-particle well depths. This allows us to find the reduction of actual well depth W that accompanies a specified reduction of zero-particle well depth W_0. The correction factor we thus find allows us to account for the fact that the loss rate dN/dW should increase exponentially with a reduction in actual well depth W rather than zero-particle well depth W_0. This correction ranges from 30% up to a factor of 2 for the coldest plasmas, and is the largest source of uncertainty in the measurement. Figure 5.2 shows the results of some of our measurements on cold $\overline{p}$ plasmas.

Figure 5.3 shows a histogram of temperatures of 5×10^5 $\overline{p}$ ramped out from LTE3, the electrode where $\overline{p}$ are initially cooled by e^-. The results indicate that the initial set of pulses used to remove e^- from the $\overline{p}$ produces a broad distribution of $\overline{p}$ energies on the order of $0.1 - 1$ eV. However, it also indicates that a small number of e^- are not ejected by the pulses and remain behind. If we wait for 600 s before measuring the temperature of the $\overline{p}$, we find that these remaining e^- have cooled the $\overline{p}$ to a temperature of 31 ± 6 K. Our results indicate that these "embedded electrons"

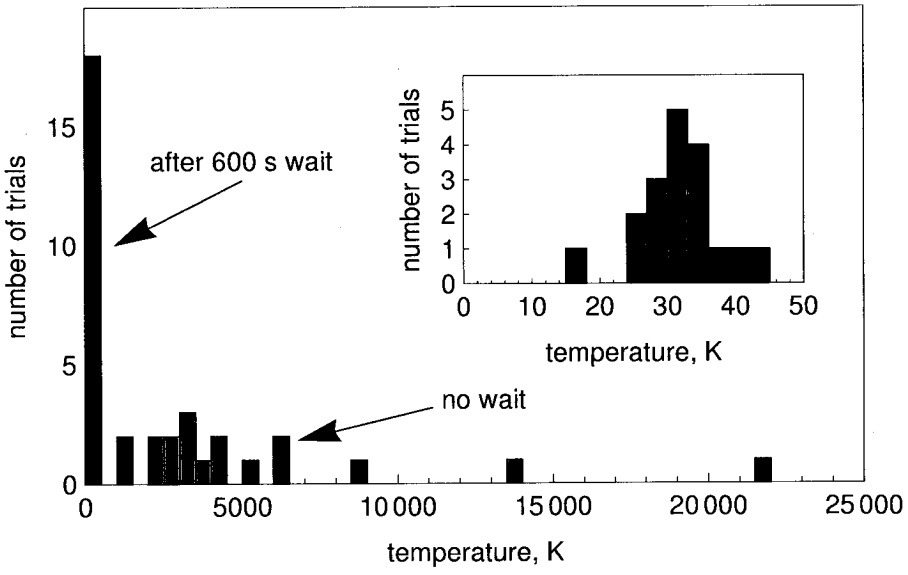

Figure 5.3: Histogram of measured $\overline{\mathrm{p}}$ temperatures with (blue) and without (red) a 600 s wait time to allow $\overline{\mathrm{p}}$ temperature to reach $T_{eq} = 31$ K. Measured temperatures have been corrected to account for adiabatic cooling (described later) which occurs during the ramp-out process.

provide effective cooling, provided that the wait time is sufficient, even though the ratio $N_{e^-}/N_{\bar{p}} < 10^{-3}$.

In the absence of any external source of heating, we would expect that the e^- synchrotron radiation would cool the e^- to the 1.3 K temperature of the trap electrodes [51]. The elevated equilibrium temperature of 31 K seems to depend on external noise sources which make their way into the trap. We may model the relaxation of the plasma to equilibrium, assuming that rethermalizing collisions themselves are a rapid process within the plasma, by

$$\frac{dT}{dt} = -\gamma_c(T - T_{electrode}) - \gamma_2(T - T_{noise}), \tag{5.11}$$

where $\gamma_c = (0.2\text{s})^{-1}$ is the synchrotron cooling rate of the particles and γ_2 represents the rate at which a noise source with effective temperature T_{noise} heats the particles. This equation results in familar exponential relaxation to an equilibrium temperature, with

$$T_{eq} = \frac{\gamma_c T_{electrode} + \gamma_2 T_{noise}}{\gamma_c + \gamma_2}, \tag{5.12}$$

and overall rate $\gamma_{total} = \gamma_c + \gamma_2$. The equivalent temperature of the external noise source, T_{noise}, is likely much higher than 300 K if this noise is due to rf signals from electrical equipment or nearby radio or TV stations; we can take room temperature as a lower limit since no active electronics or resistors are located at an intermediate temperature between the 1.3 K trap electrodes and room temperature. Since the observed equilibrium temperature of 31 K is much closer to 1.3 K than to 300 K, we know that the coupling γ_c to the trap electrodes is much stronger than the coupling γ_2 to the external noise source. Using Equation 5.12 and the known $\gamma_c = (0.2\text{ s})^{-1}$ in the 3.7-T field, γ_2 is constained to be no more than $(1.7\text{ s})^{-1}$. It is appropriate to think

of the particles reaching an equilibrium in a time scale governed by the synchrotron radiation.

Due to the much greater mass of the $\overline{\mathrm{p}}$, only the electrons cool via synchrotron radiation, and experiments on adiabatic cooling (described below) suggest that external noise sources which heat the particles also act primarily on the e^-. The $\overline{\mathrm{p}}$ thus contribute additional heat capacity but do not directly heat or cool the combined plasma. The actual rate of equilibration thus seems to be

$$\gamma_{eq} = \gamma_c \frac{N_{e^-}}{N_{e^-} + N_{\overline{\mathrm{p}}}} \approx \gamma_c \frac{N_{e^-}}{N_{\overline{\mathrm{p}}}} \approx (200\ \mathrm{s})^{-1}. \tag{5.13}$$

We typically introduce wait periods of 600 s into our experiments to make sure that our particles have reached their equilibrium temperature.

5.3 Cooling methods for antiprotons

Cooling by collisions with cold e^-, as described earlier, is the workhorse method by which we cool $\overline{\mathrm{p}}$ from keV energies to much less than 1 eV. If no external noise sources were present, we would expect particles to cool to the 1.3 K temperature of the trap walls. However, as we discovered that the actual temperature of e^--cooled $\overline{\mathrm{p}}$ in our apparatus was no colder than 31 K, we looked to other methods to further reduce this temperature.

One method to reduce $\overline{\mathrm{p}}$ temperature is evaporative cooling, where the potential well confining the particles is reduced in strength until particle loss begins. At this point, the most energetic particles are lost, and elastic collisions within the plasma cause a redistribution of the remaining energy. Evaporative cooling was the method

by which clouds of atoms were first cooled to the regime of Bose-Einstein condensation [122, 53]. Evaporative cooling of antiprotons was mentioned as a possible $\overline{\mathrm{p}}$ cooling mechanism shortly after the first $\overline{\mathrm{p}}$ were high-voltage trapped [11], but was first studied carefully in 2010 [29]. Unfortunately, due to the relatively low numbers of $\overline{\mathrm{p}}$ that can be trapped and confined (compared with the orders of magnitude larger number of matter atoms that can be trapped as a precursor to Bose-Einstein condensate formation), the necessary losses incurred during the evaporation process limited the total number of cooled $\overline{\mathrm{p}}$ to 3×10^3 and the final temperature to 9 K in this demonstration. ATRAP instead sought a technique of $\overline{\mathrm{p}}$ cooling which did not require any particle loss.

5.3.1 Adiabatic cooling of antiprotons

Adiabatic cooling is a method which can produce efficient cooling without particle losses. A classical ideal gas which expands slowly and while not in contact with a thermal reservoir (that is, adiabatically), will cool from an initial temperature T_i to a final temperature

$$T_f = T_i \left(\frac{V_i}{V_f} \right)^{2/3}, \tag{5.14}$$

with V_i and V_f the initial and final volumes of the gas. In the appropriate rotating frame, particles in the bulk of an uncorrelated trapped plasma feel no effective force and so the plasma system acts much like an ideal gas [123]. If the confining potential for the plasma is reduced, the plasma length and therefore volume will increase so adiabatic cooling is expected [124].

Adiabatic cooling requires reversibility. If the time for the plasma to redistribute

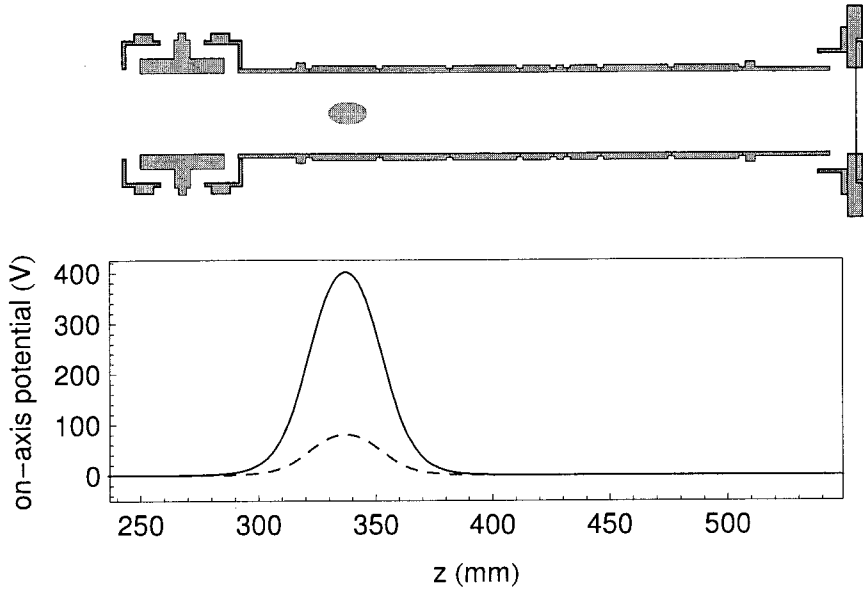

Figure 5.4: Potentials used for adiabatic cooling of $\overline{\mathrm{p}}$. (Solid curve) $\overline{\mathrm{p}}$ are held in a deep well of depth W_i for 600 s to allow them to reach T_{eq}. (Dashed curve) Once the plasma has reached its equilibrium temperature, the well depth is reduced, causing the plasma to expand and adiabatically cool.

in response to a change in confining potential is τ, the general requirement is that

$$\tau \ll \frac{W}{dW/dt}, \tag{5.15}$$

where the second term represents the time scale for the energy of the plasma to change appreciably. If our plasma acts much like an ideal gas, then the time for response to a change in confining potential should be $\tau \approx l_z/v_{th}$, with l_z the plasma axial extent and v_{th} the axial thermal velocity of the particles. For ATRAP's $\overline{\mathrm{p}}$ plasmas, v_{th} ranges from 200 to 600 m/s, while the plasma axial extent is typically 1 – 2 cm. This gives response times τ less than 100 μs. If our external changes to the potential are much slower than this, adiabaticity should be maintained.

In order to produce the coldest $\overline{\mathrm{p}}$ clouds, we take advantage of both adiabatic

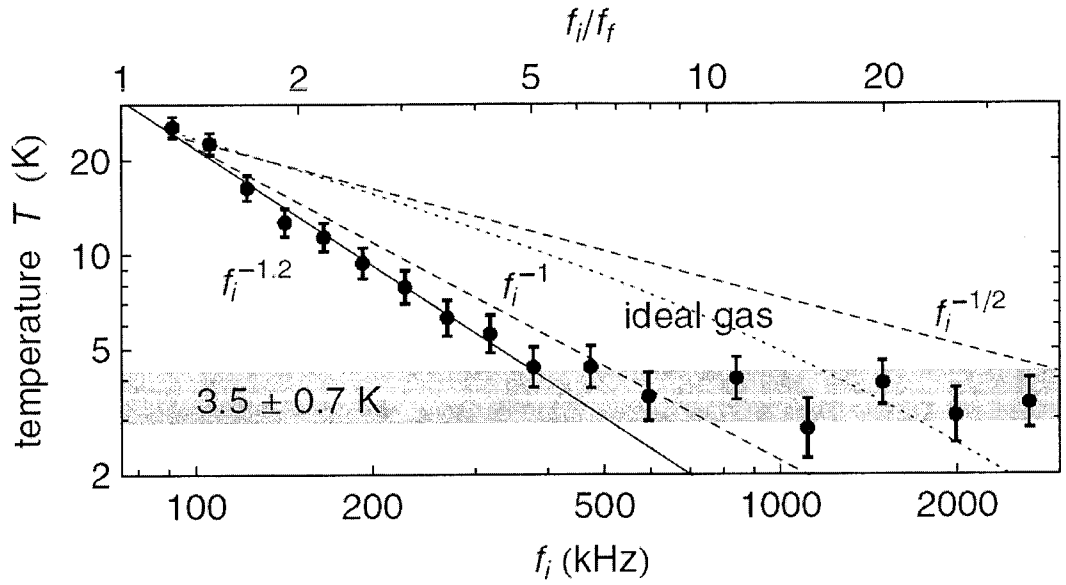

Figure 5.5: Adiabatic cooling and (dashed curves) predicted cooling as a function of initial well depth W_i.

cooling and the cooling provided by leftover e^- in the $\overline{p}$. Figure 5.4 shows the method by which we use these two different methods of cooling to produce a low-temperature cloud of $\overline{p}$. The particles begin in a well of depth $W = W_i$. We then wait for a period of 600 s, during which the cyclotron damping of the remaining e^- slowly reduces the cloud temperature to our equilibrium temperature, $T_{eq} = 31$ K.

Once the $\overline{p}$ have reached T_{eq}, we then reduce W, allowing the plasma to expand and cool. Figure 5.5 shows the cooling we observe as a function of initial well depth W_i. The deeper the initial well, the more expansion occurs as the well depth is reduced and the colder the final temperature. When the initial well in which the $\overline{p}$ equilibrate is sufficiently deep, we observe a final temperature equal to 3.5 ± 0.7 K. This value may represent a limitation of our measurement technique, in which case the actual temperatures for the deepest starting wells may be even lower than 3.5 K.

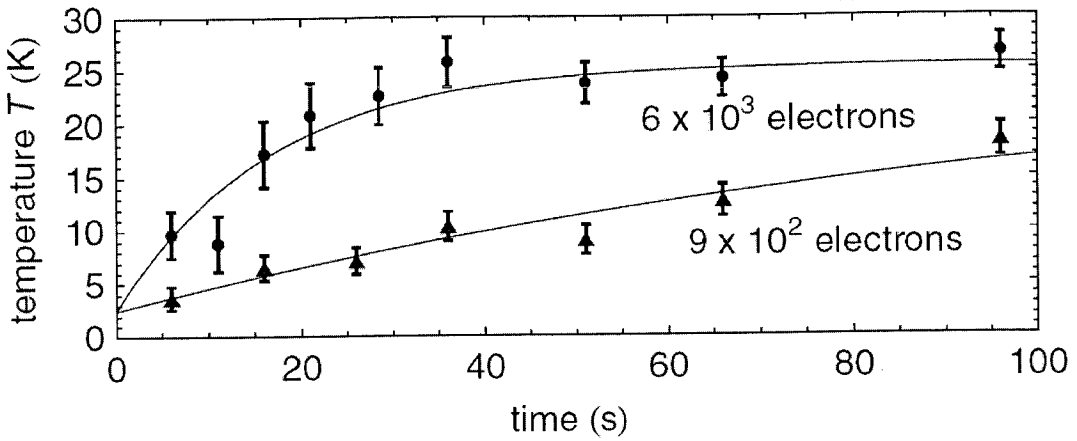

Figure 5.6: After the adiabatic cooling process is complete, the temperature of the plasma gradually relaxes to $T_{eq} = 31$ K. The relaxation time is longer when 4 high voltage pulses leave $N_{e^-} = 900$ e^- remaining in the trap than when only 3 pulses leave an order of magnitude more e^- remaining.

However, it is also possible that the efficiency of the cooling changes for our deepest initial wells or that some unknown noise source prevents cooling the $\overline{p}$ to below 3.5 K.

Figure 5.5 indicates that observed cooling does not follow the ideal gas prediction. The ideal-gas model for the plasma is an approximation which may not be entirely valid, particularly at the edges of the plasma where the density of the plasma drops exponentially to zero over a Debye length. These edge effects may be responsible for the observed dependence of the adiabatic cooling on initial well depth.

Once W has been reduced and the $\overline{p}$ have been adiabatically cooled, collisions with the e^- remaining in the $\overline{p}$ cloud will again heat the $\overline{p}$ to the equilibrium temperature of 31 K. Figure 5.6 shows the equilibration of $\overline{p}$ temperature to the final temperature of 31 K. The time for this equilibration changes according to the number of e^- confined with the $\overline{p}$, which we can control by varying the number of high-voltage pulses used

to initally eject most e^- from the $\overline{p}$. If we use many more than 4 pulses, the number of e^- remaining is small enough that we have at least ten minutes before the $\overline{p}$ warm appreciably.

The dependence of the heating rate on number of e^- remaining shows that the source of heating appears to directly couple to the e^-, which then in turn heat the $\overline{p}$ through collisions. (If the heating is due to rf inteference from radio or television stations, radio frequencies on the order of 100 MHz may more readily couple to e^- than to the $\overline{p}$. The frequencies of trapped $\overline{p}$ motions are all much less than 100 MHz). This fact allows us to keep the adiabatically cooled $\overline{p}$ at a low temperature for times sufficient for us to produce cold $\overline{H}$.

Further support for the hypothesis that external noise sources heat the particles to 31 K is provided by the fact that unplugging a known source of noise (the HV-pulsing cable) from the experimental apparatus immediately drops this equilibrium temperature to 17 K. As mentioned earlier, this still-elevated temperature may be due to radio-frequency noise coupling into our experiment from nearby radio or TV stations, or from the many pieces of electrical equipment located in the AD hall. A more thorough investigation into any noise sources that may be heating our particles remains to be completed. Given the large number of leads attached to the trap electrodes and the ease with which small amounts of noise can heat particle clouds, eliminating this source of heating may be a challenge.

5.3.2 Conclusions

In summary, efficient trapping of $\overline{H}$ requires that the $\overline{H}$ be produced at low energies, preferably comparable to or lower than the maximum trapping energy of the superconducting Ioffe trap used to confine them. Producing $\overline{H}$ with these energies certainly requires that either the e^+ or $\overline{p}$ plasma used in $\overline{H}$ formation be at a very low temperature, although merely having cold plasmas does not guarantee that $\overline{H}$ will form at this temperature. ATRAP's experiments have demonstrated the cooling of up to 3×10^6 $\overline{p}$ to 3.5 K, the coldest measured temperature yet reported for $\overline{p}$. We have also demonstrated that the $\overline{p}$ so cooled can remain at these low temperatures for times sufficient for us to use them in $\overline{H}$ formation and trapping experiments. Two important future avenues of research for us include a more thorough investigation into the noise sources that produce the initial $T_{eq} = 31$ K, and the possible combination of evaporative cooling with adiabatic cooling to produce even lower final $\overline{p}$ temperatures.

Chapter 6

Antihydrogen production in a combined Penning-Ioffe trap

The most promising route to precise spectroscopy of antihydrogen is confinement of the $\overline{\mathrm{H}}$ in a magnetic trap [15]. Since state-of-the-art Ioffe traps can confine only those $\overline{\mathrm{H}}$ atoms with energies less than $k_B \cdot 1$ K, production of very cold $\overline{\mathrm{H}}$ is required. This route to $\overline{\mathrm{H}}$ spectroscopy raises many questions: how can cold $\overline{\mathrm{H}}$ be formed? Will $\overline{\mathrm{H}}$ formation be compatible with the nonuniform fields of a magnetic trap for atoms? Can $\overline{\mathrm{H}}$ be trapped? This chapter discusses recent results related to $\overline{\mathrm{H}}$ production and trapping in a Penning-Ioffe trap. The discussion begins by outlining theory related to radiative recombination and three-body recombination formation of $\overline{\mathrm{H}}$. The production of antihydrogen by three-body recombination in a nested Penning trap [21, 22, 23], experiments establishing the stability of particles in a combined Penning-Ioffe trap [24], the first production of antihydrogen in a combined Penning-Ioffe trap [25], and antihydrogen trapping experiments are also discussed in this chapter. Anti-

hydrogen production by two-stage charge exchange is discussed in Chapter 7.

6.1 Methods of antihydrogen formation

Antihydrogen is the bound state of a $\overline{\mathrm{p}}$ and e^+. The nonzero binding energy means that some third body is required to carry away excess energy and momentum from the initially free $\overline{\mathrm{p}}$ and e^+, leaving them in the bound state. Several mechanisms for $\overline{\mathrm{H}}$ formation at low temperatures have been proposed [14, 115, 125]. In the method of radiative recombination, a $\overline{\mathrm{p}}$ and e^+ can combine while emitting a photon. In three-body recombination, or TBR, a second e^+ is the required third body. Due to its high rate of $\overline{\mathrm{H}}$ formation, TBR has become the workhorse method of $\overline{\mathrm{H}}$ production in Penning traps. Finally, in the method of charge-exchange, the third body is an e^-, typically contained within a metastable Positronium (Ps) atom. Antihydrogen production by two-stage charge exchange is discussed in Chapter 7. One further proposed mechanism for $\overline{\mathrm{H}}$ formation, that of field-induced recombination [125], was tried unsuccessfully and is not discussed in this thesis.

6.1.1 Radiative recombination

The use of radiative recombination for $\overline{\mathrm{H}}$ production was considered long ago [126] and compared to other methods [14]. In radiative recombination, a $\overline{\mathrm{p}}$ and e^+ combine to form $\overline{\mathrm{H}}$ and a photon is emitted. The reaction can be written as

$$\overline{\mathrm{p}} + \mathrm{e}^- \rightarrow \overline{\mathrm{H}} + \gamma. \tag{6.1}$$

The cross-section for radiative recombination into a state with principal quantum number n can be written [127]

$$\sigma_{rr}(n) = (2.1 \times 10^{-22}\mathrm{cm}^2)\,\frac{E_0^2}{nE(E_0 + n^2E)}, \tag{6.2}$$

with $E_0 = 13.6$ eV the ground state energy of $\overline{\mathrm{H}}$, and E the thermal energy of the e^+ involved. It is worth noting that the cross-section is largest for the lowest n states. Recent simulations suggest that the cross-section should not be strongly affected by magnetic fields in the 1-2 T range [128]. The total radiative recombination cross-section at 4.2 K for states $n < 100$ is 4.2×10^{-17} cm^2; states with $n > 100$ are likely to immediately ionize anyway due to stray electric fields within the trap. The overall radiative recombination rate for a cloud of e^+ with temperature 4.2 K and density 5×10^7 cm^{-3} is 2.1×10^{-3} s^{-1} $\overline{\mathrm{p}}^{-1}$. If 10^6 $\overline{\mathrm{p}}$ are used in an experiment, then the overall rate of $\overline{\mathrm{H}}$ formation is 2100 s^{-1}, a significant rate. However, an actual signal from radiative recombination of $\overline{\mathrm{H}}$ has proved difficult to see, as at low temperatures the rate for $\overline{\mathrm{H}}$ production by three-body recombination is orders of magnitude larger.

A laser can be used to enhance the rate of radiative recombination through stimulated emission. The enhancement rate can be written [126]

$$g = \frac{I\lambda^3}{8\pi hc(\Delta\nu)}, \tag{6.3}$$

with I the laser intensity and $\Delta\nu$ the frequency width of the laser. Laser-stimulated recombination was reported in merged beams of protons and electrons [129, 130], with a gain of up to 10^3. Experiments to produce $\overline{\mathrm{H}}$ by this method were performed with a 15-W CO_2 laser operating at wavelength of 11 μm (corresponding to recombination into the $n = 11$ state), but no signal of $\overline{\mathrm{H}}$ production was observed [131].

6.1.2 Three-body recombination

A much higher rate of $\overline{\mathrm{H}}$ formation results from three-body recombination (TBR), where a second e^+ is used to carry away excess energy from the bound $\overline{\mathrm{p}} - \mathrm{e}^+$ pair. This reaction can be written as [14]

$$\overline{\mathrm{p}} + \mathrm{e}^+ + \mathrm{e}^+ \rightarrow \overline{\mathrm{H}} + \mathrm{e}^+. \tag{6.4}$$

Because the reaction requires two e^+ to be present, the rate depends strongly on the e^+ density. An approximate form for the rate of $\overline{\mathrm{H}}$ formation by TBR can be written [132]

$$\Gamma_{TBR} = C n_{\mathrm{e}^+}^2 v_{\mathrm{e}^+} b_c^5, \tag{6.5}$$

with n_{e^+} and v_{e^+} the e^+ density and velocity, and $b_c \equiv e^2/4\pi\epsilon_0 k_B T$ the classical distance of closest approach (see Chapter 4 for more details). This reaction rate can be understood as the typical collision rate for a $\overline{\mathrm{p}}$ and e^+, nvb_c^2, multiplied by the probability nb_c^3 that a second e^+ also is located within the collision radius b_c. Calculations of the cross-section in zero magnetic field for this process find a coefficient C of order unity [133, 132]. Further calculations in the strong magnetic field limit found a ten times reduced coefficient $C \approx 0.07$ [80]. Even further calculations have found a coefficient of the same order of magnitude but which exhibits some dependence on magnetic field B and e^+ temperature T [134]. These calculations also found that the formation rate of $\overline{\mathrm{H}}$ is suppressed when the speed of the $\overline{\mathrm{p}}$ is greater than that of the e^+, corresponding to $\overline{\mathrm{p}}$ energies of $T_{\mathrm{e}^+}(m_{\overline{\mathrm{p}}}/m_{\mathrm{e}^+})$ which are on the scale of eV.

The factor b_c^5 is responsible for the strong temperature dependence of the TBR process, which is predicted to scale as $T^{-9/2}$. At low temperatures, three-body is

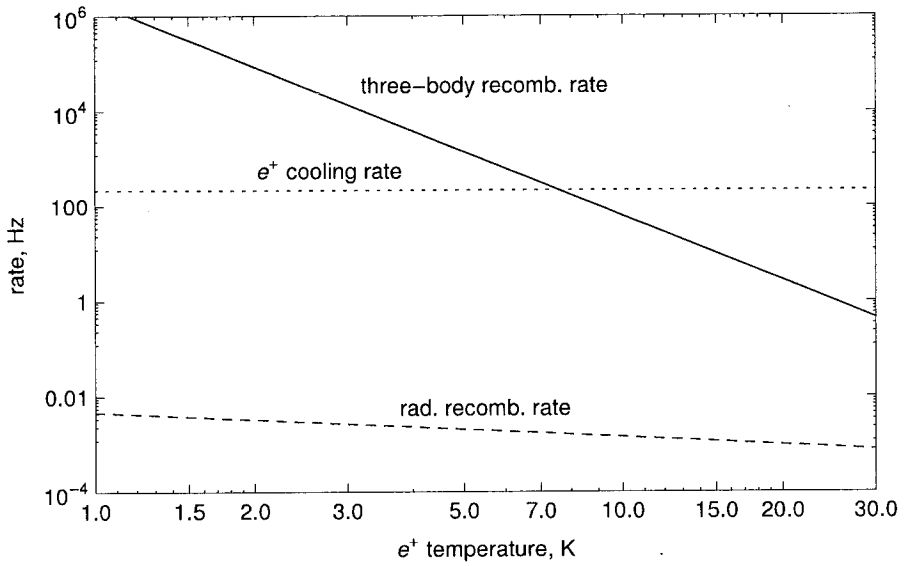

Figure 6.1: Calculated rates for $\overline{\mathrm{H}}$ formation by radiative recombination and three-body recombination, and the expected rate for e^+ cooling of $\overline{p}$.

the high-rate mechanism for the formation of $\overline{\mathrm{H}}$, but it is not predicted to have an appreciable rate for room-temperature experiments.

Figure 6.1 shows the predicted rates of TBR and radiative recombination formation of $\overline{\mathrm{H}}$ for typical ATRAP experimental conditions with a e^+ density of 5×10^7 cm^{-3}. The figure also shows the expected rate of e^+ collisional cooling of $\overline{p}$, given by [135]

$$F_{drag} = \frac{d\vec{p}}{dt} = -(4.3 \times 10^{-12}\,\mathrm{T}^{-1}\mathrm{m}^3\mathrm{s}^{-1})\,\vec{p}\,\frac{n_{e^+}}{B}, \tag{6.6}$$

with B the field in T. The expected rate of TBR formation of $\overline{\mathrm{H}}$ dominates radiative recombination at the temperatures and densities typically used by ATRAP experiments. Below approximately 8 K, the $\overline{\mathrm{H}}$ formation rate becomes higher than the rate of cooling by e^+, so that cooling of the $\overline{p}$ below 8 K is not expected. Some additional collisional cooling of the $\overline{\mathrm{H}}$ may occur, though, as the $\overline{\mathrm{H}}$ atoms exit the e^+ plasma.

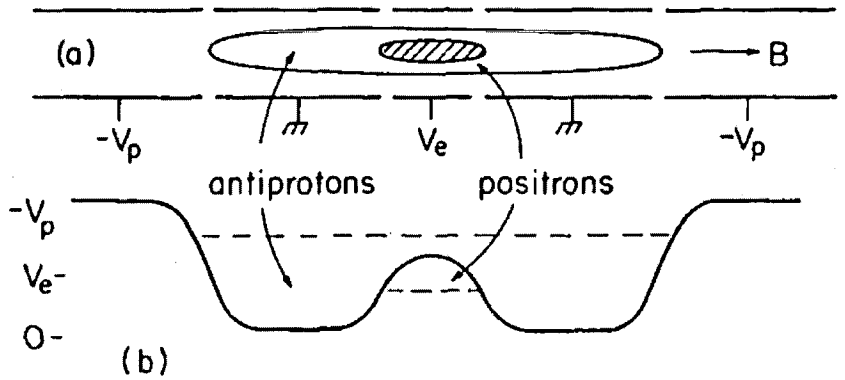

Figure 6.2: Overview of the nested well structure allowing e^+ and $\overline{p}$ to interact and form $\overline{H}$. (a) Overlapping clouds of $\overline{p}$ and e^+ allowed by high-energy ejection of $\overline{p}$ into (b) a nested well structure containing a smaller, inverted well for e^+ within a larger well for $\overline{p}$. From [14].

6.2 Demonstrations of cold antihydrogen formation in a Penning trap

The first demonstration of $\overline{H}$ production resulted from collisions between GeV-energy $\overline{p}$ and atomic nuclei [17]; as the relativistic $\overline{p}$ passed close to a target nucleus production of an $e^- - e^+$ pair with subsequent capture of the e^+ by the $\overline{p}$ produced 11 ± 2 high-energy $\overline{H}$. This method requires relativistic $\overline{p}$ and is therefore not suitable for cold $\overline{H}$ production.

In parallel to these experiments, earlier proposals to produce cold $\overline{H}$ by three-body recombination in a Penning trap [14, 136] led to the simultaneous confinement of e^+ and $\overline{p}$ [19] and the subsequent e^+ cooling of $\overline{p}$ [20]. These results opened the way to $\overline{H}$ experiments at low temperatures and the possibility of magnetically trapped $\overline{H}$, first proposed in [15].

Experiments to produce $\overline{\mathrm{H}}$ utilized the nested Penning trap methods suggested in [14] and closely followed the experimental procedures used to realize e^+ cooling of $\overline{p}$. In these experiments, a "nested Penning trap" (Figure 6.2) composed of a large (positive-voltage) well which can contain $\overline{p}$ has within it a region where a smaller negative-voltage well can simultaneously confine e^+. A cloud of e^+ is initially confined within this smaller well, while $\overline{p}$ begin in a small well located nearby but not within the nested Penning trap. A voltage pulse lowers the barrier between the $\overline{p}$ and the nested well, quickly injecting them into the nested well with several eV of energy. Collisions with the trapped e^+ cool the $\overline{p}$ into the side-wells of the nested well. Finally, the confining potential for the e^+ is slowly reduced, bringing them into contact with the $\overline{p}$ and allowing them to collisionally cool the $\overline{p}$ further and form $\overline{\mathrm{H}}$.

Evidence for $\overline{\mathrm{H}}$ production by this method was first observed in [21], where coincidence annihilations of $\overline{p}$ and e^+ (as suggested in [14]) served as a signal of $\overline{\mathrm{H}}$ production. A resonantly heated e^+ cloud (in which the $T^{-9/2}$ formation rate is strongly suppressed) served as a control experiment. At roughly the same time, a background-free observation of $\overline{\mathrm{H}}$ production was made [22], where a high electric field stripped Rydberg $\overline{\mathrm{H}}$ and allowed the resulting $\overline{p}$ to be captured in a "detection well" as the signature of $\overline{\mathrm{H}}$ production. This detection well method allowed an analysis of the n states of produced $\overline{\mathrm{H}}$. A further analysis suggested a distribution of produced n states scaling as n^{-5} [23]. This later paper also introduced the use of a resonant drive to add energy to an initially cold cloud of $\overline{p}$ in order to allow them to interact with e^+, leading to an order-of-magnitude increase of the $\overline{\mathrm{H}}$ production rate over previous efforts.

Further studies into $\overline{H}$ production investigated the temperature dependence of the $\overline{H}$ production rate. In [137], the temperature of the e^+ used for $\overline{H}$ formation was varied from 15 K to 3500 K with application of an axially resonant drive. While this experiment yielded an unexpected $T^{-0.7}$ behavior of the formation rate, it is not clear that the $\overline{p}$ would have had time to thermalize with the e^+ cloud before forming $\overline{H}$ in these trials. This paper also gave an estimate of the total $\overline{H}$ formation rate at cold temperatures of $432 \pm 44\ s^{-1}$ per 10^4 $\overline{p}$, a rate significantly higher than that expected for radiative recombination but lower than expected for three-body methods.

Another unexpected result came from an investigation into the velocity distribution of produced $\overline{H}$ [138]. In this experiment, a time-varying electric field "pre-stripped" $\overline{H}$ before they could reach the detection well; only $\overline{H}$ fast enough to pass through this pre-stripping region in less than one field oscillation period could reach the detection region and be counted. These experiments suggested the production of at least some $\overline{H}$ with roughly 2400 K of axial energy, much higher than the thermal energy of the few-K e^+ used for $\overline{H}$ production. However, $\overline{H}$ production may not have been monoenergetic, and the experiment did not rule out the possibility of other atoms produced at lower velocities. Later theoretical studies suggested that these high-velocity $\overline{H}$ might result from charge-exchange with fast $\overline{p}$ in the side wells of the nested trap, suggesting that a significant number of much slower $\overline{H}$ might have been produced as well in these experiments [139].

Overall, early investigations of $\overline{H}$ formation demonstrated a promisingly high formation rate. However, some factors were difficult to calculate, such as the geometric overlap of $\overline{p}$ and e^+, the relative rates of thermalization and $\overline{H}$ formation in a dense

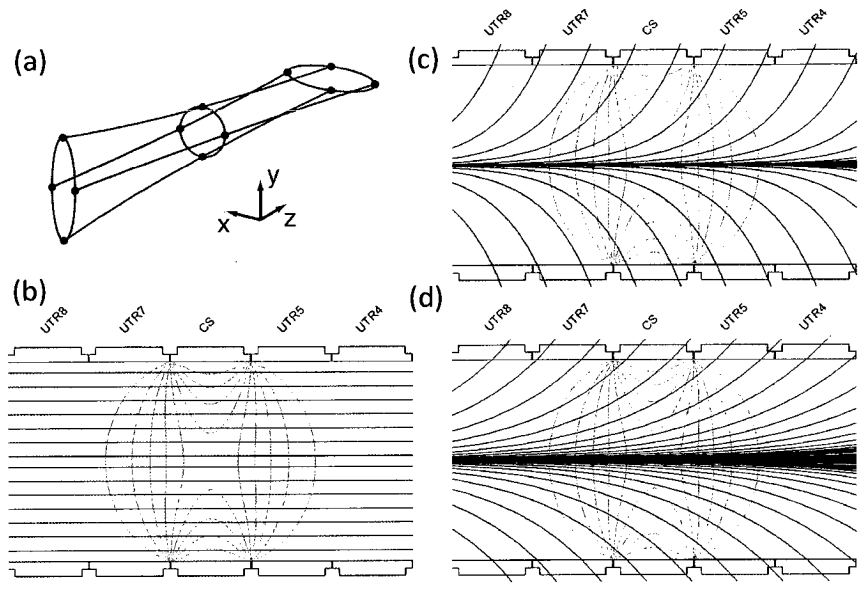

Figure 6.3: Fields in the Penning-Ioffe trap. (a) The Ioffe trap distorts cylindrically symmetric field lines into characteristic twisted bow-tie shapes. (b-d) Electrostatic contours (grey) and magnetic field lines (blue) for particles held in a 50 V well in (b) the 1-T background field only, (c) the field produced by the quadrupole racetrack coil only, (d) the full field of the Penning-Ioffe trap including the solenoidal pinch coils.

e^+ plasma, and the possibly non-isotropic distribution of final $\overline{H}$ velocities.

6.3 Particle stability in a combined Penning-Ioffe trap

Trapping $\overline{H}$ requires both the Penning trap configuration to confine the charged particles which are the ingredients of $\overline{H}$ and a magnetic (Ioffe) trap to confine the resulting neutral atoms. A traditional Penning trap of course uses a uniform B field to provide radial confinement of the particles, but magnetic trapping of neutral atoms relies on a nonuniform magnetic field with a minimum located at the trap center. The two traps are thus in conflict with one another to some degree, and debate has ensued

over the stability of charged particles when the fields of a Ioffe trap are superimposed on the uniform Penning trap fields.

The lowest-order nonuniform magnetic field which can radially confine neutral atoms is a quadrupole field, which can be written as

$$\vec{B}_{quad} = \beta(x\hat{x} - y\hat{y}). \tag{6.7}$$

The magnitude of the magnetic field in this case increases linearly with radial distance ρ from the center of the trap. Quadrupole magnetic traps are described in more detail in Chapter 2, but use four vertical current-carrying bars to produce the required field configuration. The cylindrical symmetry of the pure Penning trap is removed due to the non-symmetric quadrupole field, so the simple and separable single-particle motions described in Chapter 2 become coupled. However, it has been suggested that adiabatic invariants for single-particle motion allow confinement within a combined Penning-Ioffe trap [140]. These adiabatic invariants apply so long as resonances or collisions which couple the magnetron and axial motion of the particle together can be avoided.

In addition, early theoretical studies of single-particle motion in a quadrupole Penning-Ioffe trap noted that there is no confinement for particles beyond a certain radius [140]. The electric field in Penning traps is not confining in the radial direction and a particle trajectory which leads along field lines to the electrode which applies the confining voltage is not a trapped trajectory. If a quadrupole magnetic field is gradually increased in a Penning trap, some of the field lines on which particles lie will intersect the trapping electrode and the particles will be transported to the wall. If the electrode length is comparable to the electrode radius, only field lines starting at

a large radius will end on the same electrode; field lines nearer to the center will end on adjacent electrodes which provide a confining electric field and the particle is not lost (see Figure 6.3). This loss mechanism was investigated in a Malmberg-style trap with electrode axial extent much greater than the radius [141], where the quadrupole field led to very large losses.

The motion of a trapped plasma in a Penning-Ioffe trap is more complicated as the single-particle motion is also perturbed by the self-field of the plasma. Preliminary investigations into the stability of plasmas in this field configuration were conducted in a Malmberg-style trap (with electrodes of length much greater than their radius) [142]. These experiments found that a resonance condition,

$$\omega_r \tau_z = \frac{N\pi}{2}, \tag{6.8}$$

with ω_r the plasma rotation frequency and τ_z the axial bounce time, leads to particle orbits which are rapidly transported outward by field lines. In a Malmberg-style apparatus with long axial extent, the axial bounce time τ_z is maximized, while other experimental conditions (low B field and relatively high e^- density) conspired to make ω_r large as well. However, in a shorter-electrode Penning trap and at a higher background B, the resonance condition (which can be rewritten as $f_r/f_z < 1/4$) is easier to avoid and in fact ATRAP's plasmas lie significantly below the resonance condition for diffusive loss of this type.

Early results of particle instability when quadrupole magnetic fields were added in Malmberg-style traps led to claims that quadrupole fields were incompatible with particle confinement [141]. It is also possible to magnetically trap atoms with a higher-order multipole trap, such as an octupole trap. These higher-order traps con-

tain a correspondingly higher number of current-carrying bars to produce the radial gradient. The radial component of magnetic field in a general multipole trap grows with radius ρ as $B_{radial} \propto \rho^{n-1}$, with $2n$ the number of current-carrying bars in the Ioffe trap. ($2n = 4$ for a quadrupole trap and $2n = 8$ for an octupole trap). Higher-order traps cause less perturbation of the fields near the center of the Penning trap electrodes. However, quadrupole traps result in greater compression of the trapped atoms and, because they contain less current-carrying bars, make it easier to add ports for laser access to the trap. While concerns about particle stability in a quadrupole Penning-Ioffe trap led the ALPHA Collaboration to construct an octupole magnetic trap for antihydrogen, ATRAP instead chose to build a quadrupole trap and investigated the stability of plasmas in this field configuration.

ATRAP's experiments demonstrated stable confinement of e^- and $\overline{p}$ plasmas in a quadrupole Penning-Ioffe trap [24]. These experiments started with a particle cloud held on a single radius-length electrode, initially in only the 1-T background field of the Penning trap. The quadrupole field of the Ioffe trap was then slowly ramped up. As explained further in Chapter 2, the full Ioffe field includes radial confinement by a quadrupole coil and axial confinement by a pair of circular "pinch coils" which produce a gradient in the axial direction. At the specification currents of 69 A in the quadrupole coil and 80 A in the pinch coils, the ATRAP Ioffe trap depth (including the background field of the 1 T) solenoid is 375 mK. For these particle stability experiments, the quadrupole Ioffe fields were ramped up at a rate of 0.1A / s, so reaching full field required 690s.

Fig. 6.4 shows the retention fraction of a plasma of 36×10^6 e^- as the quadrupole

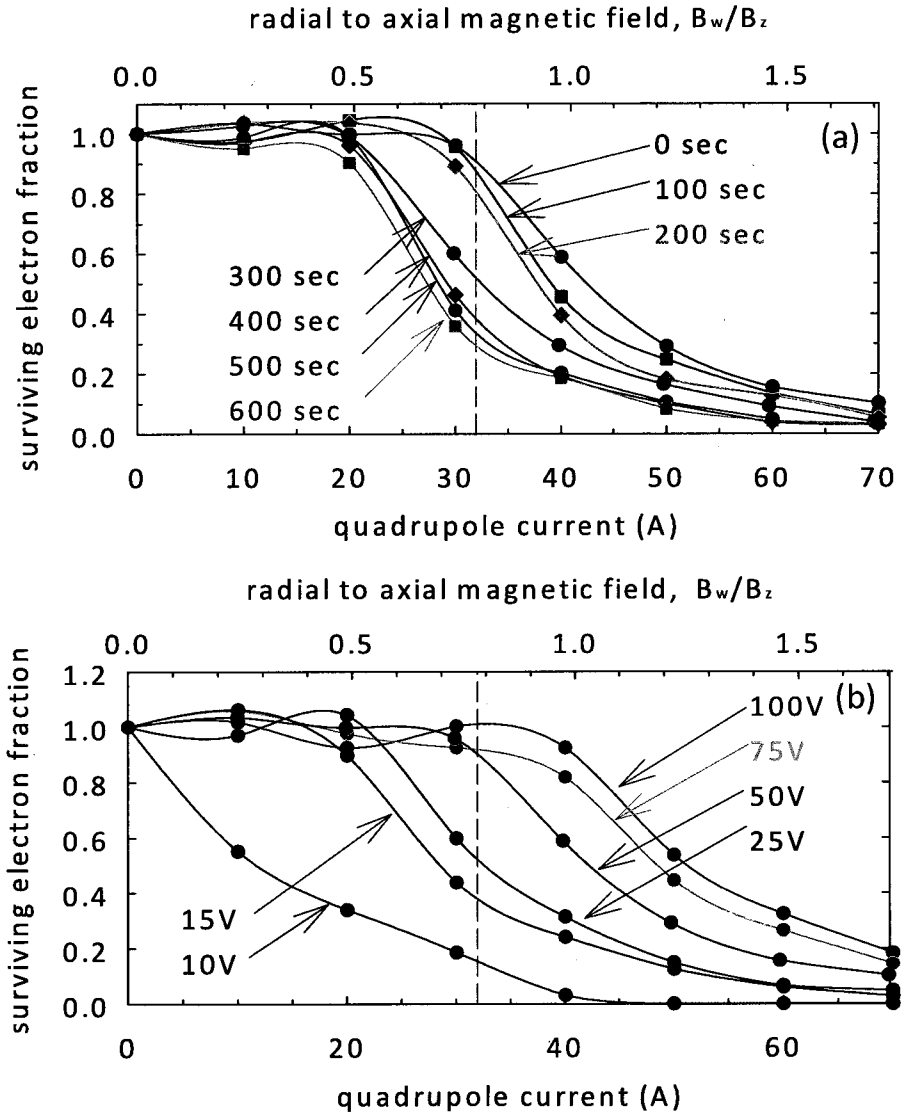

Figure 6.4: Retention of e^-in the quadrupole field of the Ioffe trap. (a) Retention fraction of 36 $\times 10^6$ e^- as a function of final quadrupole current for different holding times at the specified quadrupole current. (b) Retention fraction of 36 $\times 10^6$ e^- as a function of final quadrupole current for different well depths.

current is ramped up to a specified value, held at that value for a certain amount of time, then ramped back to 0 A. The line at $\beta r/B_0 = 0.78$ represents the ratio of radial-to-axial field at which the full Ioffe trap operates, as the pinch coils act to increase the axial field to approximately 2 T in the center of the trap. A significant fraction of e^- survive even for 600 s at this ratio of radial to axial field, long enough to produce $\overline{H}$ by either three-body recombination methods or by the charge-exchange method to be described in Chapter 7. Fig. 6.4 (b) also indicates that e^- loss tends to increase sharply at a "knee." This knee occurs at a higher currents for deeper confining potentials, which is not surprising since the plasma axial extent $l_z \propto V^{-1/2}$. Longer axial extent of the plasma increases the inhomogeneity of the fields sampled by the e^- and makes it more likely that resonances leading to diffusive loss of the plasma are encountered.

Fig. 6.5 shows the fraction of clouds of 90,000 and 280,000 $\overline{p}$ retained as the quadrupole current is ramped up to a specified value, held for 300 s, and then ramped down. The $\overline{p}$ were held in a 50 V well for this study. The retention of the $\overline{p}$ is quite good. This is understandable given that the density of $\overline{p}$ used in this trial is low enough that the cloud is not a plasma and single-particle dynamics should apply. Most of the $\overline{p}$ losses which do occur are observed during the ramp-up of the quadrupole fields and the stability of the cloud after the specified current is achieved is very good.

The observed stability of $\overline{p}$ and e^- clouds in a combined Penning-Ioffe trap resolved a longstanding controversy and suggested that it should be possible to produce $\overline{H}$ in a Penning-Ioffe trap. This motivated ATRAP's investigations into antihydrogen

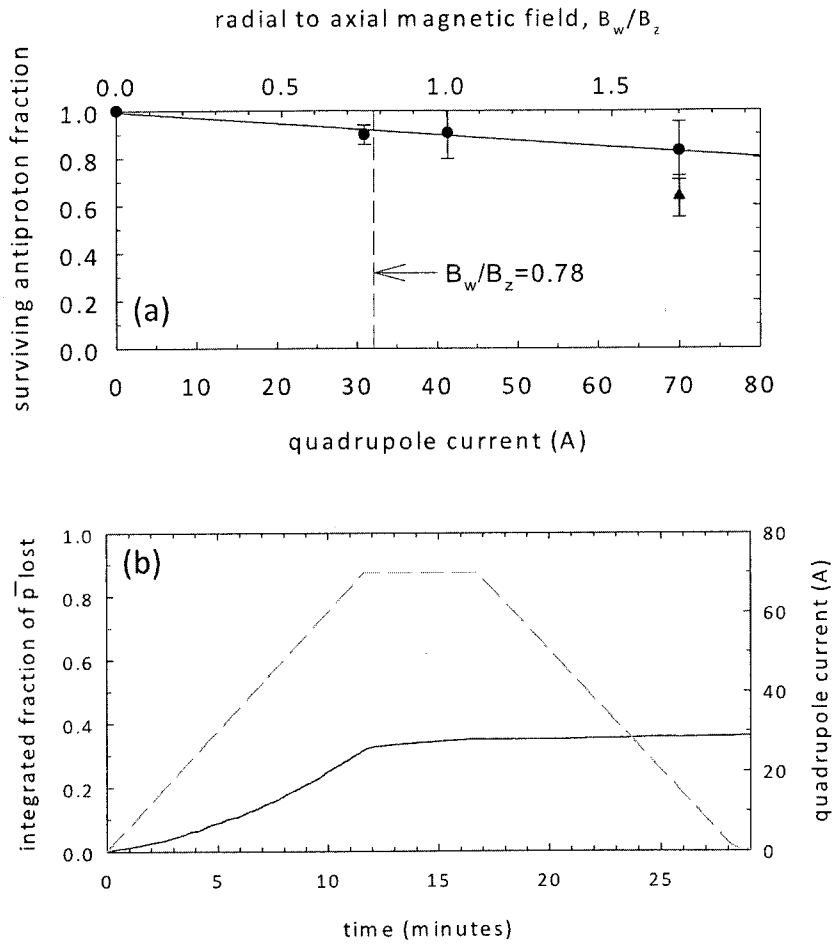

Figure 6.5: Retention of $\overline{p}$ in the quadrupole field of the Ioffe trap. (a) Retention of (filled circles) 90,000 and (filled triangle) 280,000 $\overline{p}$ as a function of final quadrupole current. (b) Rate of $\overline{p}$ loss as the Ioffe quadrupole current is ramped to its maximum value of 69 A at a rate of 0.1 A/s, held at that value for 300 s, then ramped down to zero at the same rate.

formation in a Penning-Ioffe trap.

6.4 Antihydrogen production in a combined Penning-Ioffe trap

ATRAP carried out the first demonstration that $\overline{H}$ could be formed when a quadrupole magnetic field is superimposed on the uniform magnetic field of a Penning trap [25]. Fig. 6.6 shows the procedure by which $\overline{H}$ was formed and detected in these experiments. The trials were performed with an average of 6×10^7 e^+ and 200,000 $\overline{p}$. Initially a nested well structure is formed with e^+ in the center; the $\overline{p}$ are located in a nearby electrode but are not yet in the nested well. The Ioffe trap is then ramped up to a certain fraction of full field at ramp rates of 0.1 A/s in the quadrupole coil and 0.2 A/s in the pinch coils.

A 1.75-ms voltage pulse temporarily lowers the barrier between the $\overline{p}$ and the nested well, allowing the $\overline{p}$ to enter the nested well region. As the $\overline{p}$ fall into the nested well, they gain several eV of energy. Collisional cooling with the e^+ reduces the energy of the $\overline{p}$ until they are cool into the side wells, at which point they no longer have sufficient energy to interact with the e^+. About 50 % of the $\overline{p}$ are lost during this process. Once sufficient time has passed for $\overline{p}$ to cool into the side wells, the potential applied to the e^+-confining electrode is increased over 660 s, bringing the $\overline{p}$ into contact with the e^+. $\overline{p}$ enter the e^+ cloud and form $\overline{H}$.

A detection well for Rydberg $\overline{H}$ is located above (to the left of in the figure) the $\overline{H}$ formation region. A high electric field in this region can field-ionize Rydberg $\overline{H}$ and

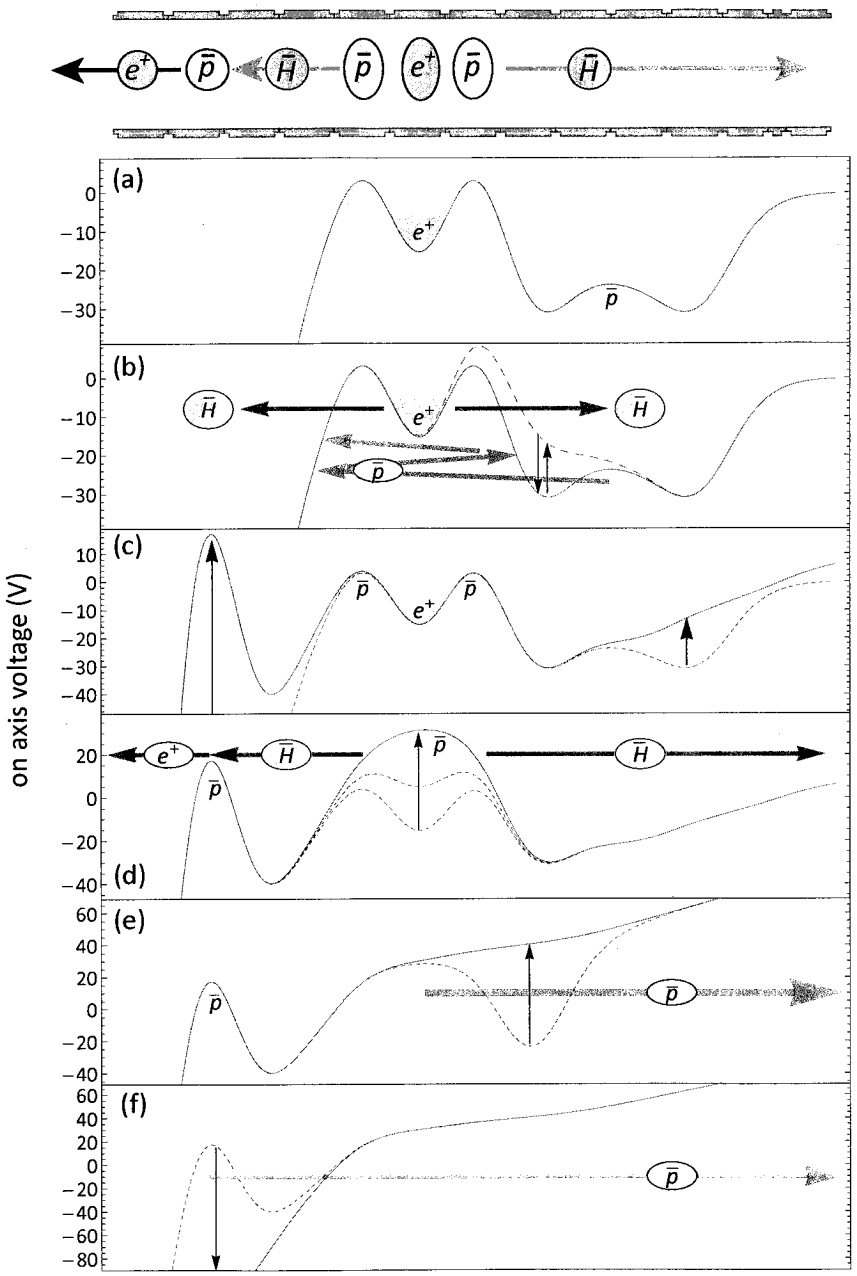

Figure 6.6: Procedure for forming $\overline{\mathrm{H}}$ by three-body recombination. (a) 200,000 $\overline{\mathrm{p}}$ are confined near a nested well structure containing 6×10^7 e^+. (b) A 1.75 ms voltage pulse allows $\overline{\mathrm{p}}$ to enter the nested well region, where they collisionally cool into the side wells. (c) After Ioffe fields are ramped up, a detection well is formed. (d) The confining well for e^+ is reduced over 660 s, allowing $\overline{\mathrm{p}}$ to interact with e^+ and form $\overline{\mathrm{H}}$. (e) Any remaining particles in the nested well are removed from the trap with electric fields. (f) Particles are rapidly removed from the detection well, allowing us to count the number of $\overline{\mathrm{p}}$ captured from field-ionized $\overline{\mathrm{H}}$.

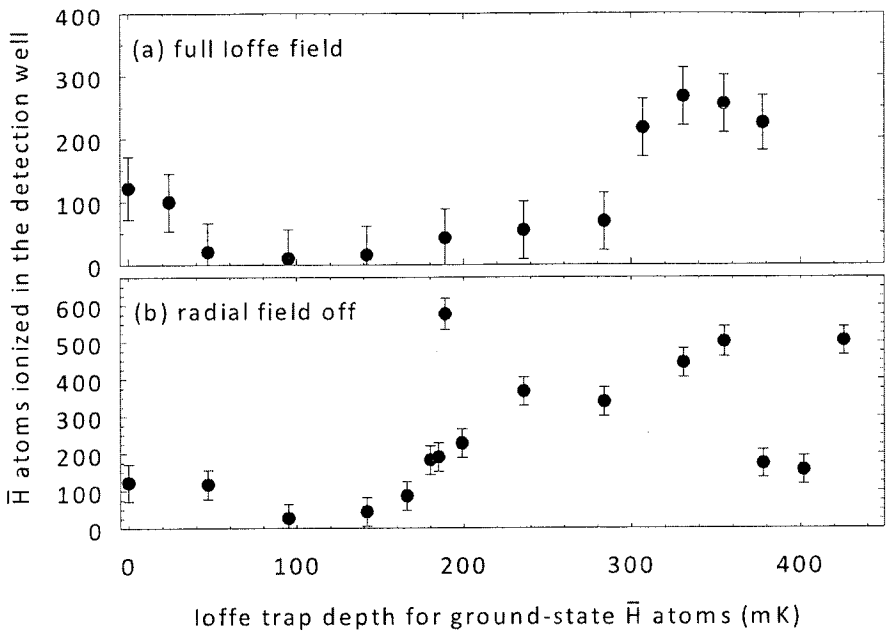

Figure 6.7: Production of antihydrogen in (a) the full Penning-Ioffe trap, (b) the Penning-Ioffe trap with only pinch coils energized.

trap the $\bar{p}$ which result from $\overline{H}$ ionized between 20 V/cm and 120 V/cm. The resulting $\bar{p}$ remain trapped in the detection well and can be counted after the experiment is over. The detection well is designed so that any $\bar{p}$ not bound within a neutral $\overline{H}$ will not have enough energy to enter the detection well, and even if they did, the $\bar{p}$ would simply enter, bounce and exit the detection well and then be ramped to the lower trap where they would annihilate. The detection well is not formed until $\bar{p}$ have collisionally cooled into the side wells.

Fig. 6.7 shows the results of $\overline{H}$ production experiments in a combined Penning-Ioffe trap [25]. The surprising result of somewhat enhanced $\overline{H}$ production within the quadrupole field is enhanced even more by the higher axial fields provided by the pinch coils. This first demonstration of $\overline{H}$ production within the combined Penning-Ioffe

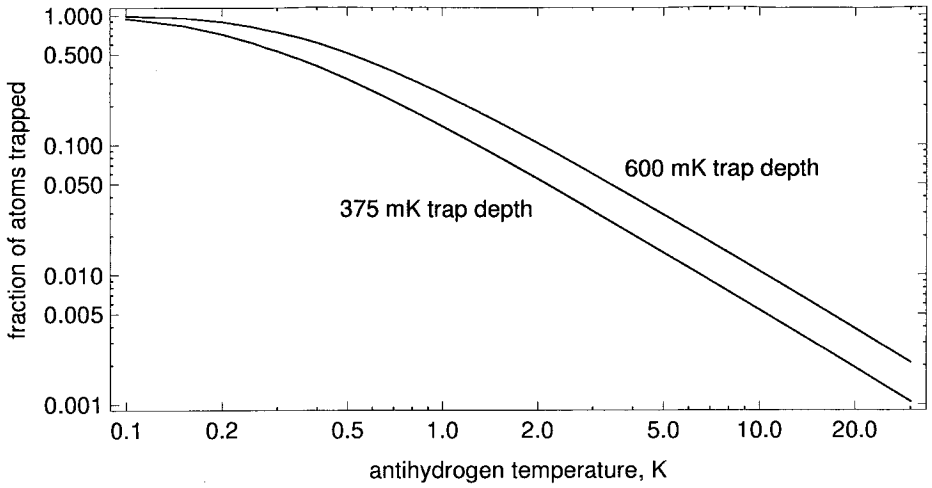

Figure 6.8: Fraction of $\overline{\mathrm{H}}$ trappable in 375 mK trap depth (blue) and 600 mK trap depth (red) Ioffe traps as a function of $\overline{\mathrm{H}}$ temperature. The plot assumes a thermal distribution and does not take into account the additional factor lost by recombination into non-trappable states.

trap opened the way towards $\overline{\mathrm{H}}$ trapping experiments.

6.5 Experiments on trapping antihydrogen in a Penning-Ioffe trap

Even given the encouraging demonstration of $\overline{\mathrm{H}}$ production within a Penning-Ioffe trap, trapping $\overline{\mathrm{H}}$ is not an easy matter. To begin with, only the coldest atoms produced can be trapped within the sub-K trap depth of state-of-the-art Ioffe traps. If the $\overline{\mathrm{H}}$ form from a thermal distribution of energies at temperature T, then the energies will follow a Maxwell-Boltzmann distribution,

$$f(E) = 2\sqrt{\frac{E}{\pi(k_B T)^3}}e^{-E/k_B T}. \tag{6.9}$$

Figure 6.8 shows the fraction of $\overline{\mathrm{H}}$ which can be thermally trapped for trap depths of 375 mK (corresponding to the current ATRAP Ioffe trap) and 600 mK (corresponding to the next-generation Ioffe trap). For temperatures T larger than the depth of the Ioffe trap, the trappable fraction scales as $T^{-3/2}$.

In addition, only those atoms combining into low-field seeking states can be trapped, no matter their energy. In zero magnetic field, symmetry would guarantee equal recombination into the magnetic quantum states $m_j = +1/2$ and $m_j = -1/2$. However, calculations for nonzero magnetic field have suggested that a smaller fraction of produced $\overline{\mathrm{H}}$ will recombine into low-field-seeking states [143, 144]. The fraction of low-field-seeking $\overline{\mathrm{H}}$ produced is nevertheless expected to be in the range of 16 - 31 %.

One final concern in trapping $\overline{\mathrm{H}}$ is the rotational velocity of the e^+ cloud in which $\overline{\mathrm{H}}$ forms. For a typical ATRAP e^+ plasma of 6×10^7 e^+ with radius of 5 mm in the 2-T field at the center of the combined Penning-Ioffe trap, the rotational frequency is 50 kHz. This corresponds to a rotational velocity of $314\,r$ m/s, with r the radius in mm. Antiprotons entering this plasma acquire this rotational velocity within one cyclotron period, more quickly than they can form $\overline{\mathrm{H}}$ through three-body recombination. Since the rotational velocity is an $\vec{E} \times \vec{B}$ drift, its magnitude does not depend at all on the mass of the particles. Any $\overline{\mathrm{H}}$ formed with speed greater than 90 m/s (the maximum speed for a trapped $\overline{\mathrm{H}}$ atom in our Ioffe trap) cannot be trapped unless collisions as it exits the e^+ plasma reduce this speed below 90 m/s. For the above plasma, only $\bar{p}$ entering at radius of less than 0.28 mm will produce $\overline{\mathrm{H}}$ slow enough to be confined by the magnetic trap. As a result, reducing the rotational frequency of the e^+ cloud

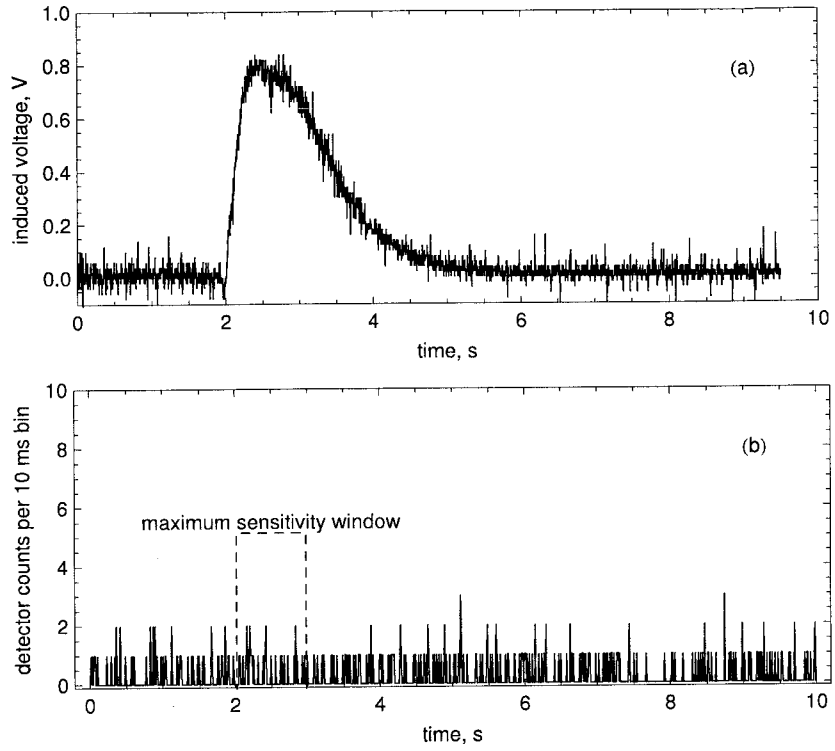

Figure 6.9: (a) Record of voltage induced across antiproton-loading solenoid during Ioffe quench provides an indication of the time interval during which to look for a signal from trapped $\overline{H}$. (b) Detector counts recorded during the Ioffe trap quench after a trapping trial, with 1-s window of maximum sensitivity during which we look for an excess annihilation signal.

is crucial to trapping $\overline{H}$ produced by three-body recombination. Some fraction of $\overline{H}$ untrappable due to high rotational velocities will probably occur even in the best-case scenario. ($\overline{H}$ formation by two-stage charge exchange, discussed in Chapter 7, gets around this problem by not requiring the $\overline{p}$ to enter the e^+ plasma at all).

Attempts to trap $\overline{H}$ proceed by forming $\overline{H}$ in a combined Penning-Ioffe trap, sweeping any remaining charged particles out of the trap with electric fields, then ejecting any trapped $\overline{H}$ as rapidly as possible and looking for the resulting annihilation signal. Although various schemes might be used to annihilate trapped $\overline{H}$, in practice,

both collaborations working at CERN do so by turning off the Ioffe trap fields as quickly as possible. In ATRAP's case, this is accomplished by means of a resistive heater mounted on one of the side-ports of the Ioffe trap. This resistor is heated with a current of 2 A for 1 - 2 s. The heater is located as close as possible to one of the quadrupole magnet coils, although the heat must pass through the Ti body of the Ioffe trap. The heater causes the nearby quadrupole coil to stop superconducting and quench, opening a large "hole" in the magnetic trap through which confined $\overline{\mathrm{H}}$ can pass, hit the trap walls, and annihilate. The quench heater reliably allows us to quench the Ioffe trap on demand. Protection diodes within the Ioffe trap limit the turn-off time to roughly 1 s, though.

In order to determine the exact time at which the quench occurs we monitor the voltage induced across the antiproton-loading solenoid as the Ioffe fields rapidly ramp down (Fig. 6.9(a)). The induced voltage $V = M_{12}dI/dt$ can be integrated to get a time-profile of the current, from which we find that 80 % of the trapping depth reduction occurs within 1 s of the quench initiation. We thus search in the 1-s window following the quench for an excess of annihilation events corresponding to trapped $\overline{\mathrm{H}}$ being released. Fig. 6.9 (b) shows a typical data record for a quench event. We use a series of cuts on the recorded data to further eliminate background events, as described in Chapter 2. These cuts have an estimated 25 % overall sensitivity to $\overline{\mathrm{p}}$ annihilations and a measured 0.5 Hz background rate. If the background events are Poissonian, there is a 98.6 % chance of 2 or less events in the 1-s window following the quench, so that 3 detected events (corresponding to approximately 12 trapped $\overline{\mathrm{H}}$) indicate a likely signal for trapped $\overline{\mathrm{H}}$.

Despite a number of attempts, a signal for trapped $\overline{H}$ was not seen in ATRAP's experiments. ATRAP's initial report of antihydrogen production within a Penning-Ioffe trap set a limit of no more than 20 atoms trapped per trial [25], and subsequent improvements allowed us to lower this limit to no more than 12 atoms per trial. This is consistent with the trapping efficiency observed in the recent report of trapped $\overline{H}$. The 2010 ALPHA collaboration report of one trapped atom per 9 trials [26] (recently improved to one trapped atom in 2 trials [145]), was enabled by a Ioffe trap able to turn off in only 10 ms. In these experiments a resonant drive was used to give approximately 30,000 $\overline{p}$ per trial the energy needed to interact with a plasma of 2×10^6 e^+. The efficiency of $\overline{H}$ trapping was approximately one trapped anti-atom per 2×10^4 $\overline{H}$ atoms produced. It is encouraging that at least some of the trapped $\overline{H}$ atoms have been confined for up to 1000 s, which shows that trapped $\overline{H}$ can reach the ground state without decaying into untrapped states.

6.6 Conclusions and future plans

Much progress has been made since the first proposals to produce [14] and trap [15] antihydrogen in a magnetic trap. Three-body recombination production of $\overline{H}$ in a nested Penning trap was first observed in 2002 [21, 22, 23]. ATRAP's experiments in 2006 established that charged particles could be confined in a Penning-Ioffe trap for times long enough to produce $\overline{H}$ [24]. The first observation of $\overline{H}$ production in a combined Penning-Ioffe trap [25] opened the way to $\overline{H}$ trapping experiments. The recent ALPHA report of small numbers of trapped $\overline{H}$ atoms is an important proof-of-principle demonstration. However, precision spectroscopy on $\overline{H}$ will likely

require many more than one trapped atom per trial. A crucial goal now is scaling up $\overline{\mathrm{H}}$ trapping to much larger numbers in an apparatus compatible with precision spectroscopy.

ATRAP's next-generation apparatus includes a Ioffe trap compatible with rapid turn-off which can use either a quadrupole or octupole field to confine atoms. This apparatus also includes laser-access ports and is compatible with the charge-exchange method of $\overline{\mathrm{H}}$ production (see Chapter 7) which may exhibit more favorable scaing to larger numbers of trapped atoms. We hope that these advances will allow us to confine many $\overline{\mathrm{H}}$ atoms for precise spectroscopy.

Chapter 7

Antihydrogen Production by Two-Stage Charge Exchange

As discussed in the previous chapter, antihydrogen formation always requires some third body to carry away excess momentum and energy from the bound $\overline{p}$ and e^+ pair. In three-body recombination (TBR) experiments a second positron performs this function. In 2004, ATRAP demonstrated a second method: laser-controlled charge-exchange formation of antihydrogen [146]. Here, the electron from a Ps atom is the required third body. While too few atoms were produced in the 2004 experiment for detailed study, this proof-of-principle demonstration encouraged ATRAP to further pursue the charge-exchange method. An important goal of ATRAP's research in the 2009 and 2010 beam runs was to implement a new apparatus to produce $\overline{H}$ by laser-controlled charge exchange with the much larger clouds of particles now available to us. We were able to demonstrate a factor of 500 increase in on-axis Ps production (the first stage of the two-stage reaction to produce $\overline{H}$) from the 2004 results, and

found good evidence of the production of 3600 ± 600 $\overline{\mathrm{H}}$ atoms per trial, a factor of 200 increase from the earlier proof-of-principle experiment. This chapter describes our new charge-exchange apparatus and related experiments.

The production of $\overline{\mathrm{H}}$ by charge-exchange between positronium and antiprotons was first proposed in 1987 [147] and the formation of hydrogen by charge-exchange between ground-state Ps and protons was first observed in 1997 [148]. The cross-section for ground-state Ps to charge-exchange and produce $\overline{\mathrm{H}}$ is very small, on the order of $10^{-16}\,\mathrm{cm}^2$. This low cross-section makes the formation of $\overline{\mathrm{H}}$ from ground state Ps prohibitively difficult given the scarcity of $\overline{\mathrm{p}}$ as an input to the process. However, the cross-section for charge-exchange scales as n^4, where n is the principal quantum number of the atom involved in the reaction [149]. Hence a proposal was made to produce large quantities of Rydberg Ps through an initial charge-exchange reaction with a Rydberg alkali atom, then to use these highly-excited Ps atoms to efficiently produce $\overline{\mathrm{H}}$ [115].

Figure 7.1 shows a schematic of the charge-exchange process for forming antihydrogen using Rydberg Cs atoms as the initiator of the process. The reaction can be written as:

$$\begin{aligned} \mathrm{Cs} + h\nu &\rightarrow \mathrm{Cs}^* \\ \mathrm{Cs}^* + \mathrm{e}^+ &\rightarrow \mathrm{Ps}^* + \mathrm{Cs}^+ \\ \mathrm{Ps}^* + \overline{\mathrm{p}} &\rightarrow \overline{\mathrm{H}} + \mathrm{e}^- \end{aligned} \tag{7.1}$$

A beam of Rydberg Cs* is produced via laser excitation inside a cryogenic Penning trap in which e^+ and $\overline{\mathrm{p}}$ plasmas are stored near one another. The Cs* atoms enter the e^+ plasma and undergo a first charge-exchange, producing Rydberg Ps* and leaving

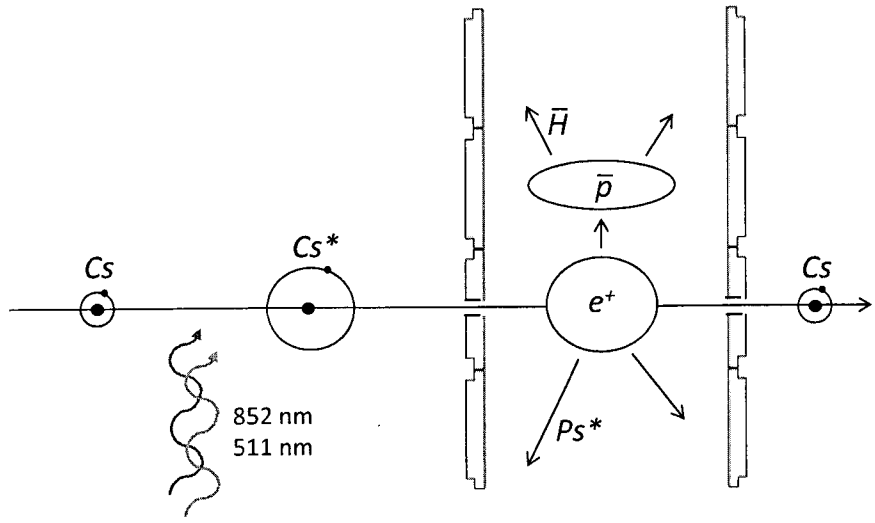

Figure 7.1: Schematic of the charge-exchange process.

behind a positive Cs^+ ion core. The Rydberg Ps* atoms thus formed are no longer confined by the Penning trap as they are electrically neutral. They will thus leave the trapping region for e^+. Some of the Ps* will enter the region where $\bar{p}$ are trapped, where they can undergo a second charge-exchange reaction and form $\overline{H}$.

The method of two-stage charge exchange has several benefits towards the goal of trapping $\overline{H}$ when compared with $\overline{H}$ production by three-body recombination. One of the most important is that $\overline{H}$ produced by this process should be formed with velocities given by the thermal velocities of the $\bar{p}$ from which they form [115]. Ps* atoms enter the trapped $\bar{p}$ cloud and interact with the $\bar{p}$ without any need to add energy to the $\bar{p}$. This enables charge exchange $\overline{H}$ production to easily take advantage of $\bar{p}$ that have been cooled via adiabatic or evaporative cooling (perhaps to a temperature lower than that of the surrounding electrodes), dramatically increasing the fraction

of atoms that can be magnetically confined.

A second advantage of two-stage charge exchange is that the $\overline{\mathrm{H}}$ atoms produced will form with binding energies similar to the binding energies of the Cs* atoms which initiated the process [115]. Since the initial n state of the Cs atoms is set by the laser excitation frequencies used, charge exchange offers a way to tune the final binding energy of the $\overline{\mathrm{H}}$ atoms produced. This binding energy is typically much deeper than that of atoms produced by TBR methods, so atoms produced by two-stage charge exchange are much more likely to survive stray electric fields in the trap.

One final advantage of $\overline{\mathrm{H}}$ production by two-stage charge exchange relates to the rotational velocities acquired by $\overline{\mathrm{p}}$ as they enter a dense e^+ plasma during TBR experiments. As shown in chapter 6, $\overline{\mathrm{p}}$ entering such a plasma will acquire a rotational velocity $v_\theta = (\vec{E}\times\vec{B})/B^2$ within one cyclotron period. In a dense plasma any $\overline{\mathrm{p}}$ beyond a certain radius will quickly acquire a rotational velocity high enough to prevent them from being confined by a magnetic trap. In contrast, charge-exchange $\overline{\mathrm{H}}$ production does not require $\overline{\mathrm{p}}$ to enter the e^+ plasma at all; as long as the density of the $\overline{\mathrm{p}}$ cloud and the electric fields within it are kept small enough, rotational velocities should not be large enough to eject $\overline{\mathrm{H}}$ formed by this method from the magnetic trap.

Compared to TBR methods for producing $\overline{\mathrm{H}}$, two-stage charge exchange does incur certain drawbacks as well. No source of alkali atoms can produce an appreciable atom flux until it reaches a temperature of (at minimum) the atoms' melting point of roughly 300K. Producing an alkali beam therefore requires heating an atom source to a temperature much greater than the surrounding cryogenic Penning trap environment. Although radiation shielding can minimize the heat load, some heating of the

apparatus will always occur during charge-exchange experiments. In addition, the requirement for two charge-exchanges to occur before $\overline{H}$ is produced introduces two solid-angle factors into the reaction rate, so that making large numbers of $\overline{H}$ by this method requires longer times than making similar numbers via TBR methods.

The ATRAP Collaboration first demonstrated Ps production by a single charge-exchange with a Rydberg alkali atom [150] and production of $\overline{H}$ by two-stage charge exchange in 2004 [146]. In this proof-of-principle experiment, approximately 17 $\overline{H}$ atoms per trial were produced in an earlier generation apparatus used by the ATRAP Collaboration for the study of $\overline{H}$ formation. Implementing an apparatus to produce much larger quantities of $\overline{H}$ in a manner compatible with magnetic trapping of the $\overline{H}$ produced was one of ATRAP's major goals for the 2009 and 2010 beam runs.

7.1 Apparatus

A central challenge is to produce a Rydberg Cs beam inside of the cryogenic Penning-Ioffe trap and send it through the electrode stack without introducing excessive heating of the 1.3-K electrodes. Figure 7.2 shows the apparatus we built to accomplish this goal. The Cs source (Alvatec AS-3-Cs-150-V) consists of a Bi_2Cs alloy enclosed in a nonmagnetic stainless steel "boat." A current of 4-5 A through the stainless boat heats the source to a temperature of approximately 600K. Within 360 s, pure Cs begins to sublimate from the alloy and leaves the stainless boat. The Cs source is enclosed within an aluminum box to limit radiative heating of nearby parts of the apparatus during operation. The Cs source is electrically and thermally isolated from this box by alumina and G-10 spacers. Radiation baffles provide ther-

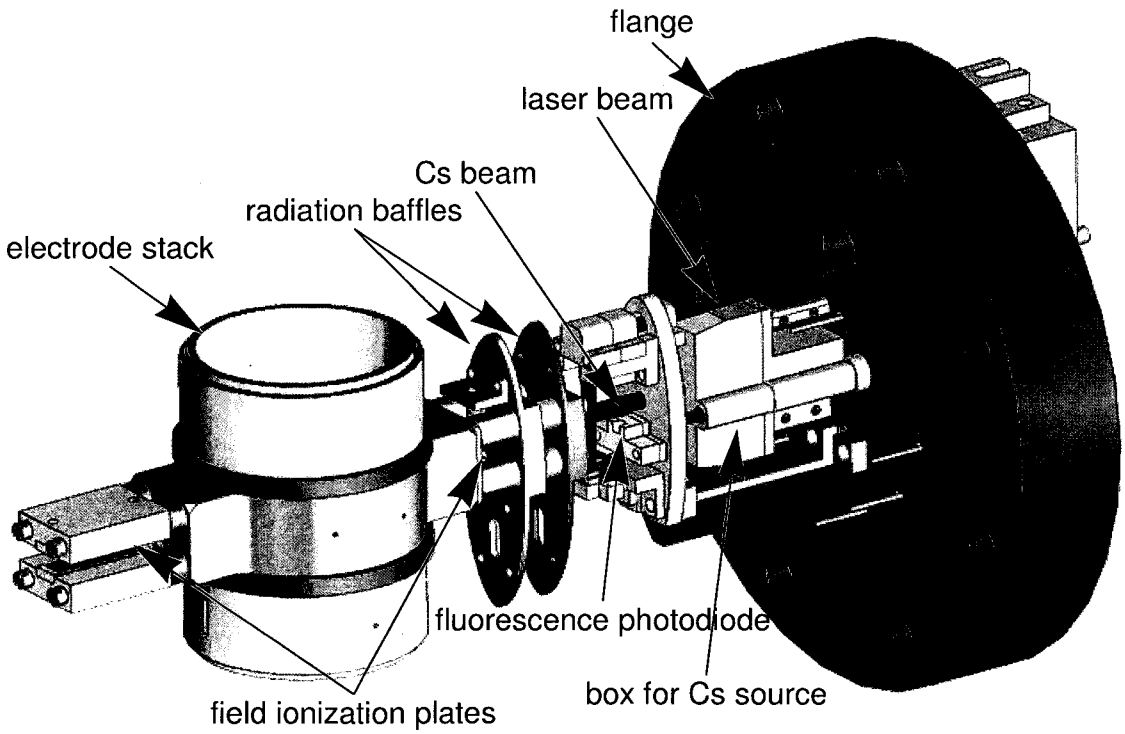

Figure 7.2: Assembly used for charge-exchange experiments.

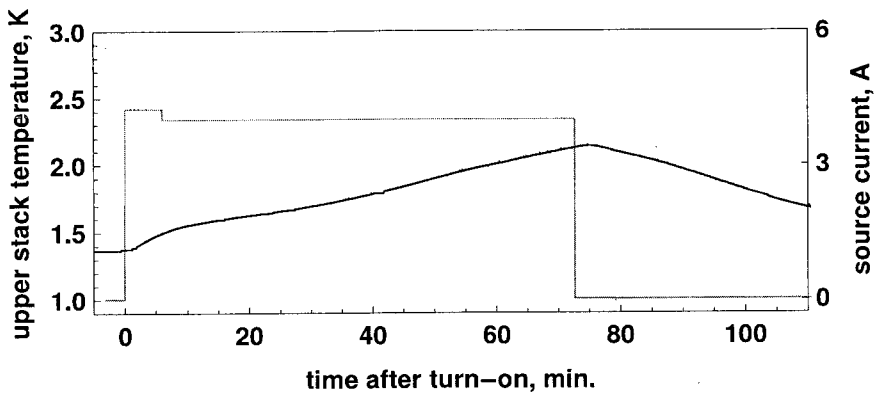

Figure 7.3: Temperature of the Penning trap electrodes as the Cs source heats to 600K and remains at this temperature during a 4000-s Ps production experiment.

mal shielding of the 1.3 K electrode stack from the source. As will be discussed in a later section, our longest charge exchange experiments require 4000 s (67 minutes) of operation after the Cs source has heated up to its operating temperature. Figure 7.3 shows the temperature of the electrode stack during this process. From an initial temperature close to 1.3K, the stack heats up to approximately 2.1 K over the course of an hour. Once the source is turned off, the stack slowly returns to its base temperature over about an hour. As the source itself cools very rapidly, this slow cooling of the stack is probably related to thermal energy stored in the radiation baffles which is slowly conducted away through the baffles' insulating supports.

The Cs beam enters the laser excitation region (described below) and then passes through an 0.8 mm diameter collimating hole in one radiation baffle before entering the Penning trap electrode stack through a second 0.8 mm diameter collimating hole in one of these electrodes. The collimating elements are designed to ensure that any Cs atom entering the electrode stack will leave via a larger 2.5 mm diameter hole in the opposite side of the stack without any atoms striking an electrode. This prevents a

buildup of Cs inside the stack that could produce a short between adjacent electrodes.

The Cs source contains a total of approximately 150 mg Cs. This corresponds to approximately 6×10^{20} atoms of Cs, many orders of magnitude more than we would need for charge-exchange experiments. However, the amount of Cs available for experiments is significantly reduced by the small solid angle for Cs atoms to actually enter the Penning trap electrodes and is further reduced by the finite lifetime of the Cs Rydberg state. In practice, one Alvatec source contained enough Cs for us to perform experiments throughout the 2010 beam run without the need to warm up the experiment and exchange the source. The Alvatec source was a major improvement over a previous Cs source which contained significantly less Cs and did not last an entire beam run.

As the quantity of Cs remaining in the source is depleted, the signal from Rydberg Cs we observe at a given current slowly declines and we must run the source at a slightly higher current to compensate. Our base "operating current" in the 2010 beam run increased from 4.0 A at the beginning of the beam run to 4.25 A at the end of the beam run, corresponding to the source retaining approximately one-third of its original quantity of Cs.

7.1.1 The Cs atom in a magnetic field

Although any alkali atom could in principle be used for these experiments, we chose Cs primarily for the convenient laser wavelengths used for excitation to a Rydberg state. We use a two-photon process to produce Rydberg Cs, first using 852 nm photons to excite Cs from the ground $6S_{1/2}$ state to the $6P_{3/2}$ state, and then using

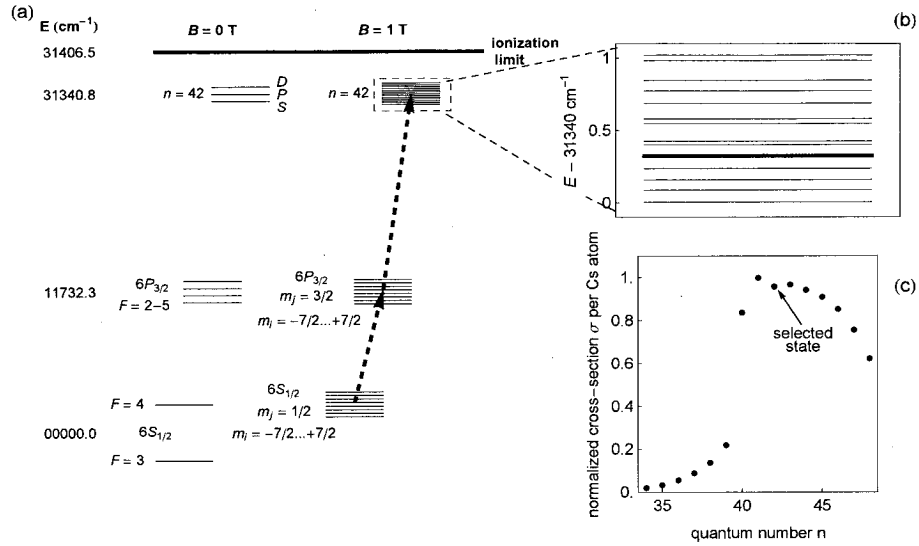

Figure 7.4: (a) Simplified level diagram of Cs atom in 0 T and 1 T field. (b) Zoom-in of calculated Rydberg levels in the 1-T field, with green curve showing chosen level. (c) Optimization of the n state to use based on state lifetime, amount of D character, and cross-section for Ps production, leads to a narrow window of optimal states in the range $n = 41$ to $n = 44$.

511 nm photons to excite to a Rydberg state. Figure 7.4 shows the Cs energy levels relevant to our excitation scheme in magnetic fields of 0 T and in the background field of 1 T. In the higher field provided by the Ioffe trap, the n-states are even more mixed and the final n of our Rydberg state is not well defined. A detailed examination of the Cs D lines can be found in [151].

The $6S_{1/2} \rightarrow 6P_{3/2}$ transition

In a magnetic field, the Hamiltonian for the ground state ($n = 6$) levels of Cs can be written:

$$H_B = A_{hfs}\vec{I} \cdot \vec{J} + g_J \mu_B \vec{J} \cdot \vec{B} + g_I \mu_B \vec{I} \cdot \vec{B}, \tag{7.2}$$

where A_{hfs} is the hyperfine constant for the particular fine structure level under consideration, $\vec{J} = \vec{L} + \vec{S}$ represents the total angular momentum (spin plus orbital) of the electron, $\vec{I}$ is the nuclear angular momentum, and g_J and g_I are the electron and nuclear g-factors.

g_J $(6S_{1/2})$	2.0025
g_J $(6P_{3/2})$	1.3340
g_I	-.0003989
$A_{6S_{1/2}}$	$h\cdot$ 2.298 GHz
$A_{6P_{3/2}}$	$h\cdot$ 50.275 MHz
I_{sat}	2.71 mW / cm^2
μ_b	$h\cdot$ 13.996 GHz / T
Zero-field $6S_{1/2}$ hyperfine splitting	$h \cdot 9.2$ GHz
1-T field energy shift $g_J\mu_B m_J B$	$h \cdot 14$ GHz

Table 7.1: Parameters for the Cs $6S_{1/2} \rightarrow 6P_{3/2}$ transition.

In the case that the energy shift due to the field is much greater than the hyperfine splitting but less than the fine structure splitting between the D levels, F is no longer a good quantum number but m_I, m_J, I, and J are. We can write

$$H_B = A_{hfs} m_I m_J + g_J \mu_B m_j B_0 + g_I \mu_B m_I B_0. \tag{7.3}$$

In a 1 T field the magnetic field energy shift $g_J\mu_B m_J B_0 \approx 14$ GHz. This greatly exceeds the hyperfine splittings in the $6P_{3/2}$ state which are only a few hundred MHz, but is on the order of the 9.2 GHz hyperfine splitting between the ground-state $6S_{1/2}$

levels. Fortunately, an expression has been derived for the ground state energies of alkali atoms in intermediate fields [152],

$$E(F_{\pm} = I \pm 1/2, m) = -\frac{\Delta E}{2(2I+1)} - g_I \mu_B m B_0 \pm \sqrt{\Delta E^2 + \frac{4m}{2I+1}(g_J - g_I)\mu_B \Delta E + (g_j - g_I)^2 \mu_B^2 B_0^2}, \tag{7.4}$$

where ΔE is the zero-field hyperfine splitting between the levels and $m = m_I + m_J$. This equation (known as the Breit-Rabi equation) gives rise to 16 sublevels in the ground state corresponding to two manifolds of 8 nuclear sublevels each separated by a larger energy gap corresponding to whether the single electron is aligned or anti-aligned with the magnetic field. As an electric dipole transition cannot change the nuclear spin, the transitions to the $6P_{3/2}$ state are split into 6 manifolds of 8 transitions each. The manifolds correspond to the transitions $m_J = +1/2 \rightarrow m_J = -1/2, +1/2, +3/2$ and $m_J = -1/2 \rightarrow m_J = -3/2, -1/2, +1/2$. Of these manifolds, only two ($m_J = +1/2 \rightarrow m_J = +3/2$ and $m_J = -1/2 \rightarrow m_J = -3/2$) will be closed-cycling transitions appropriate for our use; exciting a transition in another manifold will quickly pump the Cs atoms into a different ground state not addressed by our laser.

The $6P_{3/2}$ to nD transition

We must now excite the Cs atom to a Rydberg state. The selection rule $\Delta l = \pm 1$ means we must excite to either an nS or an nD state. As we will see, the magnetic field couples those states together differing by $\Delta \ell = \pm 2$. The zero-field lifetime of both S and D states is quite short, but the D state mixes more readily with higher-l states with longer lifetimes. We therefore aim to excite to an nD state.

Cs is a hydrogenic atom, so the energy levels and wavefunctions for high principal quantum number n correspond very closely to those of hydrogen. The zero-field energy levels for principal quantum number n and orbital quantum number l are given by

$$E_{nl} = \frac{-13.6\text{eV}}{(n - \delta(n,\ell))^2}, \tag{7.5}$$

where $\delta(n,\ell)$ is the quantum defect for the level [153]. The Hamiltonian terms due to a nonzero magnetic field $\vec{B} = B_0\hat{z}$ are given by [154]

$$H_B = \mu_B B_0(g_\ell m_\ell + g_S m_S) + \frac{1}{8}\frac{e^2 B_0^2}{m_e c^2} r^2 \sin^2(\theta). \tag{7.6}$$

In a sufficiently strong magnetic field (of order 0.1 T for $n = 40$) the energy shifts due to the field become comparable to the energy differences between n states so n itself is not a good quantum number, although m_L and m_S remain good quantum numbers. The second term in the Hamiltonian above serves to couple states differing by $\Delta l = 0, \pm 2$. In a 1-T field we are able to calculate the energy of states with some D character by diagonalizing a Hamiltonian containing all relevant zero-field states from $n = 10$ to $n = 60$. In the higher field of the Ioffe trap we found that the number of energy levels required to get an accurate calculation by this method was prohibitive, but we were able to use the high-field approximation [155]

$$\int_{r_1}^{r_2} (\frac{2m_e}{\hbar^2}(E - V_{eff}))^{1/2}\, dr = (n_r - \frac{1}{2})\pi, \tag{7.7}$$

where $n_r = n' - m_l - 1$ is the "radial quantum number." $n' > 0$ gives a rough idea of the binding energy but does not correspond exactly to the zero-field n. The effective potential V_{eff} is given by

$$V_{eff} = \frac{\hbar^2}{2m_e}\frac{(m_\ell + 1/2)^2}{r^2} - \frac{e^2}{4\pi\epsilon_0 r} + \frac{1}{8}\frac{e^2}{m_e c^2} B_0^2 r^2 - \mu_B B_0 m_\ell. \tag{7.8}$$

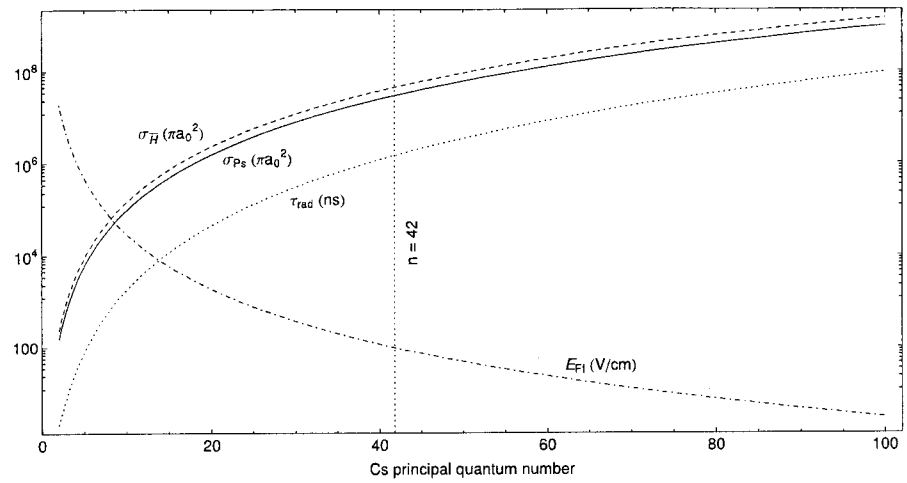

Figure 7.5: Quantities relevant to the choice of principal quantum number n for Rydberg excitation of Cs.

Although the zero-field principal quantum number n is not a good quantum number in the field, quantized energy levels spaced by $\mu_B B_0 g_\ell$ exist and can be found by this method.

The choice of n state (or, more correctly, the choice of binding energy of the final Cs state) represents a compromise between multiple requirements. Figure 7.5 demonstrates some of the relevant parameters. The Rydberg state must survive for 6 cm to reach the center of the trap which corresponds to a lifetime of 250 μs at typical thermal velocities. The lifetime of a Cs D state is given by

$$\tau_{nD} = 0.67\text{ns}\,(n - \delta(n,\ell))^3\,, \tag{7.9}$$

with the quantum defect for D states approximately equal to 2.5. The higher ℓ states which are mixed in significantly enhance this lifetime. The lifetime for a fully-mixed state corresponding to principal quantum number n is given by [156]

$$\tau_n \approx \frac{3}{4} n^5 \alpha^{-5} \frac{\hbar}{\mu c^2} \frac{1}{\ln(2n-1) - 0.365}, \tag{7.10}$$

with μ the electron reduced mass.

Equally importantly, the cross section for both charge-exchange reactions scales as n^4. Classical trajectory Monte Carlo calculations [115] predict zero-field cross sections of

$$\sigma_{Ps} = 9.7 n_{Cs}^4 \pi a_0^2, \tag{7.11}$$

$$\sigma_{\overline{\mathrm{H}}} = 58 n_{Ps}^4 \pi a_0^2 \approx 14.5 n_{Ps}^4 \pi a_0^2 \tag{7.12}$$

where $a_0 = .529$ is the Bohr radius. Further calculations have found that the predicted charge-exchange cross sections are not strongly affected by magnetic fields [144].

Set against these arguments for using the highest n state possible are the fact that the higher-n states are more mixed and contain less D component to which we can excite. In addition, the electrical field which will ionize the Rydberg atoms,

$$E_{SI} = n^{-4} (\frac{\mu}{m_e})^2 \, 3 \times 10^8 \mathrm{V/cm}, \tag{7.13}$$

drops below 50 V/cm around $n = 50$. We would run the risk of Stark-ionizing such atoms by electrical fields generated either by the trapping potentials or by the space charge of the e^+ cloud. In practice, we optimized the choice of level by taking all of these factors (lifetime, D fraction of the state, and cross-section for charge exchange) into account. This optimization, shown in Figure 7.4(c), suggested a narrow window of states in the range $n = 41$ to $n = 44$, of which we chose $n = 42$. Rydberg Cs with this approximate n can also survive electric fields up to approximately 100 V/cm, sufficient to avoid ionization by electric fields within our Penning trap. This appproximate n state is slightly higher than the $n \approx 37$ state used in ATRAP's 2004 proof-of-principle experiment [150]; in that case the n state was set by the fixed

frequency of the commercially available copper vapor laser.

In the higher and nonuniform magnetic field due to the Ioffe trap, more ℓ-states mix in at a lower binding energy (equivalent to lower n), and the lifetime becomes much longer for lower equivalent n. For excitation within the Ioffe field, we could not repeat the exact optimization calculation described above (too many states were required to be included for the optimization). Instead we chose a state with binding energy corresponding to $n \approx 37$, representing a rough compromise between higher cross-section for charge-exchange (scaling as n^4) and D fraction of the state to which we can excite (which is higher for lower n). This state is also similar to the state used successfully in a high magnetic field in ATRAP's earlier demonstration.

7.1.2 Production of Rydberg Cs

Figure 7.6 shows an overview of the laser systems built by ATRAP collaborators from the University of Mainz for excitation of Cs atoms to a Rydberg state. The laser system is a substantial improvement over that used in the 2004 proof-of-principle experiments, in that we can now tune the 511 nm laser to select an optimized Rydberg state for an experiment. In the earlier 2004 charge-exchange experiments, a commercially available copper vapor laser provided the second-stage excitation. This laser's frequency could not be tuned, and its 10 GHz bandwidth meant that only a fraction of its power was available to excite atoms to a Rydberg state.

The $6S_{1/2} \rightarrow 6P_{3/2}$ transition is excited by a grating-stabilized 852 nm tunable diode laser. The 852 nm diode can provide up to 200 mW maximum power, but we typically use only a few mW as the D_2 Cs line is easy to saturate.

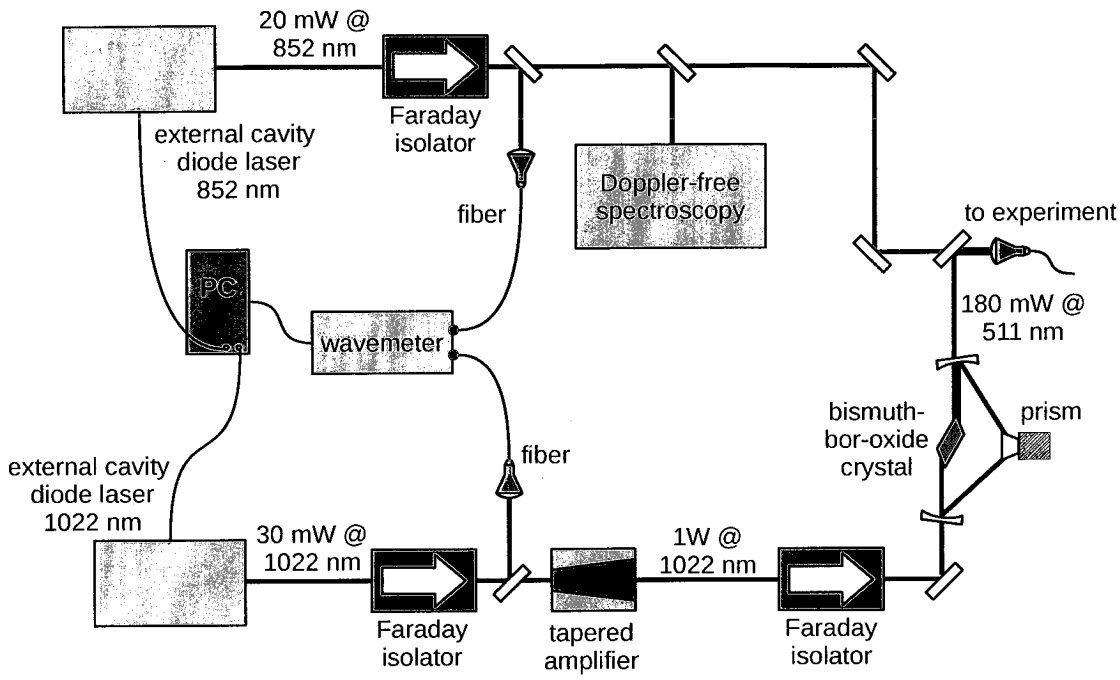

Figure 7.6: Schematic of lasers used in the charge-exchange process.

The $6P_{3/2} \rightarrow 42D$ transition is excited by a frequency-doubled diode laser system. A grating-stabilized 1022 nm tunable diode laser provides up to 100 mW of infrared power. 20 mW of power from this laser are fed into a tapered amplifier which can produce up to 1W of power at 1022 nm. The amplified laser enters a frequency-doubling cavity where it is converted to 511 nm light. The cavity is stabilized with a Hansch-Couillaud locking scheme [157], where a linear polarizer inside the cavity produces an elliptically polarized reflected beam when the cavity is not in resonance; a differential photodiode can use the ellipticity of the reflected beam as an error signal in order to stabilize the cavity. The frequency doubling element in the cavity is a BiB_3O_6 (BiBO) crystal. The BiBO crystal is birefringent and serves as the linear polarizer as well. This system can produce up to 180 mW of 511 nm light.

Both laser systems are locked to a wavemeter. The grating angle and temperature of the laser system are adjusted to stabilize the frequency. The linewidth for both lasers is approximately 1.5 MHz, well below the Doppler broadening we observe from Cs transitions in the apparatus. The wavemeter is housed inside of a thermally insulated box which prevents significant drifts due to changing ambient temperatures over the course of an experiment. We still observe day-to-day drifts in the wavemeter readings which we correct by periodic Doppler-free spectroscopy of a room-temperature Cs vapor cell (not in a magnetic field).

A dichroic mirror allows us to couple both Cs excitation lasers into a 10-m, 62.5 μm-core multimode optical fiber (THORLABS M31L10) which transmits the laser light to our experimental zone. Light from this fiber is coupled into our experimental space through a fiber feedthrough and enters a second optical fiber. This second fiber mounts off of the main CF flange which supports the Cs source (see Fig. 7.2). The tip of this fiber butts up against a 10mm ball lens (Edmund Optics NT48-897) with index of refraction 2.00, so that the focal length of the ball lens is equal to its radius. This ball lens therefore collimates the light from the fiber with an angle of divergence caused by the finite size of the fiber output given by $\theta = r/f = 0.2°$.

Once it has been collimated by the ball lens, the laser light passes through a 1/4" window in the vacuum flange. It is redirected downwards by a right-angle mirror and encounters the Cs beam. At this point the laser beam is roughly 1.5mm in diameter, ensuring that we can excite Cs atoms which will enter our electrode stack even if minor misalignments to the laser system occur during cooldown. The distance of the laser excitation point from the center of the electrode stack is carefully chosen to be

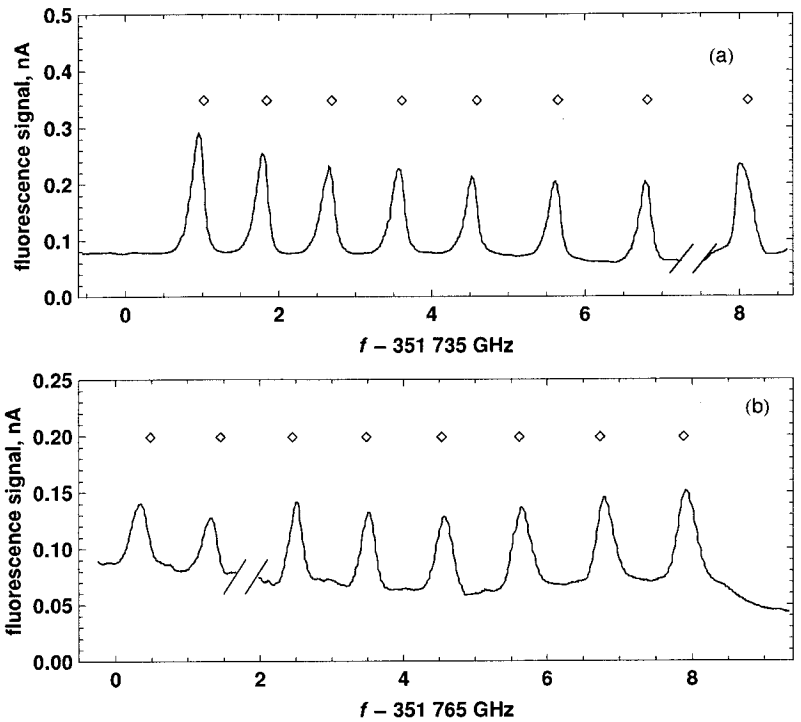

Figure 7.7: Fluorescence signal observed from excitation of Cs to the $6P$ state in (a) the 1-T solenoid background field and (b) the full combined field of the 1-T solenoid and Ioffe trap. Diamonds indicate calculated values for the transition frequencies. Breaks in signal traces indicate points at which it was necessary to re-tune the laser in order to cover the entire frequency range.

the point where the $\vec{B}$ field due to the the Ioffe trap is at a maximum. This minimizes the broadening of the optical transitions due to magnetic inhomogeneities when the Ioffe trap is energized.

Excitation of the $6S_{1/2} \rightarrow 6P_{3/2}$ transition

Figure 7.7 shows excitation from the $|6S_{1/2}, m_J = +1/2\rangle$ to $|6P_{3/2}, m_J = +3/2\rangle$ states. An InGaAs photodiode (Hamamatsu Photonics G8941-01) positioned close to the region of excitation measures fluorescence from the transition. We chose InGaAs

for a photodiode material as this semiconductor does not undergo carrier freeze-out until below 4K, and is also insensitive to the large amount of green laser power we put in to the trap to excite the Rydberg transition. We observe 8 different peaks, corresponding to the nuclear sublevels. We are able to excite to the $6P$ level in both the 1T background field of the solenoid and the 3.11 T field due to the Ioffe trap and 1T solenoid. The $6S \rightarrow 6P$ transition shows no appreciable broadening in the Ioffe field.

The saturation intensity for the Cs $6S_{1/2} \rightarrow 6P_{3/2}$ transition is 2.7 mW / cm^2. We typically use 3 mW of laser power focused into a 1.5 mm diameter spot to excite this transition; even accounting for some losses from the uncoated input optics, we expect to be well above the saturation intensity for this transition. Because we can only address one of the 16 sublevels of the ground state, though, we can excite at maximum 50% /16 of the Cs atoms into the $6P$ state at one time. A battery of 16 852 nm diode lasers would be able to excite all ground-state Cs atoms to the $6P$ state and could provide a major improvement to the efficiency of our Rydberg excitation, although we would also need 16 511 nm lasers for the Rydberg excitation. We have not yet undertaken this significant apparatus upgrade.

Excitation of the $6S_{1/2} \rightarrow nD$ transition

After excitation to the $6P$ level, the 511 nm laser excites atoms to an $n \approx 42$ Rydberg state. While the 852 nm laser intensity greatly exceeds the saturation intensity for the D_2 transition, the saturation intensity is much higher for the Rydberg transition and even with 180 mW of power at 511 nm we are well below this value.

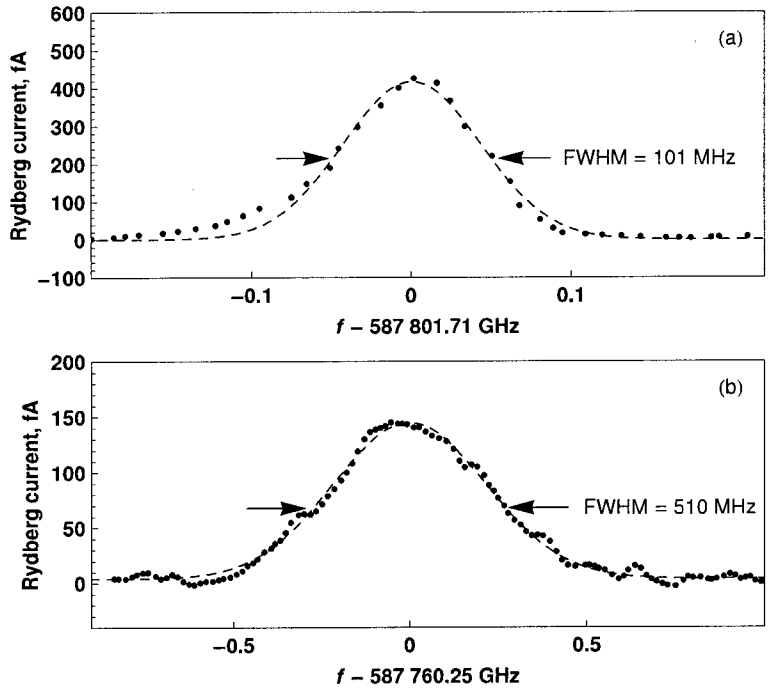

Figure 7.8: Field-ionization current from Rydberg atoms observed in (a) the 1-T solenoid background field and (b) the full combined field of the 1-T solenoid and Ioffe trap, about 3.1 T.

The lifetime of the $6P$ state is only 30 ns, so we must excite to the Rydberg state at the same location as we excite to the $6P$ state.

In order to verify that we have excited to the Rydberg state, we apply a high electric field between two conducting plates on the near side of the electrode stack to Stark-ionize the atoms and measure the resulting current collected on one of the two plates. This current is amplified by a low-noise current amplifier (Femto DLPCA-200) and is then read through a lock-in amplifier. We modulate the current produced by chopping the 852 nm laser with a standard laboratory chopping wheel. Figure 7.8 shows the field-ionization current seen as we sweep the laser frequency over the Rydberg transition while applying a stripping field of 200V/cm between the plates. We are able to excite to the Rydberg state in both the 1T background field of the solenoid and in the higher field due to the Ioffe trap. The width of the Rydberg transition in the uniform 1T background field is consistent with the Doppler width due to a beam of 600K Cs atoms with angular divergence of 9°. In the Ioffe field we do see significant broadening due to the inhomogeneous magnetic field, and a consequent loss of signal, but we are still able to excite without difficulty.

Figure 7.9 shows the field ionization current we observe as a function of the ionizing electric field. The current changes sign as we change the direction of the field since in the one case we collect positive Cs^+ ions while in the other case we collect negative e^-. The shape of the field ionization curves is similar in the 1T background field and in the field of the Ioffe trap. In both cases we also observe a small but noticeable residual current at 0 V/cm field. We believe this is because our Rydberg collection plate doubles as a radiation baffle in a region where the Cs beam is not

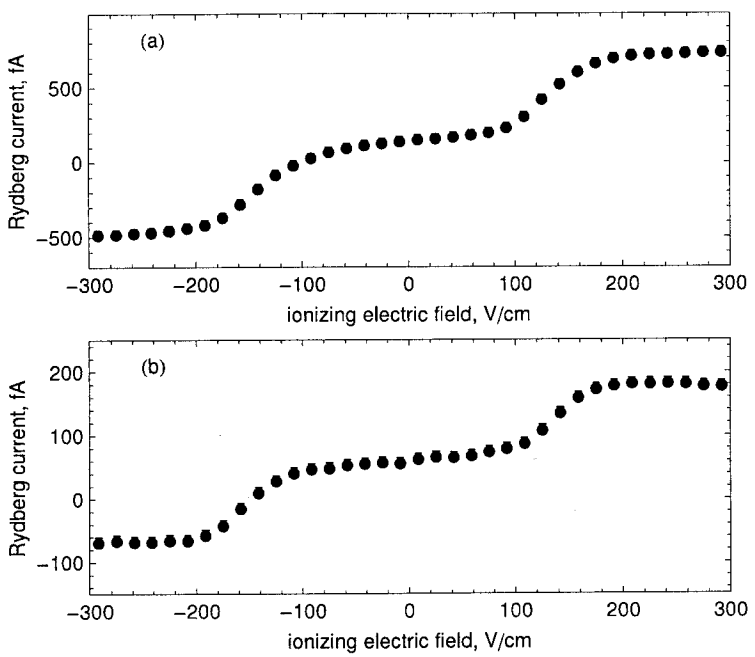

Figure 7.9: Field-ionization current from Rydberg atoms as a function of applied electric field in (a) the 1-T solenoid background field and (b) the full combined field of the 1-T solenoid and Ioffe trap, about 3.1 T.

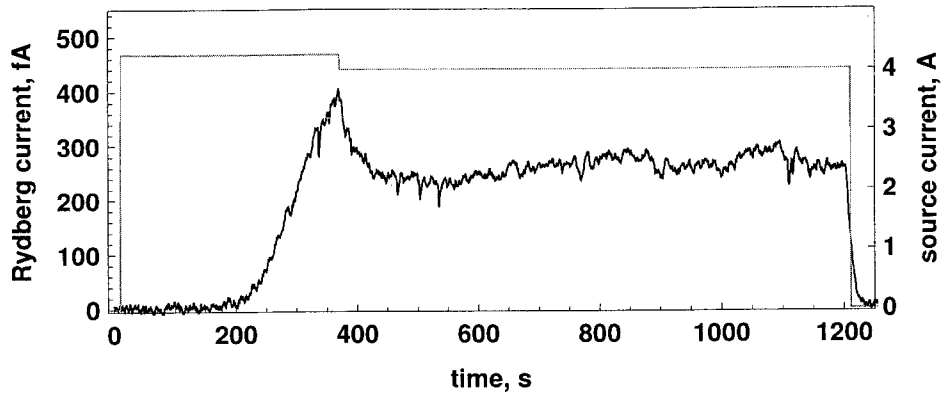

Figure 7.10: (Black) Rydberg field-ionization current observed as a function of time as (gray) current through the Cs source is turned on at 4.25 A for 360 s and then lowered to an operating value of 4 A. The current schedule we use allows us to produce a relatively constant Rydberg current of 250 fA once the 360-s warm-up period is complete.

perfectly collimated. Some Rydberg Cs atoms may strike the front of the baffle and be collisionally ionized. It appears that we collect some positive Cs^+ ions as a result of this process while the lighter electrons are not collected (or are collected in smaller quantities). The overall Rydberg current observed is symmetric about this zero-field "offset current."

The Cs apparatus also contains a pair of field-ionization plates on the far side of the electrode stack from the Cs source. Observing a Rydberg signal here provides confirmation that the Cs beam has passed through the electrode stack and should avoid the "offset" current described earlier. We observed a Rydberg signal at these plates at the end of the 2009 run, but we did not observe any signal at these plates during the 2010 run. It is likely that one of the signal wires to the plates broke during the apparatus installation or cool-down. During the 2010 beam run, we used Ps production (described below) to confirm that the Rydberg Cs beam was entering the electrode stack and functioning as expected.

During our Ps and $\overline{H}$ production experiments we desire a beam of Rydberg Cs entering the trap whose intensity is constant in time. This is difficult to achieve if a constant current is supplied to the source as the source takes a long time to reach its final equilibrium temperature and the rate of Cs release depends exponentially upon the source temperature. To more quickly achieve a constant beam intensity we first pre-heat the source with a current 0.25A higher than our final operating current for 360 s. Figure 7.10 shows the Rydberg current we observe as a function of time. It takes a few minutes before any Rydberg Cs is observed at all; after this point the Rydberg current increases exponentially in time as the source temperature increases. After 360 s we reduce the current to its final operating value. The observed field-ionization current rapidly drops to a stable value of approximately 250 fA. Over the course of the 2010 beam run we would periodically increase the source current used in order to keep the observed Rydberg signal constant as the source was gradually depleted. When we perform Ps or $\overline{H}$ production experiments we use a similar current schedule to heat the source and only introduce the green laser to begin charge-exchange after 390 s, after the beam has reached a reasonably constant intensity.

7.2 Production of Rydberg Ps by charge-exchange

Figure 7.11 shows the trap potentials used for experiments to produce Rydberg Ps. Typically 30 million positrons, spun to a radius of 4.5 ± 0.5 mm, are loaded into a harmonic multi-electrode well. We found that a reasonably harmonic well was necessary to prevent expansion of the e^+ plasma during the experiment. The harmonic

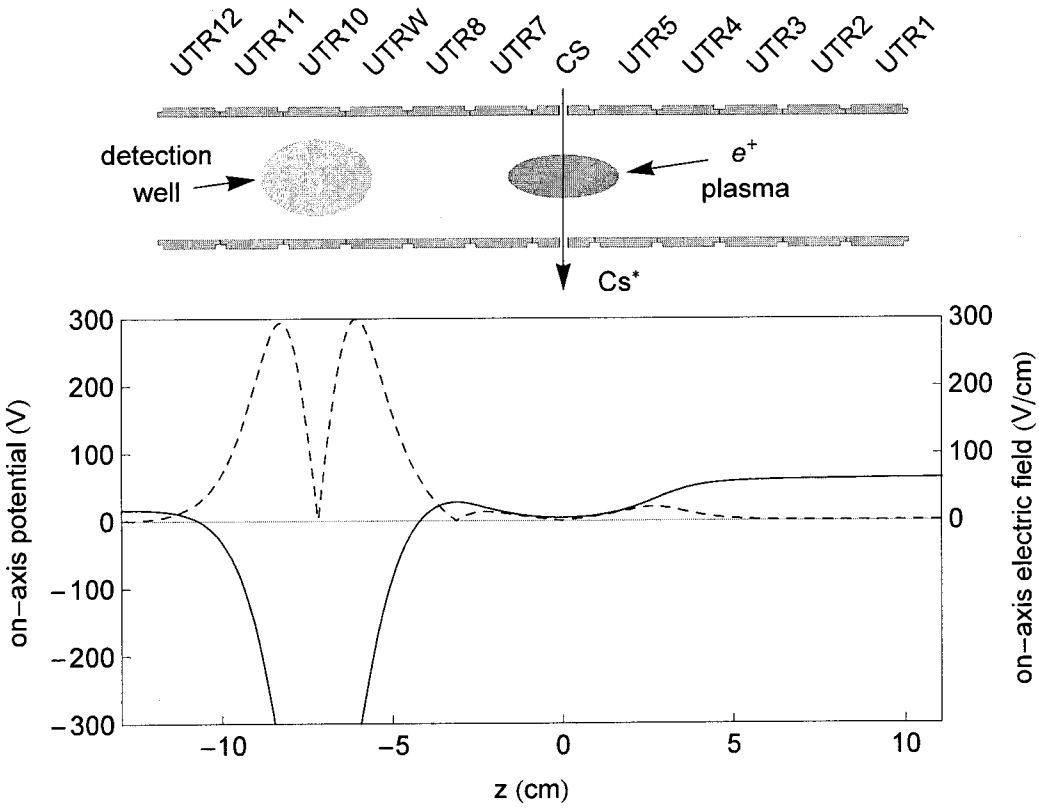

Figure 7.11: Potential structure used during Ps production experiments.

well also reduces the radial electric field seen by entering Cs* atoms, allowing us to perform the experiment with more e^+ without field-ionizing the Cs* before they reach the e^+ plasma.

Near the e^+ cloud we form a detection well. Ps* atoms entering the region of the detection well will be field-ionized and the e^+ from these atoms will be trapped in the detection well. The detection well has a maximum field of 300 V/cm (on-axis) which exceeds the highest fields we need to ionize incoming Cs* atoms (see Figure 7.9). The e^+ from on-axis Ps atoms which ionize at a field of less than 50 V/cm will not be trapped by the detection well, but instead will pass through it and will exit the trap through the top of our electrode stack (left in the figure). The detection well remains good out to a radius of $\rho \approx 16$ mm, although the minimum ionizing field required for the stripped e^+ to be caught at that radius has increased to 80 V/cm. The detection well is also designed so that any e^+ which escape the main positron well by some mechanism other than Ps formation will simply pass through the detection well region; the chance for them to collide with other trapped e^+ in a single pass and remain trapped in the detection well is extremely small. The potential structure is designed so that any electrons resulting from field-ionization of Ps atoms will quickly be accelerated downwards (to the right in the figure) and will eventually hit our Be degrader.

As described before, we preheat the source at a slightly higher current for 360 s, then reduce the current by 0.25A to provide a relatively stable Rydberg Cs beam. At 390 s after turning on the source we introduce the 511 nm laser into the experiment and begin producing Ps by charge-exchange with Rydberg Cs. After a specified

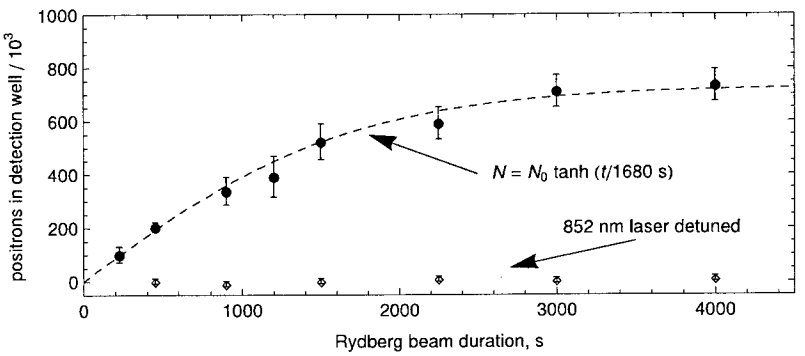

Figure 7.12: Ps production as a function of Rydberg Cs beam duration exhibits rise to a maximum value with a time constant of 1,680 s. No Ps production is observed when the 852 nm laser is detuned from resonance.

Rydberg beam duration (Figure 7.12) we turn off the Cs source; the source cools within seconds by radiation and Ps production ceases. We dump any remaining e^+ towards the Be degrader by inverting the voltage well in which they are stored. We can count how many e^+ remain in this well by observing the counts recorded by our detector system due to the γ photons emitted as the e^+ annihilate. We then do the same for the detection well. The detection well dump is done in 100 ms so we can observe the relatively small signal from e^+ in the detection well over the natural background count rate of our detectors.

Figure 7.12 shows the number of e^+ collected in the detection well as a function of duration of the introduced Cs^* beam. The production is initially linear in time and demonstrates a time constant of 1,680 s. For our longest trials (4,000 s), we do not observe any e^+ remaining in the initial e^+ holding well. We do not observe any e^+ in the detection well in control trials where we detune the 852 nm laser from resonance.

If charge-exchange Ps^* is to be used for $\overline{H}$ production, only the Ps^* which travels relatively parallel to the trap axis will pass through a confined $\overline{p}$ cloud and have a

chance to produce $\overline{\mathrm{H}}$. We can therefore write the number of $\overline{\mathrm{H}}$ produced as

$$N_{\bar{\mathrm{H}}} = \left.\frac{dN_{\mathrm{Ps}}}{d\Omega}\right|_{\theta=0} \Omega_{\bar{\mathrm{p}}} n_{\bar{\mathrm{p}}} \sigma_{\mathrm{Ps}\,\bar{\mathrm{p}}}, \tag{7.14}$$

with $\Omega_{\bar{\mathrm{p}}}$ the solid angle subtended by the $\bar{\mathrm{p}}$ cloud, $n_{\bar{\mathrm{p}}}$ the $\bar{\mathrm{p}}$ density, and $\sigma_{\mathrm{Ps}\,\bar{\mathrm{p}}}$ the cross section for Ps* to charge-exchange a second time and produce $\overline{\mathrm{H}}$. Our detection well subtends a small solid angle on axis and thus gives us a very good estimate of the quantity $\frac{dN_{\mathrm{Ps}}}{d\Omega}$ relevant to production of $\overline{\mathrm{H}}$ by two-stage charge exchange.

For our longest trials we find $\frac{dN_{\mathrm{Ps}}}{d\Omega} = 2.1 \times 10^6$ atoms/sr, a factor of 520 increase from earlier experiments in a similar apparatus [158]. Much of this increase is due to the larger number of e^+ loaded in the ATRAP2 apparatus, but a factor of three increase in the efficiency per e^+ input into the process is also observed. We attribute this increase to greater care in ensuring that high-energy e^- from field-ionized Ps* cannot make multiple passes through the e^+ well and collisionally heat the e^+. If the e^+ temperature exceeds the Cs Rydberg electron velocity $v = \alpha c/n \approx 5 \times 10^4$ m/s, the predicted cross-section for charge exchange has been found to be significantly reduced [159].

The overall efficiency for Ps production depends on the angular distribution of produced Ps and on the effective solid angle of the detection well, which in turn depends on the electric field required to ionize the Ps. We estimate that 92 $\pm$ 7.5 % of the e^+ ultimately form Ps in our longest trials. This estimate is based in part on classical-trajectory Monte Carlo calculations which we use to estimate the field at which Ps* with binding energies equivalent to those of $n = 42$ Cs will field-ionize either from the axial electric field in the detection well or the transverse electric field generated by the relativistic transform of the Ps motion in the 1 T background mag-

netic field. Our calculations suggest that the pinning of e^- and e^+ to B-field lines suppresses field-ionization of Ps^* by an electric field transverse to the B-field. Thus, the distribution of Ps^* trajectories should be close to isotropic. This calculation generally agrees with earlier simulations [144] on the trajectories of Ps^* in a background magnetic field. Those e^+ which do not ultimately form Ps^* probably slowly annihilate over the 4,000-s run time due to collisions with the Cs^+ ions which are captured in the e^+ holding well.

7.3 Antihydrogen production by two-stage charge-exchange

Figure 7.13 shows the trap potentials we used for antihydrogen production experiments. A large plasma of e^+ is held in a multiple-electrode harmonic well centered on the Cs electrode. Up to 5 million $\overline{p}$ are held nearby in a two-electrode-long well that is harmonic enough to prevent significant expansion of the $\overline{p}$ during the hour-long experiment. We typically used 300 million e^+ per experiment. The space charge from this many e^+, combined with the trapping fields, produces radial electric fields of 50 V/cm which start to approach field-ionization of the incoming Cs^* (which would occur around 100 V/cm). The need to avoid field-ionizing incoming Rydbergs sets a limit on how many e^+ can be used as an input to the process.

A detection well which field-ionizes $\overline{H}$ is located below (Figure 7.13(b)) the containment well for $\overline{p}$. As with the Ps production experiments, the high electric fields in this region can field-ionize Rydberg $\overline{H}$ and the resulting $\overline{p}$ may be trapped in the

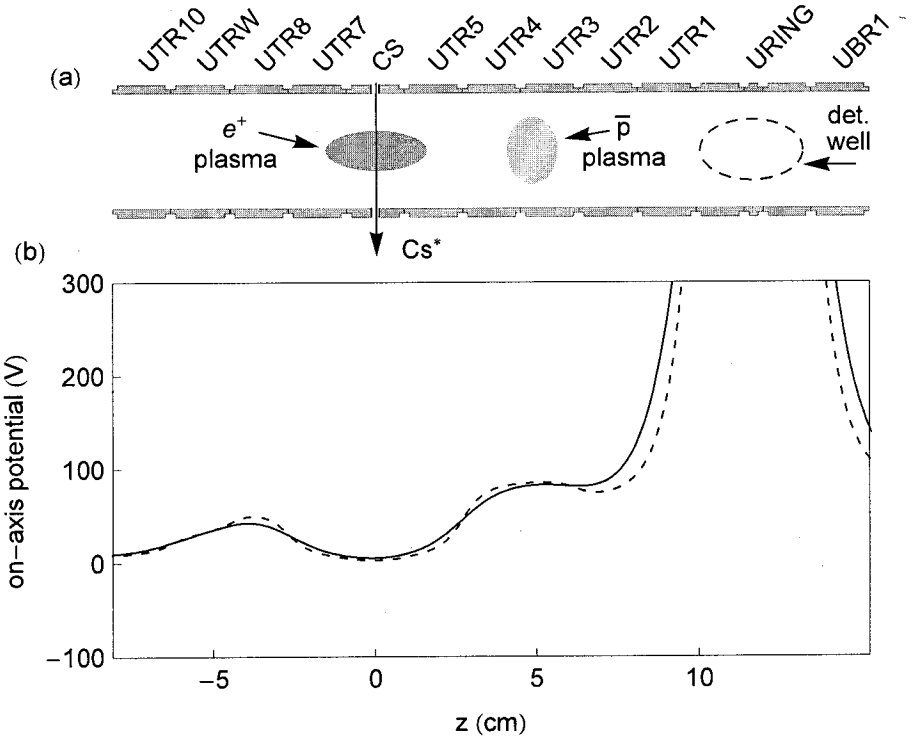

Figure 7.13: (a) Location of particle clouds and detection well in the electrode stack during charge-exchange $\overline{H}$ production experiments. (b) On-axis (solid curve) and 12 mm off-axis (dashed curve) trap potentials used during $\overline{H}$ production experiments.

detection well.

As with Ps production experiments, the potential structure for $\overline{H}$ production must fulfill several criteria. The detection well produces a maximum electric field of 300 V/cm and should be able to trap any $\overline{H}$ which ionize between 50 V/cm and 300 V/cm. Moreover the detection well is designed to trap the $\bar{p}$ from any $\overline{H}$ which ionize within a radius of 10 mm from the center of the trap. The potential structure is designed to minimize the electric fields experienced by Rydberg Cs atoms entering the electrode stack. It is also designed to guarantee that any high-energy e^+ produced by the field-ionization of Ps* will be ramped towards the upper end of our electrode stack and that any e^- produced by the same process will be ramped down towards the Be degrader. All of these high-energy particles should leave the $\overline{H}$ production region in a single pass so they will have a minimal chance to heat any of the e^+ or $\bar{p}$ used in the charge-exchange process.

Our typical $\overline{H}$ production experiments lasted approximately 1 hour. Due to the very large number of e^+ used, we increased the current through our Cs source by 0.25A compared to the current used for the Ps production experiments. This increased the intensity of the Cs beam by a factor of three relative to earlier Ps experiments. After the hour-long experiment, only a few percent of the initially trapped e^+ remained. Although we always observe some background losses of $\bar{p}$ when clouds of several million $\bar{p}$ are held in the upper stack for periods of tens of minutes or longer, we retained more than 90% of the initial $\bar{p}$ through the entire charge-exchange experiment. The scintillating fiber detectors showed a clear increase of about 500 counts per second (where normal background is around 3,000 counts per second) due to e^+ loss as we

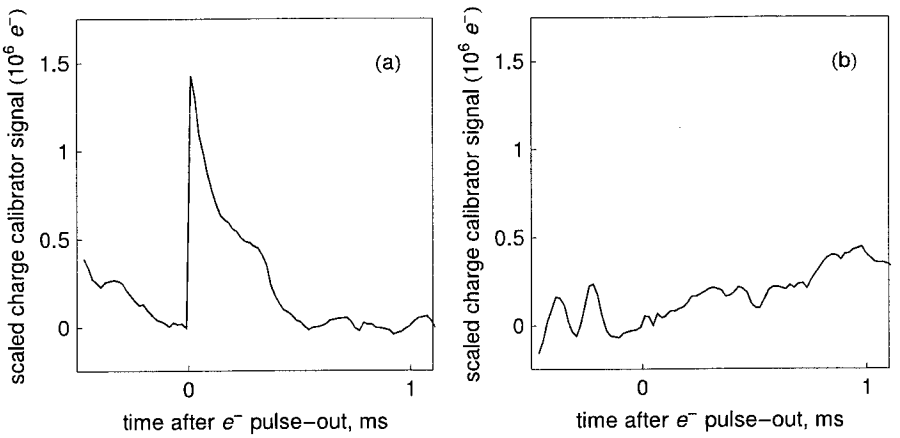

Figure 7.14: Charge-sensitive preamplifier showing (a) 1.2×10^6 e^- pulsed from the charge-exchange detection well at the end of an $\overline{H}$ production trial, (b) no e^- pulsed from the detection well in an otherwise identical trial with the 852 nm laser detuned from resonance.

produced Rydberg Cs, corresponding to Ps production. This signal would disappear if we briefly blocked the 511 nm laser light from entering the trap.

Despite the large number of particles used and the well-controlled parameters in the experiments, we did not find any $\overline{p}$ in our detection well at the end of any $\overline{H}$ production experiment. It is not the first time that lofty ambitions have not met with immediate success [160]. In order to understand these results we performed additional experiments. The first type of experiment is based on the observation that the detection well for $\overline{H}$ can also strip Ps* atoms and that the resulting e^- can also be caught in the detection well. Our annihilation detectors cannot see electrons, but we were able to use a 75-ns voltage pulse to remove e^- from the detection well at the end of our experiment and measure the charge deposited onto a collection electrode (as used for calibration of our e^- loading, described in Chapter 3). Figure 7.14 shows the electrons pulsed out of the detection well in one full $\overline{H}$ experiment and in one

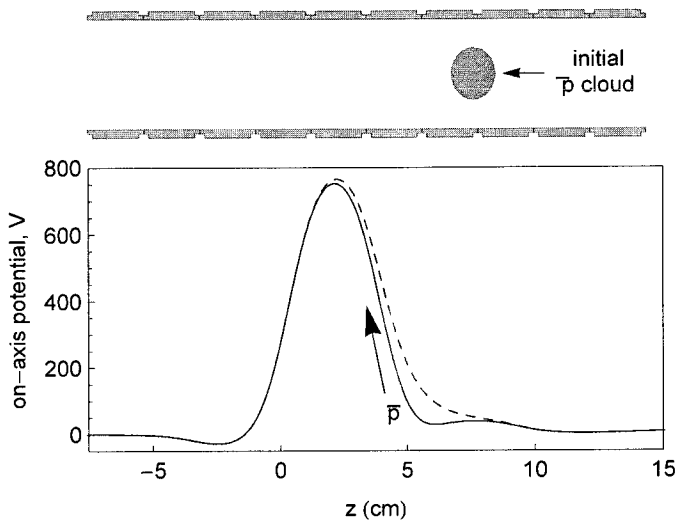

Figure 7.15: Example potential used for studies of $\overline{p}$ loss when dropped into deep wells similar to the charge-exchange detection wells. 90,000 $\overline{p}$ in an initial shallow well drop into the deep well when the barrier separating the wells is removed (dashed curve) either adiabatically or with a 1.75-ms voltage pulse. Trials with many different shapes of deep well were performed.

control experiment where all particles were present and the Cs source was run but the 852 nm laser was detuned from resonance. In two full experiments we pulsed out an average of $1.0 \pm 0.28 \times 10^6$ electrons and in two red-detuned control experiments no electrons were pulsed out. This result verifies that we were producing Ps during the full $\overline{H}$ experiments, that Ps atoms were traveling through the $\overline{p}$ cloud (since they must have done so in order to reach the detection well), and that our detection well was able to strip Rydberg atoms and confine the resulting particles.

In order to confirm that the more massive $\overline{p}$ would not be lost as they dropped into a very deep detection well, we conducted a series of experiments where a small number of antiprotons were dropped from a shallow well into an empty but very deep well. A typical potential structure used for these experiments is shown in 7.15. In

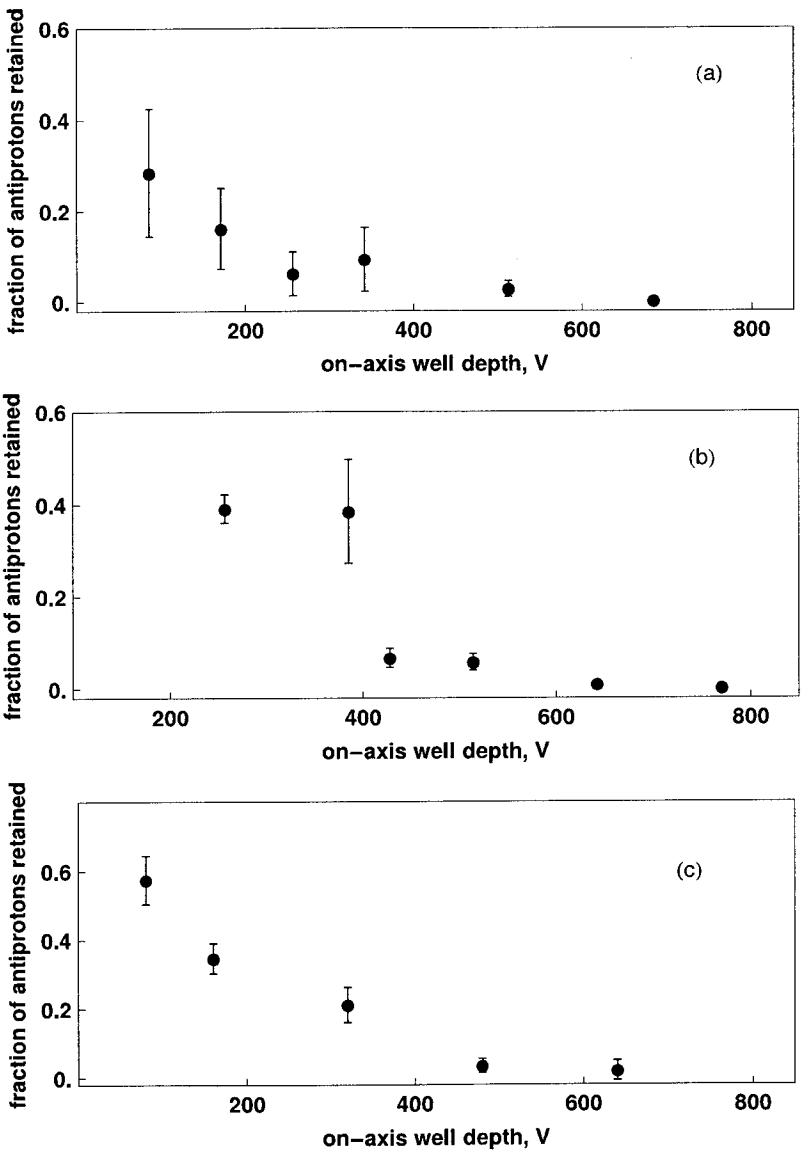

Figure 7.16: Fraction of $\overline{p}$ surviving when dropped into a deep potential well as a function of on-axis well depth, in (a) the upper stack, with $\overline{p}$ introduced to the deep well by adiabatic ramp-in process, (b) the upper stack, with $\overline{p}$ introduced to the deep well by a pulse-in process, (c) the lower stack, with $\overline{p}$ introduced to the deep well by adiabatic ramp-in.

these experiments, a cloud of 90,000 $\overline{p}$ begin in a shallow well separated from a deep well by a potential barrier. The barrier is inverted and the $\overline{p}$ then drop into the deep well, gaining hundreds of eV of energy in the process. The barrier can be removed either adiabatically, by slowly inverting the barrier over a period of 1 s, or quickly by a 1.75-ms voltage pulse. The number of $\overline{p}$ which survive either type of process decreases drastically for the deepest wells. We obtained similar results whether any cooling e^- were present in the deep well or not (1.5 million e^- were typically used) and at different physical locations within our electrode stack. Figure 7.16 shows the result of several of these experiments as a function of well depth. The results of many of these trials are also summarized in Table 7.2. We also confirmed that the wells themselves were not the cause of the loss. When $\overline{p}$ are initially placed in a shallow potential well and the depth of this well is increased adiabatically, the $\overline{p}$ remain stable. We confirmed this with clouds of 90,000 $\overline{p}$ adiabatically placed into a harmonic well formed by electrodes UTCE, URING and UBCE (on-axis well depth of 765 V) and a 5-electrode flat well formed by electrodes UTR8, UTR7, CS, UTR5, and UTR4 (on-axis well depth of 975 V).

Note that the much less deeply bound atoms produced by TBR experiments can be stripped at a lower field and therefore require a less deep detection well; Figure 7.16 shows that these shallower detection wells do not lead to the same loss as the very deep wells. We do not understand yet why the more massive $\overline{p}$ cannot survive this "drop-in" process while lighter lepton species are not lost in similar experiments. There are two main differences between our conditions and those in the 2004 charge-exchange experiment, where counts from a few $\overline{p}$ in the detection well were observed.

One is the much higher energy gained by our $\overline{p}$ as they drop into this well, 760 V in our case but less than 300 V in 2004. The other difference is that the 2004 experiments were conducted in a much higher field (5.3 T as opposed to our 1 T field).

The results of our experiments suggested that detection wells were an inappropriate tool to look for $\overline{H}$ production by charge-exchange under our experimental conditions. As a result we switched to a different detection method. In a second series of experiments we use a rotating chopper wheel to modulate the intensity of 852 nm laser light entering the trap. During periods when the 852 nm laser is allowed into the trap, charge-exchange $\overline{H}$ formation should take place. This $\overline{H}$ formation should cease during the periods when the chopper blocks 852 nm light from entering the trap. We thus look for an excess of $\overline{p}$ annihilations during periods when the laser is entering the trap compared to those periods when it is blocked. A beam sampler sends a small portion of the 852 nm light after the chopper to a photodiode, which allows us to tell whether detector events occur while the laser is entering the trap or while it is blocked. We acquire full readout data for each detector event during the experiment.

These trials assume that $\overline{H}$ production by charge-exchange will be the only effect to produce $\overline{p}$ losses that results in an observable difference in the loss rate between periods when the chopper is open (allowing the laser into the trap) and periods when the chopper blocks the laser. Since some possible effects producing $\overline{p}$ losses, such as laser-induced heating of the $\overline{p}$, are expected to take times longer than the chopper period to begin and end, they would average out over many chopper oscillations and would not contribute to our signal. We developed a numerical simulation to further

Location	Barrier removal	e^- present?	Well type	On-axis depth (V)	% of $\overline{p}$ retained
Upper stack	Ramp-in	No	5-electrode flat	975	0.3 %
Upper stack	Ramp-in	Yes	5-electrode flat	975	0.2 %
Upper stack	Ramp-in	No	3-electrode harmonic	960	0.4 %
Upper stack	Ramp-in	No	5-electrode flat	975	0.5 %
Upper stack	Ramp-in	No	Single electrode	230	< 0.1 %
Upper stack	Ramp-in	No	2-electrode	680	0.2 %
Upper stack	Ramp-in	No	3-electrode flat	760	0.3 %
Upper stack	Ramp-in	No	5-electrode harmonic	740	0.2 %
Upper stack	Pulse-in	No	3-electrode harmonic	880	0.2 %
Upper stack	Pulse-in	No	2-electrode	770	0.2 %
Upper stack	Pulse-in	Yes	3-electrode flat	385	0.6 %
Upper stack	Pulse-in	Yes	2-electrode	430	0.1 %
Lower stack	Ramp-in	No	Single (endcap)	640	2.0 %

Table 7.2: Summary of experiments allowing $\overline{p}$ to drop into deep detection wells. This table shows the fraction of $\overline{p}$ retained for the deepest wells used for each type of experiment. For shallower wells a larger fraction of $\overline{p}$ could be retained, as shown in Figure 7.16.

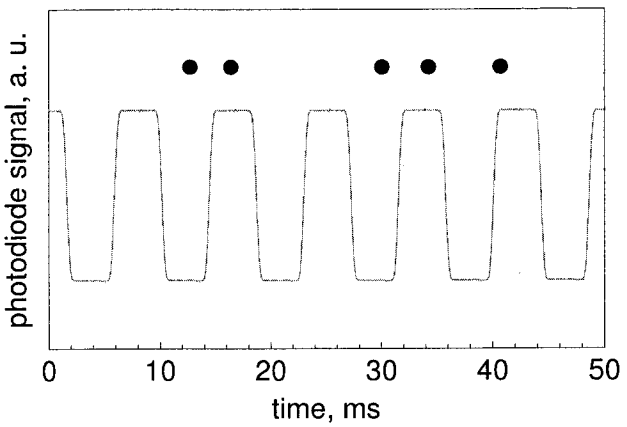

Figure 7.17: Signal recorded from chopped $\overline{\mathrm{H}}$ production experiments. The gray curve represents the photodiode signal recording the modulation of 852 nm laser intensity entering the trap by the chopper wheel. The black dots represent the times at which $\overline{\mathrm{p}}$ annihilation events are recorded from the detection system.

analyze these effects, which is described later in this chapter.

Figure 7.17 shows a short sample of data from one of these chopped-laser experiments. After the experiment is over we look at the timestamp for each recorded annihilation. Following the procedure described in Chapter 3, we discard those events whose detector profile makes them more likely to be cosmic rays than real $\overline{\mathrm{p}}$ annihilations. We then subtract the number of annihilation events occurring during time windows where the laser is definitely entering the trap from the number of events occurring during time windows where the laser is blocked. We refer to this excess annihilation count when the laser is entering the trap as ΔN. Events that occur during the shorter time periods when the photodiode signal is increasing or decreasing are discarded.

Figure 7.18 shows the results of several chopped-laser experiments. When the 852 nm laser is tuned to resonance, we observe an excess of $\Delta N = 3600 \pm 610\,\overline{\mathrm{p}}$

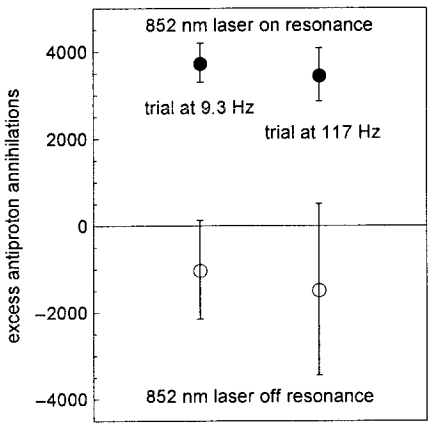

Figure 7.18: Excess $\overline{\mathrm{p}}$ annihilations seen during periods when the 852 nm laser is entering the trap in chopped $\overline{\mathrm{H}}$ production experiments.

annihilations during periods where the laser is entering the trap. The observed excess ΔN is the same when the chopping wheel modulates the laser intensity at 117 Hz or 9.3 Hz. In two trials with the 852 nm laser detuned from resonance, no excess is observed. The error bars are given by the square root of background counts observed in the experiment. The excess in each of the two on-resonant trials exceeds 5 standard deviations from zero. If we assume a Gaussian distribution of counts from the trials, the probability of obtaining the 5.7-σ result from the 117 Hz trial by chance is 1.3×10^{-8}; the probability to obtain the 8.3-σ result from the 9.3 Hz trial is less than 10^{-15}. While come cosmic-ray events contribute to the background observed in the experiment, the majority of background counts are due to slow losses of $\overline{\mathrm{p}}$ throughout the experiment. While these losses total less than 10 % of the number of $\overline{\mathrm{p}}$ used in each experiment, they vary some from trial to trial, and the somewhat higher losses in the control trials are responsible for the larger error bars in these trials.

The chopped-laser trials suggest that $\overline{\mathrm{H}}$ formation is taking place in our charge-exchange experiments. To further exclude the possibility that some process other

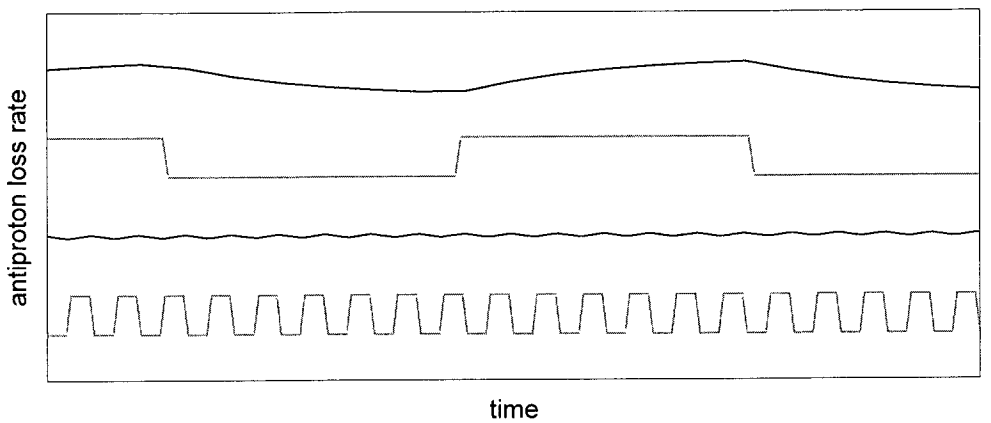

Figure 7.19: Numerically integrated model of $\overline{\mathrm{p}}$ loss for chopped $\overline{\mathrm{H}}$ experiments. (Gray curves) Periodic forcing function $\Gamma_{max}(t)$ representing the effect of 852 nm light entering the trap. (Black curves) Simulated response of $\overline{\mathrm{p}}$ loss signal to the forcing function given time constants $\tau_1 = \tau_2 = 25$ ms.

than $\overline{\mathrm{H}}$ formation could be responsible for the excess loss observed only when the 852 nm laser is on resonance, we developed a model of the loss process. Any laser-induced loss must require some time constant τ_1 before it reaches a maximum value; τ_1 must be at least 200 μs (the time required for 600 K Cs atoms to travel from the excitation region to the center of the trap). After the laser is blocked, there must be some second time constant τ_2 over which the loss returns to its lower background level. The observed agreement between the chopped-laser trials at frequencies of 9.3 Hz and 117 Hz constrains the values which this second time constant may take.

We modeled the process of antiproton loss by writing the loss rate of antiprotons $\Gamma_{\bar{p}}$ as

$$\frac{d\Gamma_{\bar{p}}(t)}{dt} = \frac{\Gamma_{max}(t) - \Gamma_{\bar{p}}(t)}{\tau_i}, \tag{7.15}$$

where Γ_{max} is a function which varies according to the laser power entering the trap and represents the observed effect of the 852 nm laser on the antiproton annihilation

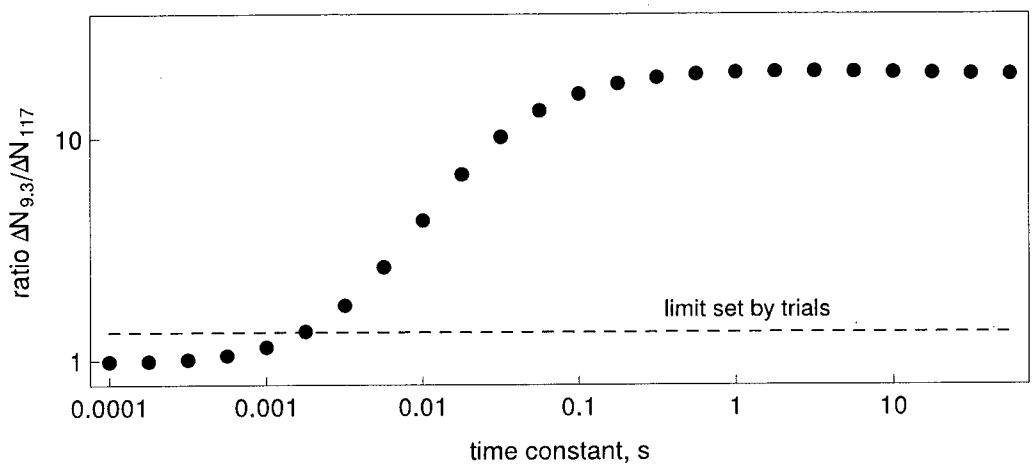

Figure 7.20: Comparison of the ratio $\Delta N_{9.3}/\Delta N_{117}$ produced by the simulation for different time constants τ_2. Only those $\tau_2 < 2$ ms are consistent with the observed agreement in experimental trials.

rate, and

$$\tau_i = \begin{cases} \tau_1 & : \Gamma_{\bar{p}} < \Gamma_{max} \\ \tau_2 & : \Gamma_{\bar{p}} > \Gamma_{max} \end{cases} \tag{7.16}$$

represent the two time constants for excess $\overline{\mathrm{p}}$ loss to begin and end. We can easily numerically integrate the expected antiproton loss over time, as illustrated in Figure 7.19 for the case where $\tau_1 = \tau_2 = 25$ ms. In the example the antiproton loss rate responds sufficiently fast to follow a signal modulated at 9.3 Hz, but cannot effectively follow a signal modulated at 117 Hz.

The simulated antiproton loss rate can be analyzed in the same way as the actual antiproton annihilation events recorded during our trials. We obtain ΔN_{sim}, the simulated excess events, by subtracting the total expected events during time periods when the laser is not entering the trap from the total expected events during time periods when the laser is entering the trap. The difference in expected events depends on the magnitude of Γ_{max}; however, the ratio of this difference in a trial at 117 Hz to

the difference in a trial at 9.3 Hz will not depend on the magnitude of Γ_{max}. Figure 7.20 shows the ratio of the expected difference $\Delta N_{9.3}/\Delta N_{117}$ as a function of time constant τ_2 assuming that $\tau_1 = 100$ μs. For long times τ_2 this ratio approaches the ratio of the two frequencies, (117 Hz)/(9.3 Hz), as expected.

From the observed experimental results we can see that

$$\frac{\Delta N_{9.3}}{\Delta N_{117}} = 1.08 \pm 0.21, \tag{7.17}$$

so that at the 5-σ confidence level we can say that $\Delta N_{9.3}/\Delta N_{117} < 2.13$. As shown in 7.20, this constrains the time τ_2 to be less than 2 ms. Note that assuming a longer time τ_1 would impose a stricter constraint on τ_2. By assuming that $\tau_1 \ll \tau_2$ we thus find the limit for times τ_2 which are not consistent with any τ_1.

The agreement of the experiments with the laser chopped at 117 Hz and 9.3 Hz thus constrains the "turn-off" time constant τ_2 of any process responsible for the excess antiproton losses to be less than 2 ms. Heating of the antiprotons by energetic e^+ or e^- is thus ruled out, because the fastest possible time constant for cooling of particles in the trap is given by the electron synchrotron damping time which is 2.6 s in a 1 T field.

The observed agreement between different frequencies also rules out centrifugal separation as a possible source of the excess $\overline{p}$ annihilations observed. The time scale for radial transport in a plasma may be written as [85]

$$\tau_{rt} \approx \tau_{coll} \frac{\omega_c^2}{\omega_p^2}, \tag{7.18}$$

with τ_{coll} the collision time. In the $\overline{p}$ cloud, even with as many as 5 million electrons trapped with the $\overline{p}$ the time scale for centrifugal separation exceeds 10 s and is not

consistent with the observed results. The chopped-laser trials therefore provide strong evidence that 3600 ± 610 $\overline{\mathrm{H}}$ atoms per trial have been produced by two-stage charge-exchange, a factor of 200 increase from the number of $\overline{\mathrm{H}}$ produced per trial by this method in 2004.

7.4 Conclusions

Although production of $\overline{\mathrm{H}}$ by two-stage charge-exchange is more difficult than production of $\overline{\mathrm{H}}$ by other methods, the technique has benefits which may be important in the quest to trap larger numbers of $\overline{\mathrm{H}}$ atoms. The technique does not require $\overline{\mathrm{p}}$ to enter an e^+ cloud in order to form $\overline{\mathrm{H}}$, allows control over the final state of the $\overline{\mathrm{H}}$ produced, and does not require any energy to be added to the $\overline{\mathrm{p}}$ during the process. Two-stage charge exchange therefore allows $\overline{\mathrm{H}}$ formation compatible with initially cold $\overline{\mathrm{p}}$ and from large clouds of e^+ and $\overline{\mathrm{p}}$. We have demonstrated robust formation of Rydberg Ps and strong evidence of the formation of 3600 ± 610 $\overline{\mathrm{H}}$ atoms by two-stage charge exchange. The Rydberg Cs source used to initiate this process is also compatible with use inside of an energized Ioffe trap, allowing us to use this method in $\overline{\mathrm{H}}$ trapping trials. The production of cold $\overline{\mathrm{H}}$ by two-stage charge exchange may play an important role in trapping sufficient numbers of $\overline{\mathrm{H}}$ atoms to perform spectroscopic comparisons of H and $\overline{\mathrm{H}}$.

Chapter 8

Conclusions

At the outset of this research, experiments on $\overline{H}$ production in a Penning trap had revealed some of the intricacies of the formation process, but experiments on particles in a combined Penning-Ioffe trap were just beginning. Early $\overline{H}$ production results [21, 22, 23] had shown that $\overline{H}$ could be produced in nested Penning traps [136]. Subsequent measurements of the state distribution [23] and velocity of produced $\overline{H}$ atoms [138] had been performed, and some claims about the temperature dependence of $\overline{H}$ production by three-body recombination [137] had been made. ATRAP's experiments demonstrated the stability of charged particles in a Penning-Ioffe trap [24] and the first production of $\overline{H}$ within a combined Penning-Ioffe trap [25]. ATRAP also established that less than 12 atoms per trial were being trapped, leading us to seek ways to increase the number of $\overline{H}$ atoms we might hope to trap.

Several important advances towards the trapping and eventual precision spectroscopy of antihydrogen are described in this thesis. First, the capability to load much larger clouds of e^+ and $\overline{p}$ has been demonstrated. New plasma control tech-

niques allow the loading of up to several billion e^+ in a timely fashion. A field-boosting solenoid now allows us to load up to 10 million antiprotons in two hours. With the addition of rotating wall techniques to compress the radius of the e^- plasma which cools the $\overline{p}$, we can retain over 90 % of these $\overline{p}$ in a 1-T field in a manner compatible with $\overline{H}$ experiments. These larger numbers of particles will be necessary as we seek to scale up antihydrogen trapping to the numbers necessary for spectroscopy.

We now understand and control our plasmas much more precisely. We can now measure plasma modes, an indicator of plasma geometry, within a few seconds and for clouds of as few as 30 million positrons or electrons. A rotating wall drive allows us to reduce the radius of our trapped plasmas to as little as 2 mm. These new techniques allowed us to study changes in the geometry of plasmas in our trap and to optimize our $\overline{H}$ production trials. In combination with the antiproton-loading solenoid, these techniques led to the demonstration of centrifugal separation of e^- and $\overline{p}$ [27], the first such demonstration with elementary particles.

Techniques for measuring and lowering the temperature of cold $\overline{p}$ were implemented. Temperature measurements made by studying the loss rate of the first few $\overline{p}$ to leave the trap as the confining potential is reduced allowed us to discover that our particles do not yet cool to the temperature of the electrode stack walls. We now have a diagnostic allowing us to find ways to reduce the temperature of our particle clouds. Adiabatic cooling of up to 3×10^6 $\overline{p}$ to temperatures of 3.5 K or below was demonstrated [28]. This temperature is three times lower than any other reported temperature of $\overline{p}$ to date. This method of cooling does not require any particle loss and is thus compatible with producing very large clouds of cold $\overline{p}$.

Important upgrades to the ATRAP experimental apparatus were made to enhance its reliability and versatility. A MgF window for Lyman-α access and a plasma imaging system were added to the moveable window flange to allow access for laser-cooling of $\overline{\mathrm{H}}$ and to enable direct measurements of plasma geometry. Copper thermal links were added to the pumped helium system, reducing the cooldown time of the apparatus from 4.5 days to 2.5 days. In a major reliability upgrade, a failure-prone titanium bellows assembly connecting to the movable stage was replaced with a more durable stainless-steel assembly.

Finally, and most importantly to this work, a cryogenic Rydberg Cs source was implemented for the production of antihydrogen by two-stage charge exchange. Production of a Rydberg Cs beam was demonstrated in both the 1-T background field of the experiment and the higher, nonuniform field produced by the Ioffe trap. Well-controlled production of Rydberg Ps was demonstrated. We observed a factor of 520 increase in on-axis Ps production per experiment and three times higher efficiency per e^+ used than previous Ps-production experiments. Good evidence of the production of 3600 ± 600 $\overline{\mathrm{H}}$ atoms per trial by charge-exchange was obtained. This is a factor of 200 increase over the production rate per trial in a previous proof-of-principle experiment. $\overline{\mathrm{H}}$ production by two-stage charge exchange in a Penning-Ioffe trap is ideally suited to take advantage of the larger numbers and colder temperatures of $\overline{\mathrm{p}}$ we can now produce.

ATRAP's 2008 demonstration of $\overline{\mathrm{H}}$ production in a combined Penning-Ioffe trap established that less than 20 atoms were being trapped per trial [25]. Two different approaches were taken in response to this limit. Better detection sensitivity enabled

the 2010 report of one trapped antihydrogen atom per 9 trials [26], an important proof-of-principle demonstration. Believing that more trapped $\overline{H}$ atoms will be required for the envisioned [15] high-precision spectroscopy of antihydrogen, ATRAP instead sought to increase the number of atoms that could be trapped. ATRAP's demonstration of the accumulation of greatly increased numbers of particles [27] and the coldest $\overline{p}$ clouds yet observed [28] are important advances towards trapping larger numbers of $\overline{H}$ atoms.

There are several avenues of research the ATRAP Collaboration hopes to pursue during the 2011 beam run. One important priority for ATRAP will be finding ways to improve the stability of larger particle clouds in a Penning-Ioffe trap. This will permit the collaboration to take full advantage of the large particle clouds used during $\overline{H}$ trapping experiments. Equally important is demonstrating cold $\overline{p}$ in the Penning-Ioffe field, and finding ways to reduce the base temperature of lepton clouds in the apparatus to the temperature of the 1.3 K electrode stack.

During the 2011 beam run, the collaboration also hopes to implement the next-generation Penning-Ioffe trap platform. The key upgrade to this apparatus is a new Ioffe trap with 600 mK trapping depth which can be turned off in 10 ms. This will greatly boost the signal-to-noise ratio of ATRAP's $\overline{H}$ trapping experiments and will hopefully allow ATRAP to see a signal from trapped $\overline{H}$. In conjunction with our ability to load large clouds of trapped particles, we hope to be able to optimize to trap many more than one $\overline{H}$ atom per trial.

Production of $\overline{H}$ in the next-generation Ioffe trap by two-stage charge-exchange with up to 10 million cold antiprotons is ATRAP's most promising route to a large

number of trapped atoms. If, as predicted, one-sixth of atoms formed by charge exchange are produced in low-field-seeking states [144], and if the antiprotons can be cooled to a thermal 1 K distribution, as many as 170 antihydrogen atoms may be trapped given our current efficiency for $\overline{\mathrm{H}}$ production. It may also be possible to further optimize this method of $\overline{\mathrm{H}}$ formation.

ATRAP also plans to install lasers and microwave sources for measurements on trapped $\overline{\mathrm{H}}$. The collaboration will install a 30 GHz microwave source which can drive spin-flips of $\overline{\mathrm{H}}$ in a 1 T field. This source permits a measurement to be made of the magnetic moment of $\overline{\mathrm{H}}$ and might also be used to eject $\overline{\mathrm{H}}$ from the trap as confirmation of $\overline{\mathrm{H}}$ trapping. Installing 121-nm lasers for laser cooling of trapped $\overline{\mathrm{H}}$ is an even more important objective. ATRAP members from the University of Mainz are building a continuous-wave Lyman-α source which we hope to install this year.

While many challenges lie ahead, ATRAP's recent advances and upcoming improvements give reason for optimism. With luck and hard work, ATRAP will soon be able to demonstrate large numbers of trapped antihydrogen atoms. The next few years will hopefully see the dawn of precision measurements on this unique antimatter system.

Bibliography

[1] P.A.M. Dirac, Proc. Roy. Soc. **A133**, 62 (1931).

[2] P. A. M. Dirac, Proceedings of the Royal Society of London. Series A, Containing Papers of a Mathematical and Physical Character **126**, pp. 360 (1930).

[3] Carl D. Anderson, Phys. Rev. **43**, 491 (1933).

[4] P. M. S. Blackett, Nature **132**, 917 (1933).

[5] O. Chamberlain, E. Segrè, C. Wiegand, and T. Ypsilantis, Phys. Rev. **100**, 947 (1955).

[6] R. L. Golden, S. Horan, B. G. Mauger, G. D. Badhwar, J. L. Lacy, S. A. Stephens, R. R. Daniel, and J. E. Zipse, Phys. Rev. Lett. **43**, 1196 (1979).

[7] W. Kells, G. Gabrielse, and K. Helmerson, "On Achieving Cold Antiprotons in a Penning Trap", 1984, fermilab - Conf. 84/68E.

[8] W. Kells, G. Gabrielse, and K. Helmerson, in *Proceedings of ICAP IX* (University of Washington, Seattle, 1984), Vol. B88, abstract.

[9] Hans G. Dehmelt, "Autobiography for 1989 Nobel Prize in Physics", Published in "Les Priz Nobel", 1990.

[10] G. Gabrielse, X. Fei, K. Helmerson, S. L. Rolston, R. L. Tjoelker, T. A. Trainor, H. Kalinowsky, J. Haas, and W. Kells, Phys. Rev. Lett. **57**, 2504 (1986).

[11] G. Gabrielse, X. Fei, L. A. Orozco, R. L. Tjoelker, J. Haas, H. Kalinowsky, T. A. Trainor, and W. Kells, Phys. Rev. Lett. **63**, 1360 (1989).

[12] G. Gabrielse, D. Phillips, W. Quint, H. Kalinowsky, G. Rouleau, and W. Jhe, Phys. Rev. Lett. **74**, 3544 (1995).

[13] G. Gabrielse, A. Khabbaz, D. S. Hall, C. Heimann, H. Kalinowsky, and W. Jhe, Phys. Rev. Lett. **82**, 3198 (1999).

[14] G. Gabrielse, S. L. Rolston, L. Haarsma, and W. Kells, Hyperfine Interact. **44**, 287 (1988).

[15] G. Gabrielse, in *Fundamental Symmetries*, edited by P.Bloch, P. Paulopoulos, and R. Klapisch (Plenum, New York, 1987), pp. 59–75.

[16] G. Baur, Phys. Lett. B **311**, 343 (1993).

[17] G. Baur, G. Boero, S. Brauksiepe, A. Buzzo, W. Eyrich, R. Geyer, D. Grzonka, J. Hauffe, K. Kilian, M. Lo Vetere, M. Macri, M. Moosburger, R. Nellen, W. Oelert, S. Passaggio, A. Pozzo, K. Rohrich, K. Sachs, G. Schepers, T. Sefzick, R.S. Simon, R. Stratmann, F. Stinzing, and M. Wolke, Phys. Lett. B **368**, 251 (1996).

[18] G. Blanford, D. C. Christian, K. Gollwitzer, M. Mandelkern, C. T. Munger, J. Schultz, and G. Zioulas, Phys. Rev. Lett. **80**, 3037 (1998).

[19] G. Gabrielse, D. S. Hall, T. Roach, P. Yesley, A. Khabbaz, J. Estrada, C. Heimann, and H. Kalinowsky, Phys. Lett. B **455**, 311 (1999).

[20] G. Gabrielse, J. Estrada, J. N. Tan, P. Yesley, N. S. Bowden, P. Oxley, T. Roach, C. H. Storry, M. Wessels, J. Tan, D. Grzonka, W. Oelert, G. Schepers, T. Sefzick, W. Breunlich, M. Cargnelli, H. Fuhrmann, R. King, R. Ursin, J. Zmeskal, H. Kalinowsky, C. Wesdorp, J. Walz, K. S. E. Eikema, and T. Haensch, Phys. Lett. B **507**, 1 (2001).

[21] M. Amoretti, C. Amsler, G. Bonomi, A. Bouchta, P. Bowe, C. Carraro, C. L. Cesar, M. Charlton, M. J. T. Collier, M. Doser, V. Filippini, K. S. Fine, A. Fontana, M. C. Fujiwara, R. Funakoshi, P. Genova, J. S. Hangst, R. S. Hayano, M. H. Holzscheiter, L. V. Jorgensen, V. Lagomarsino, R. Landua, D. Lindelof, E. L. Rizzini, M. Macri, N. Madsen, G. Manuzio, M. Marchesotti, P. Montagna, H. Pruys, C. Regenfus, P. Riedler, J. Rochet, A. Rotondi, G. Rouleau, G. Testera, A. Variola, T. L. Watson, and D. P. van der Werf, Nature **419**, 456 (2002).

[22] G. Gabrielse, N. S. Bowden, P. Oxley, A. Speck, C. H. Storry, J. N. Tan, M. Wessels, D. Grzonka, W. Oelert, G. Schepers, T. Sefzick, J. Walz, H. Pittner, T. W. Hänsch, and E. A. Hessels, Phys. Rev. Lett. **89**, 213401 (2002).

[23] G. Gabrielse, N. S. Bowden, P. Oxley, A. Speck, C. H. Storry, J. N. Tan, M. Wessels, D. Grzonka, W. Oelert, G. Schepers, T. Sefzick, J. Walz, H. Pittner, T. W. Hänsch, and E. A. Hessels, Phys. Rev. Lett. **89**, 233401 (2002).

[24] G. Gabrielse, P. Larochelle, D. Le Sage, B. Levitt, W.S. Kolthammer, I. Kuljanishvili, R. McConnell, J. Wrubel, F.M. Esser, H. Glueckler, D. Grzonka, G.

Hansen, S. Martin, W. Oelert, J. Schillings, M. Schmitt, T. Sefzick, H. Soltner, Z. Zhang, D. Comeau, M.C. George, E.A. Hessels, C.H. Storry, M. Weel, A. Speck, F. Nillius, J. Walz, and T.W. Haensch, Phys. Rev. Lett. **98**, 113002 (2007).

[25] G. Gabrielse, P. Larochelle, D. Le Sage, B. Levitt, W. S. Kolthammer, R. McConnell, P. Richerme, J. Wrubel, A. Speck, M. C. George, D. Grzonka, W. Oelert, T. Sefzick, Z. Zhang, A. Carew, D. Comeau, E. A. Hessels, C. H. Storry, M. Weel, J. Walz, and A. T. R. A. P. Collaboration, Phys Rev Lett **100**, 113001 (2008).

[26] G. B. Andresen *et al.*, Nature **468**, 673 (2010).

[27] G. Gabrielse, W. S. Kolthammer, R. McConnell, P. Richerme, J. Wrubel, R. Kalra, E. Novitski, D. Grzonka, W. Oelert, T. Sefzick, M. Zielinski, J. S. Borbely, D. Fitzakerley, M. C. George, E. A. Hessels, C. H. Storry, M. Weel, A. Müllers, J. Walz, and A. Speck, Phys. Rev. Lett. **105**, 213002 (2010).

[28] G. Gabrielse, W. S. Kolthammer, R. McConnell, P. Richerme, R. Kalra, E. Novitski, D. Grzonka, W. Oelert, T. Sefzick, M. Zielinski, D. Fitzakerley, M. C. George, E. A. Hessels, C. H. Storry, M. Weel, A. Müllers, and J. Walz, Phys. Rev. Lett. **106**, 073002 (2011).

[29] G. B. Andresen, M. D. Ashkezari, M. Baquero-Ruiz, W. Bertsche, P. D. Bowe, E. Butler, C. L. Cesar, S. Chapman, M. Charlton, J. Fajans, T. Friesen, M. C. Fujiwara, D. R. Gill, J. S. Hangst, W. N. Hardy, R. S. Hayano, M. E. Hayden, A. Humphries, R. Hydomako, S. Jonsell, L. Kurchaninov, R. Lambo, N. Madsen, S. Menary, P. Nolan, K. Olchanski, A. Olin, A. Povilus, P. Pusa, F. Robicheaux, E. Sarid, D. M. Silveira, C. So, J. W. Storey, R. I. Thompson, D. P. van der Werf, D. Wilding, J. S. Wurtele, and Y. Yamazaki, Phys. Rev. Lett. **105**, 013003 (2010).

[30] T. D. Lee and C. N. Yang, Physical Review **104**, 254 (1956).

[31] C. S. Wu, E. Ambler, R. W. Hayward, D. D. Hoppes, and R. P. Hudson, Phys. Rev. **105**, 1413 (1957).

[32] T. D. Lee and C. N. Yang, Phys. Rev. **105**, 1671 (1957).

[33] Jerome I. Friedman and V. L. Telegdi, Phys. Rev. **106**, 1290 (1957).

[34] Richard L. Garwin, Leon M. Lederman, and Marcel Weinrich, Phys. Rev. **105**, 1415 (1957).

[35] L. D. Landau, Nucl. Phys. **3**, 127 (1957).

[36] J. H. Christenson, J. W. Cronin, V. L. Fitch, and R. Turlay, Phys. Rev. Lett. **13**, 138 (1964).

[37] G. Lüders, Ann. Phys. **2**, 1 (1957).

[38] M. Niering, R. Holzwarth, J. Reichert, P. Pokasov, Th. Udem, M. Weitz, T. W. Hänsch, P. Lemonde, G. Santarelli, M. Abgrall, P. Laurent, C. Salomon, and A. Clairon, Phys. Rev. Lett. **84**, 5496 (2000).

[39] R. Bluhm, V. A. Kostelecky, and N. Russell, Physical Review Letters **82**, 2254 (1999).

[40] C. Zimmerman and T. Hänsch, Hyperfine Interact. **76**, 47 (1993).

[41] G. Gabrielse, Hyperfine Interact. **44**, 349 (1988).

[42] J. Walz and T. Hänsch, General Relativity and Gravitation **36**, 561 (2004).

[43] M. Amoretti *et al.*, *Proposal for the AEGIS experiment at the CERN Antiproton Decelerator* (http://cdsweb.cern.ch/record/1037532/files/spsc-2007-017.pdf, CERN, 2007).

[44] P. Oxley, Ph.D. thesis, Harvard University, 2003.

[45] N. Bowden, Ph.D. thesis, Harvard University, 2003.

[46] A. Speck, Ph.D. thesis, Harvard University, 2005.

[47] W. S. Kolthammer, Ph.D. thesis, Harvard University, 2011.

[48] L. S. Brown and G. Gabrielse, Rev. Mod. Phys. **58**, 233 (1986).

[49] G. Gabrielse and F. Colin MacKintosh, Intl. J. Mass Spec. Ion Proc. **57**, 1 (1984).

[50] G. Gabrielse, Phys. Rev. A **27**, 2277 (1983).

[51] J. Wrubel, G. Gabrielse, W.S. Kolthammer, P. Larochelle, R. McConnell, P. Richerme, D. Grzonka, W. Oelert, T. Sefzick, M. Zielinski, J.S. Borbely, M.C. George, E.A. Hessels, C.H. Storry, M. Weel, A. Muellers, J. Walz, and A. Speck, Nuclear Instruments and Methods in Physics Research Section A: Accelerators, Spectrometers, Detectors and Associated Equipment **640**, 232 (2011).

[52] D. E. Pritchard, Phys. Rev. Lett. **51**, 1336 (1983).

[53] M. H. Anderson, J. R. Ensher, M. R. Matthews, C. E. Wieman, and E. A. Cornell, Science **269**, 198 (1995).

[54] K. B. Davis, M. O. Mewes, M. R. Andrews, N. J. van Druten, D. S. Durfee, D. M. Kurn, and W. Ketterle, Phys. Rev. Lett. **75**, 3969 (1995).

[55] C. L. Cesar, D. G. Fried, T. C. Killian, A. D. Polcyn, J. C. Sandberg, I. A. Yu, T. J. Greytak, D. Kleppner, and J. M. Doyle, Phys. Rev. Lett. **77**, 255 (1996).

[56] D. Lesage, Ph.D. thesis, Harvard University, 2008.

[57] S. L. Rolston and G. Gabrielse, Hyperfine Interact. **44**, 233 (1988).

[58] B. Levitt, G. Gabrielse, P. Larochelle, D. Le Sage, W.S. Kolthammer, R. McConnell, J. Wrubel, A. Speck, D. Grzonka, W. Oelert, T. Sefzick, Z. Zhang, D. Comeau, M.C. George, E.A. Hessels, C.H. Storry, M. Weel, and J. Walz, Physics Letters B **656**, 25 (2007).

[59] A. Einstein, Ann. Phys. **17**, 132 (1905).

[60] Xinrong Jiang, C. N. Berglund, Anthony E. Bell, and William A. Mackie, *OS3: Photoemission from gold thin films for application in multiphotocathode arrays for electron beam lithography* (AVS, Chicago, IL, 1998), No. 6, pp. 3374–3379.

[61] R. D. Dixon and L. A. Lott, Journal of Applied Physics **40**, 4938 (1969).

[62] C. M. Surko, M. Leventhal, and A. Passner, Phys. Rev. Lett. **62**, 901 (1989).

[63] D. Comeau, Ph.D. thesis, York University, to be published.

[64] A. Mills and E. Gullikson, Appl. Phys. Lett. **49**, 1121 (1986).

[65] G. Gabrielse, X. Fei, K. Helmerson, S. L. Rolston, R. L. Tjoelker, T. A. Trainor, H. Kalinowsky, J. Haas, and W. Kells, Phys. Rev. Lett. **57**, 2504 (1986).

[66] S. Maury, Hyperfine Int. **109**, 43 (1997).

[67] P. Belochitskii, T. Eriksson, and S. Maury, Nuclear Instruments and Methods in Physics Research Section B: Beam Interactions with Materials and Atoms **214**, 176 (2004), low Energy Antiproton Physics (LEAP'03).

[68] Yasunori Yamazaki, Nuclear Instruments and Methods in Physics Research Section B: Beam Interactions with Materials and Atoms **154**, 174 (1999).

[69] H Herr, Ettore Majorana Int. Sci. Ser., Phys. Sci. **17**, 633 (1982).

[70] G. Gabrielse, N. S. Bowden, P. Oxley, A. Speck, C. H. Storry, J. N. Tan, M. Wessels, D. Grzonka, W. Oelert, G. Schepers, T. Sefzick, J. Walz, H. Pittner, and E. A. Hessels, Phys. Lett. B **548**, 140 (2002).

[71] D. J. Wineland and H. G. Dehmelt, J. Appl. Phys. **46**, 919 (1975).

[72] G. Gabrielse, X. Fei, L. A. Orozco, R. L. Tjoelker, J. Haas, H. Kalinowsky, T. A. Trainor, and W. Kells, Phys. Rev. Lett. **65**, 1317 (1990).

[73] P. Larochelle, Ph.D. thesis, Harvard University, 2009.

[74] A. Weiss, R. Mayer, M. Jibaly, C. Lei, D. Mehl, and K. G. Lynn, Phys. Rev. Lett. **61**, 2245 (1988).

[75] G. Bendiscioli and D. Kharzeev, La Rivista del Nuovo Cimento (1978-1999) **17**, 1 (1994), 10.1007/BF02724447.

[76] Zhongdong Zhang, Ph.D. thesis, Ruhr-Universitat Bochum, 2007.

[77] R. J. Goldston and P. H. Rutherford, *Introduction to Plasma Physics* (Inst. of Phys., London, 1995).

[78] J. D. Huba, *2009 NRL Plasma Formulary* (Naval Research Laboratory, Washington, D. C., 2009).

[79] D. H. E. Dubin and T. M. O'Neil, Rev. Mod. Phys. **71**, 87 (1999).

[80] M. Glinsky and T. O'Neil, Phys. Fluids **B3**, 1279 (1991).

[81] Setsuo Ichimaru and Marshall N. Rosenbluth, Physics of Fluids **13**, 2778 (1970).

[82] David Montgomery, Glenn Joyce, and Leaf Turner, Physics of Fluids **17**, 2201 (1974).

[83] T. M. O'Neil and P. G. Hjorth, Phys. Fluids **28**, 3241 (1985).

[84] B. R. Beck, J. Fajans, and J. H. Malmberg, Phys. Rev. Lett. **68**, 317 (1992).

[85] T. M. O'Neil and C. F. Driscoll, Physics of Fluids **22**, 266 (1979).

[86] H. Goldstein, C. Poole, and J. Safko, *Classical Mechanics*, 3rd ed. (Addison Wesley, Reading, MA, 2002).

[87] Ronald C. Davidson and Nicholas A. Krall, Phys. Fluids **13**, 1543 (1970).

[88] J. J. Bollinger and D. J. Wineland, Phys. Rev. Lett. **53**, 348 (1984).

[89] Leaf Turner, Phys. Fluids **30**, 3196 (1987).

[90] R. L. Spencer, S. N. Rasband, and R. R. Vanfleet, Phys. Fluids B **5**, 4267 (1993).

[91] M. Amoretti, et al., Phys. Plas. **10**, 3056 (2003).

[92] J. H. Malmberg and J. S. deGrassie, Phys. Rev. Lett. **35**, 577 (1975).

[93] D. J. Heinzen, J. J. Bollinger, F. L. Moore, Wayne M. Itano, and D. J. Wineland, Phys. Rev. Lett. **66**, 2080 (1991).

[94] D. H. E. Dubin, Phys. Rev. Lett. **66**, 2076 (1991).

[95] D. H. E. Dubin, Phys. Fluids B **5**, 295 (1993).

[96] C. S. Weimer, J. J. Bollinger, F. L. Moore, and D. J. Wineland, Phys. Rev. A **49**, 3842 (1994).

[97] M. Amoretti, et al., Phys. Rev. Lett. **91**, 55001 (2003).

[98] A. Speck, G. Gabrielse, P. Larochelle, D. Le Sage, B. Levitt, W.S. Kolthammer, R. McConnell, J. Wrubel, D. Grzonka, W. Oelert, T. Sefzick, Z. Zhang, D. Comeau, M. C. George, E.A. Hessels, C. Storry, M. Weel, and J. Walz, Phys. Lett. B **650**, 119 (2007).

[99] C. F. Driscoll, K. S. Fine, and J.H. Malmberg, Phys. Fluids **29**, 2015 (1986).

[100] X. P. Huang, F. Anderegg, E. M. Hollmann, C. F. Driscoll, and T. M. O'Neil, Phys. Rev. Lett. **78**, 875 (1997).

[101] F. Anderegg, E. M. Hollmann, and C. F. Driscoll, Phys. Rev. Lett. **81**, 4875 (1998).

[102] X. P. Huang, J. J. Bollinger, T. B. Mitchell, and W. M. Itano, Phys. Rev. Lett. **80**, 73 (1998).

[103] X.-P. Huang, J. J. Bollinger, T. B. Mitchell, W. M. Itano, and D. H. E. Dubin, Physics of Plasmas **5**, 1656 (1998).

[104] E. M. Hollmann, F. Anderegg, and C. F. Driscoll, Physics of Plasmas **7**, 2776 (2000).

[105] R. G. Greaves and C. M. Surko, Phys. Rev. Lett. **85**, 1883 (2000).

[106] J. R. Danielson and C. M. Surko, Phys. Rev. Lett. **94**, 035001 (2005).

[107] J. R. Danielson and C. M. Surko, Physics of Plasmas **13**, 055706 (2006).

[108] L. V. Jørgensen, M. Amoretti, G. Bonomi, P. D. Bowe, C. Canali, C. Carraro, C. L. Cesar, M. Charlton, M. Doser, A. Fontana, M. C. Fujiwara, R. Funakoshi, P. Genova, J. S. Hangst, R. S. Hayano, A. Kellerbauer, V. Lagomarsino, R. Landua, E. Lodi Rizzini, M. Macrì, N. Madsen, D. Mitchard, P. Montagna, A. Rotondi, G. Testera, A. Variola, L. Venturelli, D. P. van der Werf, and Y. Yamazaki, Phys. Rev. Lett. **95**, 025002 (2005).

[109] R. Funakoshi, M. Amoretti, G. Bonomi, P. D. Bowe, C. Canali, C. Carraro, C. L. Cesar, M. Charlton, M. Doser, A. Fontana, M. C. Fujiwara, P. Genova, J. S. Hangst, R. S. Hayano, L. V. Jørgensen, A. Kellerbauer, V. Lagomarsino, R. Landua, E. Lodi Rizzini, M. Macrì, N. Madsen, G. Manuzio, D. Mitchard, P. Montagna, L. G. C. Posada, A. Rotondi, G. Testera, A. Variola, L. Venturelli, D. P. van der Werf, Y. Yamazaki, and N. Zurlo, Phys. Rev. A **76**, 012713 (2007).

[110] T. M. O'Neil, Physics of Fluids **24**, 1447 (1981).

[111] G. B. Andresen, M. D. Ashkezari, M. Baquero-Ruiz, W. Bertsche, P. D. Bowe, E. Butler, C. L. Cesar, S. Chapman, M. Charlton, A. Deller, S. Eriksson, J. Fajans, T. Friesen, M. C. Fujiwara, D. R. Gill, A. Gutierrez, J. S. Hangst, W. N. Hardy, M. E. Hayden, A. J. Humphries, R. Hydomako, S. Jonsell, N. Madsen, S. Menary, P. Nolan, A. Olin, A. Povilus, P. Pusa, F. Robicheaux, E. Sarid, D. M. Silveira, C. So, J. W. Storey, R. I. Thompson, D. P. van der Werf, J. S. Wurtele, and Y. Yamazaki, Phys. Rev. Lett. **106**, 145001 (2011).

[112] D. J. Larson, J. C. Bergquist, J. J. Bollinger, W. M. Itano, and D. J. Wineland, Phys. Rev. Lett. **57**, 70 (1986).

[113] B. M. Jelenkovic, A. S. Newbury, J. J. Bollinger, W. M. Itano, and T. B. Mitchell, Phys. Rev. A **67**, 063406 (2003).

[114] R. G. Greaves and J. M. Moxom, Physics of Plasmas **15**, 072304 (2008).

[115] E. A. Hessels, D. M. Homan, and M. J. Cavagnero, Phys. Rev. A **57**, 1668 (1998).

[116] M. Amoretti, C. Amsler, G. Bonomi, A. Bouchta, P. D. Bowe, C. Carraro, C. L. Cesar, M. Charlton, M. Doser, V. Filippini, A. Fontana, M. C. Fujiwara, R. Funakoshi, P. Genova, J. S. Hangst, R. S. Hayano, L. V. Jorgensen, A. Kellerbauer, V. Lagomarsino, R. Landua, D. Lindelof, E. L. Rizzini, M. Macri, N. Madsen, G. Manuzio, P. Montagna, H. Pruys, C. Regenfus, A. Rotondi, G. Testera, A. Variola, L. Venturelli, D. P. van der Werf, and Y. Yamazaki, Phys. Lett. B **590**, 133 (2004).

[117] D. Griffiths, *Introduction to Electodynamics, 3rd ed.* (Prentice Hall, Upper Saddle River, New Jersey, 1999).

[118] M. D. Tinkle, R. G. Greaves, C. M. Surko, R. L. Spencer, and G. W. Mason, Phys. Rev. Lett. **40**, 352 (1994).

[119] D. L. Eggleston, C. F. Driscoll, B. R. Beck, A. W. Hyatt, and J. H. Malmberg, Physics of Fluids B: Plasma Physics **4**, 3432 (1992).

[120] Daniel H. E. Dubin, Phys. Rev. E **53**, 5268 (1996).

[121] M. D. Tinkle, R. G. Greaves, and C. M. Surko, Physics of Plasmas **2**, 2880 (1995).

[122] Harald F. Hess, Phys. Rev. B **34**, 3476 (1986).

[123] T. M. O'Neil and Daniel H. E. Dubin, Physics of Plasmas **5**, 2163 (1998).

[124] G. Li, R. Poggiani, G. Testera, and G. Werth, Hyperfine Interactions **76**, 281 (1993), 10.1007/BF02316725.

[125] C. Wesdorp, F. Robicheaux, and L. D. Noordam, Phys. Rev. Lett. **84**, 3799 (2000).

[126] R. Neumann, H. Poth, A. Winnackker, and A. Wolf, Z. Phys. A **313**, 253 (1983).

[127] D. R. Bates and A. Dalgarno, in *Atomic and Molecular Processes*, edited by D. R. Bates (Academic Press, New York, 1962), pp. 245–271.

[128] F Robicheaux, Journal of Physics B: Atomic, Molecular and Optical Physics **41**, 192001 (2008).

[129] U. Schramm, J. Berger, M. Grieser, D. Habs, E. Jaeschke, G. Kilgus, D. Schwalm, A. Wolf, R. Neumann, and R. Schuch, Phys. Rev. Lett. **67**, 22 (1991).

[130] F. B. Yousif, P. Van der Donk, Z. Kucherovksy, J. Reis, E. Brannen, J. B. A. Mitchell, and T. J. Morgan, Phys. Rev. Lett. **67**, 26 (1991).

[131] M. Amoretti, C. Amsler, G. Bonomi, P. D. Bowe, C. Canali, C. Carraro, C. L. Cesar, M. Charlton, A. M. Ejsing, A. Fontana, M. C. Fujiwara, R. Funakoshi, P. Genova, J. S. Hangst, R. S. Hayano, L. V. Jorgensen, A. Kellerbauer, V. Lagomarsino, E. Lodi Rizzini, M. Macri, N. Madsen, G. Manuzio, D. Mitchard, P. Montagna, L. G. C. Posada, H. Pruys, C. Regenfus, A. Rotondi, H. H. Telle, G. Testera, D. P. Van der Werf, A. Variola, L. Venturelli, Y. Yamazaki, and N. Zurlo ATHENA Collaboration, Physical Review Letters **97**, 213401 (2006).

[132] J. Stevefelt, J. Boulmer, and J. F. Delpech, Phys. Rev. A **12**, 1246 (1975).

[133] D. R. Bates, A. E. Kingston, and R. W. P McWhirter, Proc. Roy. Soc. Lond. A **267**, 297 (1962).

[134] F. Robicheaux and J. D. Hanson, Phys. Rev. A **69**, 010701(R) (2004).

[135] J. L. Hurt, P. T. Carpenter, C. L. Taylor, and F Robicheaux, J. Phys. B **41**, 165206 (2008).

[136] G. Gabrielse, S. L. Rolston, L. Haarsma, and W. Kells, Phys. Lett. A **129**, 38 (1988).

[137] M. Amoretti, et al., Phys. Lett. B **583**, 59 (2004).

[138] G. Gabrielse, A. Speck, C. H. Storry, D. Le Sage, N. Guise, D. Grzonka, W. Oelert, G. Schepers, T. Sefzick, H. Pittner, J. Walz, T. W. Hänsch, D. Comeau, and E. A. Hessels, Phys. Rev. Lett. **93**, 073401 (2004).

[139] T. Pohl, H. R. Sadeghpour, and G. Gabrielse, Physical Review Letters **97**, 143401 (2006).

[140] T. M. Squires, P. Yesley, and G. Gabrielse, Phys. Rev. Lett. **86**, 5266 (2001).

[141] J. Fajans, W. Bertsche, K. Burke, S. F. Chapman, and D.P van der Werf, Phys. Rev. Lett. **95**, 155001 (2005).

[142] E. P. Gilson and J. Fajans, Phys. Rev. Lett. **90**, 015001 (2003).

[143] F Robicheaux, Phys. Rev. A **73**, 033401 (2006).

[144] M. L. Wall, C. S. Norton, and F. Robicheaux, Phys. Rev. A **72**, 052702 (2005).

[145] G. B. Andresen *et al.*, Nature Physics **7**, 558 (2011).

[146] C. H. Storry, A. Speck, D. Le Sage, N. Guise, G. Gabrielse, D. Grzonka, W. Oelert, G. Schepers, T. Sefzick, H. Pittner, M. Herrmann, J. Walz, T. W. Hänsch, D. Comeau, and E. A. Hessels, Phys. Rev. Lett. **93**, 263401 (2004).

[147] J W Humberston, M Charlton, F M Jacobson, and B I Deutch, Journal of Physics B: Atomic and Molecular Physics **20**, L25 (1987).

[148] J. P. Merrison, H. Bluhme, J. Chevallier, B. I. Deutch, P. Hvelplund, L. V. Jørgensen, H. Knudsen, M. R. Poulsen, and M. Charlton, Phys. Rev. Lett. **78**, 2728 (1997).

[149] M. Charlton, Physics Letters A **143**, 143 (1990).

[150] A. Speck, C.H. Storry, E.A. Hessels, and G. Gabrielse, Physics Letters B **597**, 257 (2004).

[151] D. A. Steck, *Cesium D Line Data (rev. 2.1.4)* (http://steck.us/alkalidata, University of Oregon, 2010).

[152] G. Breit and I. I. Rabi, Phys. Rev. **38**, 2082 (1931).

[153] C. J. Lorenzen and K. Niemax, Zeitschrift fur Physik A Hadrons and Nuclei **315**, 127 (1984), 10.1007/BF01419370.

[154] L. I. Schiff and H. Snyder, Phys. Rev. **55**, 59 (1939).

[155] N. P. Economou, R. R. Freeman, and P. F. Liao, Phys. Rev. A **18**, 2506 (1978).

[156] Edward S. Chang, Phys. Rev. A **31**, 495 (1985).

[157] T.W. Hansch and B. Couillaud, Optics Communications **35**, 441 (1980).

[158] A. Speck, C. H. Storry, E.A. Hessels, and G. Gabrielse, Phys. Lett. B **597**, 257 (2004).

[159] K. B. MacAdam, N. L. S. Martin, D. B. Smith, R. G. Rolfes, and D. Richards, Phys. Rev. A **34**, 4661 (1986).

[160] William Shakespeare, *King Lear* (Edward Blount, Isaac Jaggard, William Jaggard, London, 1623), "We are not the first / Who with best meaning have incurred the worst." (V.iii.3-4).